DEVELOPMENT OF A VERSATILE HIGH SPEED NANOMETER LEVEL SCANNING MULTI-PROBE MICROSCOPE

by

Feilong Lin

A dissertation submitted to the faculty of
The University of North Carolina at Charlotte
in partial fulfillment of the requirements
for the degree of Doctor of Philosophy in
Mechanical Engineering

Charlotte

2011

Approved by:

____
Dr. Stuart T. Smith

____
Dr. Robert J. Hocken

____
Dr. Patrick J. Moyer

____
Dr. Gloria D. Elliott

____
Dr. Andriy Baumketner

©2011
Feilong Lin
ALL RIGHTS RESERVED

ABSTRACT

FEILONG LIN. Development of a versatile high speed nanometer level scanning multi-probe microscope (Under the direction of DR. STUART T. SMITH)

The motivation for development of a multi-probe scanning microscope, presented in this dissertation, is to provide a versatile measurement tool mainly targeted for biological studies, especially on the mechanical and structural properties of an intracellular system. This instrument provides a real-time, three-dimensional (3D) scanning capability. It is capable of operating on feedback from multiple probes, and has an interface for confocal photo-detection of fluorescence-based and single molecule imaging sensitivity. The instrument platform is called a Scanning Multi-Probe Microscope (SMPM) and enables 45 μm by 45 μm by 10 μm navigation of specimen with simultaneous optical and mechanical probing with each probe location being adjustable for collocation or for probing with known probe separations. The 3D positioning stage where the specimen locates was designed to have nanometer resolution and repeatability at 10 Hz scan speed with either open loop or closed loop operating modes.

The fine motion of the stage is comprises three orthogonal flexures driven by piezoelectric actuators via a lever linkage. The flexures design is able to scan in larger range especially in z axis and serial connection of the stages helps to minimize the coupling between x, y and z axes. Closed-loop control was realized by the capacitance gauges attached to a rectangular block mounted to the underside of the fine stage upon which the specimen is mounted. The stage's performance was studied theoretically and verified by experimental test. In a step response test and using a simple proportional and

integral (PI) controller, standard deviations of 1.9 nm 1.8 nm and 0.41 nm in the x, y and z axes were observed after settling times of 5 ms and 20 ms for the x and y axes. Scanning and imaging of biological specimen and artifact grating are presented to demonstrate the system operation.

For faster, short range scanning, novel ultra-fast fiber scanning system was integrated into the xyz fine stage to achieve a super precision dual scanning system. The initial design enables nanometer positioning resolution and runs at 100 Hz scan speed. Both scanning systems are capable of characterization using dimensional metrology tools. Additionally, because the high-bandwidth, ultra-fast scanning system operates through a novel optical attenuating lever, it is physically separate from the longer range scanner and thereby does not introduce additional positioning noise. The dual scanner provides a fine scanning mechanism at relatively low speed and large imaging area using the xyz stage, and focus on a smaller area of interested in a high speed by the ultra-fast scanner easily. Such functionality is beneficial for researchers to study intracellular dynamic motion which requires high speed imaging.

Finally, two high end displacement sensor systems, a knife edge sensor and fiber interferometer, were demonstrated as sensing solutions for potential feedback tools to boost the precision and resolution performance of the SMPM.

ACKNOWLEDGEMENTS

I am heartily thankful to a lot people who made this dissertation possible. First and foremost, I would like to thank my adviser Dr. Stuart Smith for his tremendous kindness, help, patience, and direction on this instrument development. Without him, I won't be able to complete his project. His knowledge on precision metrology and instrumentation as well as other fields always encourages me to study hard and learn more and more. I also want to thank Dr. Robert Hocken and the Center for Precision Metrology for the support in these years. Further thanks to Dr. Patrick Moyer and Dr. Gloria Elliot in the direction and effort of this project. I would also thanks Dr. Andriy Baumketner in serving as my dissertation committee member and his advice on presentation.

I would also like to thank Dr. Jimmie Miller for lending various measurement instruments and samples needed for this project and his help of setting up the equipments.

I would also like to thank Joel Pritchard, Roland Hege, and Brian Dutterer for their work and suggestions in manufacturing parts for this project. Also I would like to thank John Brien for his help with the electrical components and suggestions of the electrical circuit design.

I would also thank my friends, Dr. Kevin Elliot, Dr. Eric Bruce, Dr. Bartosz Nowakowski, Brandon Ring, Hua Yang, Wes Parker, Garland Vacanti, Tiffany Lemmons, and Ryan Hefti for their help in my research and this project.

I would also like to thank mechanical engineering department, Chinese scholarship Council and the Graduate Professional Student Government for funding on this project as well as tuition support.

I would also like to thank InsituTec for supplying a *xyz* stage for testing equipment

in this project.

I would like to thank my wife, Dr. Jing Huang in supporting me during these four years. Without her understanding and support, I won't be able to finish the dissertation.

Lastly, I want to thank and bless all of those who supported me in any respect during the completion of the project.

TABLE OF CONTENTS

CHAPTER 1:BACKGROUND AND MOTIVATION 1

1.1 Overview of SPM 1

1.2 SMPM introduction 4

1.2.1 Objective of this project 4

1.2.2 Previous work 10

1.2.3 Contributions of this project 12

1.2.4 Design, Schematic, Components 15

CHAPTER 2: SCANNING STAGE AND SENSOR DEVELOPMETN AND CONTROLLER CHARACTERIZATON 19

2.1 Capacitance sensor 21

2.1.1 Theory and design 23

2.1.2 Design, manufacture and assembly of the capacitance position sensors 25

2.1.3 Signal conditioning innovations 32

2.1.4 Pre-Amp design for digital demodulation 42

2.2 Error analysis and positioning uncertainty 43

2.2.1 Sensor noise 43

2.2.2 Straightness error 45

2.2.3 Other sources of uncertainty 47

2.3 Controller design and positioning performance characterization 47

2.3.1 Controller considerations 47

2.3.2 Controller design and test 49

CHAPTER 3: FAST SCANNER 60

3.1 Overview 60

3.2 Introduction and motivation for the fast scanner 61

3.3 Mechanical design of the fast scanner 63

3.4 Displacement sensor design, calibration and test 71

3.5 Controller design and implementation 77

3.5.1 System description: theoretical analysis 78

3.5.2 Experimental results 79

3.5.3 Plant modeling for controller design 81

3.5.4 Controller design 84

3.5.5 Viscous damping material 91

3.6 Issues 93

3.6.1 Bandwidth analysis 93

3.6.2 Problem 2: Ring phenomenon at the crossover point 99

3.7 Experiment setup and images 116

3.7.1 Open loop experiment using Sylgard 117

3.7.2 Closed loop imaging 119

3.8 Conclusion 124

CHAPTER 4:CONTROLLER AND USER INTERFACE 125

4.1 Controller hardware types and Pros-Cons 125

4.1.1 Real-Time 129

4.1.2 FPGA 130

4.2 Open loop and closed loop 131

4.3 Scanning algorithm 132

4.4 Graphic user interface 134

4.5 Conclusion 135

CHAPTER 5: INVERSTIAGTIONS OF OTHER HIGH BANDWIDTH DISPLACMENTS METHODS (KNIFE EDGE SENSOR AND FIBER INTERFEROMETRY) 136

5.1 Fiber interferometer 136

5.1.1 Introduction 136

5.1.2 Experiment setup 137

5.1.3 Wavelength sweep mode 139

5.1.4 Cavity sweep mode 141

5.1.5 Two subsystems 153

5.1.6 Conclusion 155

5.2 Optical fiber displacement sensor[45] 155

5.2.1 Introduction 155

5.2.2 Principle of operation 156

5.2.3 Experimental measurement 159

5.2.4 Results 162

5.2.5 Conclusion 174

CHAPTER 6:PROBES 175

6.1 Optical probe 175

6.2 Mechanical probes 179

6.2.1 Tuning fork 179

6.2.2 Capacitance probe 181

6.3 Conclusion 189

CHAPTER 7:CONCLUSIONS AND FUTURE WORK 190

7.1 Conclusions 190

7.2 Future work 192

REFERENCES 194

APPENDIX A: SPREADSHEET FOR XY FAST SCANNER FLEXURE DESIGN 200

CHAPTER 1: BACKGROUND AND MOTIVATION

1.1 Overview of SPM

Development of the scanning probe microscope has provided a new characterization tool for observing nano scale features and has become a driving force of nano-science and nano technology. These latest microscopes use different physical probes to scan the sample surface or inside. The SPM was developed based on the scanning tunneling microscope (STM) [1]. According to different principles of surface proximity detection, the SPM includes atomic force microscope [2], lateral force microscope [3], tunneling current microscope [1], magnetic force microscope [4], scanning near-field optical microscope [5], electrostatic force microscopy [6], and many others. Unlike optical microscopes whose resolution is limited by diffraction, the SPM's resolution and localization of microscopic techniques, being dependent upon both probe sensor and precision of piezoelectric actuators, has been pushed down to nanometer level or atomic level with the development. It does not require a partial vacuum condition to operate like the Scanning Electron Microscope (SEM), but can be observed in ambient or liquid environments at standard temperature and pressure. The sample does not need to be pre-processed and the variety of available SPM methods can be applied for characterization of a correspondingly broad variety of materials. Last but not least, the SPM can be adapted to become a useful tool for manufacturing and manipulation with nanometer

control. Therefore, the SPM is a universal tool nowadays in nanotechnology, material science, physics, chemical and the life sciences [7-15].

TABLE 1-1: Overview of probe sensing methods and typical lateral resolution limits

	Type	Detected signal	resolution
SPM	STM	Tunneling current between probe and sample	0.1 nm
	AFM	Force between probe and sample	
	Lateral force AFM	Lateral force between probe and sample	
	Magnetic FM	Magnetic force between probe and sample	10 nm
	Electrostatic force microscopy	Electrostatic force between probe and sample	1 nm
	SNOM	Optical Response of the optical probe-sample interaction	100 nm

There are several limitations of SPM. Because the nature of scanning pixel algorithm, the speed and range of imaging is lower than many other microscope technologies. Meanwhile, the 3D spatial information is constructed based on the time sequence from scanning, which leads to metrological uncertainty from the scanner, metrology loop drift, feedback loop oscillation, and mechanical vibration. Also the detected signal comes from the interaction between probe and sample, therefore the geometry of the probe will cause image distortion as well. In this project, methods for the improvement of scanning performance are studied, including a metrological linear scanner design, building, test and uncertainty budget, design and build of a real time high speed closed loop controller, a sensor system using various signal conditionings for nanometer resolution, an optical probe and two mechanical probes, and others.

Confocal laser scanning optical microscope (CLSM) is one type of SPM and this has served as the test platform for the studies presented in this thesis. Unlike traditional wide

field optical microscope, in which the whole sample is imaged at the same time, in confocal microscopy a focused light source (laser beam) is scanned onto the sample pixel by pixel. Spatial resolution comparable to the point spread function of the optics can be achieved using CLSM, and total internal reflection fluorescence (TIRF) microscopy [16]. In CLSM imaging, the laser spot is focused down into a diffraction-limited spot size typically of 500 nm or less in diameter and the sample or beam is scanned in the *XY* (lateral) plane so that an image can be generated one pixel at a time. At each discrete pixel, the scattered and reflected laser light as well as any fluorescent light from the focus point where the laser beam hereby behaves as a probe intersects with the specimen is collected by the objective lens, transmitted to and detected using an optical sensor (usually a photomultiplier tube (PMT) or avalanche photo-diode (APD)). A sample image is constructed with the matrix of the pixels. With metrological scanning microscope systems, the sample or lens can then be translated in the z direction so that a 3-dimensional fluorescence map can be generated. In TIRF microscopy, the imaging volume is limited to the nearest 100 nm from the top of the glass slide on which the sample resides. This severely limits applicability to live cell imaging which was one of the original goals of this thesis study.

Another type of SPM, the atomic force microscope (AFM) is the most common type of scan probe microscope in the fields of nanotechnology, chemistry, biology and materials science. This is primarily for its ability to work in ambient conditions and image electrically insulating samples with nanometer level vertical and, under suitable conditions, lateral resolution [2]. The main components of AFM are probes, optical detection system, scanner and controller. In AFM, the mechanical force interaction

between a probe on a cantilever beam and a sample surface are used for surface imaging. When the probe tip approaches the surface, the so-called atomic force (more precisely, the interaction force) causes the cantilever to bend. In most of today's commercial microscopes the cantilever deflection (Set point) is measured by a laser beam which is reflected from the cantilever arm to a four-segment positional photo-detector. By adjust the probe axis (usually positioned by a PZT actuator) where the cantilever is set up, the SP is controlled at a constant preset value. Therefore the probe will track the surface height variation which can be presented by the position of the probe axis. The ability to measure interaction forces between the probe and specimen make it a suitable characterization technique to measure topographic data, adhesion, stiffness, viscoelasticity and other dynamic process and properties of the biological samples, i.e. biopolymers, bio-molecular, organelles, and cells etc…[2]

1.2 SMPM introduction

1.2.1 Objective of this project

The ability to monitor properties of a single cell, in real-time, at high speed and under appropriate environmental conditions, offers a wide range of possibilities for fruitful biological exploration. The goals of this study were to develop a second generation scanning system that is able to perform surface measurements for physical properties of intercellular and other biological systems. This work was a collaboration between the Mechanical Engineering department, the Center for Precision Metrology, the Center for Biomedical Engineering Systems and the Center for Optical Sciences and Optical Communications at the University of North Carolina at Charlotte. It is also worth pointing out that, even though this system was specifically designed to meet the

biological measurement demands, its open source hardware and software mean that it is able to function as a versatile measurement system that can be readily interfaced to any type of proximity probe sensor. The system is currently used by researchers from Physics, Mechanical and Nano science programs.

As discussed in the previous section, since the AFM and optical microscope have advantages and disadvantages over each other, efforts have been made to combine measurement and imaging techniques with hybrid instruments utilizing both optical and mechanical probing techniques simultaneously, with, initially, a focus to investigate biological samples.

In parallel with the work carried out at UNC Charlotte there have been a number of similar researches at other institutes. Manfred Radmacher et al., [17] have developed an integrated micro-fluorescence/atomic force microscope which covers a field of view of 4×4 mm at a resolution of about 3 μm in fluorescence microscopy and a field of 15×15 μm^2 down to atomic resolution in AFM mode and get AFM images of polymerized Langmuir-Blodgett films at molecular resolution with simultaneous micro-fluorescence measurements. R.Kassies et al., [18] presented an atomic force fluorescence microscope (AFFM) which can perform simultaneous topographic and optical imaging with single molecule sensitivity over a range of 40 μm x 40 μm in open loop. Anshu Bagga Mathur et al., [19] mounted a Bioscope AFM from Digital Instruments on an inverted microscope (Zeiss Axiovert 100 TV inverted microscope) to study stress transmission from the tip to the basal surface of an adherent cell by the force-indentation curves.

The system of this project is a unique, 3D, bio-metrology instrument to enable multi-probe biological sensing. The design incorporates two different feedback mechanisms so

that the cell can be optically sectioned (such as conventional confocal microscopy) or it can be optically profiled across the cell surface. With this instrument it is possible to section at any given topographic depth below the top surface of the cell. This makes 3D optical image feasible, and is well-suited for many biophysical investigations of cells, including the study of cell membranes and the intracellular uptake of proteins and drug-containing nano-particles that can be sensed with optical (fluorescence-based) probes. There is no commercial instrument - or homebuilt instrument to our knowledge - that has the potential to provide this type of flexibility in studying individual live cells, especially with the stability and linearity that our design imparts. In particular, our design incorporates the following attributes:

- Single molecule optical imaging and lifetime sensitivity.
- 50 μm scan range in the *x* and *y* directions, and 10 μm scan range in the *z* direction with closed loop control which enable precise, linear, repeatable scans and zoom in and out operation and accurate location of individual region of interest.
- AFM imaging and force probe capabilities.
- Nanosecond temporal resolution for lifetime and rotational correlation times in the optical detection.
- Multiple profile measurement capabilities for optically sectioning or navigation in 3D with position being measured relative to the topography of the cell.
- Customized hardware and software make an open system which is readily adapted to various configurations for scanning algorithm, and implementation of multi-channels measurement.

In general, our 3D multi-probe scanning system comprises the following key components:

- A state-of-the-art *xyz* scanning stage to enable three dimensional navigation of a specimen up to 10 Hz.
- A state-of-the-art *xy* scanner for positioning of the confocal illumination source to enable ultra-fast scanning rate up to couple hundred lines per second for confocal scanning.
- Mechanical and optical probes to determine physical interaction properties in local regions on a specimen.
- Scanning systems for dynamic positioning of the probes relative to the specimen.
- A state-of-the-art controller based on LabVIEW™ FPGA and Real-Time enables high speed control and signal process with long term stability and unique functionality for multi-channel imaging.

TABLE 1-2: Comparison of current commercial and academic confocal microscopes

CLSM	Leica TCS SP5 II	Olympus FluoView™ FV1000	Nikon A1
Microscopes	Upright / Inverted	Upright / Inverted	
Coarse stage			
Scanner	galvano/ resonant scanner	galvano	galvano/ resonant scanner
Scan speed	2800 Hz / 16000 Hz		2000 Hz / 15600 Hz
Scan range	up to 22 mm	up to 18 mm	up to 18 mm
Open/closed			
Z-drive	15 nm step size(galvanometer stage)	10 nm step size (motorized)	25/50 nm stepping motor
Image resolution	/	/	/
localization precision	up to 40 nm	up to 100 nm	/
Continuous wave lasers	VIS	selectable VIS/Violet/UV	
Pulsed lasers	IR (690 nm - 1040 nm)	/	
Detector	PMT: R 9624	PMT	PMT
Channel	5 Max		32
Controller	FPGA		
Counter			
CLSM	Harvard University[20]	Florida State University[21]	SMPM
Microscopes			Inverted
Coarse stage	xy motorized 25 mm		25 mm micrometer dovetail slider
Scanner	PI xy PZT flexure	PI xy PZT flexure	xyz/xy dual scanner
Scan speed	2.5 Hz	1.25 Hz	10 Hz /100 Hz (fast scanner)
Scan range	20 μm by 20 μm	20 μm by 20 μm	45 um by 45 μm by 10 μm
Open/closed	Open	Open	Open/closed

TABLE 1-2 (continued)

Z-drive	/	/	sub nm step
Image resolution	200 nm	/	220 nm laterally and 450 nm axially
localization precision	/		0.4 nm / 5.83 nm
Continuous wave lasers	Ar+ laser	cw, doubled YAG laser	532 nm NDY/AG, argon ion laser
Pulsed lasers			pulsed picosecond 470 nm laser
Detector	APD	APD	PMT/CCD
Channel	1	1	2
Controller	National Instruments DAQ	National Instruments DAQ	National Instruments, Real time, FPGA
Counter		20 MHz	40 MHz

TABLE 1-2 compares the SMPM with several popular commercial CSLM as well as two CSLM from academic. The mains differences between the commercial products and the academic instruments are the scan range and speed. The commercial CSLMs are able to image at video frame speed at couple millimeter range by using linear galvanometer, resonant scanners, or acousto-optical device (AOD) to scan mirrors in the excitation beam path in order to scan the beam in the xy sample plane. The academic home build CSLMs use the sample scanning method via a PZT scanner which provides best image quality as the scanner can provide precision and repeatability of several nanometers. However, the imaging speed is very low and the scan range is within tens micrometers in these instruments compared to the commercial products. Our SMPM still has some unique features, i.e. z axis with ultra-fine step control enabling well focusing, dual scanner with much higher scan speed and larger scan range than the other two academic instruments, high speed controller with open/closed loop feature and multichannel support, sub-nanometer localization resolution and tens nanometer pixel/image accuracy which are higher than the commercial products.

1.2.2 Previous work

The first generation of the system was accomplished by Dr. Kevin Elliot [22]. FIGURE 1-1 shows the photo and block diagram of the mechanical parts of the system. The scanning system (fine stage) was designed based on flexure mechanism with piezoelectric (PZT) actuators. The four-axis system incorporates 64.5 μm x 49.7 μm x 31.5 μm of travel in the x, y and z scanning directions as well as an additional 16 μm of travel in the probe axis where the specimen is located in the center of the fine stage. The fine stage is modular and mounts onto a coarse xyz platform through a type II Kevin

kinematic clamp to provide an easy way to assemble and access the gauges underside. The clamps contain three fine screws enabling fine z motion plus tip-tilt adjustment for the plane of the fine stage along with the coarse stage. The xyz coarse stage comprises three orthogonal dovetail slides each capable of translations up to 25 mm and is used to adjust the height and location of the specimen relative to the fixed optics that are rigidly mounted to the base of the instrument frame and the mechanical probe that is mounted to the top vertical column of the instrument frame. Closed-loop control was realized with analog control using home built signal parallel plate capacitance gauges. The targets of the capacitance gauge are attached to a rectangular block mounted to the underside of the moving platform upon which the specimen is mounted. The three capacitance probe electrodes to form the gauges are rigidly attached to the flexure frame. The non-linearity nature of capacitance sensors were compensated through a LabVIEW™ Real Time target machine. Both optical and mechanical probes were implemented in this hybrid system. Various force probes were investigated for the initial study.

The instrument frame with base and coarse stage are manufactured from steel to provide a large thermal capacity thereby reducing thermal drifts during the short scan times. A large vertical column mounted to the instrument base provides a mounting platform for the mechanical probe axis. A long range slide is used to move the platform up to 50 mm using a micrometer. The probe mount's xy position is adjustable and lockable with a clamp. The mechanical probe mount comprised a single axis piezoelectrically driven stage where the universal dovetail mount is attached.

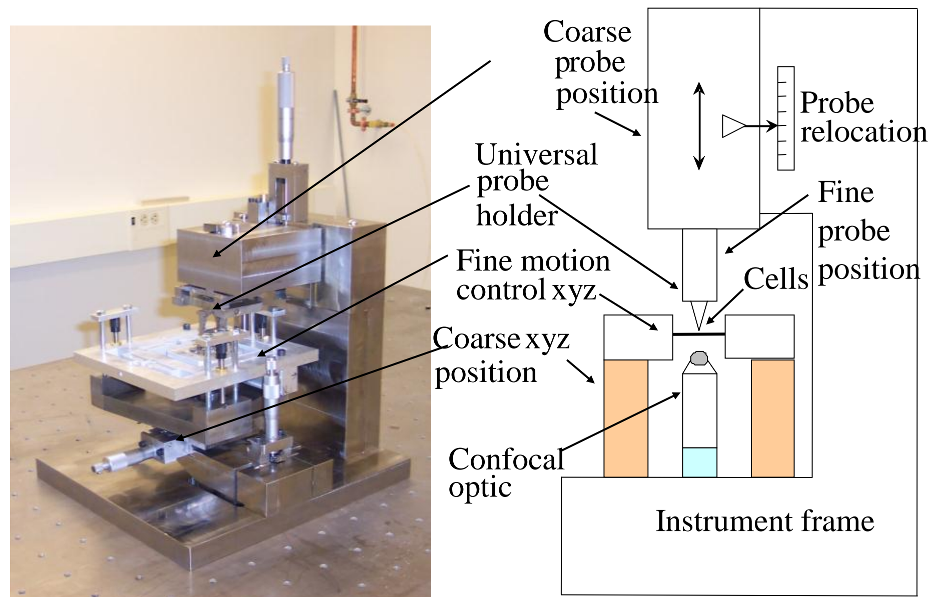

FIGURE 1-1: Mechanical photography and schematics [22].

1.2.3 Contributions of this project

The first version of the SMPM worked in open loop with the Nanoscope™ controller. However, it had several problems, i.e. closed loop noise issue limiting position resolutions to 40 nm or greater, a complicated system with analog and digital components that required considerable knowledge and skill to operate, scan speed limitation, no metrological characterization of the scanning system, lack of unique functionality supports etc.. In this dissertation, several progresses made to improve the performance of the SMPM are presented, i.e. design of the gauges for prototype stage, a complete redesign of gauging for the fine stage, integration all systems components into a single standalone real-time system, development of closed loop controller and sensor signal conditioning with high resolution and accuracy which make a lot biological studies possible, and open software enables a lot functionalities including multi-channel inputs

and multi-probes capability possible.

The SMPM implements a piezoelectric (PZT) actuated flexure design with capacitance displacement sensor for feedback control to obtain the desired positioning resolution. The sources impacting the positioning accuracy of the SMPM are studied, i.e. the sensor error, electronic and digitization noise, thermal drift, ground borne vibration, acoustic noise, drift and hysteresis of the actuator, straightness and rotation error from parasitic motions and Abbe and cosine error.

The resolution and bandwidth of the capacitance sensor for position measurement have been improved by implementing a field programmable gate array (FPGA) based digital synchronous demodulation technology as well as the custom designed, surface-mount pre-amplifier for the capacitance gages. System positional dynamics are modeled and these models used to develop controllers and implement compensation to maximize measurement precision for a variety of dynamic scanning algorithms. The microscopes dynamic response (transfer function) is also measured using a dynamic signal analyzer so that theoretical developments are based on an accurate representation of the actual microscope system.

The SMPM is digitally controlled using LabVIEW Real-time measurement system. Using this development environment, a graphical user interface for instrument control enables the measurement and positioning of specimen scanning and displays surface imaging results in real time. The software and controller is capable of realizing the basic functions of a typical commercial scanning and imaging controlled unit, e.g. scanning controls, contact mode & tapping mode, PID tuning, probe sensitivity test, force curve, multi channels imaging, etc. Because of the access to the source program, more functions

can be integrated in future, like mechanical spectroscopy, image processing technology, fluorescence analysis for resonance energy transfer, single molecule analysis and fluorescence anisotropy. The addition of these novel imaging capabilities makes the system unique and readily extended to novel mechanical and optical probe technologies as they develop. This ability to incorporate technologies as they emerge enables a versatility that is not readily obtained with commercial products. The open source hardware, software and architecture of the system also make it a versatile instrument that is able to cater to a wide variety of measurement modalities and incorporation of arbitrary algorithms for real-time diagnostics.

Using this system, measurements of several artifact gratings using optical and force probes have been achieved. These artifacts include a fluorescent coating on a thin gold film having two dimensional periodicity of 800 nm, and a 10 μm square grating (VLSI Standards Inc. Model STS3-1800P) of 180 nm step height. Many researchers in Physics and Engineering are now using this system for fluorescent imaging of biological and optical structures as well as three dimensional mapping of quantum dots in thin films and surface layers [23-26].

1.2.4 Design, Schematic, Components

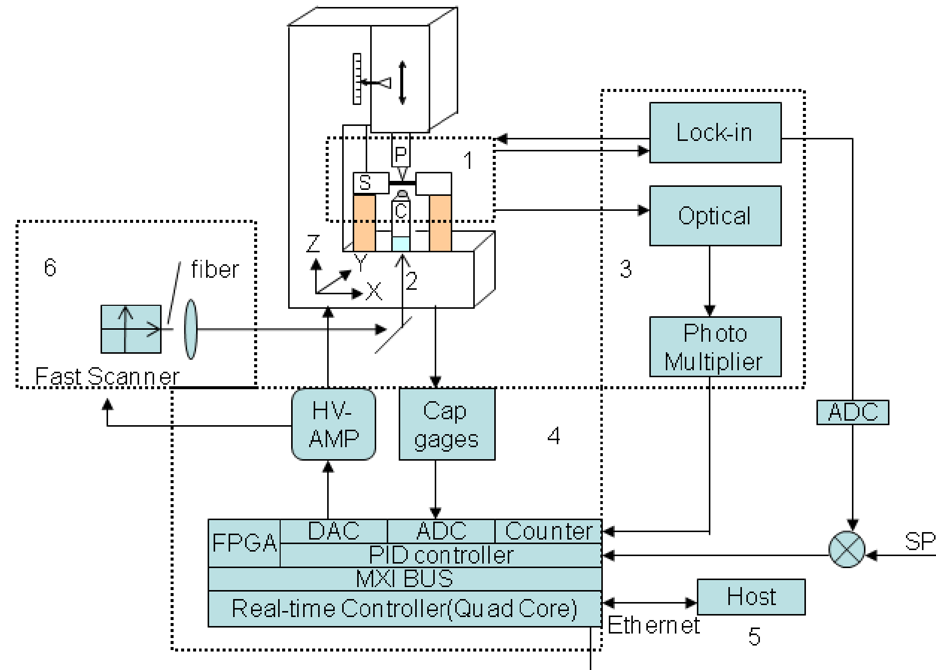

FIGURE 1-2: Schematic diagram of the Scanning Multi-Probe Microscope (SMPM).

FIGURE 1-2 shows the schematic diagram of the Scanning Multi-Probe Microscope (SMPM). It consists of six blocks. Block 1 includes the sample holder, the mechanical probe which is mounted on a 16 µm travel, high-bandwidth, single axis stage which enables tapping mode AFM, force modulation imaging, or simple standalone z motion, and facilitates the lens of the optical probe underneath the sample holder. Two types of mechanical probe were tested in the preliminary study. A tuning fork sensor was produced by attaching an etched optical fiber to one arm of a tuning fork. Another cantilever probe was produced with contact force bending of the beam being measured with a capacitance base sensor and with the probe tip being diamond stylus of radius 10 µm. Confocal laser scanning optical microscopy was employed to obtain sample information, this is so-called optical probe. This part will be introduced in Chapter 6.

Block 2 in FIGURE 1-2 is the positioning system with a fine motion stage

displacement range of 64.5 μm x 49.7 μm x 31.5 μm in x, y, and z direction using piezoelectric actuator that are capable of moving the stage with the resolution for the nanometer precision scanning. The fine stage is mounted on a coarse motion stage comprised of dovetail slides that are manually positioned using toolmakers micrometer heads. Three custom capacitance sensors are installed underneath the fine stage to measure displacement of the stage relative to its frame for closed loop, dynamic positioning. Capacitance gage sensor innovations implemented for this are demonstrated in chapter 2.

Block 3 represents the components used to process the signals from the probes. Currently an SRS 850 lock-in amplifier measures the response of the mechanical probe during its interaction with the surface force. The output of the lock-in amplifier is read by an analogue to digital converter (ADC) and feed into the controller.

Block 4 represents the hardware control systems for dynamic positioning of the probes relative to the specimen. It comprises several newly integrated hardware controls. Software implementation is achieved using LabVIEW 8.6 Real-Time™ with program code running on 2.6 GHz quad processor computer configured as a high speed real time controller. The controller connects to a PXI-7852RA chassis through an MXI bus. An FPGA based 40 MHz counter (capable of measuring several MHz TTL signal) is used to count photons to produce the image. Digital to analogue convertors (DACs) and ADCs are used to read the signals from the sensors and provide the command voltage to the piezoelectric actuators via a high voltage amplifier. Multi-channel proportional-integral-differential (PID) controllers are used for the closed loop control of fine stage scanning and probe surface tracking. It is also worth to point out that the bandwidth of the PID is

most limited by the speed of the current DAQ card system, the bandwidth of the displacement sensor and the mechanical probe (AFM like probe). Normally sensor bandwidth should be higher than PID servo loop, otherwise, setting a very high PID servo loop is meaningless. Three capacitance sensors built into the sample holder measure the displacements of three axes of the fine stage and therefore provide the measured displacement to the controller. Three high voltage amplifiers amplify the output of the PID controller and drive the piezoelectric actuator to compensate the positioning error. This component of the thesis project is discussed in chapter 4.

Block 5 is the host computer running in a Windows XP operating system. A flexible and user-friendly host software was designed and built using LabVIEW in the host computer. It realizes the function of sending control and scanning parameters to the real time controller, receiving, post processing and displaying the measurement results. This home-built controller improves upon the existing commercial controller which was designed only for open loop control. Furthermore, the open source hardware, software and architecture of the system also make it a versatile and extendable instrument that is able to adapt to a wide variety of measurements and perform functions such as mechanical spectroscopy, image processing technology and processing of photon count data for fluorescence-based imaging.

A novel scanning method for the fluorescence probe microscopy of has been designed and integrated into the SMPM. In this, the fiber from the laser diode illumination source is mounted into an xy piezoelectric actuated fast scanner represented by block 6 in FIGURE 1-2. By scanning the fiber in an xy plane, the focused beam spot is correspondingly scanned the sample. Initial experimental results show that the scan range

of the positioner was around 60 μm in each axis for the corresponding scan of 5 μm range of the confocal spot. Such an attenuation of around 12:1 for this optical system may be of particular benefit for ultra-high resolution, metrological confocal microscopy. The low mass of the optical fiber enables high speed imaging of samples without having to move the more massive sample stage and avoiding problems associated with specimens in liquid environments. This development is discussed in chapter 3.

CHAPTER 2: SCANNING STAGE AND SENSOR DEVELOPMETN AND CONTROLLER CHARACTERIZATON

To achieve high scanning speed for efficiency and live cell imaging, the scanner (fine stage) is the most basic and difficult component. A scanner should have high natural frequency, low quality factors to have fast dynamics response. Sufficient positioning range and small crosstalk between each axis should be achieved too. In the thesis of Elliot [22], the stage was designed and built to enable intracellular measurement with multi-probes in nanometer resolution in a range of 64.5 μm x 49.7 μm x 31.5 μwith closed loop control. The fine motion of the stage is achieved using three, serially connected, orthogonal flexures driven by piezoelectric actuators through a lever linkage [27]. The flexure design minimizes the coupling problem between x , y and z axes that is particularly severe with the traditional piezoelectric tube scanners. Additionally, the sample scanning design was chosen to satisfy the requirement that the optical and mechanical probes need to be stationary.

The entire fine stage was made of aluminum 6061-T for its high diffusivity, low density, cost and manufacturability. Drawbacks of using this material include the relatively low ratio of Young's modulus to density and high thermal expansion coefficient [28]. The fine stage was primarily manufactured using wire electro-discharge machining (WEDM) to minimize the overall footprint and, with reduced size, maximize stage

resonance frequencies. To add damping to the system, certain cavities created by the WEDM process were filled with a damping polymer, Sylgard 184. A stacked piezoelectric actuator (Tokin AE0505D16) of length 20 mm with a 5 mm square cross section is chosen to keep the dimensions of the stage down for high dynamic response. When applied with a voltage of 150 volts, the PZT actuators extend approximately 16 μm in length with a maximum force of 850 N [29]. Since a displacement of around 50 μm was desired for the x and y axes for the sample size requirement, a 'rowboat' flexure was designed to amplify the output range of the actuators.

Following performance characterization of the existing scanner a number of issues were identified. These included,

1. Sensor noise issue

In the preliminary work, about 40 mV (PV) noise occurred in the sensor as shown in FIGURE 2-1. Though a running average filter can improve the performance, it adds a few millisecond lag (at less than 100 kHz sample rate for hardware limitation at that time) to the system while the bandwidth is not qualified for the scan process.

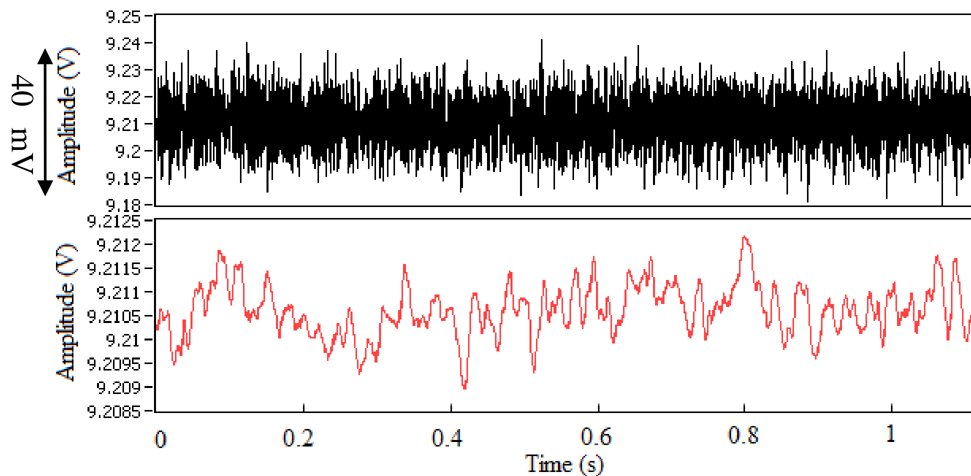

FIGURE 2-1: Noise measurement of the original sensor system, Top: before average, Bottom: after applying 100 point average, the noise level is 3 mV (PV). Total sample time is 1.1 second.

2. Controller issues

At the beginning of the work, a commercial Nanoscope™ hardware system was used as the open loop controller for the whole microscope. An analog PID circuit with Real-Time digital controller was added for closed loop control. This system was connected between the Nanoscope™ and the microscope stage. To position the platform, the analog voltage signal from the Nanoscope™ output was used as the demand to the PID controls of the real time system that subsequently controlled stage positioning. However, further improvement of the controller hardware and software are required to reduce noise and enhance dynamic performance.

To address these issues the following initiatives were undertaken. Several initiatives were made to improve the performance of the sensor. The length of cables was reduced by mounting the electrical board adjunct to the sensor in order to beat down the parasitic capacitance. The stage was ground to the earth to reduce the noise, a pre-amplifier was designed for the digital lock-in, a larger target was used and a more symmetric capacitance electrode alignment system was designed. For the purpose of this chapter, these initiatives are split into two categories that are presented in this chapter.

1. New sensor for the prototype *xyz* stage which was built before the *xyz* fine stage and re-design of the sensor for the *xyz* fine stage
2. Controller design with new hardware and software

2.1 Capacitance sensor

As the PZT actuator has hysteresis and creep, open loop positioning performance of the stage results in uncertainties that are not acceptable for most dimensional measurement requirements. Though researchers have attempted to build mathematical

models to predict the hysteresis and creep in PZT and compensate the positioning error in the open loop [30], the results have not shown great promise. Thus, to achieve the positioning at the nanometer level a feedback closed loop control system is necessary.

In a closed loop system for nano-positioning, as well as for scanning and metrology applications, the capacitance gauge is widely utilized to measure the displacement. This is because of its potential for high resolution (nanometer at a few kilohertz within 100 micrometer range), high repeatability, simplicity, cost and long-term stability [31]. It provides contact-free measurement of the target's position which does not add significant parasitic force to the motion (when the electronics wires are well-organized and the air squeeze film effects are neglected). The measurement process is free of friction and hysteresis (hysteresis/phase lag only exists in the circuit). It does not occupy a lot space, therefore it is quite suitable for miniaturization of the instrument. Also, because the gap between the electrodes are within micrometer to obtain high sensitivity, the motion between two electrodes surfaces will introduce squeeze film force that can provide damping [32], which is beneficial for the dynamics performance.

Nevertheless, capacitance sensors have several drawbacks. It requires the probe to be mounted close to the target. This increases the difficulty of alignment for the probe and the target and the probability of crashing the sensor. The environmental conditions also can affect the accuracy of the capacitance sensor. Temperature is a common one. The mechanical part will exhibit expansion or contraction when temperature drifts. Also the humidity changes the dielectric constant of the air which brings in a potential offset to the sensor output. Care must be taken to control the humidity and temperature during the scanning experiment. There is also the possibility that dust or liquids can become trapped

in the gap between electrodes, often resulting in sensor failure due to electrical or mechanical 'shorting'. Fortunately, in our experience this latter effect is rare.

2.1.1 Theory and design

Two configurations of parallel plate capacitance transducer are mostly employed in the displacement measurement these being either the Plate-distance transducer or Differential in-plane transducer. The latter one is linear with the displacement but is not applicable for high sensitivity and stability of positioning measurement at sub-nanometer level while the former one is much more suitable in short range, high precision, measurement applications [33]. The capacitance of a single plate-distance transducer can be written as:

$$C = \varepsilon_r \varepsilon_0 \frac{A}{d} \tag{2.1}$$

Where ε_0 is the permittivity of vacuum, a physical constant ($8.854787817*10^{-12}$ F/m), and ε_r is the relative permittivity of the medium filling the capacitor (~ 1 in air), A is the overlapping area, d is the distance between the electrodes. The capacitive transducers can measure capacitance changes as a result of the changes in the displacement between the plates as illustrated in FIGURE 2-2.

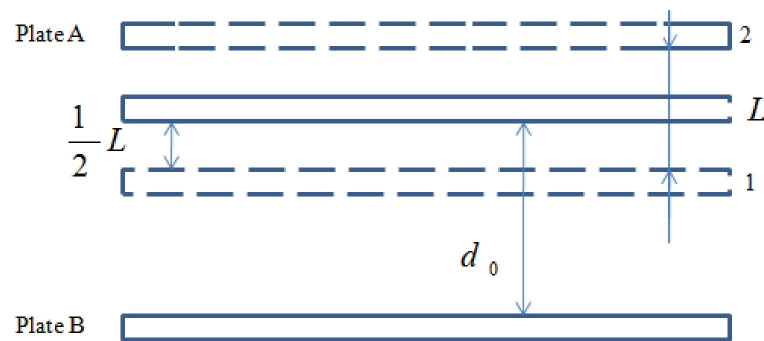

FIGURE 2-2: Configuration of the single plate-distance capacitance transducer. Plate A is the moving part, where plate B is the stationary part. Plate AB gap is minimum at location 1, and maximum at location 2, and the moving range of plate A is L.

Based on FIGURE 2-2, equation (2.1) can be rewritten as

$$\mathrm{C} = \varepsilon_r \varepsilon_0 \frac{A}{d_0 + x} \tag{2.2}$$

Where x is the displacement to be measured, d_0 is the distance of the two plates when $x = 0.5\,L$.

The sensitivity of the capacitance transducer is equal to

$$\frac{dC}{dx} = -\varepsilon_r \varepsilon_0 \frac{A}{(d_0 + x)^2} \tag{2.3}$$

Apparently the larger of the overlapped area, the smaller of the nominal distance, the higher resolution and sensitivity the transducer can achieve. In practical stage design, the problems of limited space in the stage and electrode alignment always exist. It is difficult to approach high mechanical stability when the area is too large and the gap is too small. For the transducers used in the prototype stage, the radius of the probe is designed to be 5 mm, so the overlapped area is about 78 mm^2. Suppose the resolution of the measurement electronics is 10^{-3} pF at 1 kHz bandwidth (1 kHz is usually basic speed at high speed scanning application), the required displacement resolution is 1 nm, and the sensitivity of the capacitance transducer can be calculated as 10^6 $\mathrm{pF{\cdot}m^{-1}}$. From(2.3), the distance between the plates is given by,

$$d_0 + x = \sqrt{\frac{-\varepsilon_r \varepsilon_0 \mathrm{A}}{dC/dx}} \tag{2.4}$$

$d_0 + x = 26$ μm when $x = 0.5\,L$. In the case of prototype stage, the design positioning

range L is around 20 μm, therefore the designed range of the transducer should be around 20 μm, so the gap varies from 16 to 36 μm, corresponded to capacitance varies from around 19.2 pF to 43.2 pF which was verified by using a HP 4284A LCR meter later in the assembly part. Here the more typical 1-2-3 capacitance-ratio rule [31] was not employed for the reason that the gap is set to a practical minimum to achieve high sensitivity at the expense of linearity.

The reason why we did not adopt the commercial capacitance sensor is the low cost of self-made capacitance sensor, implementation of a compact alignment feature, simplification of stage mechanical design and system integration.

2.1.2 Design, manufacture and assembly of the capacitance position sensors

As shown in FIGURE 2-3, the sensing part (probe) of the capacitance sensor is surrounded with a guard ring to maintain the linearity of the electric filed and minimize the stray capacitance coming from the edge effects [33]. Typically, this is realized by applying the same driving voltage by a separate circuit to the guard ring as the sensing part [34]. Usually any conducting material can be made for capacitance, however, aluminum, stainless steel and invar are the most used material in industry. Occasionally, the electrodes are deposited as thin films on substrate materials of higher thermal and temporal stability such as alumina, silica or Zerodur™. Here brass was used for making the probes and targets, while the guard ring was made of copper because copper has higher thermal diffusivity (1.1234×10^{-4} m²/s) than aluminum (8.418×10^{-5} m²/s) and stainless steel (4.2×10^{-6} m²/s), and lower thermal expansion coefficient (17 ppm/℃) than the aluminum (23 ppm/℃) and stainless steel (17.3 ppm/℃). The ground/shield part was made of aluminum. Using a diamond slicing wheel Fused silica shown in the left

picture in FIGURE 2-4 was cut into small pieces to electrically insulate the housing shield between the sensing area and the guard ring. Firstly the fused silica was glued to the inner bottom surface of the shield. After the recommended setting time for the epoxy to cure, the guard and the sensing probe were putted together with bottoms glued onto the insulator. After that, an LOCTITE HYSOL E-30CL epoxy adhesive was carefully poured into the gap among the sensing probe, guard ring and the shield. The sensors were placed in a vacuum jar to pump out the air bubbles, FIGURE 2-4, for a few hours. After the epoxy had cured, the sensor's surface was milled and hand polished to produce a flat surface shown in FIGURE 2-3. Surface irregularities will add an error when the probe moves across the surface. Therefore care should be taken to get a smooth surface finish.

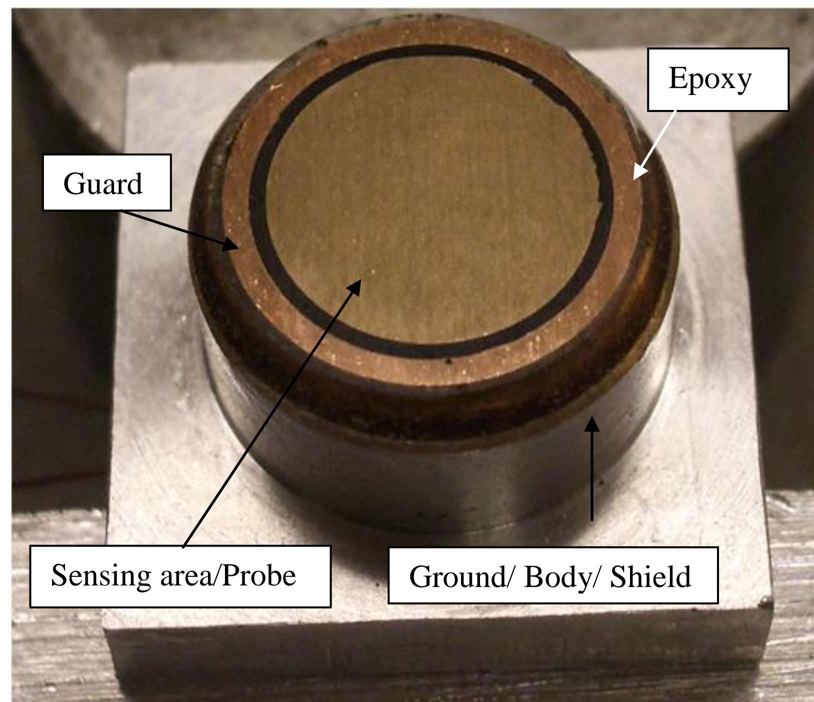

FIGURE 2-3: Capacitance probe structure, diameter of the sensing area is 10 mm, the thickness of the guard (1 mm) should be at least twice larger than the sensing distance (20 μm).

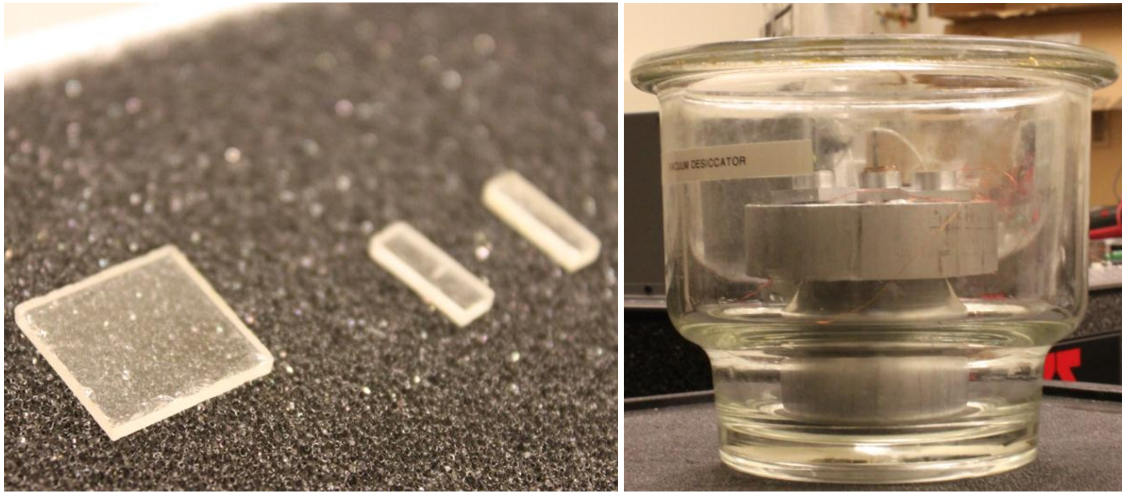

FIGURE 2-4: Left: Insulator, Right: Vacuum used for pumping out air in the epoxy.

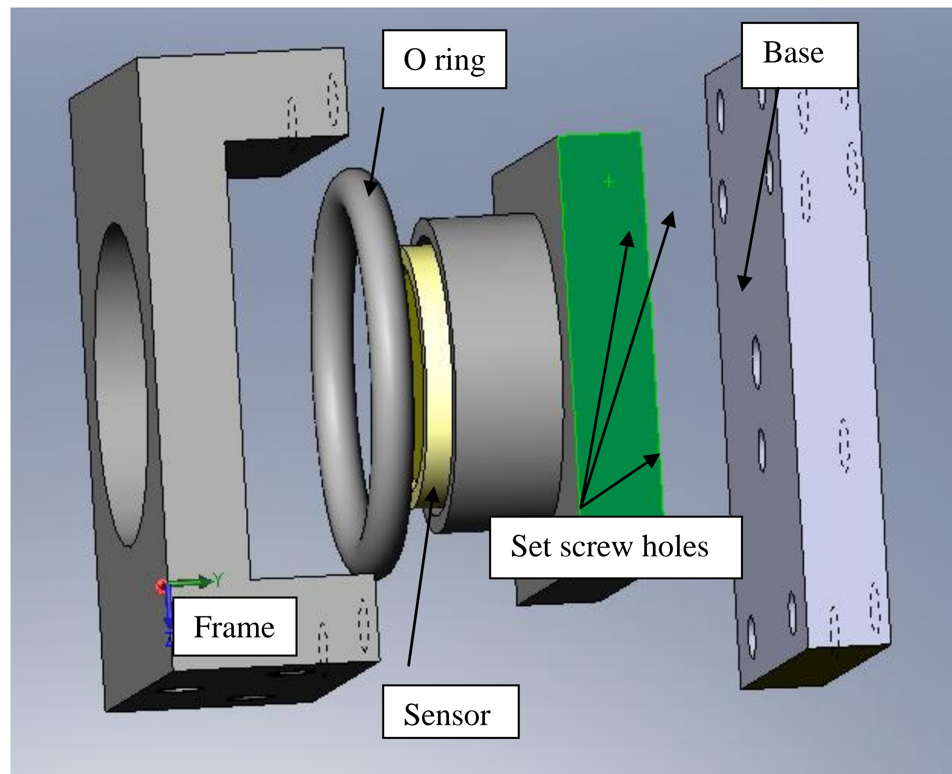

FIGURE 2-5: Assembly of the sensor with the adjustors.

FIGURE 2-5 shows the assembly of the sensor with an adjust mechanism containing an 'O' ring, frame, base and three set-screws. The sensor was sandwiched into the frame

through the ‘O’ ring by the base. The three set screws were used fine adjustment of the electrode gap and for angular alignment of the probe with the target.

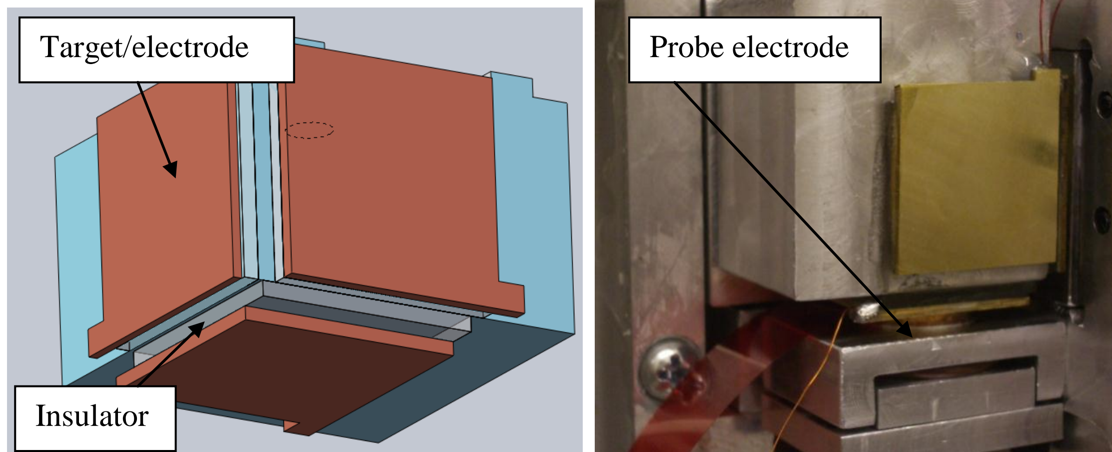

FIGURE 2-6: Left: Orthogonal target block CAD model, the blue one is the block attached to the stage whose position is to be measured, the brown plates are the target electrodes, the transparent plates are the insulators made of fused silica which is glued onto the block; Right: Assembly of the probes with the targets with z axis sensor removed.

The other mechanical part of the sensor system is the the target block to be clamped to the moving part of the stage. Three brass plates were machined into the shape shown in FIGURE 2-6. The fused silica pieces are the insulators glued on the three orthogonal surfaces of the block made of aluminum, and the target electrodes were then bonded to these insulators using epoxy. The last step was clamping the whole block onto a 1-2-3 gage block, and the surface of the the target electrodes were ground by a surface grinder. After grinding the three surface are parallelto the 1-2-3 gage block reference surfaces. It should be noted that all the parts were cleaned with alcohol or acetone before assembly.

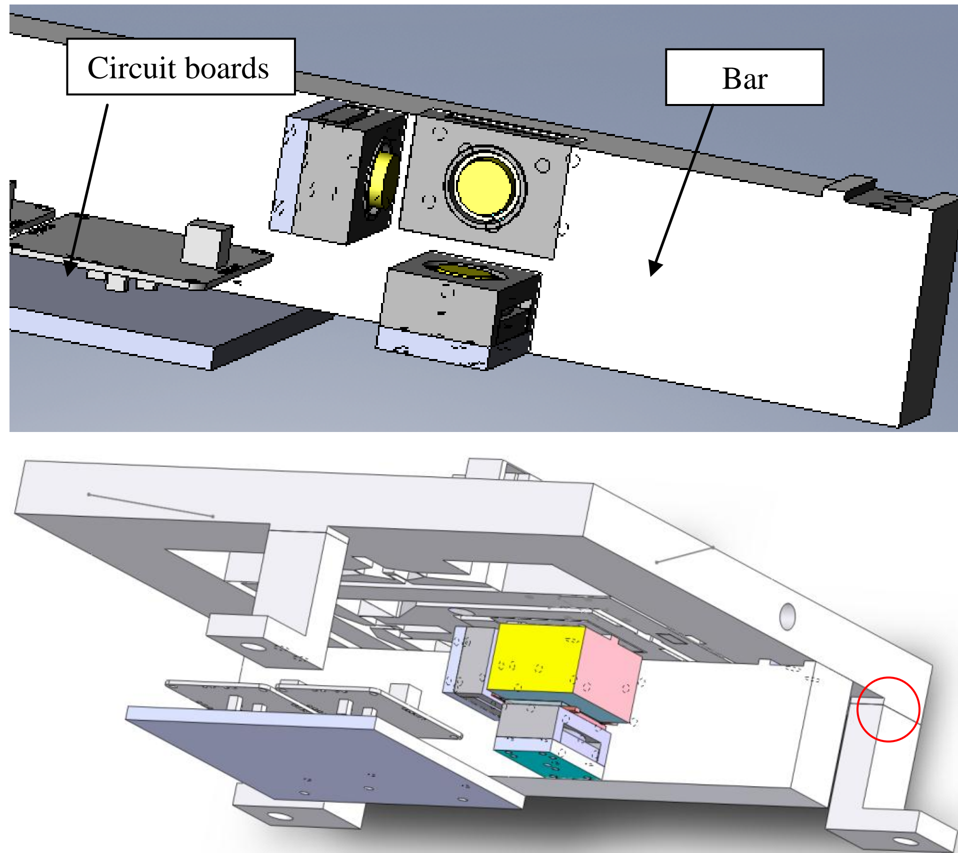

FIGURE 2-7: Sensor assembly with the prototype stage. Top: sensors with the bar, Bottom: prototype stage assembly.

During the assembly, the target block was clamped to the stage, see FIGURE 2-7. Following this, the bar where the probes locate was fixed onto the two sides of the stage frame. The relative positions of the bar, target block, and the sensor can be adjusted with around 1 mm by the two screws which clamping the the bar to the frame so that the set screws had adequate adjustment range to align the probe with the target in high sensitivity. A HP 4284A LCR meter was used to measure the capacitance during the alighment by the set screws. To obtain higest senstivity, with the design capacitance value in mind, the set screws were adjusted to make the capacitance changes from 20 to 37 pF for y sensor, from 21.7 to 46 pF for x sensor when the corresponding PZT drive voltages changed from 0 to 150 V. Care should be taken to ensure that the probes and targets won't touch

at any point following these adjustments.

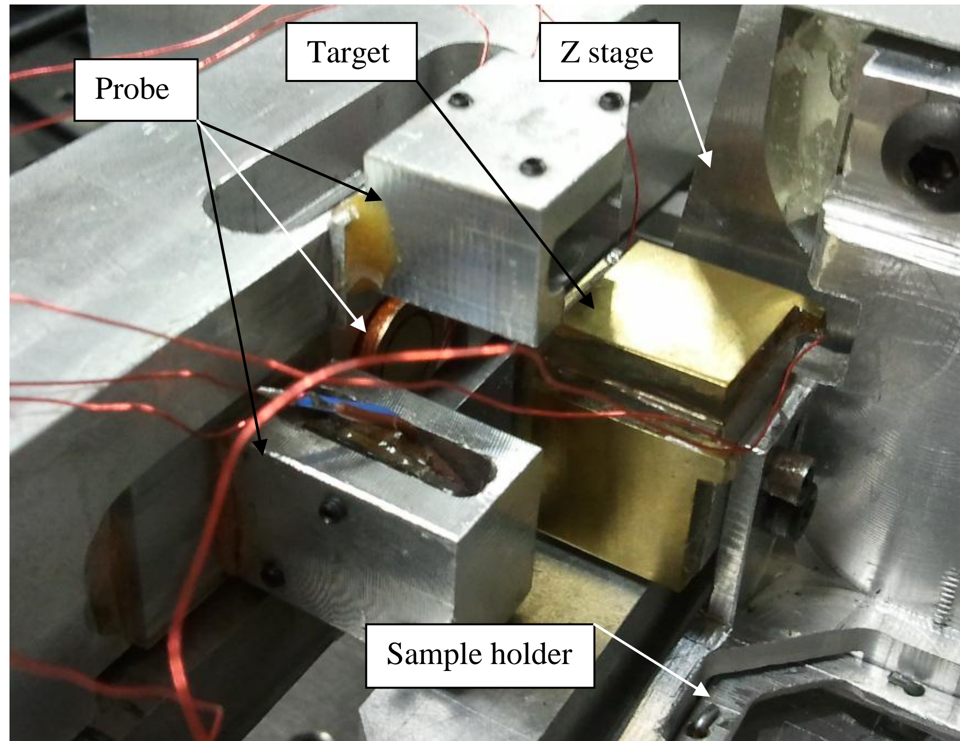

FIGURE 2-8: Sensor assembly with the xyz fine stage.

For the sensors installed in the xyz fine stage, the first version of the capacitance sensor presented a noise level around 50 nm. At the first examination, two probes were found to be a few millimetre laterally offset from the center of the target plate so that the probe electrode was measuring charge generated by fields at the edge of the target. This offset resulted in a high parasitic capacitance, therefore the probes and target block with the plates were re-machined and assembled as shown in FIGURE 2-8. In this case, the capacitances were adjusted by the set screws and changed from 7.1 to 14.2 pF for x sensor, from 8.8 to 13.4 pF for y sensor, and from 7.4 to 11 pF when the PZTs voltage changed from 0 to 150 V.

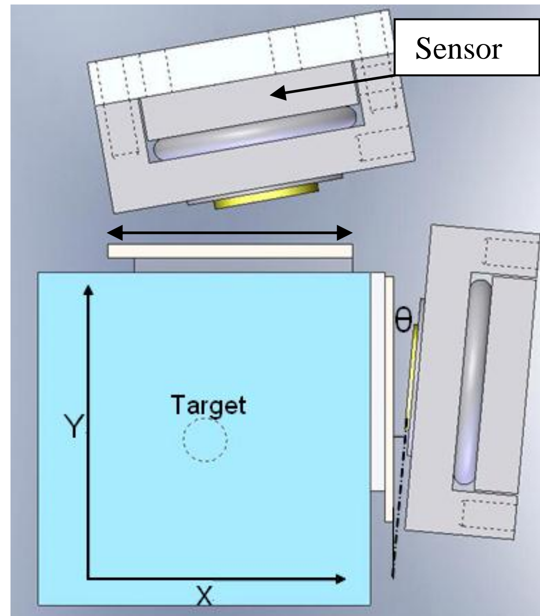

FIGURE 2-9: Tilt effect during the setup analysis.

During the alignment, it is difficult to adjust the probe to align perfectly with the target, therefore there exists a parasitic capacitance introduced by the tilt effect which may limit the range of travel. One of the equations used to calculate the capacitance with the plane tilt is derived by Harb et al.[35] :

$$\mathrm{C} = 2\varepsilon_r\varepsilon_0\frac{\pi R^2}{d}\left(\frac{1}{1+\sqrt{1-k^2}}\right) \tag{2.5}$$

Where R is the radius of the probe, θ is the tilt angle, $k = R\sin 2\theta/2d$

From the equations, R , θ parameters hold constant during the positioning, so the parasitic capacitance is a monotonic descending function of d . Although this parasitic capacitance increases the nonlinearity of the capacitance sensor, such influence is repeatable and was compensated by calibration.

In addition, the capacitance sensor suffers from the parasitic translations in the other axes. In FIGURE 2-9, the sensing area of y sensor remains the same when the other axis

translates its whole range (i.e. in x translation direction) which is around 20 μm (in the prototype stage), the ratio $2x/(L-2R)=2.6e-3$ is very small. The parasitic capacitance adding to the y sensor is negligible [36].

2.1.3 Signal conditioning innovations

After the mechanical parts of the sensor were built, a circuit is required to measure the capacitance. There are several different circuit designs for converting the variable sensor plate capacitance into an output signal for further processing. A good circuit should have the following features, good linearity, low noise, insensitivity to stray capacitance, etc…[33]. The analog AC Wheatstone bridge is the most widely adopted measurement circuit for converting the variation of the capacitance into the variation of the amplitude of an ac signal. This ac signal is converted into displacement after synchronous demodulation and calibration. In the analog AC bridge circuit, sine wave demodulation and square wave demodulation are the typical analog demodulation technologies which have the disadvantages due to gain and offset errors which are frequency dependent, amplitude drift with temperature and time and zero crossing noise. The digital lock-in demodulation can avoid these unwanted effects or can remove them using software algorithms and can now utilize high frequency modulation with commercially available, high throughput capacity and resolution DAQ cards.

Both methods were tested. A InsituTec Inc., IT-D-2-A0 board with a 2 kHz bandwidth is used for analog demodulation testing. This circuit utilizes a reference frequency set at 39 kHz and demonstrated a ripple noise of less than 2 mV. For the digital demodulation, the system takes the advantage of both the DSP and Field programmable gate array (FPGA) technology to measure the displacement with nanometer level

resolution at bandwidth of 1 kHz.

2.1.3.1 Analog demodulation testing

Analog demodulation was employed to measure the capacitance sensors in the prototype stage in Duke Hall and *xyz* fine stage at Grigg Hall.

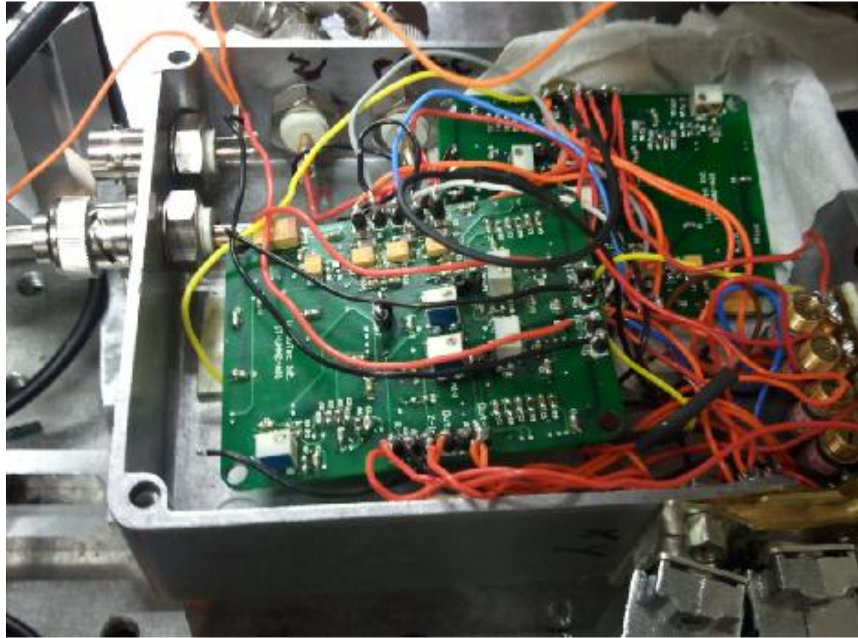

FIGURE 2-10: Two analog boards that provide four channel of synchronous demodulation (taken with *xyz* fine stage at Grigg Hall).

For the initial sensor of the stage at the start of this study, the noise level was unusually high. Upon examination a periodic signal was detected from the capacitance sensor output using IT-D-2-A0 board, see FIGURE 2-10. It had a frequency about 39.063 kHz which is the same as the carrier signal and its PV value was around 40 mV. Since the DAQ card used during that time was not fast enough to sample 39 kHz signals, an equivalent timing sampling method is employed to detect the noise by carefully choosing the sampling frequency.

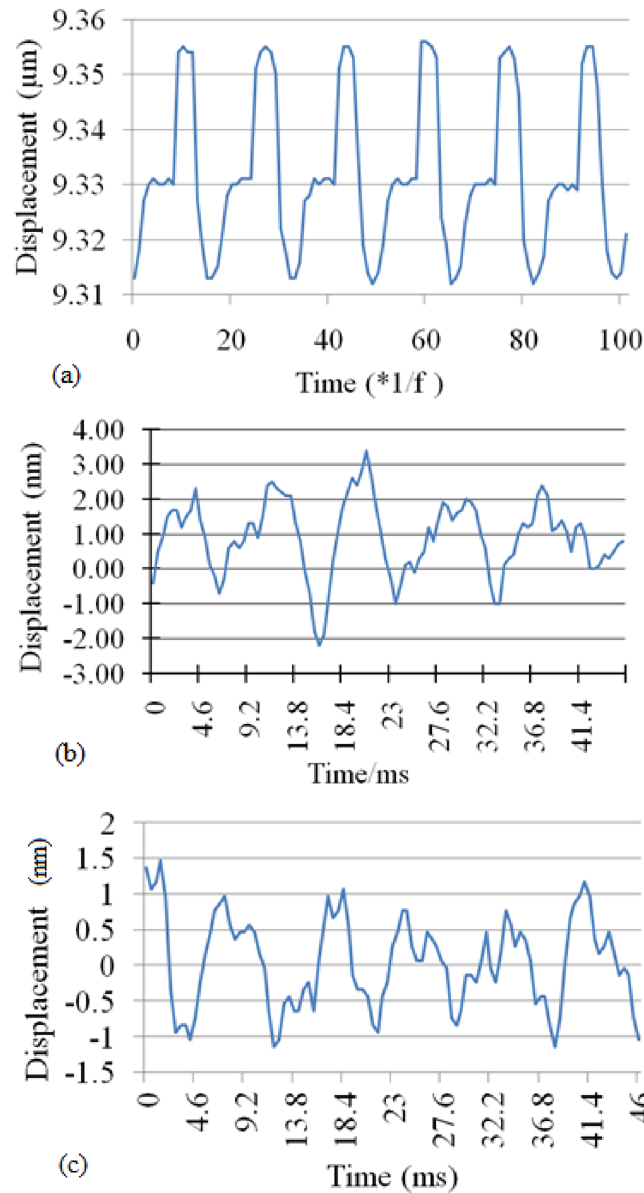

FIGURE 2-11: Noise level of capacitance sensors using analog demodulation. Bandwidth is 2 kHz, (a) noise level without equivalent timing sampling processing, (b) σ_x = 1.07 nm averaged over a period of 45 ms, σ_x = 1.5 nm for 900 ms, the signal to noise ratio (SNR) is about 18700, (c) σ_y = 0.67 nm for a period of 45 ms, σ_y = 0.63 nm for 900 ms, the SNR is about 30000.

As shown in FIGURE 2-11, the top figure presents the periodical noise in x sensor with a frequency around 39 kHz with a sample frequency at 34722 Hz (f = 39 kHz/(1+1/8)). The average noise (16 points) turns out to be 1.07 nm (1σ) for x sensor

and 0.67 nm (1σ) for y sensor. A 120 Hz frequency component appeared in both sensors which may come from a harmonic of the AC power-line contamination (60 Hz). The responded bandwidth reduced by half since the average was taken by two periods.

The same phenomenon was found lately in the sensor system used in Grigg Hall when high speed smart DAQ card with 750 kpbs ADC was employed, see FIGURE 2-12. The noise level dropped to nanometer resolution by applying a digital low pass filter using FPGA, see FIGURE 2-13. However, the circuit was not stable for some reason after a few months. It offset up or down for about one volt randomly when the power switch on/off. In addition, the circuit became hot and cause output drift when running for a few hours. Considering other drawbacks about analog demodulation mentioned in the introduction of this section, eventually a digital demodulation was applied to the sensor conditioning system and this is described in the following section.

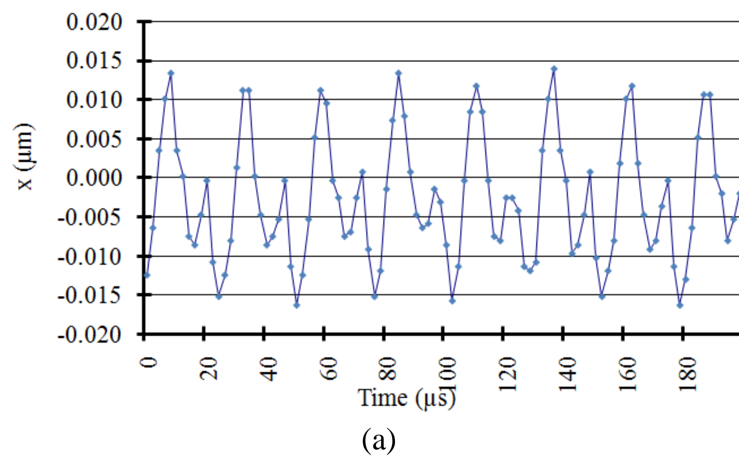

(a)

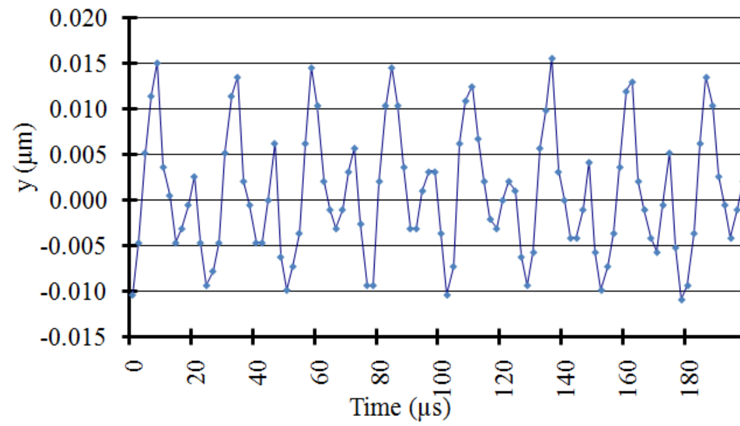

(b)

FIGURE 2-12: Noise level of capacitance sensors in *xyz* fine stage using analog demodulation, (a) x sensor noise level with 500 kHz sampling frequency, σ_x = 8 nm, (b) y sensor noise level with 500 kHz sampling frequency, σ_y = 7 nm.

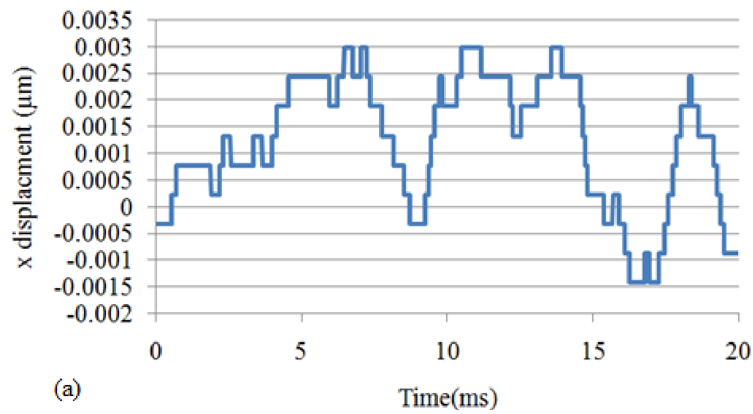

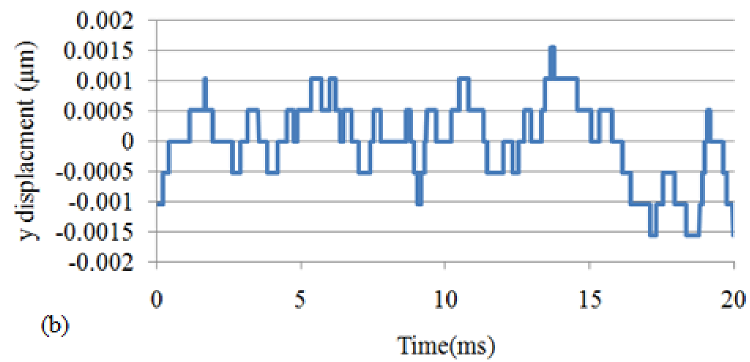

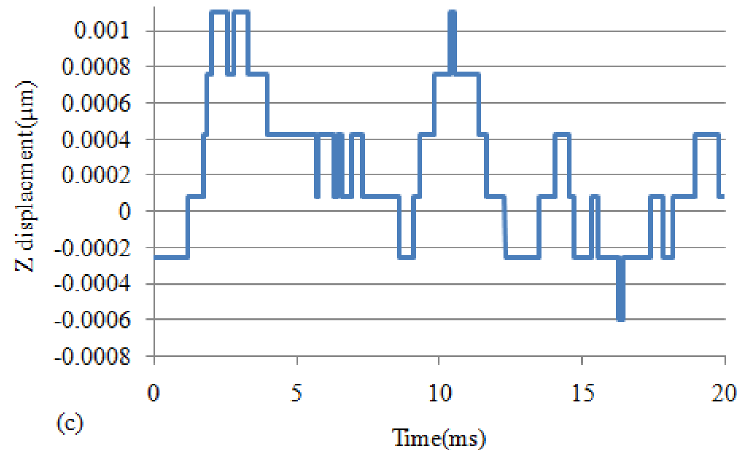

FIGURE 2-13: Sensor noise after applying a digital 2 kHz low pass filter, (a) σ_x = 1.2 nm for a period of 20 ms, (b) σ_y = 0.6 nm for a period of 20 ms, (3) σ_z = 0.41 nm for a period of 20 ms.

2.1.3.2 Digital demodulation cases

As shown in FIGURE 2-14 below, a sine wave carrier signal is generated by a digital device, i.e. DAQ/RealTime™, FPGA, and sent to the low pass filter through 16 bits digital to analog converters (DACs), the filtered signal is then fed into the AC Bridge and its amplitude is modulated by the capacitance sensor. After the operational amplifier and ADCs, the modulated signal is demodulated in the digital device. The other benefit of using digital Lock-In is its compatibility with the digital scanning controller algorithm, thus the SNR can be pushed to its maximum by eliminating unnecessary ADCs/DACs. See Chapter 4 for more details about the controller update. Digital demodulation does not mean there is no analog circuit in the signal conditioning process. The DAC is used to generate the carrier signal, control the gain while DAC readings are used to demodulate and filter the signal. An analog pre-amplifier is required to create the AC Bridge and amplify the output voltage to span the range of the ADC, see section 2.1.4.

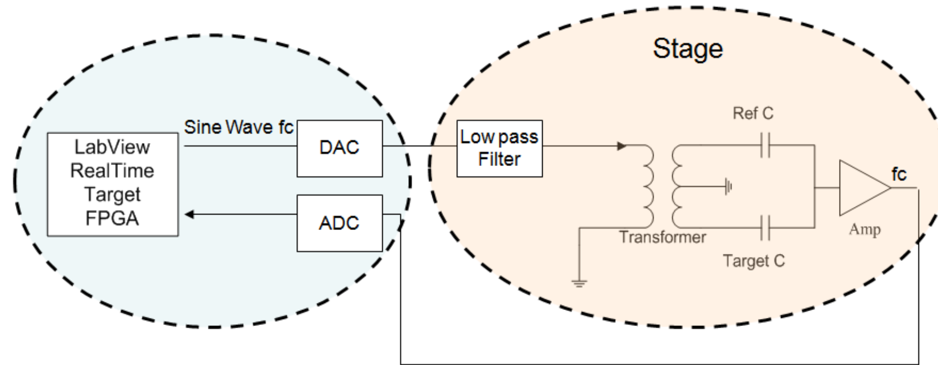

FIGURE 2-14: Layout of digital Lock-In for capacitance measurement [37].

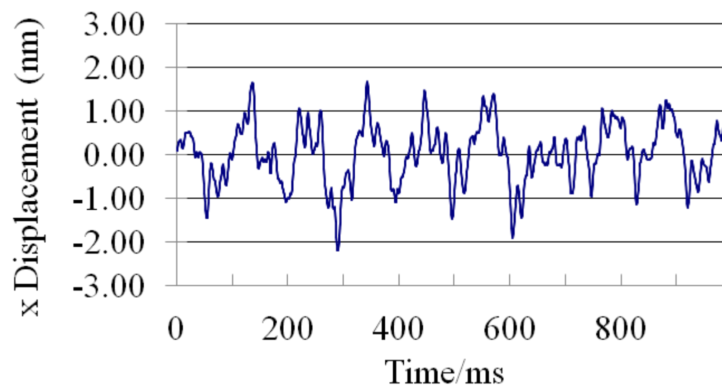

FIGURE 2-15: Noise level of x capacitance sensor in prototype stage using FPGA digital demodulation. Carrier signal frequency is 22.2 kHz, low pass filter cutoff frequency at 1 kHz resulting in σ_x = 1.3 nm for a signal measured over a period of 1 second.

FIGURE 2-15 shows the noise level of the x capacitance sensor in prototype stage using digital demodulation in LabVIEW FPGA^{TM}. The noise level is 1.3 nm at 1 kHz bandwidth for a stage capable of 17 μm displacement range. The main source of the noise appears to be a low frequency signal near 10 Hz and is of unknown origin.

The digital demodulation was applied to the sensors in xyz fine stage in Grigg Hall as well. As shown in FIGURE 2-16, the sine wave carrier signal with amplitude of 10 volts (represent as -32768 ~ 32767 as 16 bits integral format in FPGA) at a frequency 22,222.22 Hz is generated by the DAC through FPGA. Each cycle of the sine wave is

comprised of 30 data point with DAC speed 66,666.67 Hz. The carrier signal passes through the pre-amp circuit located near the stage, and the AC signal is amplitude modulated by the capacitance sensor and read by ADC through FPGA. Using the solver in the excel, the modulated signal y_{mod} is then fitted as,

$$y_{fit} = A * \sin(2\pi * f_c + \phi) \tag{2.6}$$

Where $A = 15358.28$, $f_c = 22{,}222.22$ Hz, $\phi = 2.206788$.

The carrier signal is given by,

$$y_c = 32767 * \sin(2\pi f_c) \tag{2.7}$$

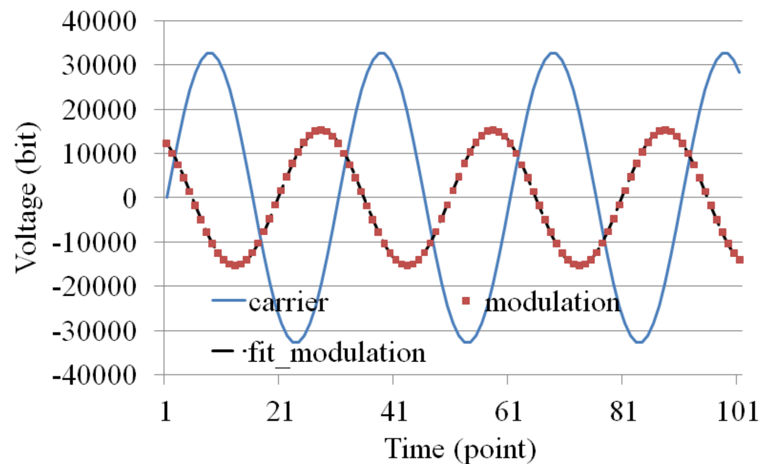

FIGURE 2-16: Carrier signal and modulated signal for x sensor.

The demodulation signal is given by,

$$y_{de} = 32767 * \sin(2\pi * f_c + \phi) \tag{2.8}$$

The demodulated signal can be obtained from equation (2.9) when two sine wave with same frequency f_c multiply together resulting a DC value plus a sine wave with a frequency $2f_c$, and then passed through a low pass filter (1 kHz cutoff freq.) to get the voltage y_v which represents the capacitance changes caused by translation.

$$y = y_{\text{mod}} * y_{\text{dem}} \tag{2.9}$$

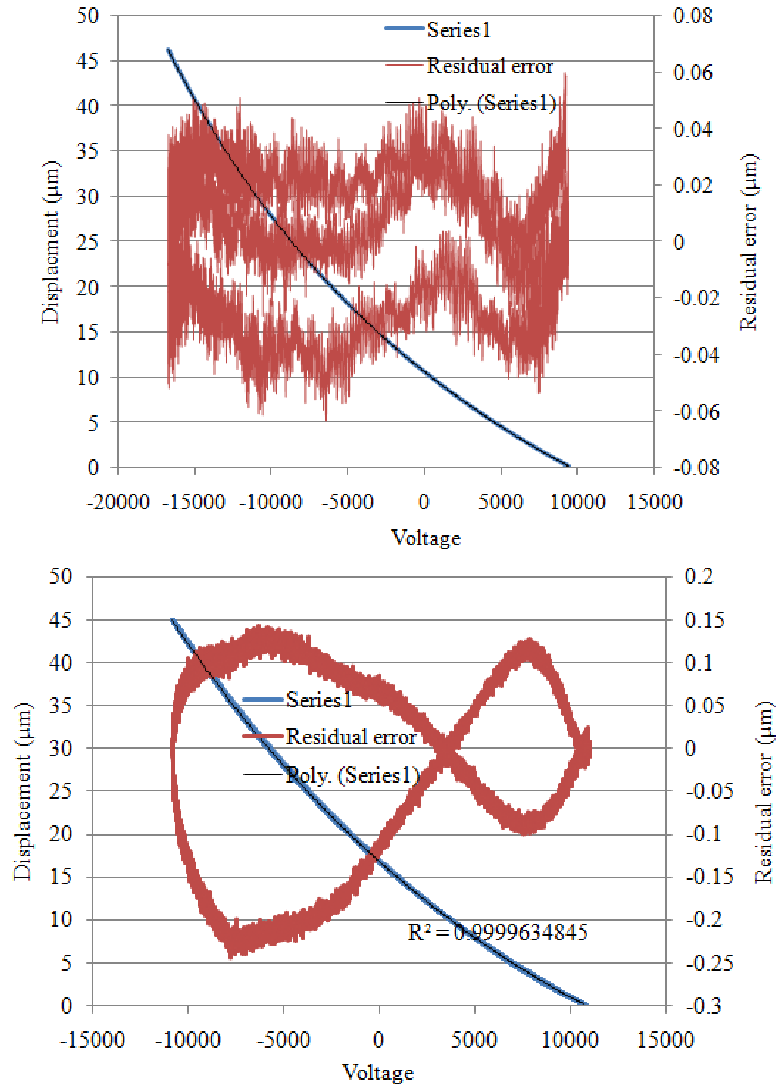

FIGURE 2-17: Raw data, fitting data and fitting residual error for x sensor (Top), and y sensor (Bottom).

After the phase calculation and demodulated signal generation presented above, the demodulated signal was calibrated with a Lion-Precision capacitance sensor (DMT 22) and the results from this calibration exercise are shown in FIGURE 2-17. The 4th order polynomial least square fit for the x axis sensor is given by,

$$x_d = 2.47063743730571\text{e-}17 * x^4 - 6.46374102005059\text{e-}13 * x^3 + 2.90836818827691\text{e-}08 * x^3 - 0.00134445503282 * x + 10.57843730739$$

(2.10)

Where $x = y_v$, the sensor has a calibrated range of 45 µm, and the correlation coefficient square is equal to 0.9999981076 for x and 0.9999634845 for y. The residual fitting error is about 50 nm (x) and 200 nm (y) which comprises part of calibration uncertainty (ignoring DMT sensor non-linearity error from the manufacture calibration).

The noise level around the zero displacement is about 1.9 nm (1σ, x) and 1.8 nm (1 σ, y) at 1 kHz bandwidth, see FIGURE 2-18. This noise level is higher than the results using analog demodulation board presented in section 2.1.3.1.

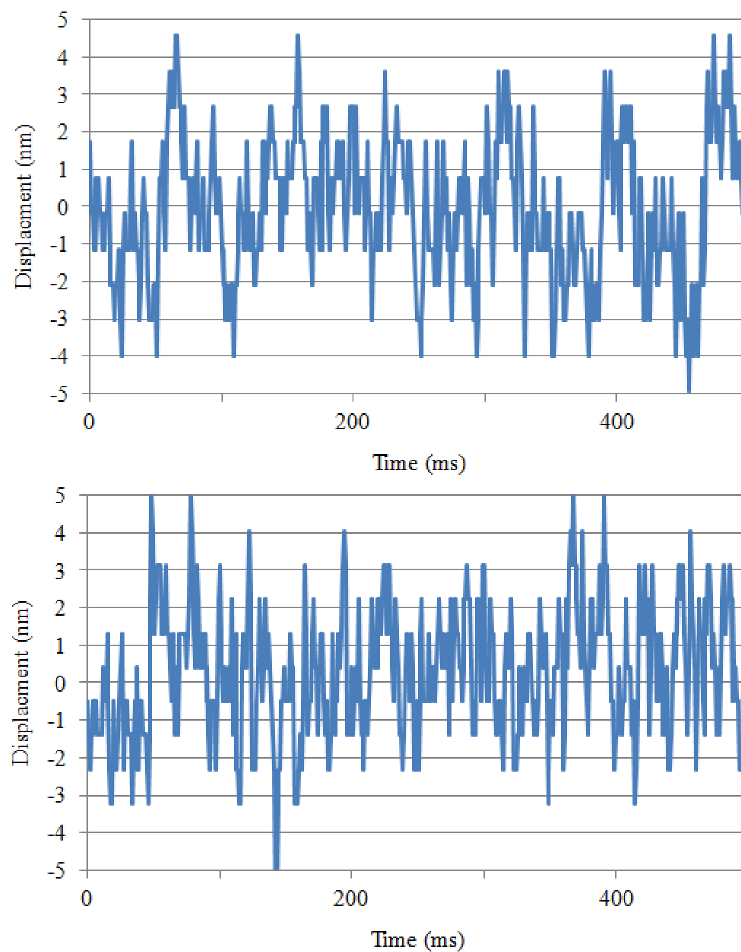

FIGURE 2-18: Noise level of sensors using FPGA digital demodulation, σ_x = 1.9 nm (Top), σ_x = 1.8 nm (Bottom) at 1 kHz bandwidth.

2.1.4 Pre-Amp design for digital demodulation

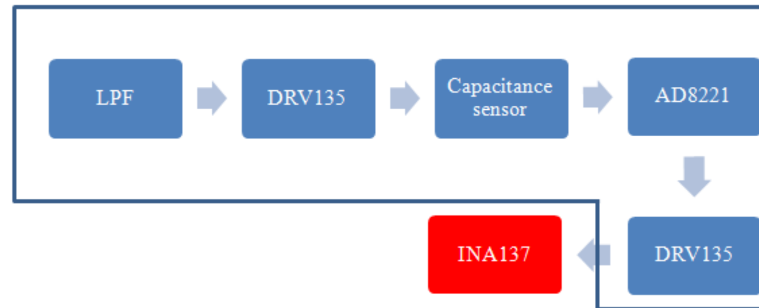

FIGURE 2-19: Schematic of the pre-amp.

A pre-amplifier was design and built as an analog signal preprocess amplifier for the digital demodulation. It contains two boards as shown in FIGURE 2-19, one is the driver board (includes components in the blue frame) which is located near the stage, and the other is the receiver board (filled in red) which is located near the PXI chassis and controller. Surface mount layout and board design was implemented by a summer intern student (Garland Vacanti). Each board has four channel built in supporting different carrier signal for individual channel. A Cat-7 Ethernet cable connects two boards providing shielding with twisted pairs for the signal which reduces the signal loss, crosstalk and noise during transmission. The audio balanced line driver DRV135 is an improve replacement for the audio transformer. The signal coming out from the capacitance sensor and reference capacitor is amplified by the AD8221 instrumentation amplifier. The amplified signal is converted to a balanced output pair by DRV135. Used in combination with the INA137 differential receiver, the pre-amp offers a complete solution for transmitting analog signals without degradation. FIGURE 2-20 shows a photograph of the PCB boards.

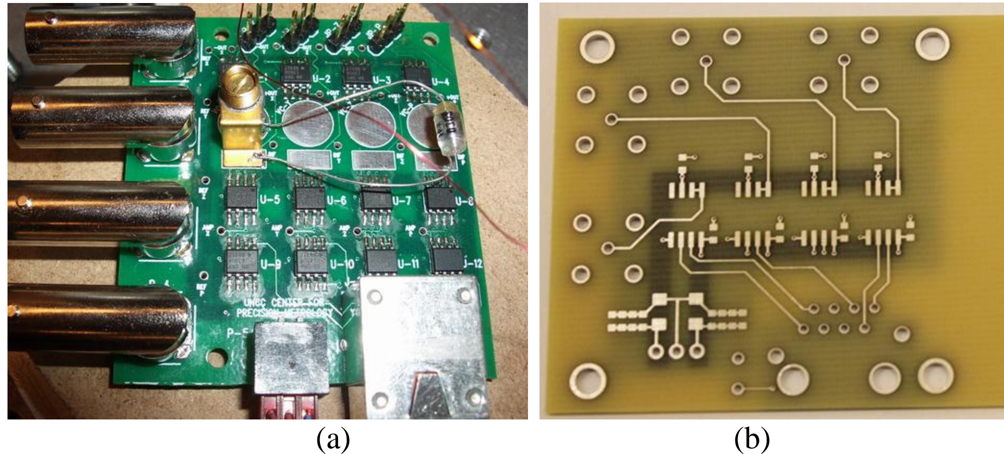

(a) (b)

FIGURE 2-20: Photography of the pre-amp, (a) driver, (b) receiver PCB board without components.

It should be noted that, for even better performance, the AD8221 instrumentation amplifier can be replaced by a simple optional amplifier, i.e. AD 549 which has lower input current noise and bias current.

2.2 Error analysis and positioning uncertainty

The positioning accuracy of the stage is generally limited by the sensor error, quantization noise, mechanical (ground borne acoustic) noise, drift and hysteresis, straightness and rotation error from parasitic motions, Abbe error, and Cosine error.

2.2.1 Sensor noise

Using analog demodulation, it is difficult to produce an oscillator with sufficient amplitude stability. This noise e_0 can be reduced by using digital oscillators. Noise can also be introduced from the preamplifier input noise e_n, the thermal noise or white noise $\sqrt{4kT\Delta fZ}$, 1/f noise which is negligible at frequencies above 1 kHz, the amplifier current noise i_n,. From these values the theoretical noise of the sensor for a 1:2:3 gage design is given by [31],

$$V_{noise} = \frac{4x_0\sqrt{B}}{V_{bs}} \sqrt{\frac{4kT}{3C_0\omega_c} + \left(\frac{2i_n}{3C_0\omega_c}\right)^2 + e_0^{\ 2} + e_n^{\ 2}} \qquad (2.11)$$

Where x_0 is the nominal electrode separation, V_{bs} is the amplitude of the carrier signal, B is the bandwidth. It is important to use low gain therefore reducing the input impedance and total noise. High voltage carrier or output from the sensor is required for low gain. Also the lock-in amplifier can alleviate the noise by limiting the bandwidth. Furthermore, when the carrier frequency increases or the gap reduces, the noise level of the measurement electronic will decrease as well.

The sensor error also comes from the quantization noise. For an N bit ADC, the effective extra noise source (quantization noise) can be expressed as [38]:

$$\delta_q = \frac{0.29 d_{range}}{2^N} \qquad (2.12)$$

So the total noise can be derived from the sensor noise given by,

$$\delta_{sensor} = \sqrt{V_{noise}^2 + \delta_q^2} \qquad (2.13)$$

This leads to an estimated theoretically noise of 0.1 mV at 1 kHz which is about 0.25 nm, where the experiment measured sensor resolution is 1.9 nm for x sensor.

Ideally, the capacitance sensor should be calibrated by using a stabilized laser interferometer which can be more stable with known frequency, more accurate than the capacitance sensor. In present experiments, a Lion-Precision capacitance sensor (DMT 22) was adopted as a calibration instrument with nanometer resolution at 100 Hz bandwidth . 4th order polynomial fit was used as described in the 2.1.3.2, and the calibration uncertainty caused by fitting was about 50 nm for x sensor. During the calibration setup, there was an angular error φ between the DMT 22 probe and the axis to be calibrated.

This caused a Cosine error which is a second order error estimated to be about $l\varphi^2/2 =$ 6.85 nm when $l = 45$ μm and a conservative estimate of $\varphi = 1$ °is used.

The total uncertainly from the x sensor is given by,

$$\delta_{xu} = \sqrt{50^2 + 6.85^2 + 1.9^2} = 50.5\,\text{nm} \tag{2.14}$$

That corresponds to an equivalent non-linearity of 0.1% within the 45 μm range. For y sensor, the non-linearity is about 0.4%. In order to reduce the Abbe error (Sine error) and Cosine error as much as possible, when doing the calibration of capacitance sensor, the reference sensors (i.e. Lion-Precision capacitance sensor)' measurement directions should lie along the extended lines of the coordinate to be measured (here is the center of the sample holder). Cosine error can be compensated when the angle φ between the reference sensors' measuring axis and the To-be-Calibrated measuring axis is known or measureable.

2.2.2 Straightness error

The other positioning uncertainty source is the straightness intruded by the alignment error and manufacturing error.

The three electrode targets on the target cube representing the measurement axes were ground orthogonally, so the best situation happens when the planes of target with drive axis align perfectly. However, x, y, z actuator axes are not perpendicular with each other due to the manufacturing error. Therefore, a straightness error occurs during positioning in open loop control. For example, $Xpzt$ showed in FIGURE 2-21 is x PZT translation axis, which brings in the δxy straightness error detected by the y sensor.

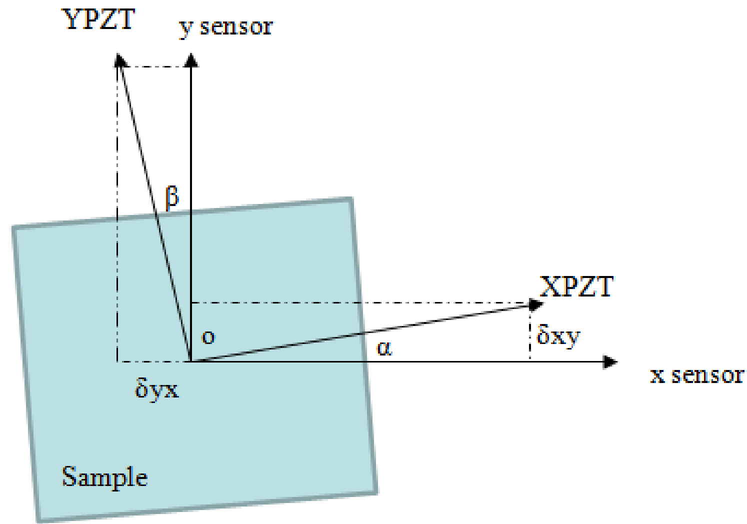

FIGURE 2-21: Straightness from angular error.

The desired displacements can be given by

$$\begin{pmatrix} x \\ y \\ z \end{pmatrix} = \begin{pmatrix} d_{xx} & \theta_{yx} & \theta_{zx} \\ \theta_{xy} & d_{yy} & \theta_{zy} \\ \theta_{xz} & \theta_{yz} & d_{zz} \end{pmatrix} \begin{pmatrix} x_{pzt} \\ y_{pzt} \\ z_{pzt} \end{pmatrix} \tag{2.15}$$

x_{pzt}, y_{pzt}, z_{pzt} are the motion outputs of the PZT actuator. x, y, z are desired positioning commands which can be measured by the capacitance sensors. θ is a small angle ($\sin\theta \approx \theta$).

Since the coefficient determinant is not zero, the equation has one solution for x_{pzt}, y_{pzt}, z_{pzt}

$$\begin{pmatrix} x_{pzt} \\ y_{pzt} \\ z_{pzt} \end{pmatrix} = \begin{pmatrix} d_{xx} & \theta_{yx} & \theta_{zx} \\ \theta_{xy} & d_{yy} & \theta_{zy} \\ \theta_{xz} & \theta_{yz} & d_{zz} \end{pmatrix}^{-1} \begin{pmatrix} x \\ y \\ z \end{pmatrix} \tag{2.16}$$

Under closed loop control, motions of the stage are controlled relative to the orthogonal target electrodes. Hence, uncertainties in this case correspond to those of the

planes of the electrode and measurement noise. Geometric errors of the target electrodes are likely to be stable. Consequently, these errors can be mapped and compensated by means of the closed loop control. Therefore, only the controller uncertainty would remain with the DAC quantization noise being the main error assuming the controller software is robust.

2.2.3 Other sources of uncertainty

The quantization noise limits the positioning resolution as well since the controller outputs the command through DACs. An ideal 16 bit DAC is able to output a voltage with a resolution one part in 2^{16}, and the standard deviation for the positioning noise is about 0.2 nm for 45 μm travel based on equation(2.12).

The high voltage amplifier output noise is 1.5 mVrms, however adding a reactive load, such as a piezoelectric actuator will decrease the noise since the capacitance will create a low pass filter with the output resistance.

Temperature drift will cause dimensional changes of mechanical components like the frame, target, electronic, thus increasing uncertainties, particularly for measurement over extended time periods. High conductivity materials like Aluminum, Brass and Copper are chosen to reach thermal equilibrium quickly. In addition, the thermal disturbance is reduced while the stage is working in a temperature controlled room. Hysteresis in the PZT actuator is compensated in closed loop control.

2.3 Controller design and positioning performance characterization

2.3.1 Controller considerations

The image is obtained by scanning in a regular grid of the sample surface. The higher spatial resolution the longer acquisition times needed. Therefore, the dynamic

performance of the system is important because the stability and speed are important for productive research. Fundamentally, the scan speed depends on the scanner's resonant frequency ω_n, damping ratio ξ, the electronics, and the controller hardware and algorithm. The scanning speed is judged by the slewing rate and the settling time approximated as $t_s = 4.6/(\xi\omega_n)$. Obviously, increasing the natural frequency and damping ratio is in the highest priority in the improvement of the design. However, control techniques with feedback sensor are able to extend the system's performance limit. For optical detection, there is a limit on intensity governed by the power of the illumination source and the tolerance level of the sample. Therefore there is always a compromise between scan time and image resolution, i.e. the number of photons collected is limited by the sample time for each pixel reducing as the speed goes up.

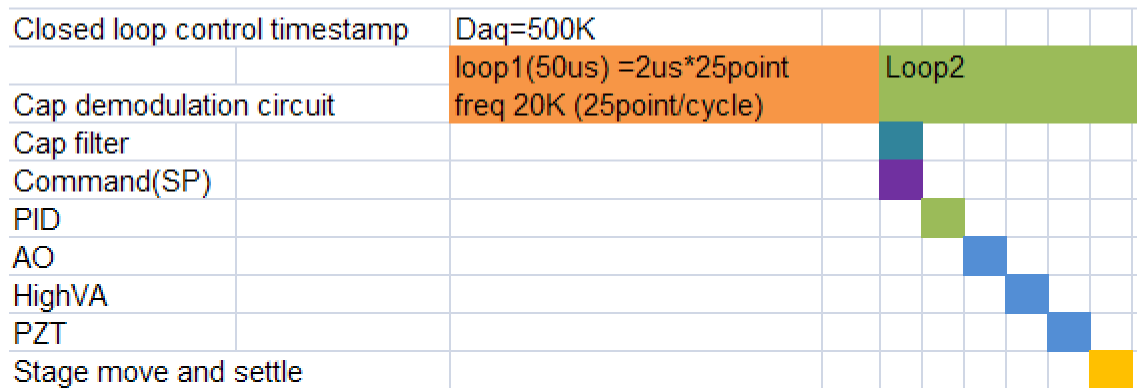

FIGURE 2-22: Time stamp of closed loop control (NI PXI FGPA 500 kHz sample rate).

There are several scanning modes the controller can implement, 1) open loop with fastest scanning speed, high resolution and low accuracy, 2) open loop with calibrated compensation, 3) open loop with unequal spatial interval of faster speed and highest accuracy while using displacement sensors to record the *xy* coordinates, 4) closed loop with unequal spatial interval while using displacement sensors to record the *xy*

coordinates, 5) closed loop with equal spatial interval having the slowest scan speed but most convenient and efficient measurement data sets. Open loop speed is only limited by the dynamics of the scanner,. With calibration, the accuracy can be improved; however, it is difficult to design a robust controller for different scanning conditions under open loop. Closed loop control has best accuracy, though adding certain delay from the sensor and controller which reduces the scan speed, also the added noise of the controller results correspondingly increases the position uncertainties. FIGURE 2-22 shows a time stamp of closed loop control. The capacitance demodulation requires a period of time, i.e. 50 μs to calculate the correct signal output to the next step, the filter, which adds another phase delay. At the same time, it and command set point join the PID servo loop, which adds a delay as well (usually but very small, i.e. a few μs). The output is sent to high voltage amplifier through DAC (a few μs). The HVA has a slew rate and bandwidth limitation as well. The PZT responses very fast (less than μs) and finally the stage positions and changes the displacement which is detector by the demodulation circuit and so on and forth. The whole process should be very carefully tuned to get best positioning dynamic performance based on the parameter of each step to set timed loop frequency, filter, series or parallel processing, and others.

2.3.2 Controller design and test

This section presents results of controller design and implementation on the prototype scanner

2.3.2.1 Prototype stage

An experiment is conducted by using a fast Fourier transform (FFT) analyzer (HP 35693A) to measure the open loop frequency response. The PZT actuators on each axis

are drove by the white noise signal from the FFT analyzer. The displacement responses of each axis are measured by the lion capacitance sensor and feed into the analyzer to be processed. FIGURE 2-23 shows the result that the natural frequencies of the axes were 430 Hz, 545 Hz for x, y axis.

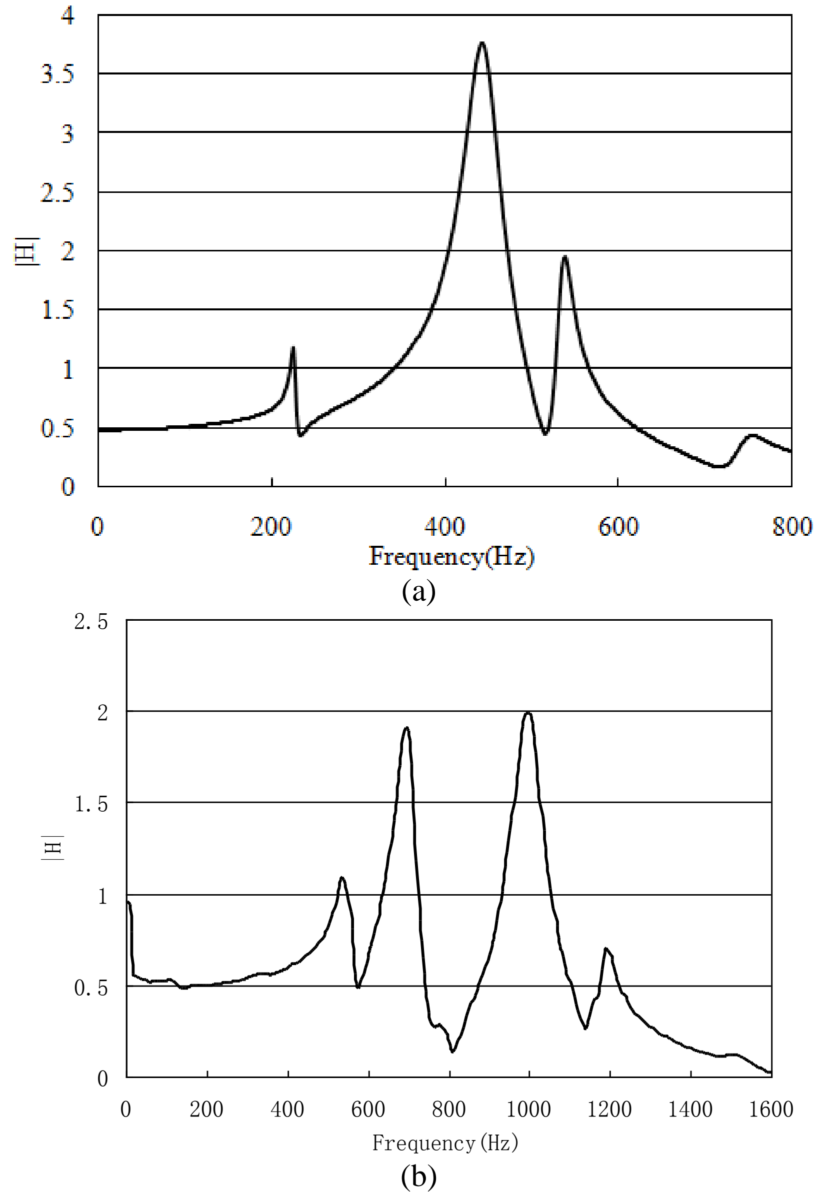

FIGURE 2-23: Frequency responses of x (a), y (b) axis of prototype stage.

The transfer function of the system including the sensor, actuator, and amplifiers can

be express as:

$$G_s = k * \frac{w_n^2}{s^2 + 2\xi w_n + w_n^2} * H_{sensor} * H_{daq}$$

The additional plant dynamics come from the capacitance probes' electronics. The capacitance probes (Lion-Precision DMT 22) have a 10 kHz bandwidth. The low pass filter in the conditional electronics can be modeled as a first order with a pole at 10 kHz.

$$H_{sensor} = \frac{62831}{S + 62831}$$

The digital controller also adds a phase lag from the discrete time sampling

$$H_{daq} = e^{-s \cdot T_d} \tag{2.17}$$

Where $T_d = 1/f_c$

Each direction of the stage movement is a second order system. Actuator and high voltage amplifier can be simplified as a gain k. A simple proportional, integral (PI) controller G_c was implemented in the Real-Time digital controller to compensate the positioning error.

$$G_c = K_p * \left(1 + \frac{1}{T_i * S}\right) \tag{2.18}$$

The P term can reduces the rise time and I term can remove steady state error between command and output of the sensor. The derivative term was not included because it amplifies the high frequency noise in the sensor although it can damp out transient oscillations and reduces the settling time. Finally the controller as described in FIGURE 2-24 is simulated in Simulink™.

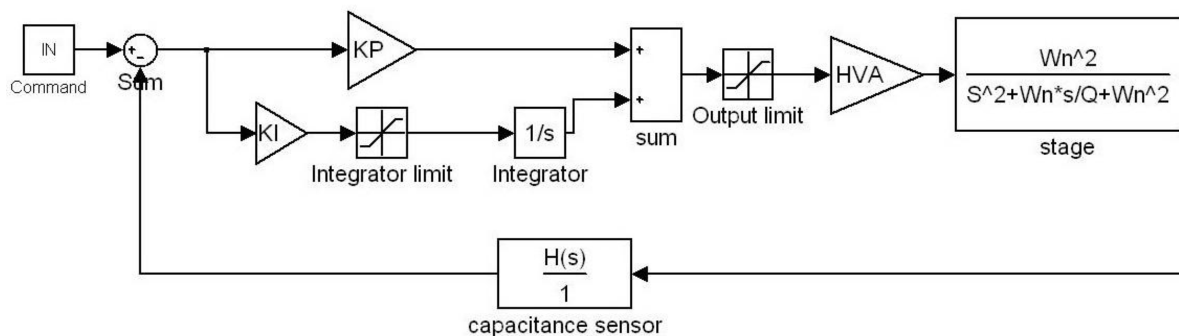

FIGURE 2-24: Controller design in Simulink.

In reality, Ziegler-Nichols's method [39] is conducted to tune the K_p and T_i parameters in real time.

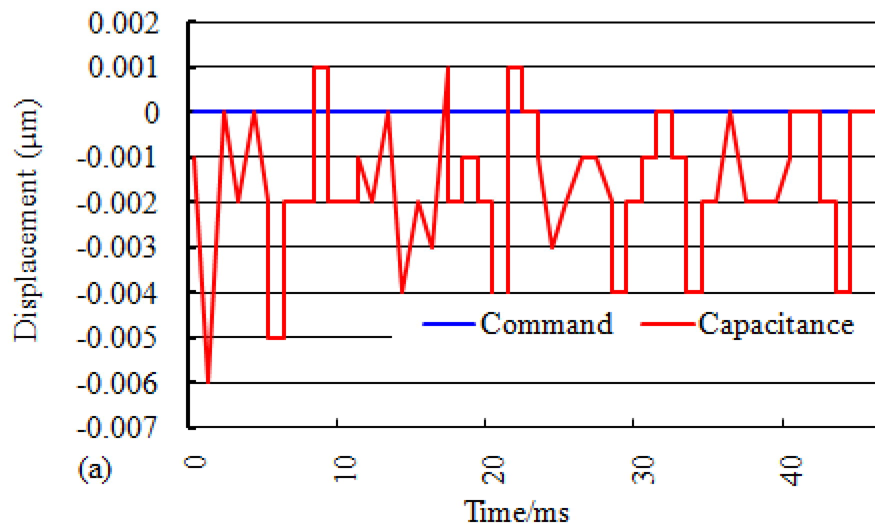

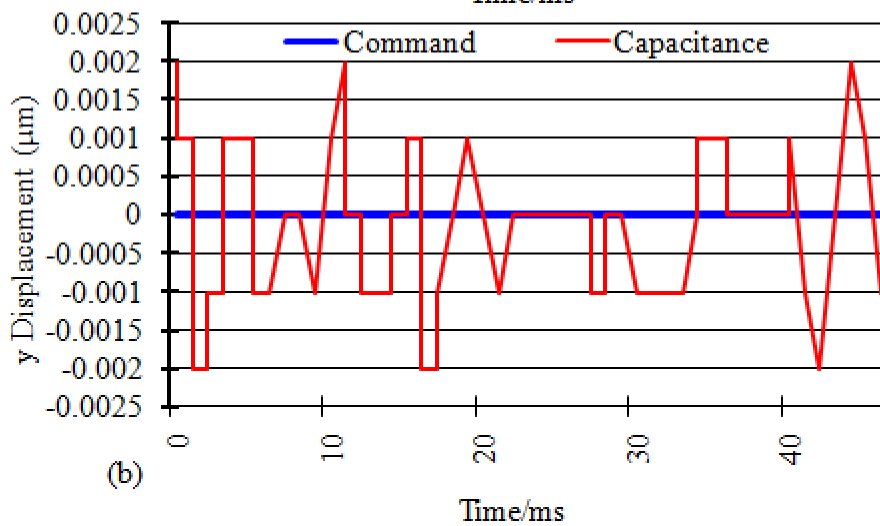

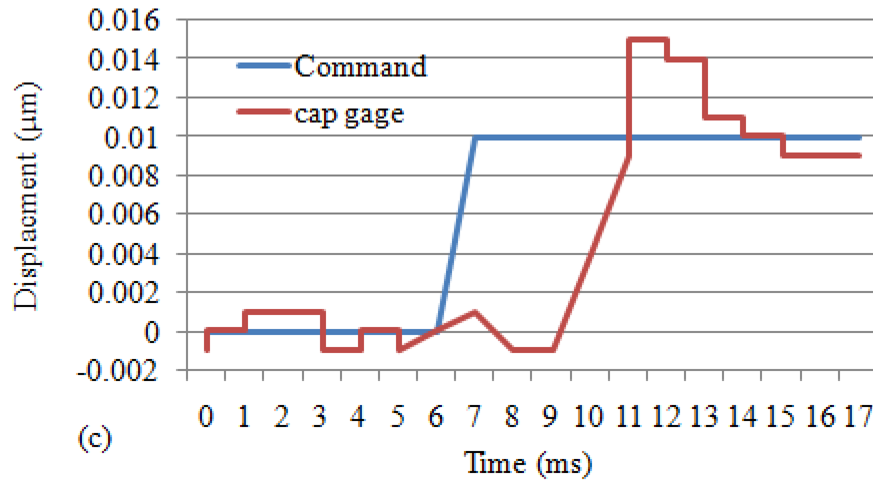

FIGURE 2-25: Positioning performance of prototype stage.

FIGURE 2-25 (a) (b) above shows the control error with PID controller. The RMS is 1.3 nm and 1 nm with respect to x, y axis. FIGURE 2-25 (c) shows a 10 nm step response of x axis. The settling time is around 5 ms.

2.3.2.2 XYZ fine stage

The xyz fine stage's positioning performance was investigated after the sensor issue (see section 2.1) and controller issue (see more details in chapter 4) was resolved, see below for comparison. As shown in TABLE 2-2, the positioning resolution (SNR) was improved from 1428 to 11842 (x axis), from 1428 to 12500 (y axis), from 2857 to 32926 (z axis).

TABLE 2-1: Performance of previous version of the stage [22].

	x	y	z
Max range (μm)	65	49.7	31.5
2σ noise (mV)	14	14	7
Signal to noise ratio	1428.57	1428.57	2857.14
Natural frequency (Hz)	299	232	754

TABLE 2-2: Performance of new version of the stage*.

	x	y	z
Max range (μm)	45	45	27
2σ noise (nm)	3.8	3.6	0.82
Signal to noise ratio	11842	12500	32926
Natural frequency (Hz)	299	232	754

* The sensor noise level value is used as the noise here (Bandwidth: 1 kHz), and digital demodulation method is used for sensors.

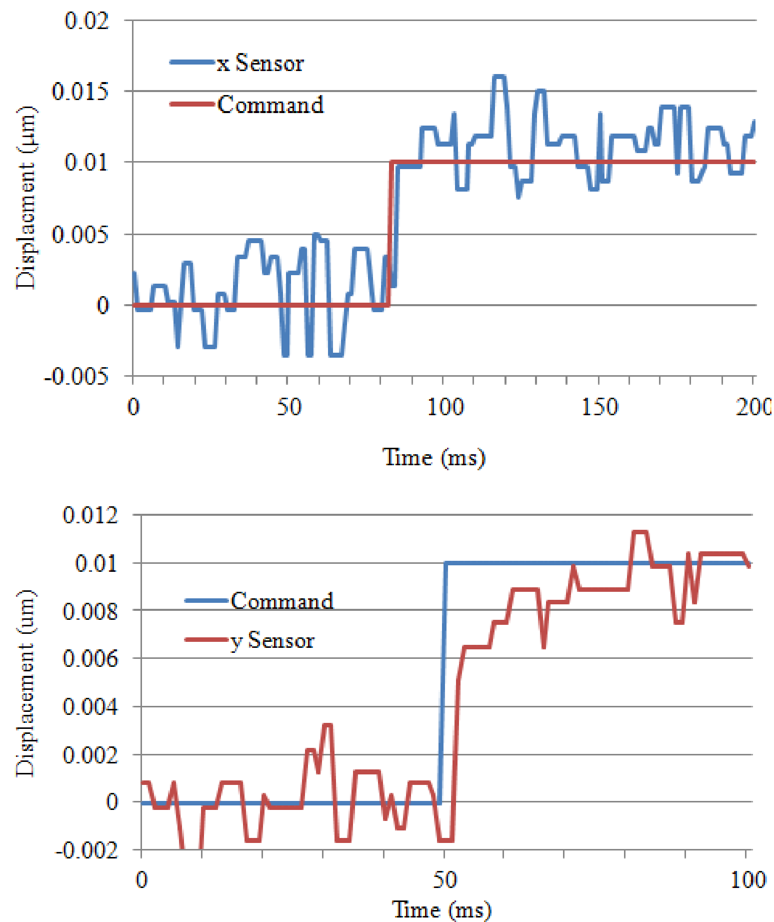

FIGURE 2-26: 10 nm step response of x, y axis, Top: x axis, Bottom: y axis.

FIGURE 2-26 shows 10 nm step response of x, y. The y axis positioning resolution is higher than x axis since the y sensor's noise level is lower than x sensor. The x step response shows a setting time of around 5 ms, while the y gives a setting time around 20 ms which may be reduced by re-tuning the controller parameters. FIGURE 2-27,

FIGURE 2-28, and FIGURE 2-29 show the straightness of each axis in open loop. TABLE 2-3 summaries the angular error among three actuator axes and sensor axes. It comes from the actuators coupling and alignment error. It is believed that these errors won't cause positioning issues since the desired position is mapped to the sensor coordinate through closed loop control.

TABLE 2-3: Angular error among actuators and sensor axes. (Unit: degree)

	x	y	z
x	0	0.318	0.636
y	1.082	0	0.152
z	0	0.091	0.320

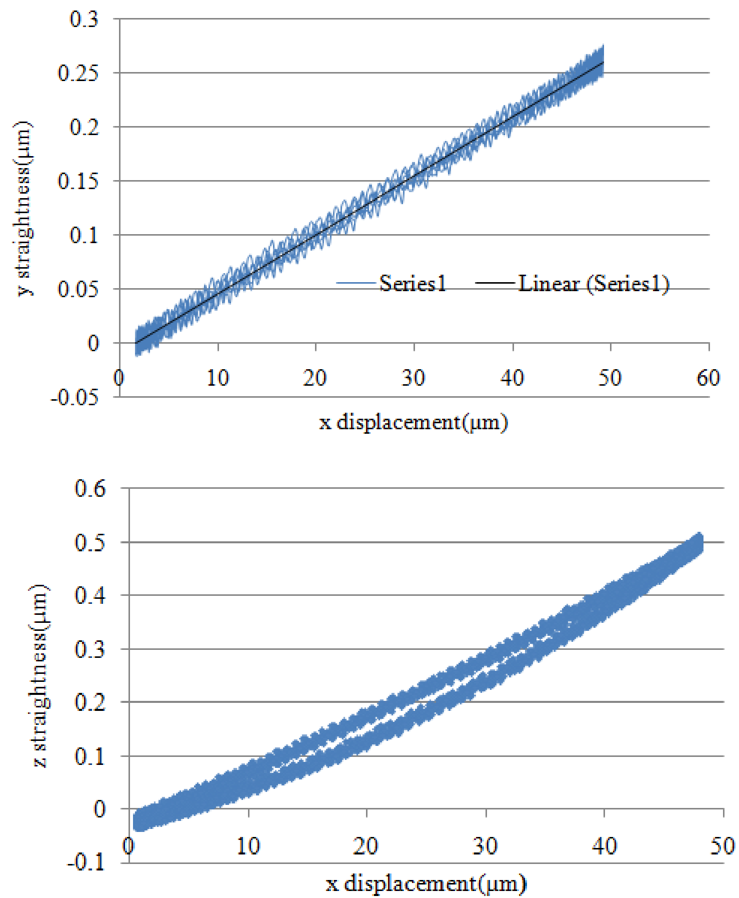

FIGURE 2-27: y , z straightness caused by x axis motion.

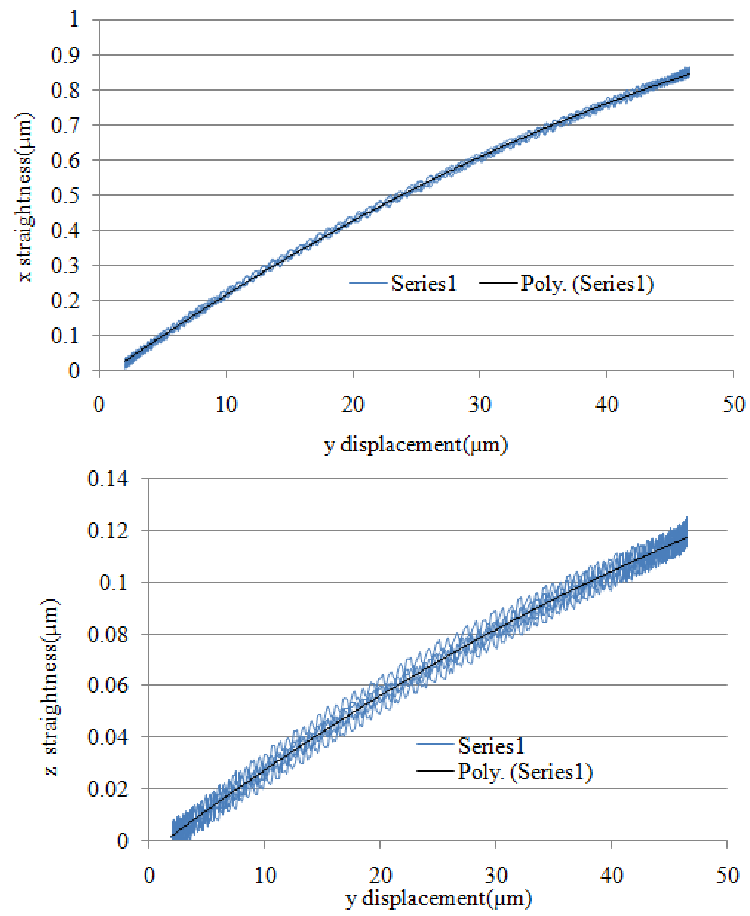

FIGURE 2-28: x, z straightness caused by y axis motion.

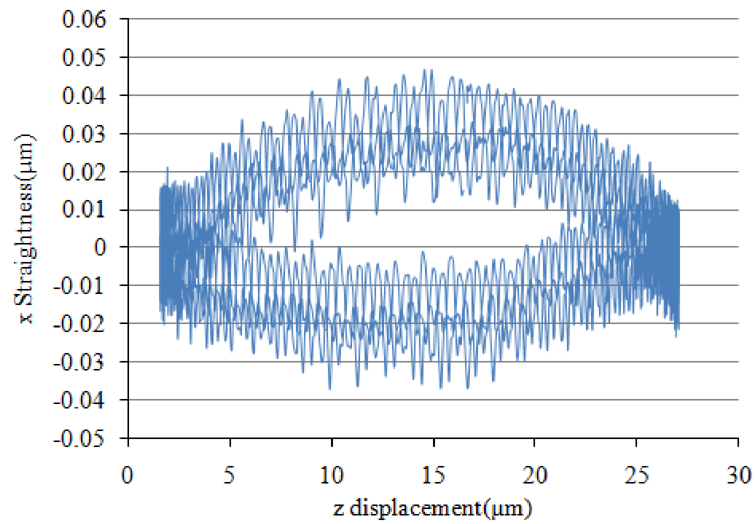

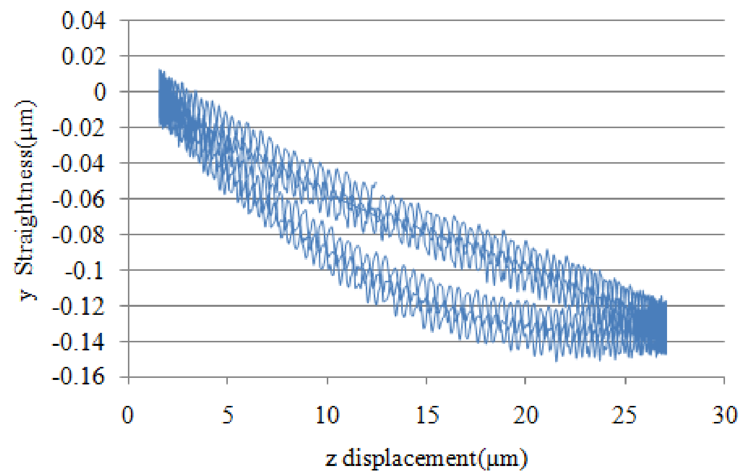

FIGURE 2-29: x, y straightness caused by z axis motion.

2.3.2.3 XYZ fine stage sample holder issue

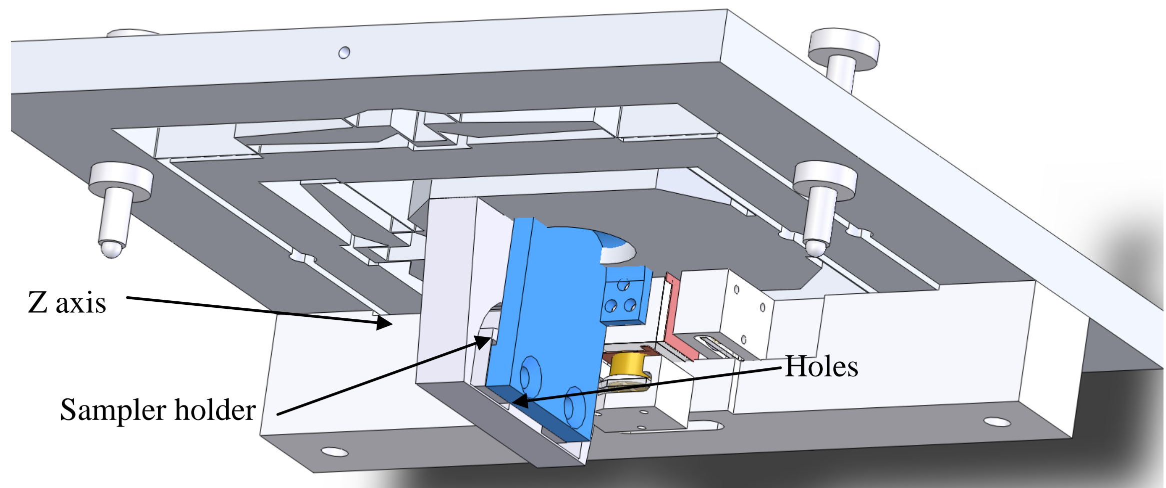

FIGURE 2-30: Sample holder issue 1 (Bottom view).

During the assembly of the new version of the sensor mechanical system, a design flaw for the sample holder was found as shown in FIGURE 2-30. The counter bore was circular cone like surface which may not be coinciding with the surface of the screw. This may cause the sampler holder to be loose during the scanning process. Therefore the surface was re-machined to be flat for socket button head screw as shown in FIGURE 2-31. However, this addressed another issue. It weakened the x stiffness of sample

holder at the L shape shoulder part. The first mode of the sampler holder is 660.56 Hz at the location of the clamp (It is a pitch tilt). The rib on one side does not help to increase the stiffness in that direction. Such low first mode on x direction will suffer the excitation from the motion on the fast x axis, leading to vibration and image distortion.

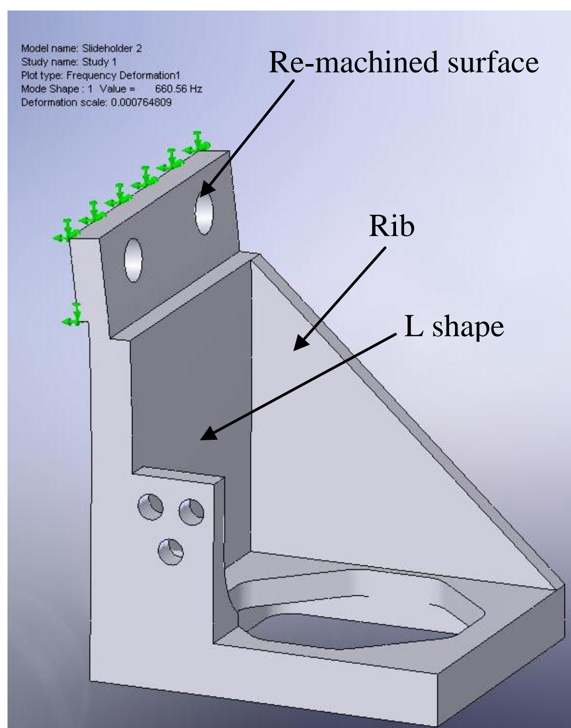

FIGURE 2-31: Sample holder issue 2.

x

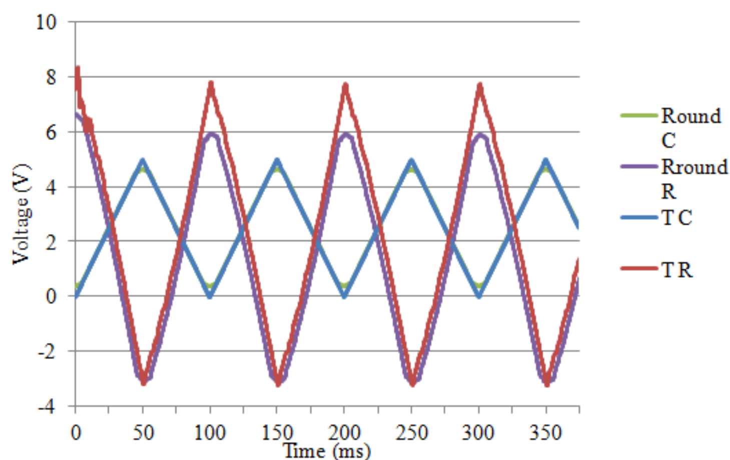

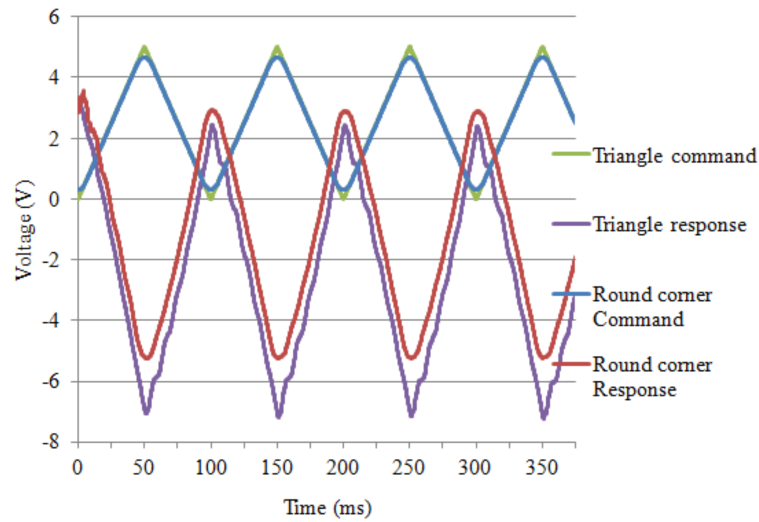

FIGURE 2-32: Vibration during scanning and method to address this issue, Top: x axis, Bottom: y axis, the responses was offset by 1 V for better comparison.

As shown in FIGURE 2-32, 5 Vpp 10 Hz triangular signals were commanded in open loop. The response was measured as voltage output by capacitance sensor. Both measured axis position showed a ripple when the stage reversed its direction. The ripple on y axis was worse than x axis. The reason for that may be the scan speed, 10 Hz, might hit the odd harmonic frequency along y axis. When a round corner method was employed to shape the command, the ripple was attenuated though the effective scan range decreased by 5-10%. To better address this issue, the sample holder need to be re-design, and the compliance axis of the sample holder should be along with low scan speed axis, i.e. y axis.

CHAPTER 3: FAST SCANNER

3.1 Overview

In the previous chapter, an update of the three-dimensional metrology stage for biomedical imaging systems (SMPM) that will enable the spatial co-registration of diagnostic information using optical and mechanical probes is presented. There are two most widespread scanning algorithms for a confocal scanning microscope. The one used in SMPM is the sample scanning method which provides best image quality as the scanner can provide precision and repeatability of several nanometers, and components forming the optical path, being stationary relative to the optical bench, can be precisely aligned; however, the imaging speed is limited by the mass of the moving components and high accelerations may result in the sample moving during the scanning process. Another method used in most of the commercial confocal microscopes is the beam scans. Linear galvanometer, resonant scanners, or acousto-optical device (AOD) are applied to laser scanning confocal imaging by scanning mirrors in the excitation beam path in order to scan the beam in the xy sample plane. This method provides very fast scanning speed at few hundred Hz (linear galvanometer), thousands of lines per second (resonant scanners), and up to 100 kHz (AOD) [40], but the image qualify is not as good as the sampling scanning method due to the alignment issue in the optical path which degrades the quality of the beam [41]. For resonant scanner, its acceleration force causes the mirror

to bend or flex which will distort the laser [41]. Also the sinusoidal motion leads to a slowing motion at the edges and maximal velocity in the middle of the scanned field where the image looks stretched when the pixel is updating at a constant rate [42]. The other disadvantage is the high uncertainty induced from the thermal drift of the magnetic actuator and transducer.

3.2 Introduction and motivation for the fast scanner

In this chapter, a novel scanning method is proposed. Instead of scanning the incoming light by using the galvanometer or AOD, the light source coming out from a fiber is positioned by a scanner in xy plane, resulting in a corresponding displacement of the focused beam in the sample object plane.

1. Use of a single mode optical fiber enables spatial filtering of the excitation beam, thus allowing for high resolution imaging and localization of single molecule sample features.
2. Further, the optical fiber enables remote light sources to be swapped in and out with minimal beam alignment issues. Delivery of the excitation sources with the single-mode fiber provides physical, mechanical, and optical decoupling (at least in a flexible sense) from the microscope. Because all of the beam alignment and optical components are openly distributed on an optical bench manual alignment is much easier than conventional microscope systems. Open access to the components of the system also simplifies implementation of different optical systems for the purpose of rapid prototyping and research.
3. The optical fiber is a single mode fiber, which has the benefit of a very well characterized beam shape and, hence, point spread function [43]. As such, the

typical use of a pinhole in the excitation path in order to shape the beam for confocal imaging is no longer necessary when using a single mode optical fiber.

4. Further, the low mass of the fiber, which is about equal to that of a human hair, enables high speed scanning for rapid biological fluorescence imaging.

An *xy* piezoelectric actuated fast scanner shown in block 6 in FIGURE 1-1 in Chapter 1 is used to control motion of the fiber. Initial experimental results showed that a scan range of the positioner of around 60 μm in each axis corresponding scan of 5 μm range of the spot. Such an attenuation of around 12:1 for this optical system may be of particular benefit for high resolution, metrological confocal microscopy, i.e. nanometer positioning resolution on the fast scanner will give sub-nanometer resolution control at the sample. The low mass of the optical fiber enables high speed imaging of samples without having to move the more massive sample stage with specimens also sometimes comprising liquid specimen environments. Furthermore, by integrating the fast fiber scanner into the whole system, a dual scanner is feasible where *xyz* scanner responses for large scale image and *xy* fast scanner zooms in for more precise imaging at points of interest with much higher imaging speed.

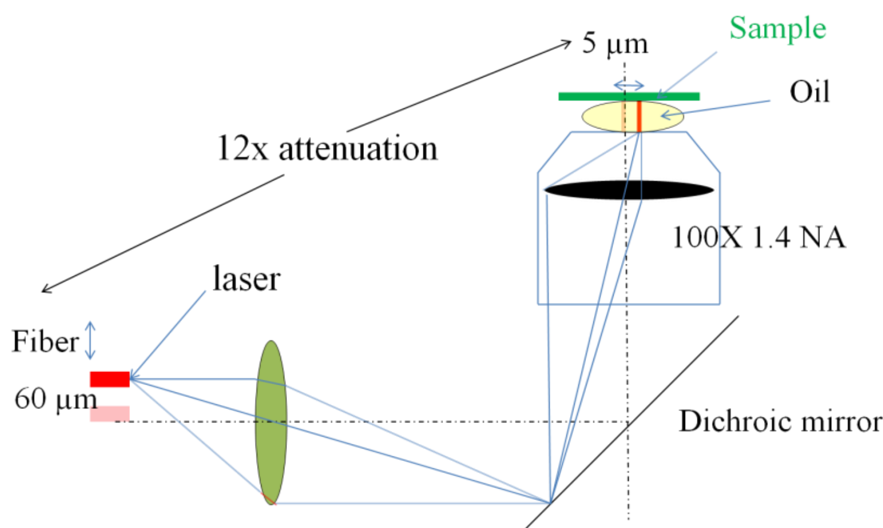

FIGURE 3-1: Principle of operation.

FIGURE 3-1 is a schematic diagram illustrating the principle of operation. The laser beam emits from the fiber, and pass through the collimator, excitation band-pass filter, then is reflect to the objective underneath the specimen by the dichromatic mirror. For the focusing mechanism in the current optical lens setup, the laser source is imaged onto the defined focal plane at the sample. Scanning and imaging is achieved using the PXI-7852R smart DAQ card in LabVIEW™ Real-time and uses an FPGA-based controller. Currently optical detection tools that can be used with this system are capable of recording fluorescent resonance energy transfer, fluorescence anisotropy and single molecule imaging.

3.3 Mechanical design of the fast scanner

To achieve smooth, frictionless, fast response, a flexure constrained, *xy* piezo-electrically actuated, scanner has been designed to have a range of 60 μm by 60 μm and more than 1 kHz bandwidth in open loop operation. Because of the optical attenuation of approximately 12:1, it is desired that the scanner maintain controller errors within 10 nm over the 60 μm scan range corresponding to a signal to noise target of around 10,000:1.

PZT actuator is employed in the design mainly because of its high bandwidth, stiffness, and resolution. Given that the available piezoelectric actuators have a maximum displacement of 16 μm, leverage is required to amplify this motion to achieve the desired range. In the first few conceptual designs, a linear leverage was proposed. It is beneficial for the low coupling between axes, easy capacitance sensor implementation. The drawbacks are the relatively high compliance and low resistance to environmental disturbance, such as temperature drift. A tip-tilt angular leverage design is adopted to obtain a displacement amplification factor of four, see FIGURE 3-2 (a). To maximize stiffness (and therefore dynamics) and match dynamic performance in the two axes, it is based on a parallel-kinematic design with two orthogonal pairs of differentially-driven piezoelectric actuators. This design provides same low inertia for x and y motion, resulting higher responsiveness and axis-independent performance. However, this mechanism may introduce more serious parasitic motion than the linear leverage for its parallel kinematics, and brings in difficulty in the sensor setup and calibration. FIGURE 3-2 (a) illustrates the amplification mechanism in one axis for which the scanning range can be calculated from,

$$\delta = \frac{L}{l}\varepsilon \tag{3.1}$$

Where ε is half of the extension of each PZT actuator and the ratio of lengths is the mechanical lever ratio.

Ignoring lost motion, the stroke is calculated to be around 60 μm for the design used in these experiments. Four, orthogonally symmetric, leaf spring flexures on the upper face of the mechanism provide the preload and guide the motion of the moving platform.

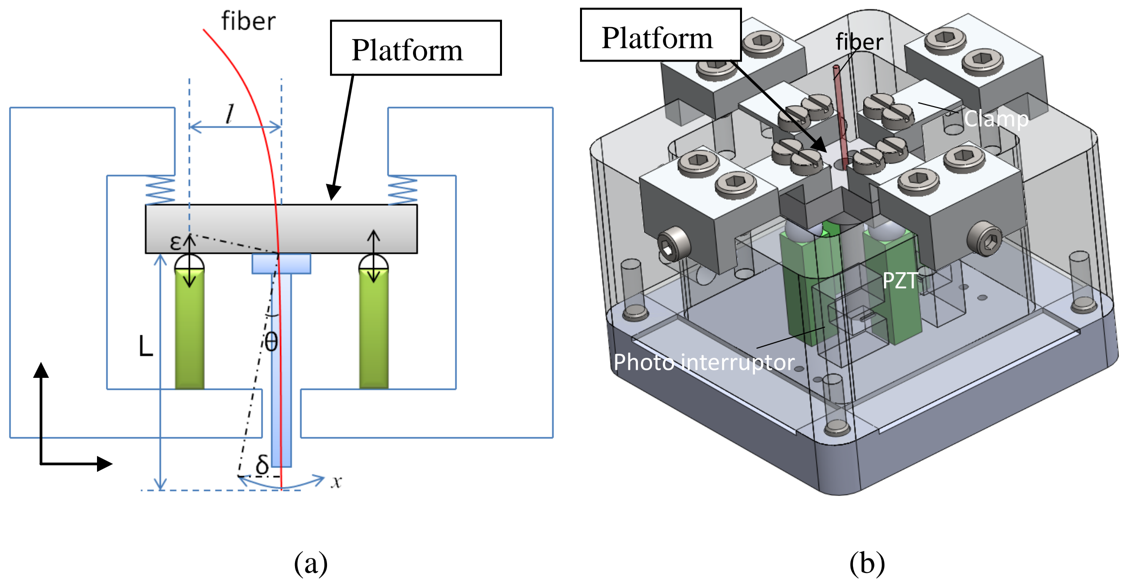

(a) (b)

FIGURE 3-2: Scanner design, (a) principle of operation L = 46mm, l = 10mm, (b) CAD model of the fast scanner.

$$\sin\theta = \frac{\delta}{L} = \frac{\varepsilon}{l} \tag{3.2}$$

$$dxz = (1 - \cos\theta)L \tag{3.3}$$

Where dxz is the displacement error in the z axis (straightness) due to translation in the x axis. It is estimated to be around 13 nm at x maximum position. This error does not affect the performance as it only changes the distance of the optical path by 13 nm during the full scanning process. Such tiny out of focus is believed to result in a trivial impact on the focus plane at the specimen.

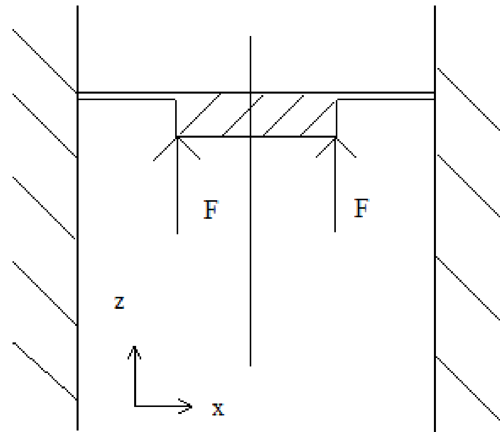

FIGURE 3-3: Cross-sectional sketch of the beam flexure.

A leaf type flexure shown in FIGURE 3-3 provides preload to the actuators and constrains x axis motion of the moving platform. Four truncated balls from Bal-tec [44] are glued on the PZTs providing two pairs pivots against the platform. The pivots provide two degree freedom, pitch along y and z linear motion. The linear z stiffness of one leaf spring is defined by [27],

$$kz = \frac{12EI}{L^3} \tag{3.4}$$

Where E is the Young's modulus of the material, I is the second moment of area about the neutral axis of bending, L is the length of the beam. For a rectangular cross sectioned beam

$$I = \frac{bt_3}{12} \tag{3.5}$$

Where b is the width of the beam and t is the thickness.

The desired beam stiffness is a compromise among the dynamics, actuator, motion loss and yield strength of the material. Considering about 10% motion loss and stiffness of the PZT, the maximum stiffness k is defined by,

$$k = \frac{1}{9} k_{pzt} \tag{3.6}$$

k is about 0.9 N·μm^{-1}

Also the maximum stress should be within a safety factor of two, where the stress σ defined by [27],

$$\sigma = \frac{Mt}{2I} \tag{3.7}$$

Where M is the bending moment applied to the flexure.

The aluminum 6061-T is used for manufacture because of availability in the lab group, easy manufacturing, and high thermal diffusivity. For aluminum, the yield strength σ_{yield} is taken to be 276 MPa [27].

The moment M can be calculated either from the total force or from the preload force plus the required force for maximum translation δ from [27],

$$M = M_s + M_{preload} \tag{3.8}$$

$$M = \frac{6EI\delta}{L^2} + \frac{F_{preload} L}{2} \tag{3.9}$$

Where δ is the maximum deflection of the flexure, which is around 15 μm.

Using the equations above and considering the size of the scanner, values for major dimensions of the flexure spring are given by TABLE 3-1. Examples of spreadsheets used for the above calculations are shown in Appendix A.

TABLE 3-1: Main parameters of the flexures.

Parameter	Value	Parameter	Value
Thickness	1 mm	Preload-Force	40 N
Width	10 mm	Force for δ	14.3 N
Length	9 mm	Stiffness k_x	0.95 N μm^{-1}

TABLE 3-1 (continued)

Stress	146 MPa	Resonant freq.	2816 Hz

A preload force is desired to provide high stiffness of the coupling between the actuator and moving platform in order to get fast dynamic response. Additionally, this preload will maintain contact caused by high accelerations during motion reversal. Manufacturing tolerance principle is used to get a close preload force by designing the gap between the clamp and the top surface of the frame to be 100 μm. Further adjustment of the preload can be obtained by applying a metal spacer between this gap or the gap between the clamp and the platform. The resonant frequency is calculated based on the linear stiffness of the four flexures and the mass of the platform.

Finite element analysis was conducted to estimate the system's static and dynamic performance as shown in FIGURE 3-4. The platform with the fiber holder located underneath has a stiffness of about 4*0.95 $N \cdot \mu m^{-1}$ and a linear resonant frequency at around 2.8 kHz predicted using FEA. The fiber holder's 4th mode of resonant frequency is about 4.6 kHz which tends to be coming from the vibration of the cantilever beam of the cylindrical ferrule mount. The simulated static displacement in FIGURE 3-4 (c) is close to theoretical value 15 μm when the desired force (14.3 N) is applied to the four flexures corresponding to a static stiffness of 0.95 $N \cdot \mu m^{-1}$. The simulated stress (83.6 MPa) is less than the theoretically predicted value (146.8 MPa) when the forces (with preload force) are applied.

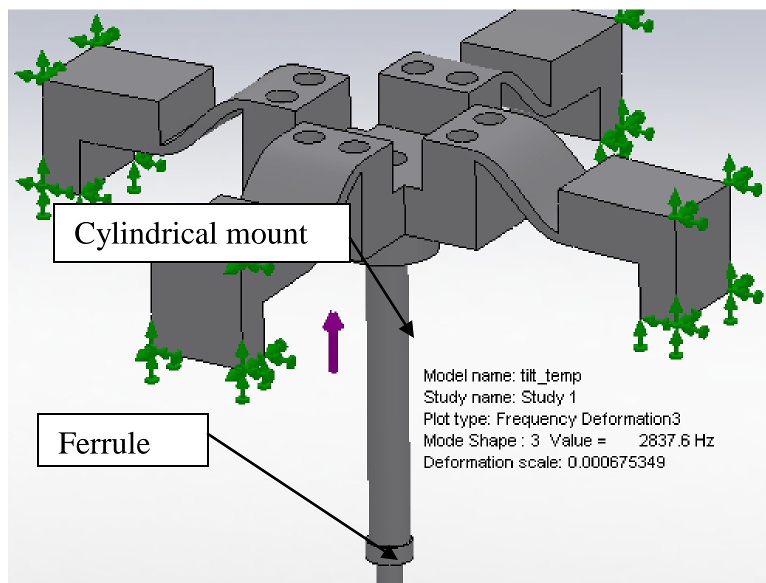

(a)

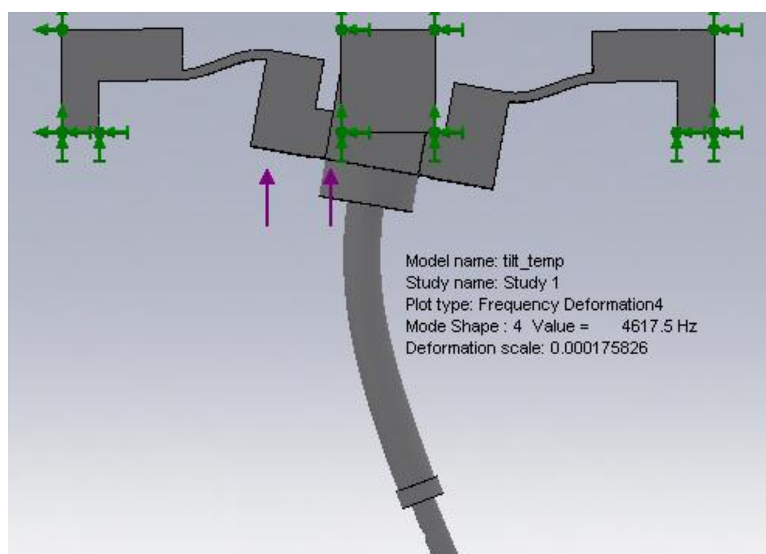

(b)

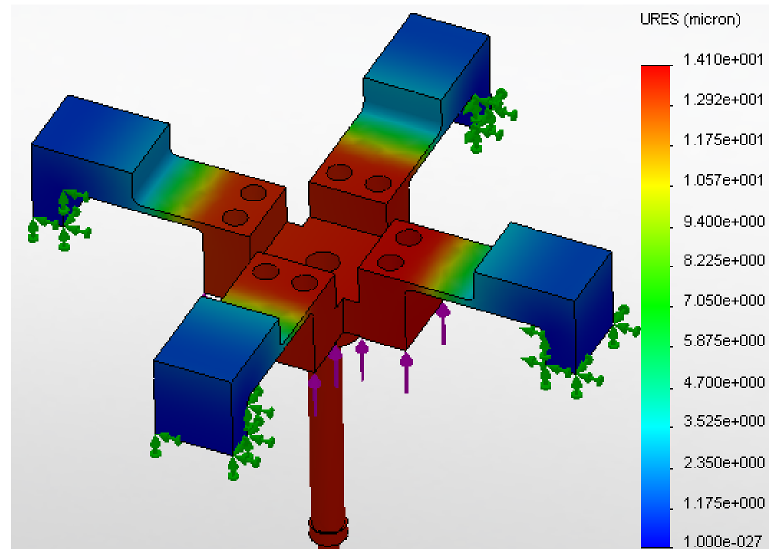

(c)

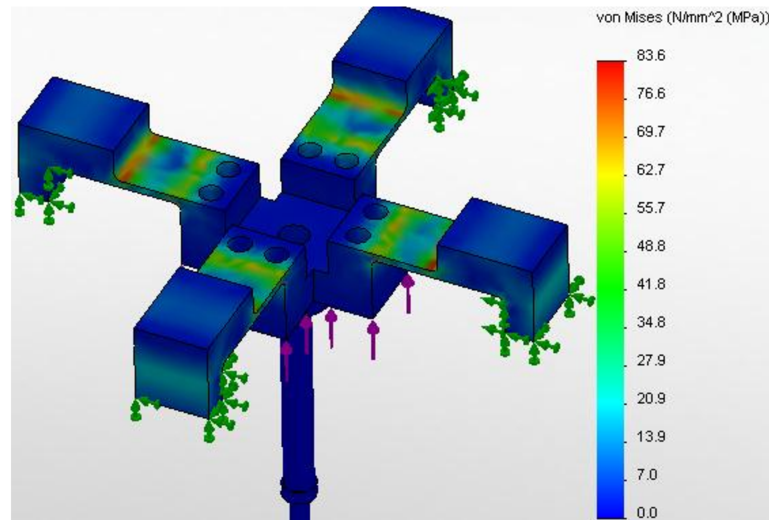

(d)

FIGURE 3-4: FEA results, (a) model shape 3 of the scanner which indicates the linear resonant frequency, (b) model shape 4 indicating the first model of the cantilever beam, (c) displacement deformation with the prescribed force, (d) deformation stress when the force are applied.

FIGURE 3-5 shows a photograph of the mechanical parts during various stages of assembly. Assembly progress shown in these figures corresponds to the four clamps with flexure beam are fixed to the frame while the platform is pushed against the clamps. The cylinder is attached to the bottom of the platform with a ferrule glued at the end. The fiber passes through the cylinder from the top of the platform and is fixed by the ferrule

and the completed assembly is attached to a three-axis micrometer stage.

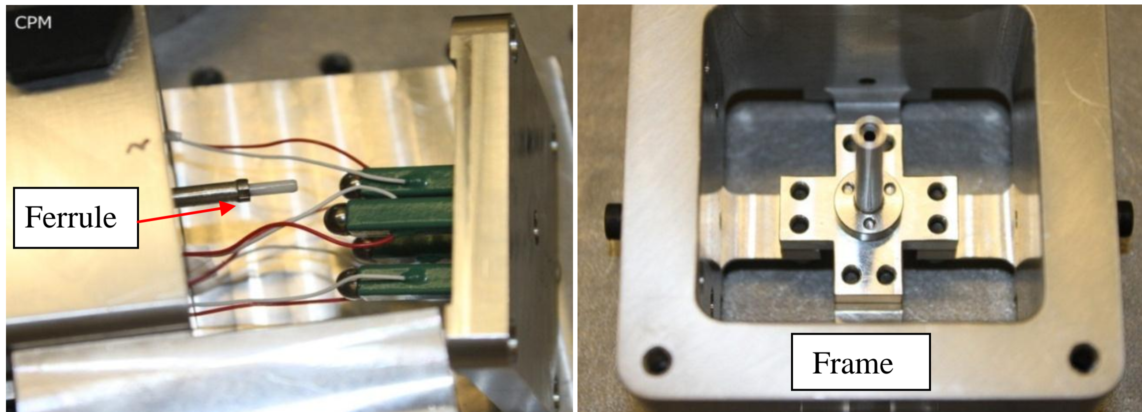

(a) (b)

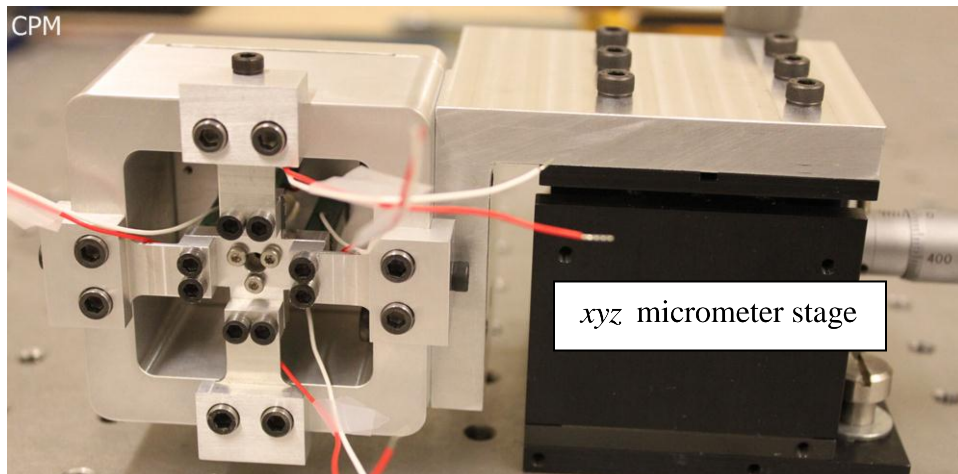

(c)

FIGURE 3-5: Photography of the scanner parts and assembly, (a) assemble the frame with the base, (b) assembly of the frame with the clamps, platform, and the cylinder, (c) a xyz micrometer stage is attached to the fast scanner for coarse adjustment in optical alignment.

3.4 Displacement sensor design, calibration and test

The angular amplify mechanism makes it difficult to install typical displacement sensors, i.e. capacitance sensor. An optical sensor (Omron EE-SX1071 photo interrupter), is employed to measure the displacement of the fast scanner. A photo interrupter is

composed of an infrared emitter on one side and a shielded infrared detector on the other. Displacement sensitivity is achieved by a straight edge that is fixed perpendicularly onto the ferrule mount cylinder. When the edge moves with the cylinder, it cuts through the beam and, therefore, the detector produces a current that varies with the displacement of the motion of the knife edge. More details on the principle of operation and performance for this sensor can be found in [45] (submitted) and Chapter 5. FIGURE 3-6 shows the current setup of the photo interrupter positioned to sense motion of the cylinder.

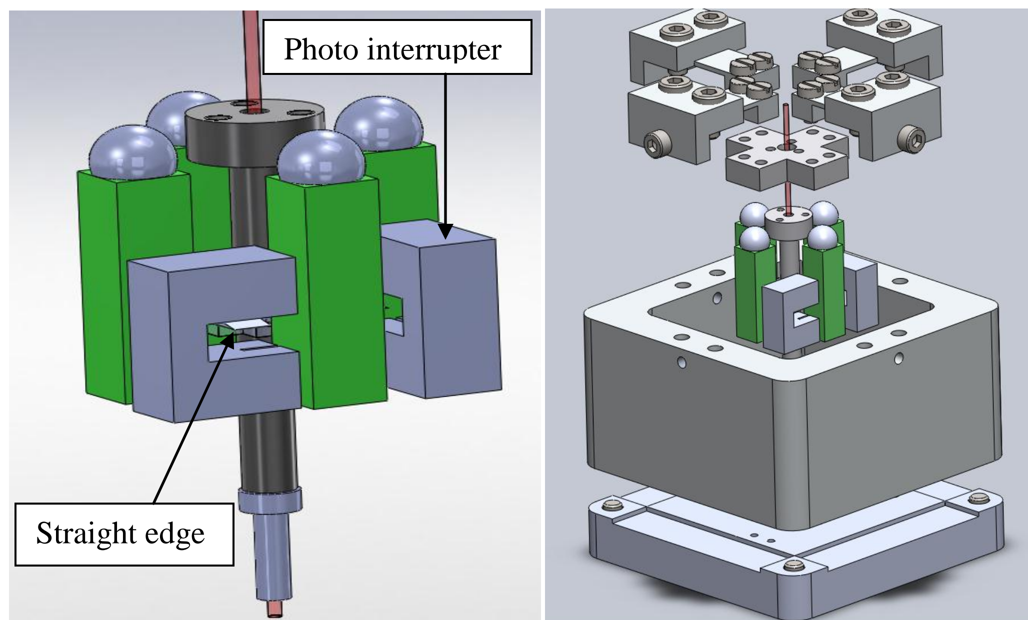

FIGURE 3-6: Sensor setup within the scanner body.

The straight edge target shown in FIGURE 3-7 is a silica slice with a straight line coated with aluminum by mask lithography. To get a straight line feature, a low profile MB-DynaSharp™ blade from Thermo Scientific was adopted as the mask where the blade edge was imaged onto the silica. Then the silica with the coated line feature was cut into several slices with desired size to fit in the scanner body and sensor. It was glued on to a piece of holder which adheres to the cylinder with the edges align with the clamps

edges, see the red lines indicating the edges to be aligned in the right image of FIGURE 3-7.

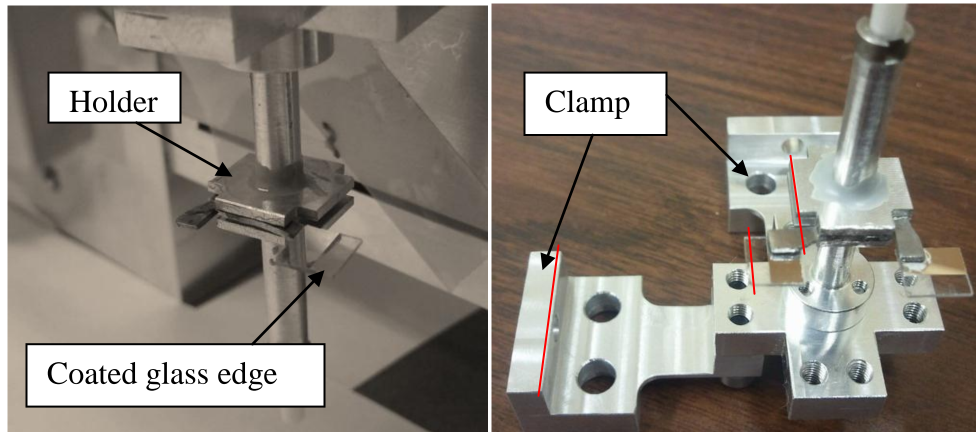

FIGURE 3-7: Assembly of the coated glass edge.

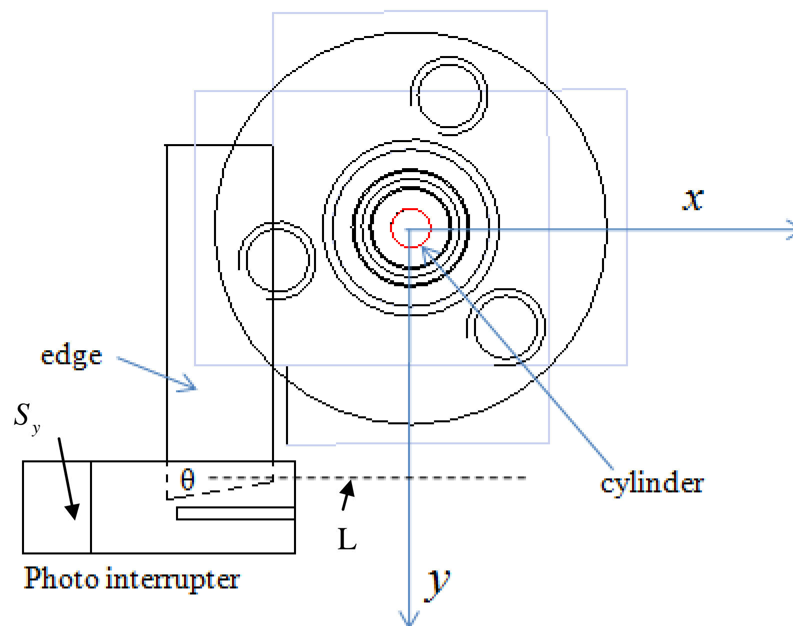

FIGURE 3-8: Setup error analysis.

During the assembly, there exists an angular error θ coming from the misalignments among the glass edge, holder and the direction of the motion as shown in FIGURE 3-8. The sensors' calibrated measurements S_x, S_y are given by,

$$S_x = y\sin\theta_x + x\cos\theta_x$$
$$S_y = x\sin\theta_y + y\cos\theta_y \quad (3.10)$$

Where x, y is the desired displacements at the ferrule end, θ_x, θ_y are the setup angular error about the z axis of the two sensors. θ_x, θ_y is calculated to be around 4.9 ° and 0.9 °by solving the equation using the data obtained when switching each axis on and off. The distance L between the motion axis and the sensor causes an Abbe error when there is an angular error during the y motion in FIGURE 3-8. However, this error is eventually compensated when x, y displacement of the center point is calibrated.

From (3.10), the command position which is the set point of the controller should be given by,

$$\begin{pmatrix} x_c \\ y_c \end{pmatrix} = \begin{pmatrix} \cos\theta_x & \sin\theta_x \\ \sin\theta_y & \cos\theta_y \end{pmatrix} \begin{pmatrix} x \\ y \end{pmatrix} \quad (3.11)$$

FIGURE 3-9 shows the experimental apparatus of the calibration experiment. The circuit for photo interrupter measurement is a simple circuit with an AD549J operational amplifier (Ultralow Input Bias Current) configured for transconductance with a selected feedback resistance providing current gain. An OP07 operational amplifier is employed as an active first order low pass filter with cutoff frequency at 1 kHz. Calibration is achieved using a closed loop capacitance based nano-positioner (InSituTec IT-XY-100) as a reference sensor. A same photo interrupter (called PI_B) is fixed onto the nano-positioner and aligns carefully with the ferrule where the ferrule blocks the center of the beam within PI_B. Firstly, the fast scanner is turned off, and let it settle down for a few hours, and then the nano-positioner is turned on with a 1 Hz sinusoid wave motion of amplitude 25 μm. The displacement of the positioned measured by the built-in

capacitance sensor is record as well as the output of the PI_B as shown in FIGURE 3-10 (a). A first order line is fit to the data using least squares. After that, the nano-positioner is set stationary, and the fast scanner is actuated by a 0.5 Hz sinusoid wave with the full range of the PZTs. The outputs of PI_B and PI_A are plotted in FIGURE 3-10 (b) where PI_A is the sensor to be calibrated inside the fast scanner.

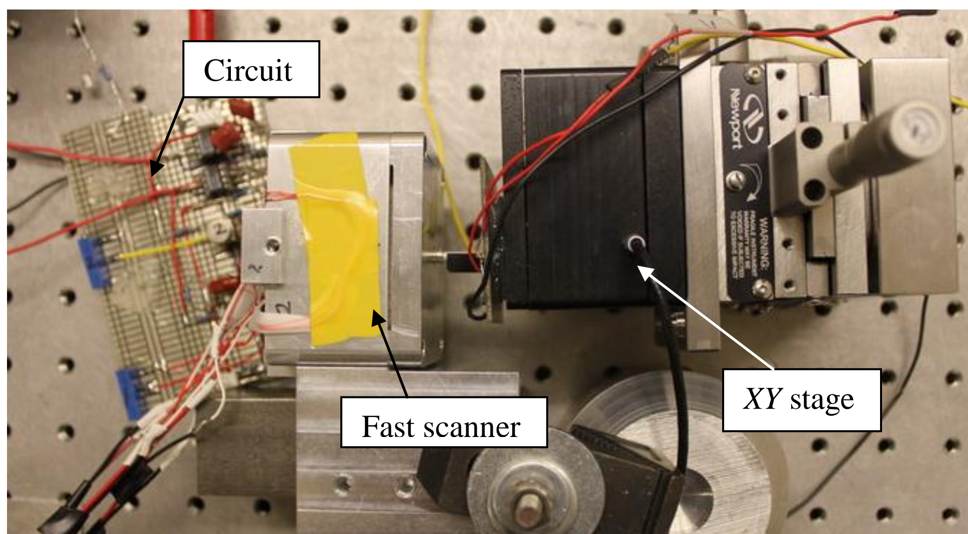

FIGURE 3-9: Calibration setup.

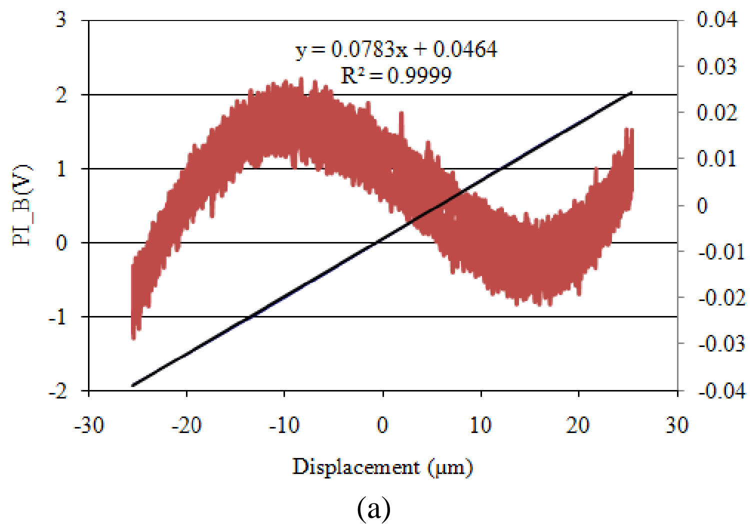

(a)

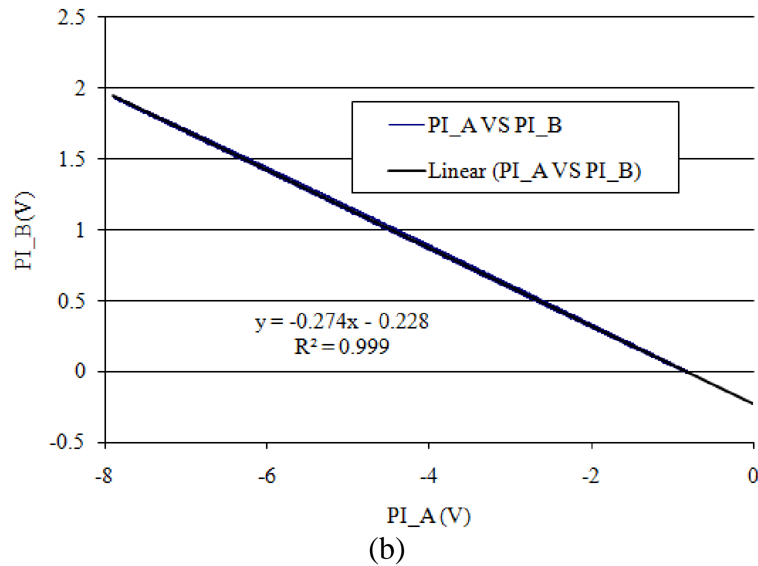

(b)

FIGURE 3-10: Calibration date of x sensor (measuring motion caused by PZT 1 and PZT 3), (a) raw and fitting data of displacement versus PI_B, (b) raw and fitting data of PI_A versus PI_B.

From the two fitted equations shown in FIGURE 3-10, the sensor PI_A is calibrated as,

$$S_x = -3.576V_x + 28 \tag{3.12}$$

Where V_x is the voltage of x channel sensor. The photo interrupter shows deviations from linearity of 1%. Then sensor for y axis is also calibrated in the same way, and its equation is given by,

$$S_y = -4.2722V_y + 27.7 \tag{3.13}$$

The full range of the sensors after calibration is around 50 μm. The signal deviation for the x sensor has an rms value of 6 nm over a time period of one second at 1 kHz bandwidth as shown in FIGURE 3-11. For y sensor, the noise level is around 13 nm. The reason is that a different type of photo interrupter from another vendor is used as y sensor where the Omron one is used up. This sensor has lower sensitivity than the Omron and

therefore a higher gain is set in the operational amplifier for y sensor where its noise is amplified as well.

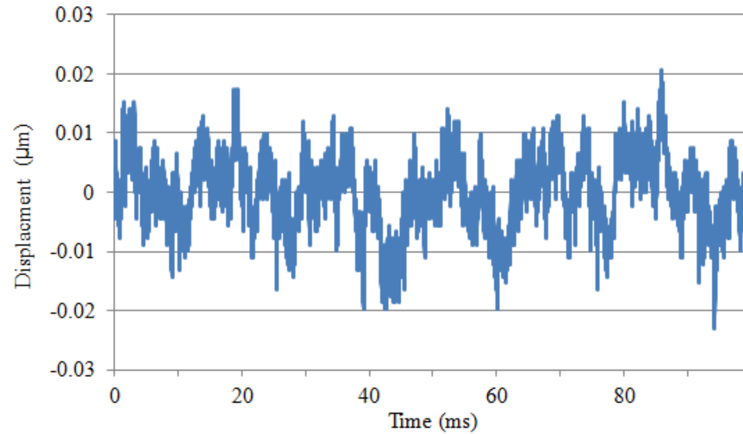

FIGURE 3-11: One hundred mini-second time period of x sensor.

3.5 Controller design and implementation

To eliminate the drawbacks of open loop control with PZT actuators a closed loop controller is required. In this section, a theoretical dynamic model of the mechanical part of the scanner is derived, and then an experiment is conducted to verify the model in open loop. A mathematical model of the entire system is built and several control algorithms implemented based on this mathematical model. Various positioning experiments give the actual performance of the controller, and, finally, several problems related to the system performance are detailed.

3.5.1 System description: theoretical analysis

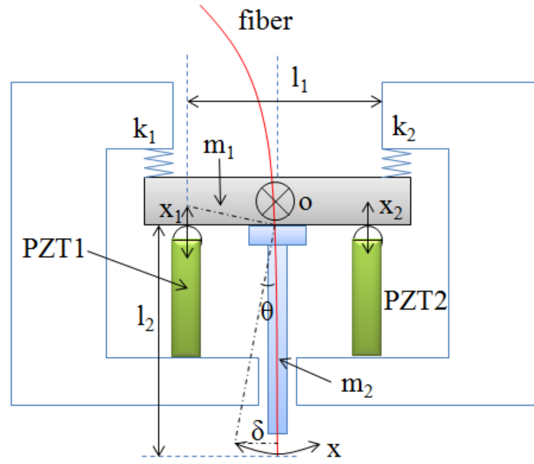

FIGURE 3-12: Theoretical analysis of the scanner dynamics.

Assume the plate (m_1) and tube (m_2) rotate along the o point, the second moment of mass, kinematic energy and potential energy is given by,

$$I \approx I_1 + I_2 = \frac{m_1}{3} l_1^2 + \frac{m_2}{12} l_2^2 \tag{3.14}$$

$$T_k = \frac{1}{2} I \omega^2 = \frac{1}{2}\left(\frac{m_1}{3} l_1^2 + \frac{m_2}{12} l_2^2\right) \frac{4 \cdot \dot{x}^2}{l_1^2} \tag{3.15}$$

$$U_p = \frac{1}{2} k_1 x_1^2 + \frac{1}{2} k_2 x_2^2, k_1 = k_2, x_1 = -x_2 = x \tag{3.16}$$

$$U_p = k_1 x^2 \tag{3.17}$$

According to the Lagrange's equation, the equation governing the motion of the mechanism is given by,

$$\frac{d}{dt}\left(\frac{\partial T}{\partial \dot{x}}\right) - \frac{\partial T}{\partial x} + \frac{\partial U}{\partial x} = 0 \tag{3.18}$$

$$\left(\frac{m_1}{3} l_1^2 + \frac{m_2}{12} l_2^2\right) \frac{4 \cdot \ddot{x}}{l_1^2} + 2k_1 x = 0 \tag{3.19}$$

From equation (3.52), (3.19) is calculated as,

$$0.92\times10^{-6}\frac{4\ddot{x}}{400\times10^{-6}}+20.92\times10^{6}x=0 \tag{3.20}$$

The first model of resonant frequency is given by,

$$f=\frac{1}{2\pi}\sqrt{\frac{2\times0.92\times10^{6}\times20^{2}}{0.92\times4}}=2232\text{ Hz}$$

3.5.2 Experimental results

As shown in FIGURE 3-13, open loop frequency responses of the fast scanner of each axis were measured using an HP 35693A Dynamic Signal Analyzer (DSA) over small displacement ranges where hysteresis is negligible. A command voltage u_o (V) from the DSA was applied to the PZT. The displacement response u_x (V) of each axis was measured by the optical sensor and fed back to the DSA to compute the frequency response curve (solid line in FIGURE 3-14).

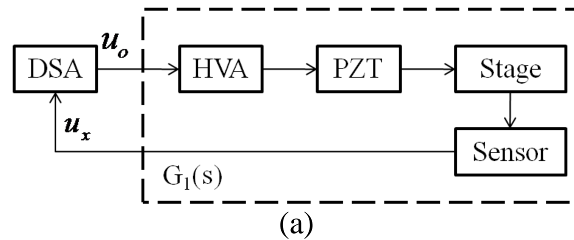

(a)

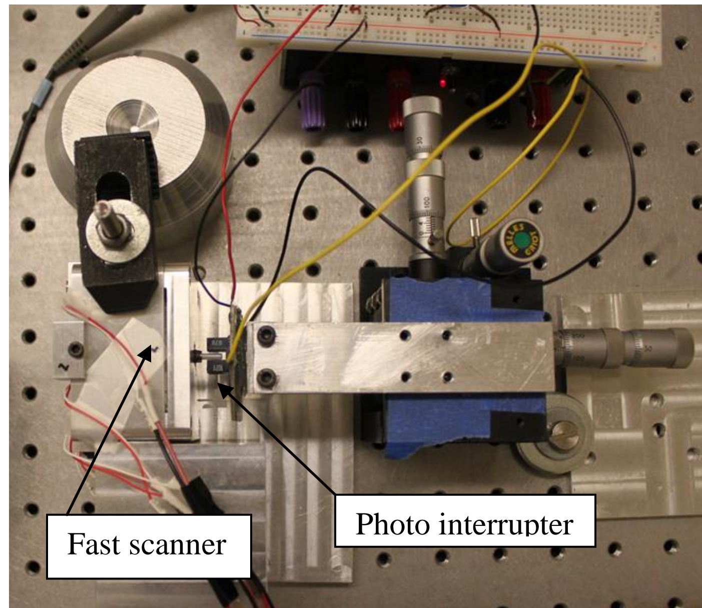

(b)

FIGURE 3-13: (a) Block diagram of the dynamic performance measurement for open loop control, (b) photograph of set up.

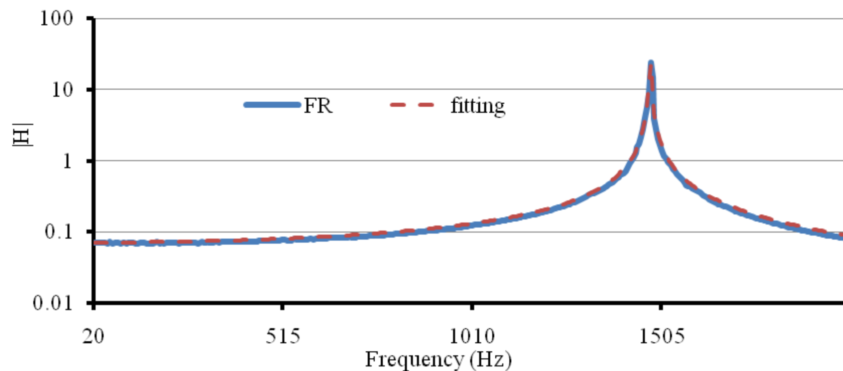

FIGURE 3-14: Frequency response experiment result and fitting model of fast scanner @ air.

The measured response shows a sharp mechanical resonance peak around 1.5 kHz with a low damping ratio which leads to a step response settling time of about 200 ms (shown in FIGURE 3-15) while the theoretical setting time is about 340 ms. The 1.5 kHz resonance frequency limits a scanning frequency (triangle signal) to about 15-150 Hz (typically 10-100 times lower than the first resonance frequency). Vibration ripples will be introduced when operating at higher scanning rate. Performance can be improved by

applying additional passive damping and implementation of optimal control algorithms performance discussed in the remainder of this section (3.5).

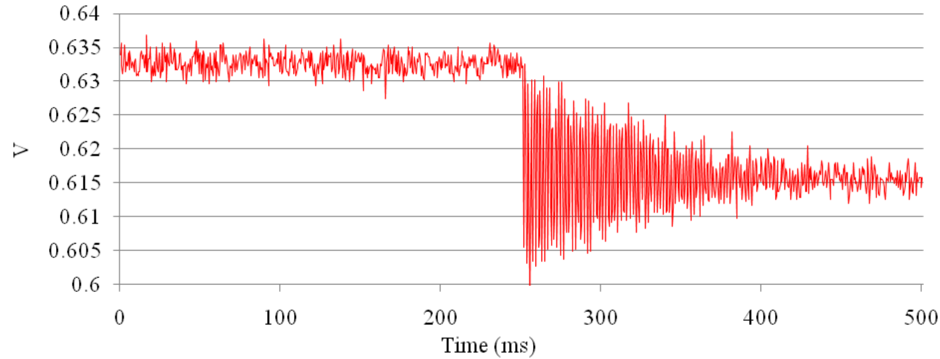

FIGURE 3-15: Experimental step response of fast scanner axis 1 @ 5V PZT.

3.5.3 Plant modeling for controller design

A second order, linear model $G_1(s)$, see Equation (3.18), is built in Excel to fit the experimental model represented as a transfer function for the command voltage u_o and the output displacement u_x. Here, the details of the dynamic system on axis 1 are presented. The rest three flexures with PZTs have similar dynamic to the axis 1.

$$G_1(s) = k_1 \frac{(s+a+jb)(s+a-jb)}{(s+\xi\omega_n + j\omega_d)(s+\xi\omega_n - j\omega_d)} \tag{3.21}$$

Where $k_1 = 0.02$, and the zeros and poles of the system are $17662\pi \pm j\,2142*2\pi$, $-1.805*2\pi \pm j\,1472*2\pi$. The resonant frequency ω_n of linear model is a good fit to approximately 1.472 kHz and the damping ratio ξ is a relatively low value about 0.001226. FIGURE 3-16 shows the Bode diagram of $G_1(s)$ by Matlab which matches very well with the fitting result by DSA in FIGURE 3-14. Therefore $G_1(s)$ is used to develop a model and further optimize performance of the closed loop controller.

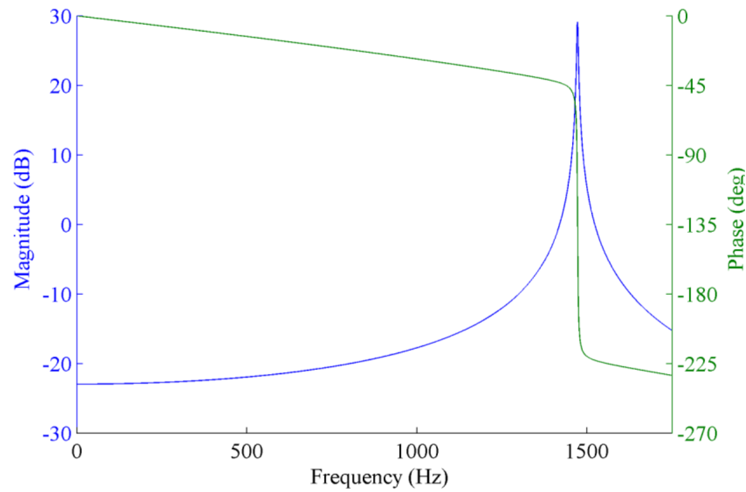

FIGURE 3-16: Bode diagram of the open loop plant model of the axis 1 of the fast scanner in air.

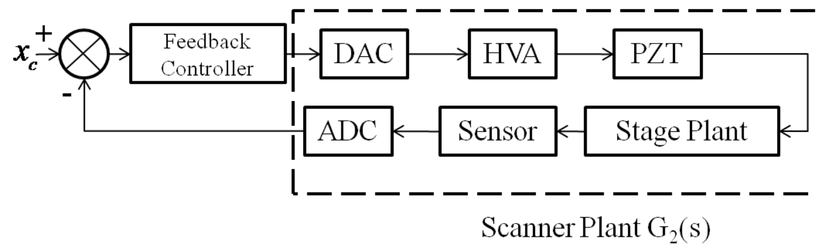

FIGURE 3-17: Block diagram of the dynamic performance measurement for closed loop control.

Based on the $G_1(s)$ plant model obtained using the DSA, another two plant dynamics components come from the sensor electronics (second version with modified gain and filter) and DAQ system is added to build a completely model $G_2(s)$. The sensor electronics is configured to have a cutoff frequency at 1 kHz with a first order low pass filter which can be modeled as,

$$H_{sensor}(s) = \frac{2\pi f}{s + 2\pi f} \tag{3.22}$$

The DAQ system adds a phase lag T_d from the sampling delay to the model, which can be modeled using Time shifting property of Laplace transform. For a sample rate of

500 kHz, $T_d = 4$ μs considering DAC and ADC process.

$$H_{delay}(s) = e^{-s \cdot T_d} \tag{3.23}$$

$$H_{delay}(s) = e^{-s \cdot 4 \cdot e-6} \tag{3.24}$$

Therefore, the transfer function is given by,

$$G_2(s) = G_1(s) \cdot H_{sensor}(s) \cdot H_{delay}(s) \tag{3.25}$$

$$G_2(s) = k_2 \frac{(s+a+jb)(s+a-jb)}{(s+\xi\omega_n + j\omega_d)(s+\xi\omega_n - j\omega_d)} \cdot \frac{(2\pi f_n)}{(s+2\pi f_n)} \cdot e^{-s \cdot T_d} \tag{3.26}$$

Considering gain adjustment and calibration of the sensor in the circuit and controller,

$k_2 \sim 100 k_1$,

$$G_2(s) = 2 \frac{(s-1766 \cdot 2\pi + j2\pi \cdot 2142)(s-1766 \cdot 2\pi - j2\pi \cdot 2142)}{(s+1.805 \cdot 2\pi + j2\pi \cdot 1472)(s+1.805 \cdot 2\pi - j2\pi \cdot 1472)} \cdot \frac{(2\pi \cdot 1000)}{(s+2\pi \cdot 1000)} \cdot e^{-s \cdot 4 \cdot e-6}$$

(3.27)

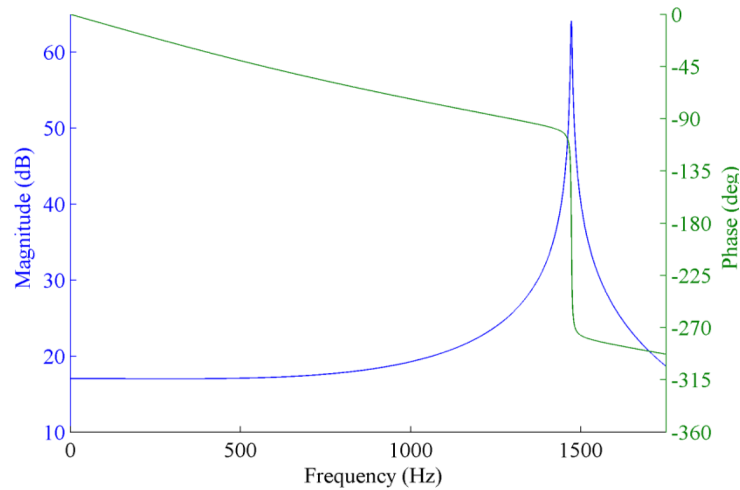

FIGURE 3-18**:** Frequency response of transfer function G_2, the low pass filter add around -60 degree phase to the open loop system at the resonant frequency, resulting in -150 degree phase.

The open loop response given by equation (3.27) is plotted in the above figure.

3.5.4 Controller design

When positioning over a relatively long range, the PZT stack exhibits non-linear characteristics in the form of hysteresis, creep and temperature dependent gain (ratio of change in displacement with applied voltage). In addition, the high gain near the crossover frequency needs to be attenuated to keep the system stable. The linear plant model built previous can only be used as a basic model to study and build a controller which will be required to operate over a relatively large scan range.

3.5.4.1 PI feedback controller

A proportional-integral-derivative controller (PID controller) was originally developed to compensate the error in open loop. The controller adjusts the output based on an error measured as the difference between the desired command (set point) and a measured displacement from the sensor (process variable). Here only a P term and I term are chosen to rapidly respond to transients and eliminate the steady-state error. The D term tended to be unstable because of the high sensitivity of the differentiation to noise in the error term. An approximation version of D term called lead-leg compensator (not implemented in this project) is more commonly used. The controller signal for a PID control can be computed from the equation,

$$u(t) = K_p e(t) + K_i \int_0^t e(\tau) d\tau + K_d \frac{d}{dt} e(t) \tag{3.28}$$

There are several methods to tune the gain for P and I to get a stable controller. One of the Ziegler–Nichols methods [39] was used. In this method, K_i, K_d is first set to zero K_p is then increased until it reaches the ultimate gain K_u, at which the output oscillates, then the K_p is set to about half of that value. $1.2\, K_p / P_u$, where P_u is the oscillation

period when the system became unstable under proportional control.

To reduce cycling, the integral gain which is inversely proportional to the integral time constant τ should be lower when a larger phase delay exists in the stage mechanical and sensor system. According to stability margins defined in the Nyquist diagram,

$$\frac{K_i}{\omega_n} G < 1 \tag{3.29}$$

Where G is the gain at ω_n ($\phi = 90°$), gain of I term is given by,

$$K_i < \frac{\omega_n}{G} \tag{3.30}$$

K_i is proportional to the resonant frequency of the scanner and inversely proportional to the open loop G which is the gain at ω_n which is a indication of the quality factor magnitude. High quality factor (low damping ratio) gives longer settling time and phase lag. From equation (3.30), K_i should be smaller than 0.6 based on ω_n and G.

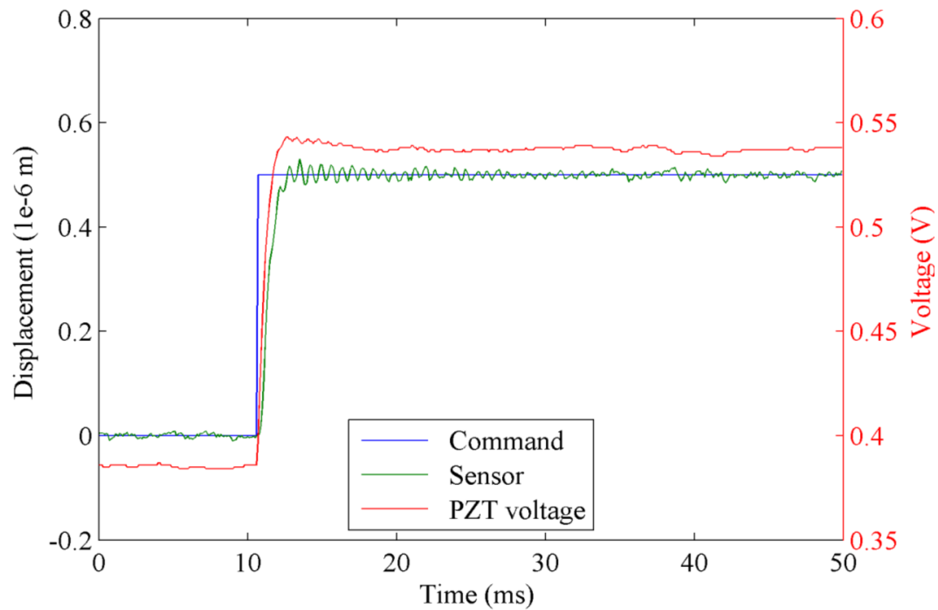

FIGURE 3-19: 500 nm step response of x axis with PI closed loop controller. The setting time is about 10-15 ms, controller parameters: P = 0.004, I = 0.02, servo frequency: 10 kHz.

Higher P gain is in favor of reducing the transient error, therefore reducing the phase lag between the desired command and actual position from sensor. However, the system becomes unstable and starts to oscillate when the P gain is too large. Therefore the phase lag is always exists because of the compromise between the phase and stability. This situation is also applicable to tuning values of the integral gain which reduces the steady-state error and settling time. FIGURE 3-19 and FIGURE 3-20 show two step responses of a tuned controller showing a controller resolution around 25 nm for x axis with the settling time having been reduced from 200 ms to 15 ms.

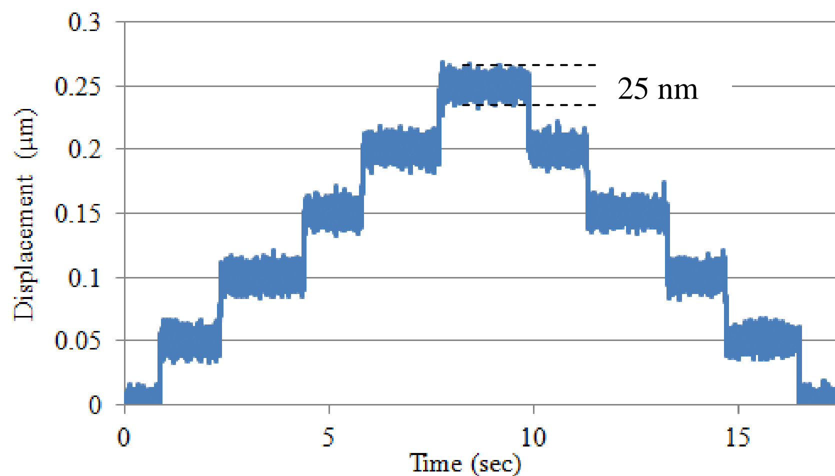

FIGURE 3-20: 50 nm step response indicating the position resolution, the PV noise is around 25 nm which mainly comes from the x sensor noise.

FIGURE 3-21 shows the performance of the controller as it tracks 5 μm (PV) triangular waves with different frequencies. The phase lag increases linearly as the frequency goes up since the time delay (dt ~ 1 ms as shown in FIGURE 3-21(b) stays constant with constant amplitude (5 μm) and controller parameters (here refers to P , I , and dt). As the frequency increases, not only the phase lag cause higher positioning error,

but also the amplitude drops as shown in FIGURE 3-21. Appropriate selection of the I gain is required to compensate this error and, to improve performance, a more aggressive controller can be designed which enables variable gain scheduling with respect to frequency changes. Another issue is the voltage to actuate the PZT grows as the frequency rises because the speed up motion requires higher force where the actuator needs to increase the power output. This issue will be detailed in the following section.

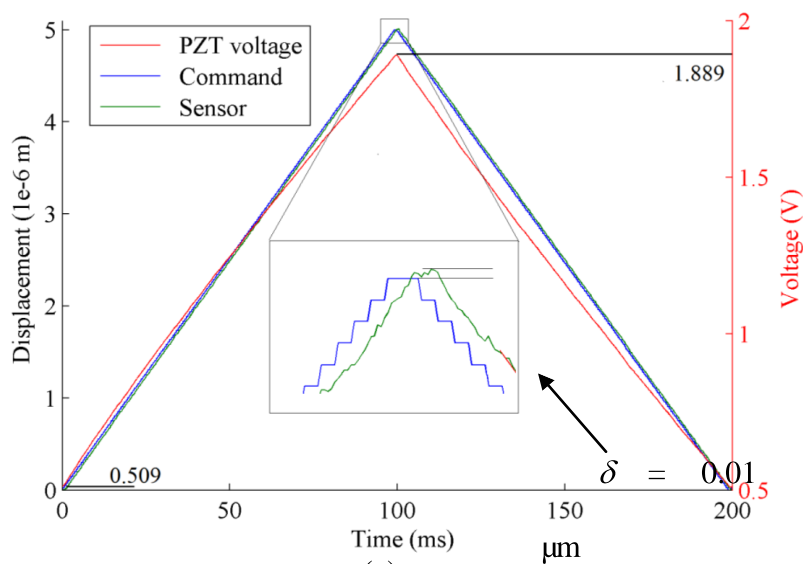

(a)

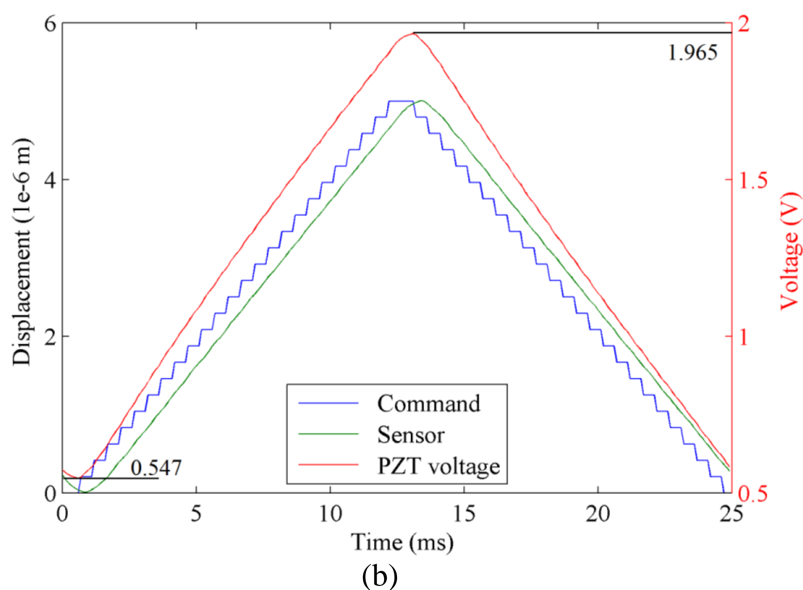

(b)

FIGURE 3-21: Triangular tracking motion comparison with x axis, PV = 5 µm, P = 0.004, I = 0.02, servo loop = 10 kHz, fc = 2 kHz, (a) 5 Hz, (b) 40 Hz.

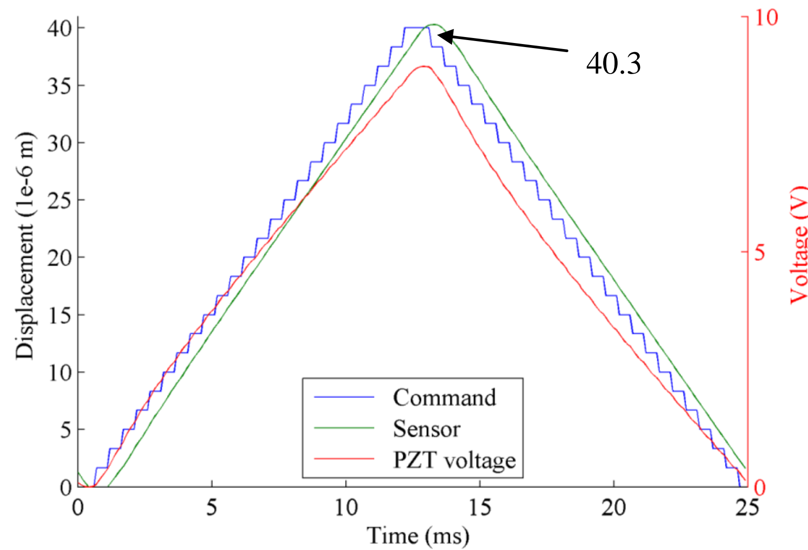

FIGURE 3-22: 40 Hz triangular tracking motion comparison with x axis, P = 0.004, I = 0.02, servo loop = 10 kHz, fc = 2 kHz, PV = 40 µm.

FIGURE 3-22 shows another issue in the controller. In this situation, the frequency keeps constant as 40 Hz, but the amplitude of the command changed from 5 μm to 40 μm. Compare this figure with FIGURE 3-21b where the frequency is 40 Hz, but the amplitude is 5 µm and it is well tracked, it is observed that the actual amplitude overshoots by 0.3 µm in the 40 µm scan with the same controller parameters. As stated above, for this amplitude integral gain should be around 0.015 to achieve the desired amplitude.

3.5.4.2 Velocity feed forward and feedback controller

While the PI controller improves positioning accuracy and linearity within the resolution and accuracy of the sensor, the controller has an undesirable phase lag leading to imaging distortion among the area where the scanner reverse its position direction. As demonstrated in FIGURE 3-21(b), although the phase increases when the frequency goes up, assuming other scanning parameters do not change, the actual time delay stays

constant. Therefore a feed-forward algorithm can be applied to the input command to pre-shape the command. The final set point y_f is given by,

$$y_f = A \cdot y(2\pi ft + \phi) \tag{3.31}$$

Where $\phi = 2\pi t_d \cdot f$, where f is the triangular wave frequency, t_d is the time delay in the controller, A is the triangular amplitude, y is the desired position (command) which is a function of time and frequency.

It is believed that the time delay will still be constant when the amplitude varies assuming the system is still linear at large scanning range. Under this assumption, it is easily perceived that the phase and amplitude lead to the transient error which can be compensated by the so called velocity feed-forward controller given by,

$$y_f = y + c \cdot \phi \cdot A \tag{3.32}$$

$$y_f = y + c \cdot t_d \cdot f \cdot A \tag{3.33}$$

Where c is constant, from $v = 4A \cdot f$, equation (3.33) becomes,

$$y_f = y + c \cdot t_d \cdot v \tag{3.34}$$

Based on the equations above, a control diagram has been designed and is shown in FIGURE 3-23. The control algorithm requires specific system parameter reorganization, i.e. the constant c and its relationship with A, f, P, I.

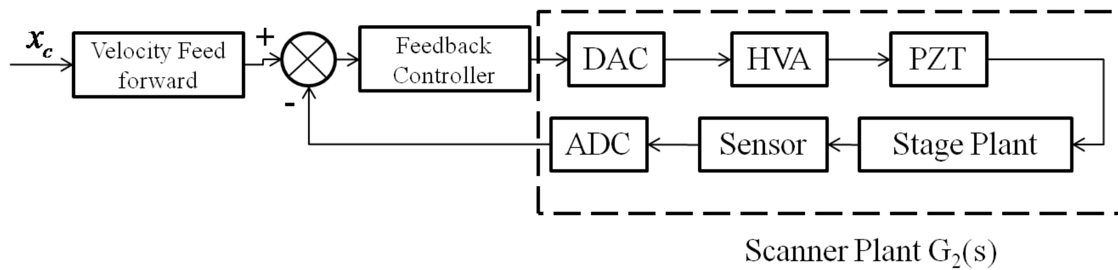

FIGURE 3-23: Velocity feed forward controller diagram.

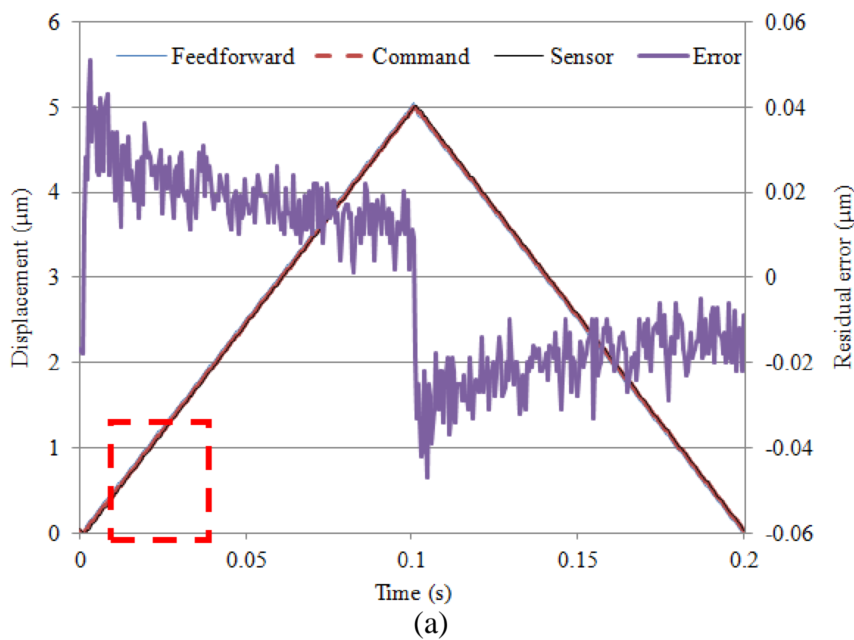

(a)

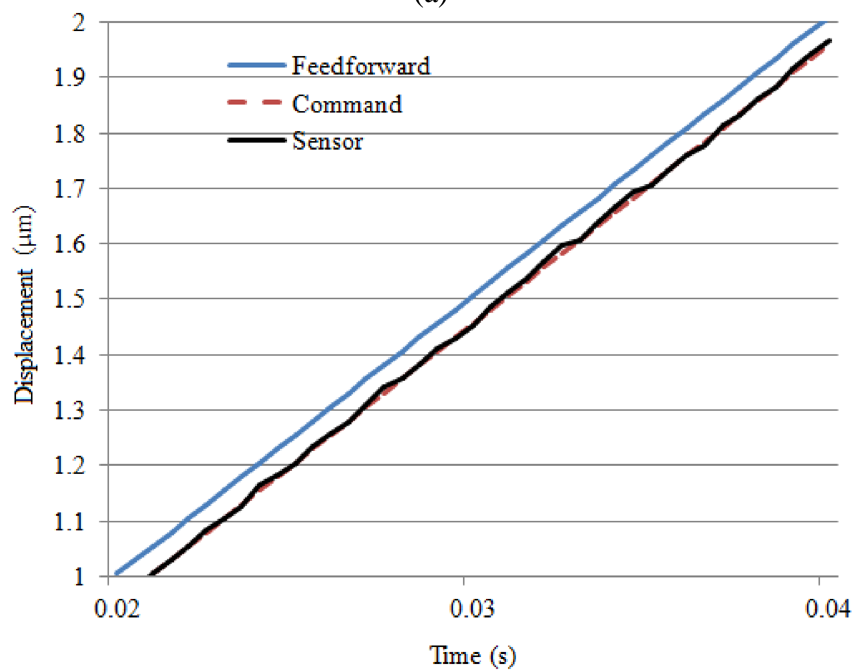

(b)

FIGURE 3-24: Feed-forward implementation result, (a) a 5Hz, 5 μm PV triangular wave tracking motion plot, (b) magnification of the red area in (a).

FIGURE 3-24 gives an example of the velocity feed forward controller performance. The transient error is greatly reduced to within 80 nm which mainly comes from the motion reversal effect and sensor noise.

3.5.5 Viscous damping material

As demonstrated previously, the damping ratio of the mechanical system is very small. This cause some issues for the scanner, i.e. long time transient oscillations, large phase lag due to limitation of controller gains with un-damped systems. Therefore, a program was undertaken to increase the mechanical damping with a variety of different treatments. TABLE 3-2 lists the measured resonant frequency of each axis for three different damping treatments (including the air damping). First attempt has been made by applying Kopr-Kote, a grease with colloidal fine copper particulates, into the gap between the center hole of the base and the tube/cylinder. It decreases the Q by 20X from around 400 to 20 (damping ration goes up to 0.025) while the resonant frequency is maintained at 1445.6Hz. FIGURE 3-25 (a) shows the result that the natural frequency of the PZT2 with Kopr-Kote. FIGURE 3-25 (b) is the step response of the PZT2 with a setting time of around 6 ms (contrasted with 200 ms in air). As an alternative damping treatment a 1:40 ratio Sylgard, a type of silica gel, was used to fill the gap. It turned out that it gave too much damping to the scanner system leading the system to be over damped as shown in FIGURE 3-26 (b) as well as adding substantial stiffness which increased the resonant frequency to 6,884 Hz, see FIGURE 3-26 (a).

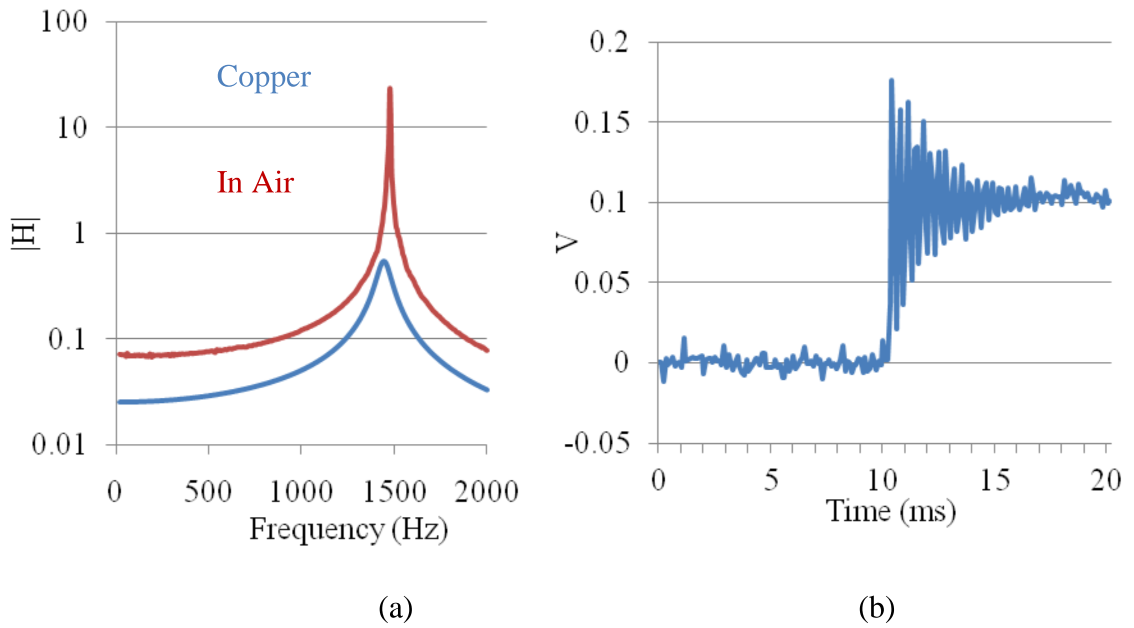

FIGURE 3-25: Fast scanner dynamic response when adding copper oil as a damper, (a) frequency response comparison, (b) step response with settling time of only 6 ms.

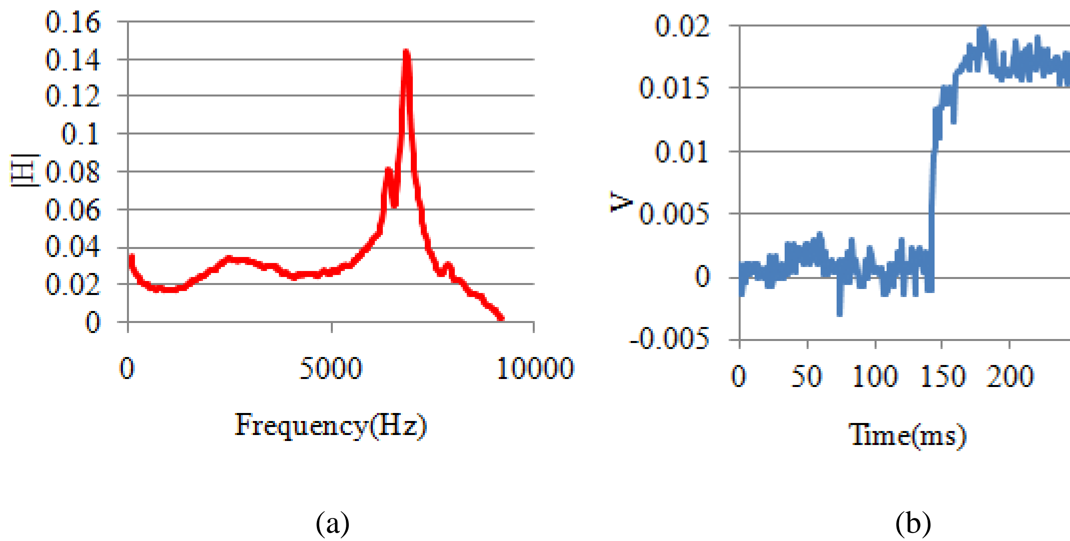

FIGURE 3-26: Fast scanner dynamic response when adding Sylgard as a damper, (a) frequency response comparison, (b) step response with settling time around 25 ms.

TABLE 3-2: Resonant frequencies of each axis with different damping treatments.

fn/Hz	Axis x1	Axis y1	Axis x2	Axis y2
Air	1475.3	1470.4	1475.3	1470.4

TABLE 3-2 (continued)

Copper oil	N/A	1445.6	N/A	1445.6
Sylgard	N/A	6884	N/A	6884

3.6 Issues

During the implementation of the controller, sources limiting the performance of the scanning process were determined and strategies to attenuate following errors are given in this section.

3.6.1 Bandwidth analysis

The actuators (AE0505D16) used in the fast scanner is the same as the ones used in xyz scanner. It is 20 mm long with a 6 mm square cross-section [29]. The other useful specifications are:

Displacement at maximum drive voltage: 17.5 μm ± 2.0

Maximum Drive Voltage (short term): 150 volts

Capacitance: 1.4 μF $\pm 20\%$

Resonant Frequency: 69 kHz (0 loads)

Recommended preload: < 425 N

The bandwidth of the scanner system is limited by the actuator, and controller, the sensor system, the high voltage amplifier and the mechanical system. Bandwidth is a measure of the scanning speed. For example, the desired maximum scanning rate is f lines per second. Usually a raster scan pattern is a triangular wave signal given by,

$$f_T(t) = \frac{8}{\pi^2}\sum_{n=1,3,5,}^{\infty}\frac{(-1)^{(n-1)/2}}{n^2}\sin\left(n\cdot 2\pi ft\right) = \frac{8}{\pi^2}\left(\sin(\omega t) - \frac{1}{9}\sin(3\omega t) + \frac{1}{25}\sin(5\omega t) - \cdots\right)$$

(3.35)

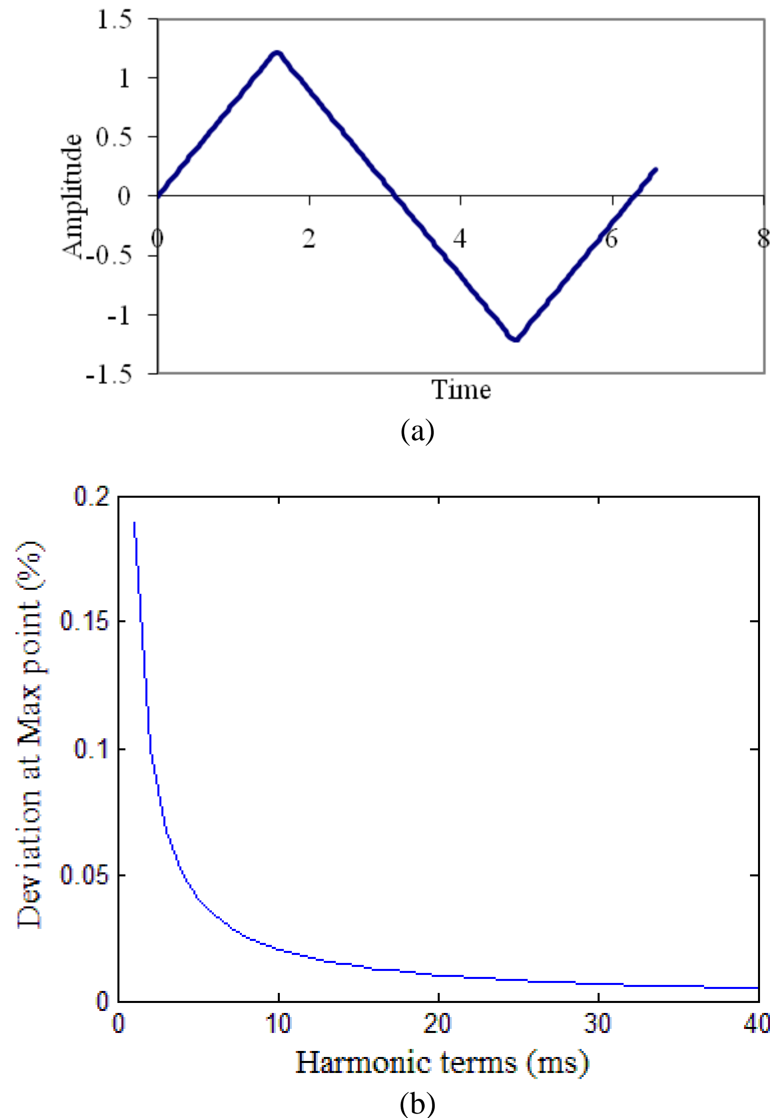

FIGURE 3-27: (a) A sum of 12 harmonics of Fourier series, (b) Deviation from triangular wave as a function of harmonics terms.

The required bandwidth is at least 20 times larger than the scanning rate f in order to get a very close approximation of triangular wave signal, i.e. the signal in FIGURE 3-27 is constructed using first 12 terms of Fourier series. The 12th harmonic frequency is $23f$. FIGURE 3-27 (b) shows the deviation at the peak point of the triangular wave from its Fourier series when the harmonics terms varies.

Therefore every component in the scanner system should at least has around 20ω

~100ω bandwidth.

For the actuator alone, the resonant frequency is 69 kHz which is able to work very well with 1 kHz triangular wave signal. The controller is built based on NI smart DAQ card which equipped with 750 kHz ADC/DAC. It is capable of sampling and re-constructing signals from DC to 10 kHz-75 kHz. Various control methods will be implemented and tested. These include feedback, feed forward, impulse shaping and lead-lag compensation. The sensor system implemented has a first order low pass filter with a cut off frequency of 1 kHz, which limits the scanning rate to less than 100 Hz. The mechanical system is a second order spring, mass, and damping system. The fast scanner's mechanical resonant frequency is around 1.5 kHz. The resonant peak should be attenuated either adding more mechanical damping to the mechanical system or using controller to provide damping (typically not optimal due to phase lag with feedback).

Another limitation comes from high voltage amplifier which can source a maximum current i_a(60 mA) and drive the load capacitance of the PZT actuator, which is 1.4 μF here. The specification of the MDT693A Thorlabs [46] shows a 250 Hz -3 dB bandwidth at full range. To verify this and get accurate working bandwidth, the slew-rate can be defined as (3.36), and the frequency is calculated in (3.37). Given C =1.4 μF, i_a = 60 mA and V_{peak} = 100 V, the 100 V range bandwidth of the amplifier is 68 Hz (sine wave). Therefore it is the slowest component of the scanner system.

$$slewrate = \frac{i_a}{C} \tag{3.36}$$

$$f = \frac{slewrate}{2\pi V_{peak}} = \frac{i_a}{2\pi V_{peak} C} \tag{3.37}$$

To verify this, open loop frequency responses of the fast scanner of each axis were measured using an HP 35693A dynamic signal analyzer (DSA) with signals limited to small displacement ranges where hysteresis is negligible. A command voltage u_o (V) from the DSA was applied to the actuator through the high voltage amplifier. The displacement response u_x(V) of each axis was measured by the optical sensor and this signal fed back to the DSA to compute the frequency response curve. Here u_o was set up to correspond as 10%, 40%, and 80% of the maximum voltage output of the amplifier respectively.

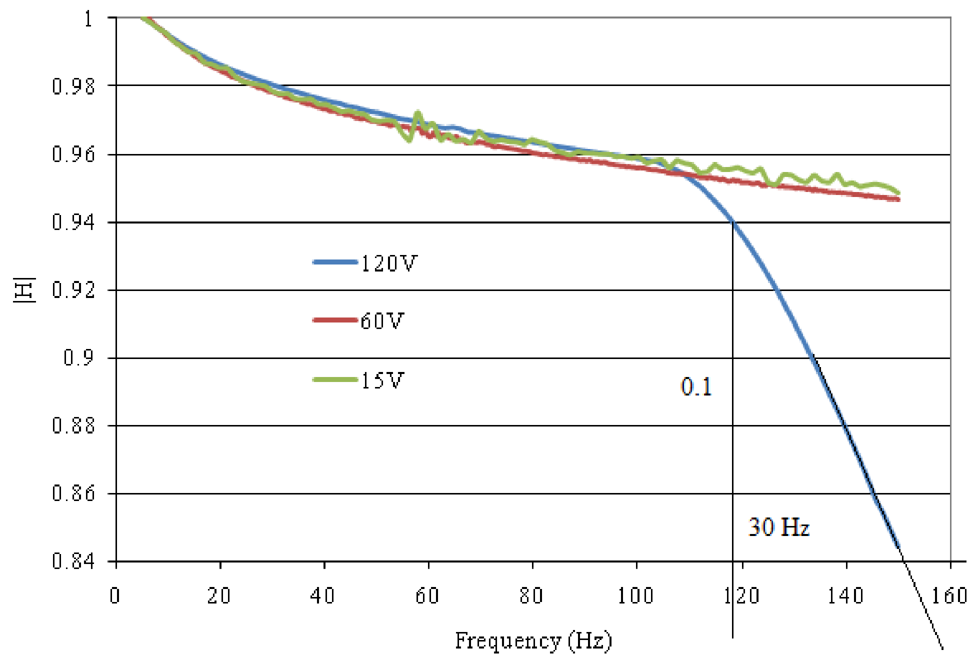

FIGURE 3-28: Open loop Frequency response of the different amplitudes of the voltage applied to piezo actuator.

As FIGURE 3-28 shown, at 10% and 40% (15, 60V) output of the amplifier, the displacement amplitude response is relative flat and linear in the test frequency range. At higher voltage range-80% (blue line) of the amplifier, the amplitude starts to drop sharply

at 110 Hz where the amplifier is not able to supply sufficient current to provide a high slew rate of the voltage. Therefore any sinusoidal motion at larger amplitude and higher frequency will be limited by this. For scanning process, the raster motion contains first harmonic and odd harmonic components with attenuated amplitudes. Therefore the current is sufficient when the raster scanning frequency does not beyond the limit, i.e. about 100 ~ 200 Hz in the current amplifier.

In closed loop control, the desired bandwidth is lower than open loop because of the adding components in the controller, i.e. sensor, data input/output, controller process. The following experiment was carried out to show the performance of 200 Hz raster scanning using fast scanner. The controller was setup as f = 200 Hz, dt = 0.1 ms, f_C = 10 kHz, P = 0.004, range= 40 μm where f is the scanning line frequency, dt is PID loop period time, f_C is the pixel scan rate, P is the proportional term of PID controller and range is the scanning amplitude times two. FIGURE 3-29 and FIGURE 3-30 show the dynamic response using two different integral terms with the PID controller. In FIGURE 3-29, I gain is not high enough, the output of the controller and the high voltage amplifier current were not large enough for the piezoelectric actuator to compensate the error. In this case, the voltage output of the high voltage amplifier is attenuated greatly due to the filtering action of the integrator. Therefore the displacement was attenuated as well. In FIGURE 3-30, the I gain is increased high enough where the controller is saturated at 10 V, however the high voltage amplifier output is still not large enough to move the platform at the desired position in such high speed for its characteristic of high frequency response shown in FIGURE 3-28. Nevertheless, this high voltage amplifier works fine in the low frequency range (less than 100 Hz) with full output as demonstrated in FIGURE 3-31.

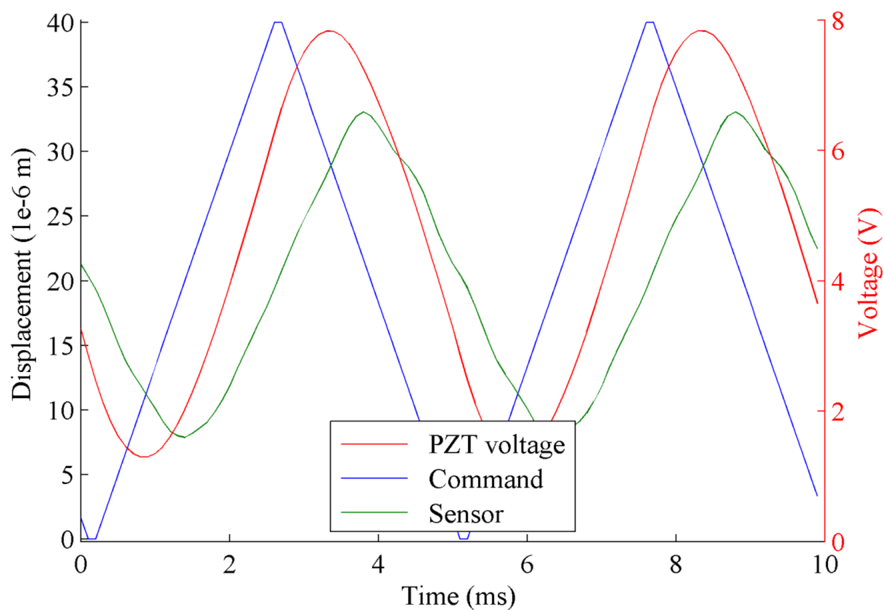

FIGURE 3-29: 200 Hz, 40 μm PV triangular wave tracking motion using simple PI controller, I = 0.01.

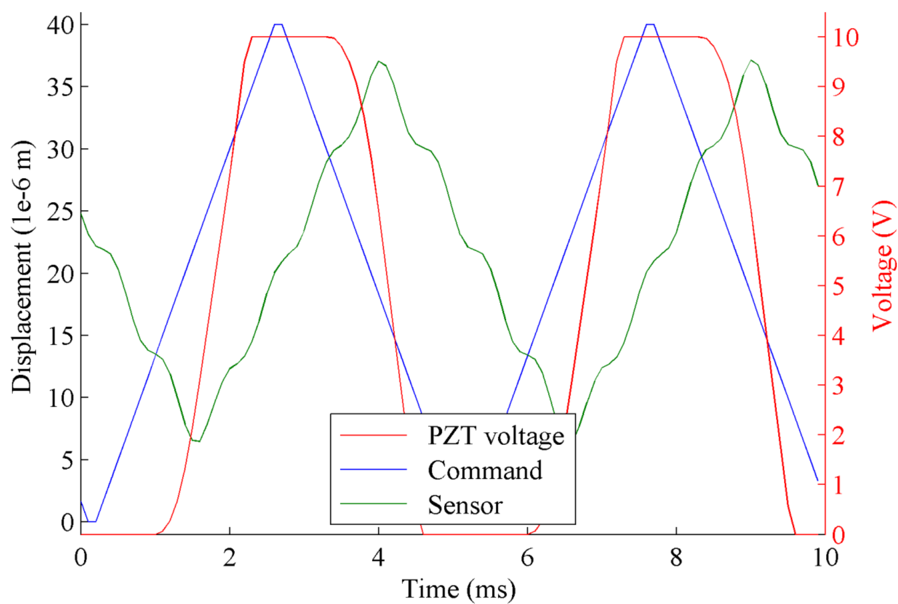

FIGURE 3-30: 200 Hz, 40 μm PV triangular wave tracking motion using simple PI controller, I = 0.03.

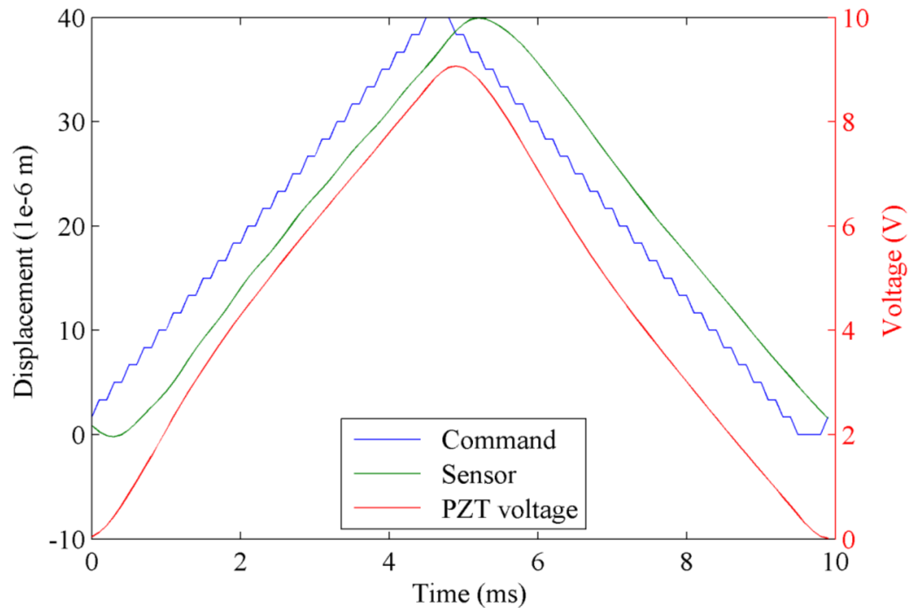

FIGURE 3-31: 100 Hz, 40 μm PV triangular wave tracking motion using simple PI controller, I = 0.02.

3.6.2 Problem 2: Ring phenomenon at the crossover point

The ringing phenomenon shown in the xyz fine stage in Chapter 2, FIGURE 2-32 is also present with the fast scanner. Introduction of an impulse shaping control strategy is proposed to attenuate this transient behavior. Impulse shaping method also called Input Shaping [47, 48] is an effective way to eliminate the residual vibrations in a system. Fundamentally the idea is that the impulse response of a system can be cancelled by another impulse with appropriately chosen amplitude and phase.

The impulse shaping algorithm was developed from a second order, linear model of a system which has a natural frequency, ω_n and damping ratio, ζ [47]. Such a system has a deterministic response, $y(t)$ to an impulse input given by

$$y(t) = A\frac{\omega_n}{\sqrt{1-\zeta^2}}e^{-\zeta\omega_n(t-t_0)}\sin\left[\omega_n\sqrt{1-\zeta^2}\left(t-t_0\right)\right] \quad t \geq 0, 0 < \zeta < 1 \tag{3.38}$$

Where A is the amplitude of the impulse input, t is time, and t_0 is the time of the impulse input. By manipulating various impulses with different amplitude and phase, the vibration caused by the first impulses will be attenuated by the subsequent impulses. FIGURE 3-32 demonstrates how the two impulse responses work together to form a no vibration motion. The blue line in FIGURE 3-32 (a) shows the system impulse response by the first impulse, while the red line is the impulse response of the second impulse. By add the two responses together either mathematically or instinctively, FIGURE 3-32 (b) shows the motion comes to a rest after the second impulse is added.

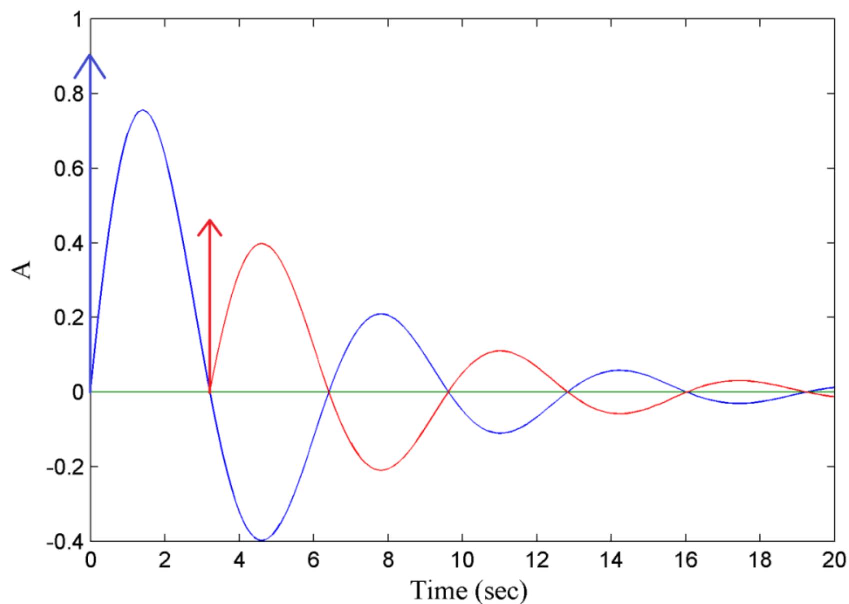

(a)

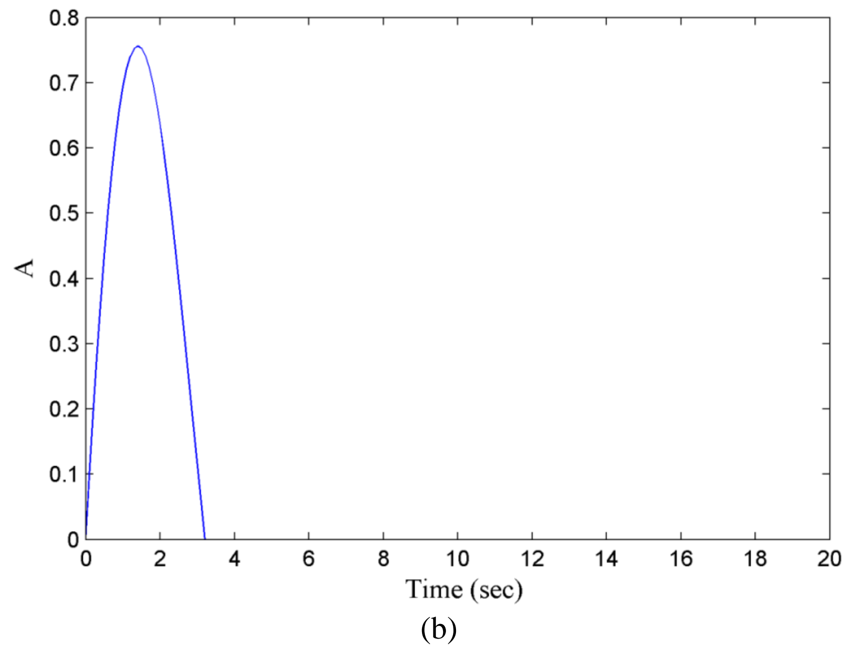

(b)

FIGURE 3-32: (a) two impulse responses at different times with different amplitude, (b) a net motion with no vibration at the time when the second impulse is added.

Generally speaking, the impulse shaping or input shaping is also applicable for step response and ramp response to reduce the vibration called by the command to get the desired position or velocity. Many researchers have examined the command shaping techniques with or without closed loop feedback for reducing the endpoint vibration. Mohamed et al [49] showed that significant reduction in the system vibrations has been achieved with the input shaping technique providing the best performance in terms of level of vibration reduction, speed of response.

Based on this idea, another approach views the impulse as proving work to remove energy from the transient response. There are two steps in the whole process are proper to implement the impulse shaping methods. One is at the set point end or command end as FIGURE 3-33 (a) shows. This method is more like a typical impulse shaping with feedback controller which requires a more sophisticated process on the shaper. The other

implement point is at the actuator end as FIGURE 3-33 (b) shows. The later one is more straightforward for the energy aspect of view because the impulse does not go through the feedback and feed forward controller but directly give a driving voltage on the piezo actuator.

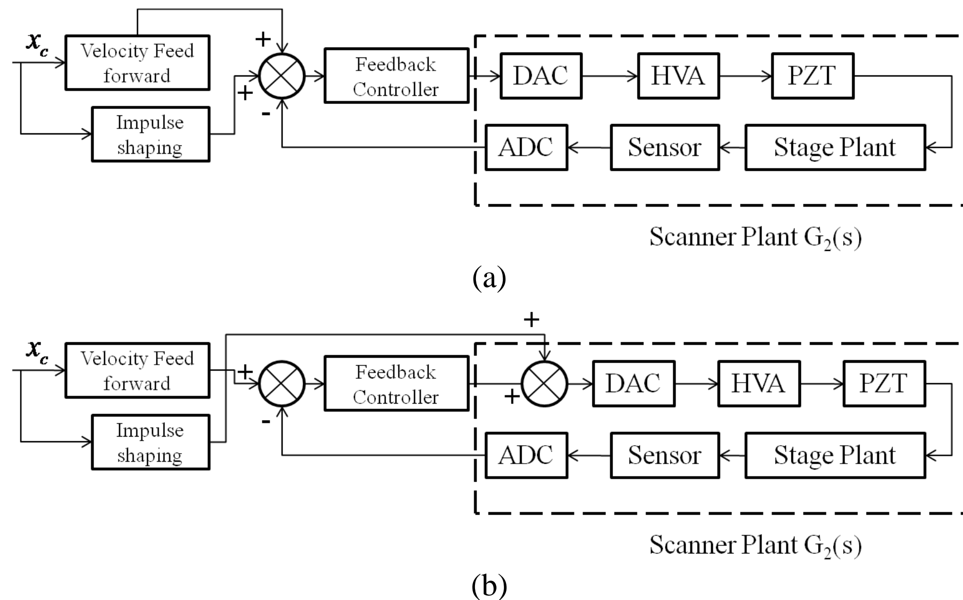

FIGURE 3-33: Two approaches for impulse shaping, (a) at the command end, (b) at the actuator end.

At the beginning, the system is examined to determinate the ability of the approaching the energy method to suppress the vibration. The ability of the piezo to position the stage depends on the piezo's mechanical property and the amplifier.

$$F_{max} = k_{pzt} \cdot \Delta x = 8 \cdot \text{N/µm} \cdot 15 \cdot \text{µm} = 120 \cdot \text{N} \tag{3.39}$$

F_{max} is the maximum force the piezo can provide to accelerate the piezo mass plus the load. k_{pzt} is the piezo stiffness calculated using 10% of the young's modulus.

For sinusoidal motion, the max force required can be expressed as

$$F_{dyn} = m \cdot A \cdot \left(2\pi f\right)^2 \tag{3.40}$$

What is where A is the amplitude of the motion [m], f is the frequency of the

motion [Hz], m is the effective mass [kg]. For raster scanning, the piezo is operated using triangular wave signal, a high acceleration is needed when the direction of the motion changes at the crossover point.

$$F_{dyn} = m \cdot a_p \tag{3.41}$$

$$a_p = \frac{\Delta v}{\Delta t} \tag{3.42}$$

In theory, $\Delta t \to 0$, the force required is given by,

$$F_{dyn} = m \cdot a_p = m \cdot \frac{\Delta v}{\Delta t}, F_{dyn} \to \infty \tag{3.43}$$

In a digital controller, the motion is discrete, $\Delta t \to \text{pixle time}$, FIGURE 3-34 shows how the displacement, velocity and acceleration changes in a perfect triangular wave scanning pattern. The sharp change of the motion direction requires an impulse force to provide enough energy.

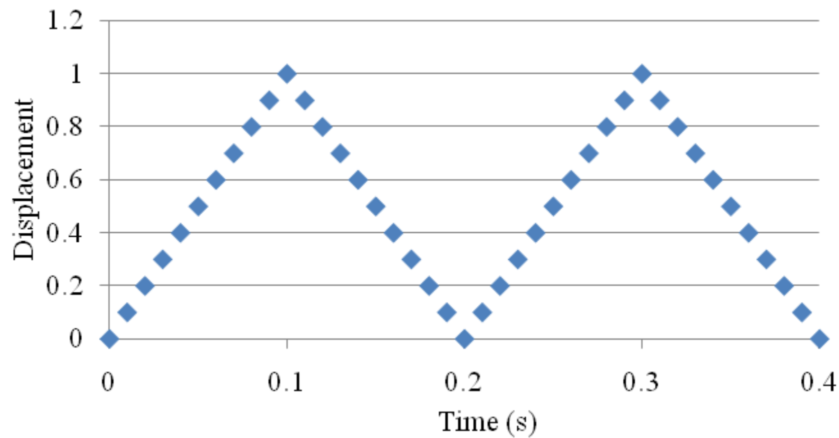

(a)

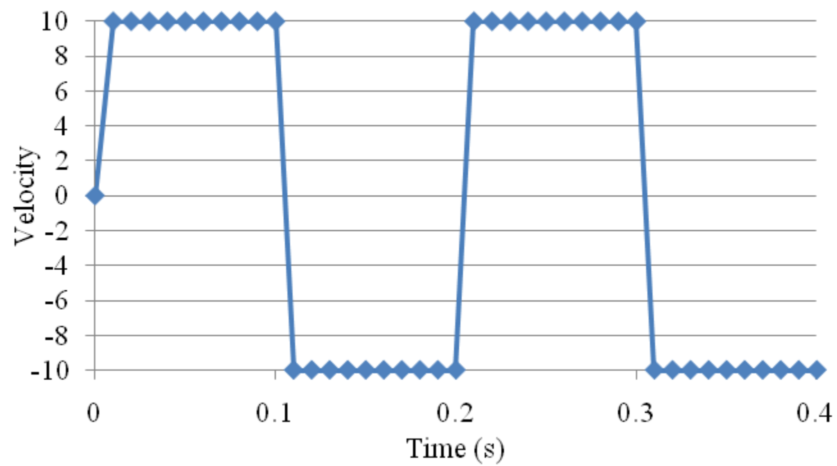

(b)

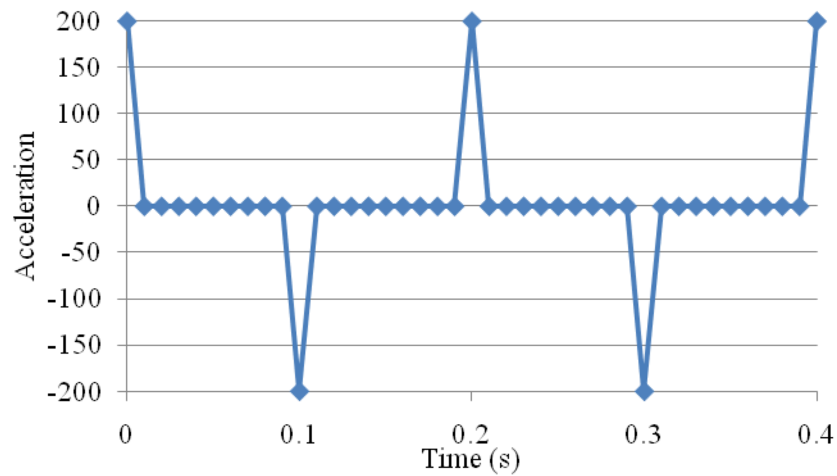

(c)

FIGURE 3-34: Displacement, velocity and acceleration plots for a digital triangular wave.

In practical, the desired scanning pattern is not a perfect triangular wave but with a short flat pattern at the crossover corner as shown in the following FIGURE 3-35.

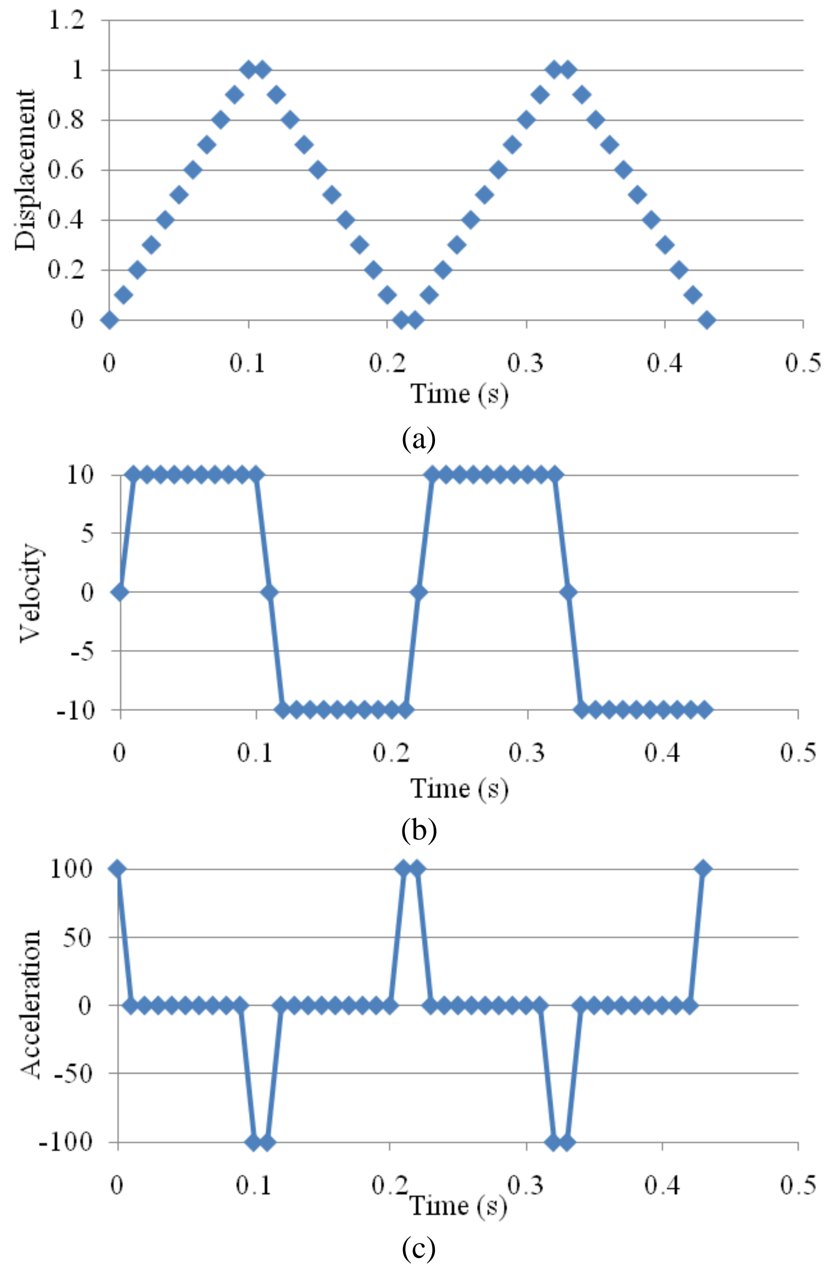

FIGURE 3-35: Displacement, velocity and acceleration plots for a practical digital triangular wave.

$$F_{dyn-e} = m_e \cdot a \tag{3.44}$$

Where m_e is the effective mass of piezo, the hemisphere ball, plate and the clamp.

$$\Delta t = \frac{1}{2 \cdot N \cdot f}, \tag{3.45}$$

Where Δt is the pixel time, N is the pixel number for each trace, f is the scan rate of line speed.

$$v = \frac{x}{t} = \frac{x}{0.5T} = 2 \cdot x \cdot f \tag{3.46}$$

$$a = \frac{\Delta v}{2\Delta t} = \frac{v-(-v)}{2\Delta t} = 4xf \cdot Nf = 4xNf^2 \tag{3.47}$$

Given that $f = 50$ Hz, $x = 15$ μm, $N = 128$, $a = 19.2$ ms^{-2}.

$$m_e = \frac{1}{3} m_{pzt} + m_{hemis} + m_{clamp} \tag{3.48}$$

Given $m_e = 3$ g,

$$F_{dyn-e} = m_e \cdot a = 0.06\,\text{N} \tag{3.49}$$

Also the kinematic energy is,

$$\Delta E_1 = m_e v^2 = 0.003 \cdot 1.5^2 \cdot 10^{-6} = 4.5 \cdot 10^{-7}\,\text{J} \tag{3.50}$$

Referring to FIGURE 3-12, the mass of several parts are given in TABLE 3-3.

TABLE 3-3: Mass of the parts.

	m_2		m_1
Part	m_tube	m_ferrule	m_plate
mass	1.47g	0.22g	4.83g

Assume the plate and tube rotate along the o point, the kinematic energy and potential energy is given by,

$$T_k = \frac{1}{2} I \omega^2 \tag{3.51}$$

$$I \approx I_1 + I_2 = \frac{m_1}{3} l_1^2 + \frac{m_2}{12} l_2^2 = \frac{0.00483}{3} 20^2 \cdot 10^{-6} + \frac{0.00169}{12} \cdot 44^2 \cdot 10^{-6} \\ = 0.92 \cdot 10^{-6} \tag{3.52}$$

$$U_p = \frac{1}{2}k_1x_1^2 + \frac{1}{2}k_2x_2^2, k_1 = k_2, x_1 = -x_2$$

(3.53)

$$U_p = k_1x_1^2 \tag{3.54}$$

When the PZTs change the motion direction at the crossover point, the total potential energy U_p of the two springs maintains constant because the pair of piezo moves in a systematical way. The potential energy only converts between the two springs. Therefore, only the kinematic energy required additional power as the PZTs reverses direction.

$$\Delta E_2 = I\omega^2 = 0.92 \cdot 10^{-6}\text{kg} \cdot \text{m}^2 \cdot \left(\frac{1.5\text{mm} \cdot \text{s}^{-1}}{10\text{mm}}\right)^2 = 2.1 * 10^{-8}\text{J} \tag{3.55}$$

$$\tau = I\alpha = I\frac{2a}{l_1} \tag{3.56}$$

$$\tau = F_p\frac{l_1}{2} \tag{3.57}$$

From equation (3.56), (3.57), the desired force is given by,

$$F_p = \frac{4aI}{l_1^2} = \frac{4 * 19.2 * 0.92 * 10^{-6}}{20^2 * 10^{-6}} = 0.176\text{N} \tag{3.58}$$

$$F_{preload} = k_f \cdot \varepsilon_{preload} = 50 \sim 100\text{N} \tag{3.59}$$

$$F = F_{dyn-e} + F_p + F_{preload} \sim 50\text{-}100\text{ N} < F_{max} \tag{3.60}$$

Therefore the clamp force by piezo is sufficient to change the acceleration direction of the motion at the desired conditions.

The other factor need to examine is the electrical power of the amplifier.

$$\Delta E = \Delta E_1 + \Delta E_2 = m_e v^2 + I\omega^2 = c * y\left(v^2\right) = c * y\left(\frac{x^2}{t^2}\right) = c * y\left(x^2 f^2\right) \tag{3.61}$$

From equation (3.61), the energy required to change the direction of the motion is proportional to the square of maximum positioning displacement and line scanning rate. An impulse energy which is also proportional to the square of maximum positioning displacement and line scanning rate need to be supplied from piezo in Δt time to be able to reverse the direction of the motion.

$$\Delta E = UI\Delta t \tag{3.62}$$

From equation (3.45) and given scanning conditions, Δt = 0.08 ms, when the piezo inverts at its maximum output, U = 150 V, therefore the minimum required current is

$$I_{\min} = \frac{\Delta E}{U\Delta t} = \frac{47.1*10^{-8}}{150*0.08*10^{-3}} = 4 \text{ mA} \tag{3.63}$$

When the piezo inverts its direction at the minimum point at the same acceleration, a much more current than 4 mA is required.

Also the energy required to reverse the motion is given by,

$$\Delta E = \int_0^{\Delta t} F(t)v(t)dt = \bar{F}\ \bar{v}\Delta t \tag{3.64}$$

Where $\bar{v}$ is proportional to v, x in the equation (3.46)

Based on equation (3.46), (3.47), (3.61), equation (3.64) can be derived as

$$\bar{F} * c_1 2xf * \frac{1}{N*f} = c_2 * y\left(x^2 f^2\right) \tag{3.65}$$

$$\bar{F} \propto Nxf^2 \tag{3.66}$$

As seen from equation (3.66), the larger of the scanning range and higher of scanning speed, the higher of the force is required. By designing a proper impulse shaper, the ringing vibration can be greatly attenuated. To evaluate implementation of the above strategy, a simple PID feedback controller was setup as f = 200 Hz, dt = 0.1 ms, P =

0.004, I = 0.03, range = 5 μm where f is the scanning line frequency, dt is PID loop period time, P, I is the proportional gain and integral gain of PID controller and range is the scanning amplitude.

In FIGURE 3-36, the f_C = 4 kHz is command (pixel) generating rate, since the PID servo loop is 10 kHz, each pixel have an average 2.5 process cycles. There are 5 process cycles for the reverse motion procedure. Therefore the ringing is not very large as seen from the sensor signal (green line) because relatively low acceleration force required. The measured amplitude 5.2 μm is larger than the desired 5 μm because I gain is too high in the current scanning setup. In FIGURE 3-37, I gain is kept constant where the f_C increased to 10 kHz causing the PID servo loop for each scan step equal to one cycle. This increased controller update rate brings the responded amplitude to be closer to 5 μm. However, this also leads to larger ringing ripples because the acceleration force increases where the controller is not able to provide proper output voltage to drive the piezo at the right time.

The other reason causing ringing is related to the settling time. Settling time is the key parameter which determinates how quick the mechanical can response to a changing command. In the current controller, the settling time is around 10 ms for the short range step response. When it starts to oscillate at the crossover points, the piezo tries to compensate the sudden jump error, but the mechanical system is too slow to follow the output of the piezo.

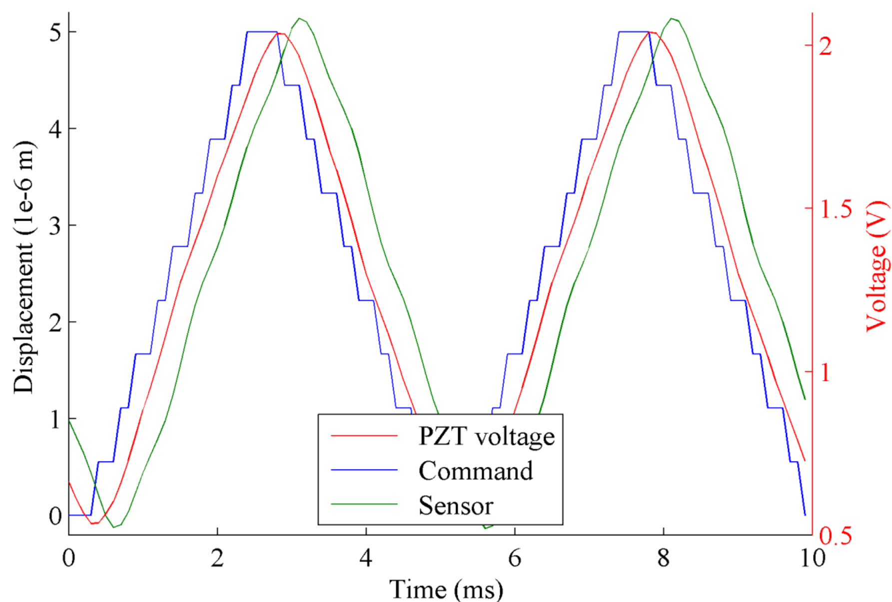

FIGURE 3-36: Normal PID controller with f_C = 4 kHz, showing the ringing exists.

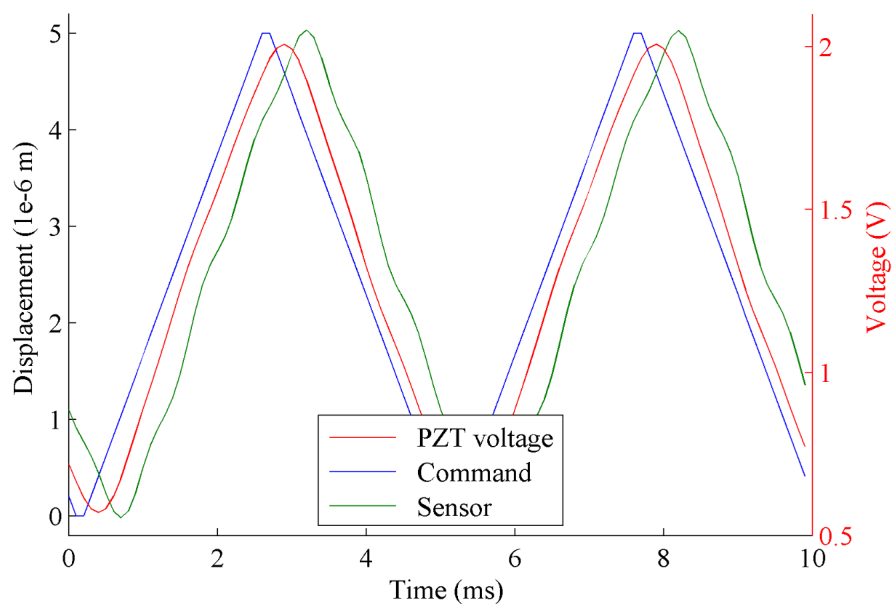

FIGURE 3-37: Normal PID controller with f_C = 10 kHz, showing the larger ringing.

To cancel out the ringing effect, based on equation (3.61), an impulse is added to the output of the command at a proper time. It is worth pointing out that what being controlled here is the whole ramp of the scanning command because processing each

small ramp (step) in each pixel adds complexity in the controller. Actually a whole line as a large ramp can be treated as an impulse when $dt \to 0$. In equation (3.61), the impulse energy is determined by a constant value c, f and A. It is difficult to determine these values quantitatively, however, an experiment can be conducted to tune the impulse value under specific scanning conditions. As shown in FIGURE 3-38, f = 200 Hz, A = 5 μm, an impulse voltage of ΔV_1= 0.038 V (a) and 0.03 V (b) was add to the output of the controller at the time t_1 when the ramp started to reverse, the ringing is suppressed though the real amplitude dropped due to the adding impulse. I term in the feedback controller needs to be increase to compensate this error. It is believed that the time for the impulse to be applied should be close to the time when the position hits the crossover point. The impulse applied time t_1 is chosen at the time when the motion reverses its direction. The impulse force would provide the energy to cancel out the kinematic energy in a short time, i.e. dt in here, and then the scanner starts the translation in the other direction from zero kinematic energy. However, to better resolve this problem and gain high vibration reduction performance, further investigation is required, i.e. how kinematic energy and potential energy play the roles in the vibration cancellation, more test needs to be conducted to get accurate and abundant results, how multiple impulse with energy spread at various time frame improve the performance and others.

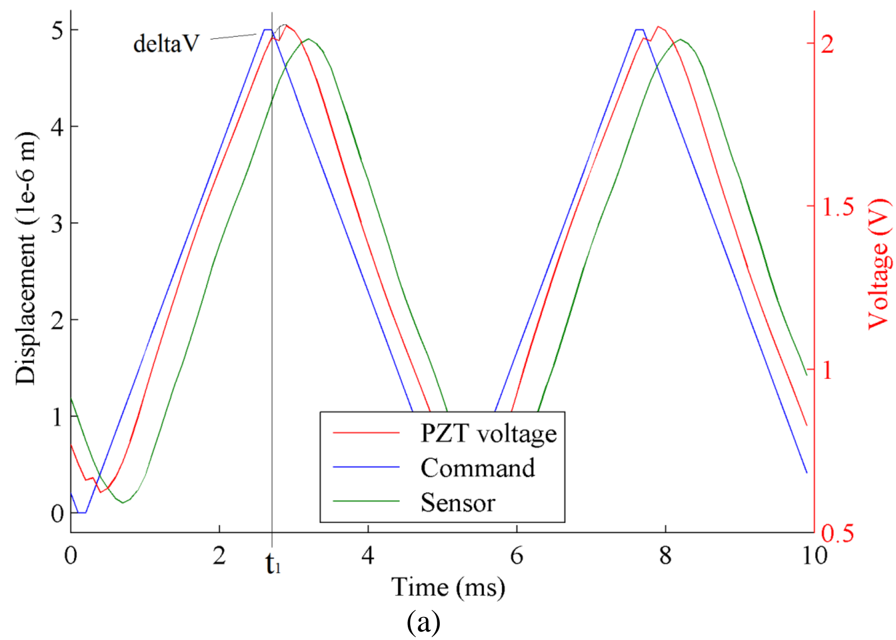

(a)

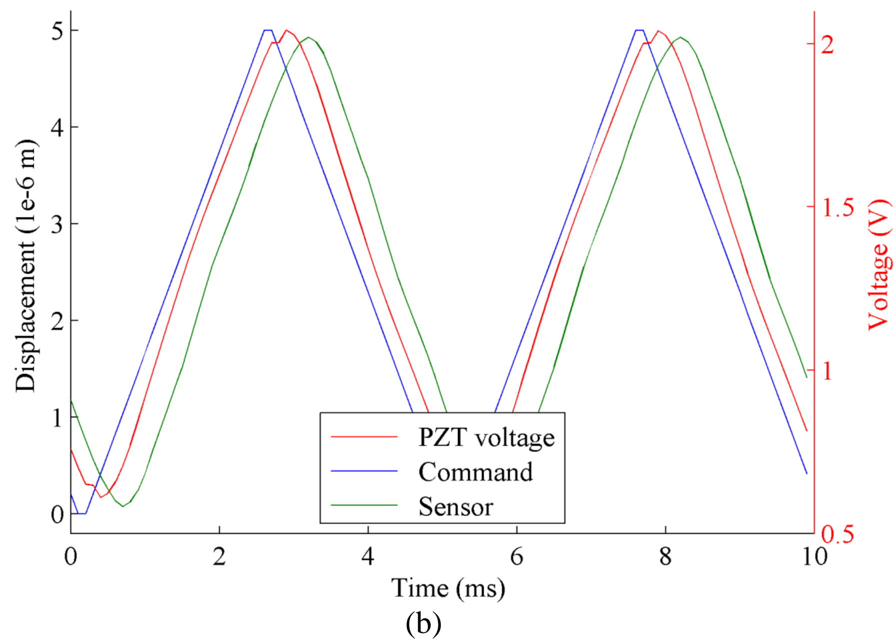

(b)

FIGURE 3-38: Impulse shaping, (a) PID controller with impulse shaping at ΔV_1 = 0.038 V, (b) PID controller with impulse shaping at $\Delta V_1 = 0.03$ V.

From equation (3.66), in other cases of different scanning application, the proper amplitude of impulse voltage can be calculated base on V_1 from the previous examples, and the scanning parameters as shown in equation (3.68). FIGURE 3-39 shows another

running with 200 Hz frequency and 10 μm range. From equation (3.68), the required voltage is twice as large as ΔV_1. The responded displacement (green line) is more linear in FIGURE 3-39 (b) than FIGURE 3-39 (a) where the ripples are clearly attenuated by around 80%.

$$\bar{F}_1 = cN_1x_1f_1^{\ 2} = \Delta V_1 \tag{3.67}$$

$$\bar{F}_2 = \Delta V_2 = \Delta V_1 * \frac{N_2x_2f_2^{\ 2}}{N_1x_1f_1^{\ 2}} = \Delta V_1 * \frac{f_{C2}x_2f_2}{f_{C1}x_1f_1} \tag{3.68}$$

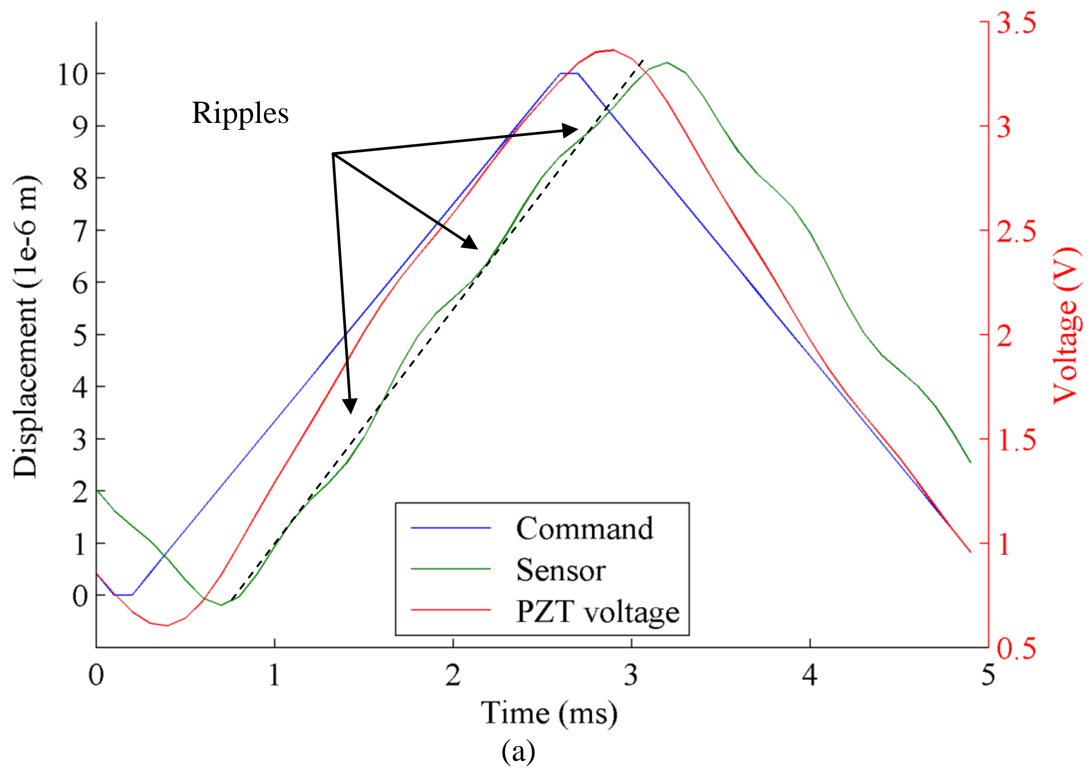

(a)

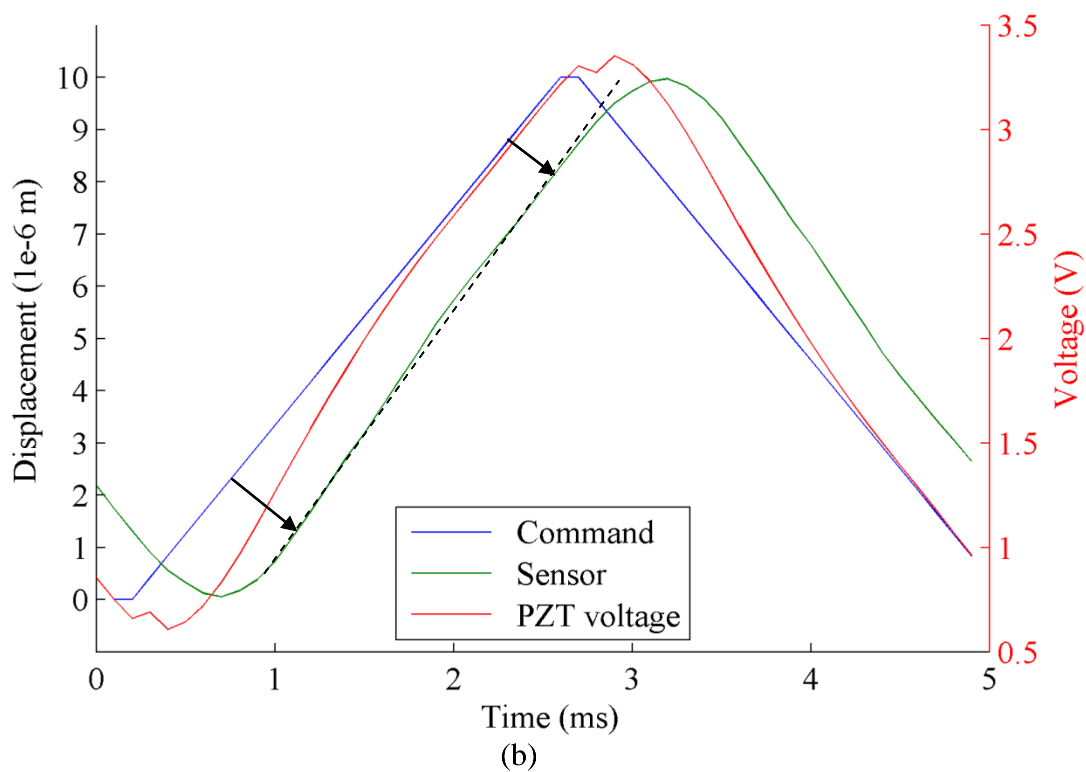

(b)

FIGURE 3-39: Impulse shaping when f = 200 Hz, A = 10 μm, (a) normal PID controller with f_C = 10 kHz, (b) PID controller with impulse shaping at ΔV = 0.08 V

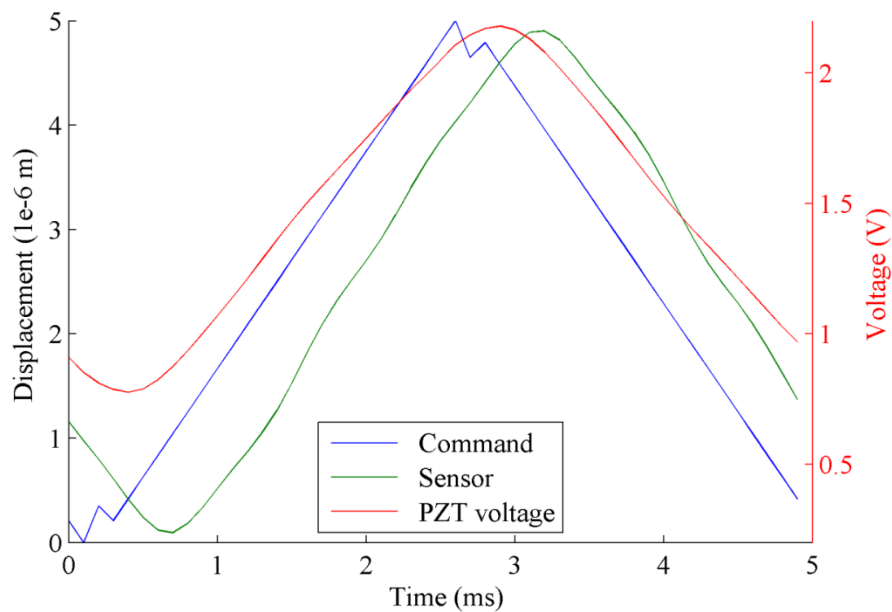

FIGURE 3-40: Impulse shaping at the command end using same scanning conditions as FIGURE 3-38.

FIGURE 3-40 shows that adding a simple impulse to shape the command results in similar positioning performance than adding impulse to the actuator in FIGURE 3-38. A more sophisticated control algorithm is necessary here to obtain more linear result, i.e. multiple impulses with different latency time, processing on each pixel, shaper design consideration involving the feedback controller performance. Nevertheless, when the electronics employed have high enough bandwidth, the ultimate limitation comes from the mechanical properties, i.e. the resonant frequency, damping factor. The control techniques can help to alleviate some limitation of the mechanical hardware, but is not able to improve the speed fundamentally. However, the advanced control techniques like impulse shaping can greatly improve the performance of the scan motion in term of vibration reduction, speed of response, robustness, accuracy and therefore the linearity as the above section demonstrates to a certain degree.

3.7 Experiment setup and images

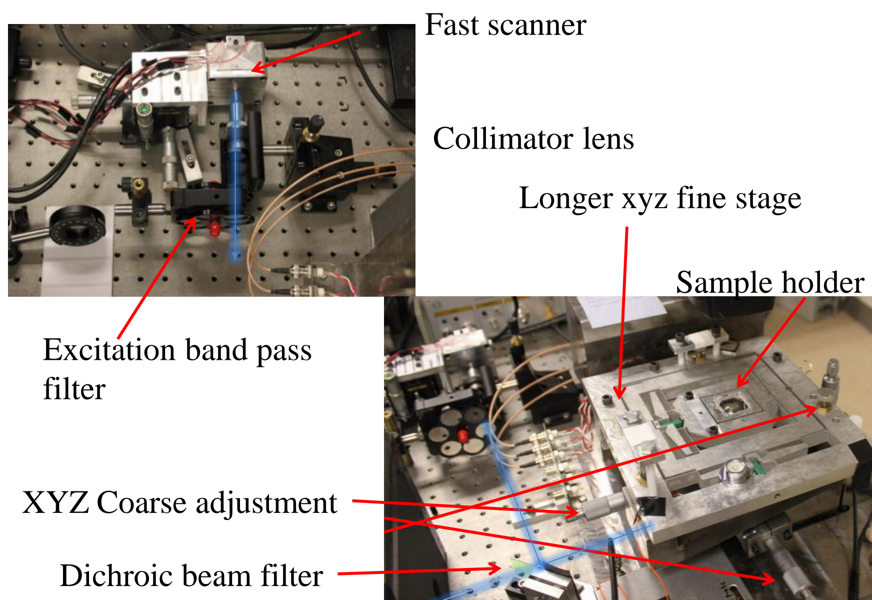

FIGURE 3-41: Experiment setup

Several imaging experiments were conducted to verify the fast scanner performance as well as validating this as an alternative optical probe scanning system. The experiment is setup as shown in FIGURE 3-41. The fiber through the top hole of the fast scanner is attached to the ferrule using epoxy. The ferrule is later glued into the cylinder inside the fast scanner body. A bracket is used to fix the fast scanner to a xyz micrometer stage by a bracket. The micrometer stage is clamped to the vibration isolation table. Ahead of the fiber is the collimator lens which is used to collimate the outgoing laser beam. An excitation band-pass optical filter is located after the collimator to remove unwanted light. The light hits the dichroic beam splitter and is reflect to the $90°$ mirror sitting perpendicular with the objective lens in the center of the longer xyz fine stage.

3.7.1 Open loop experiment using Sylgard

In this section, open loop scans of an 800 nm pitch fluorescent calibration grid as well as single quantum dots over an area of 5 x 5 μm using a 100X 1.4 NA oil immersion objective are demonstrated.

FIGURE 3-42 (a) shows a 23.2 μm x 22.8 μm fluorescence images of a calibration grid using the longer range scanner. The grid is fabricated using electron beam lithography. It consists of a thin gold film (30 nm thick) patterned with 400 nm round holes, with a periodicity of 800 nm. The sample is then spin-coated with a PMMA film that contains rhodamine 6G fluorescent molecules. The image is acquired by illuminating in the epi-fluorescence mode from the bottom of the sample with the PMMA film on top of the gold film. The light is then collected also from the same bottom objective so that bright fluorescence spots are present where the holes of the film exist. FIGURE 3-42 (b) is a 5 μm x 5 μm scan range of the grid at a speed of 4 lines per second. FIGURE 3-42 (c) shows a zoom section of 5 μm x 5 μm from the image in FIGURE 3-42 (a). The resolution is only a 5.5 pixels per micrometer.

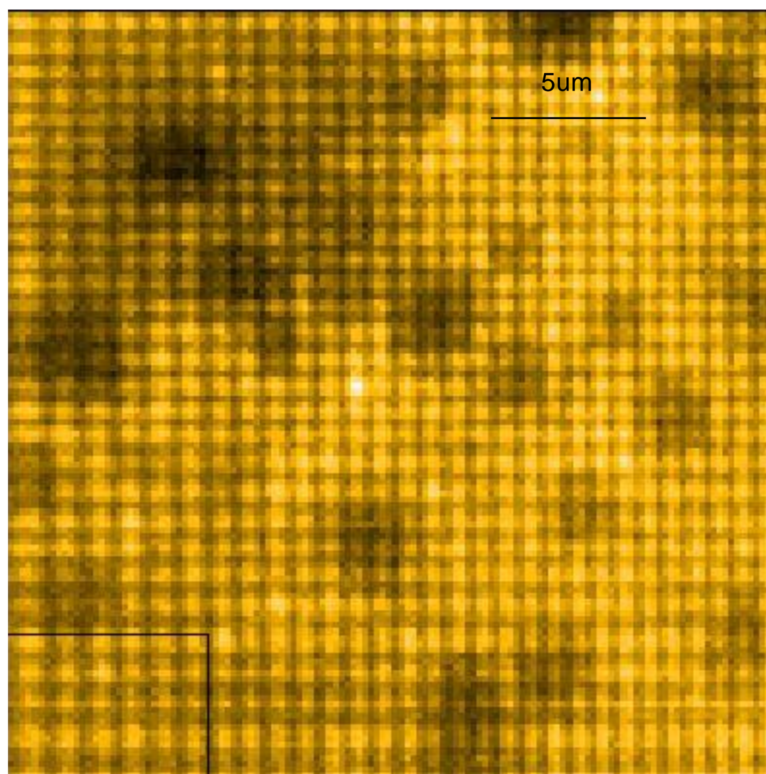

(a)

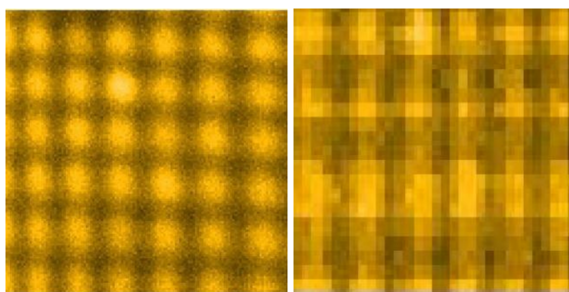

(b) (c)

FIGURE 3-42: Images obtained using large scanner, (a) range: 23.2 μm x22.8 μm, 128*128 pixels at 4 lines per second, (b) range: 5 μm x 5 μm128*128 pixels at 4 lines per second, (c) section magnifying lower left image in FIGURE 3-42 (a)

FIGURE 3-43 shows two scanning results using the fiber fast scanner. Both images are obtained at a full scan range. With an optical attenuation of about 12, the laser spot navigates over a range of 5 μm x 5 μm in the sample plane. FIGURE 3-43 (a) is captured with a line scanning speed of 4 Hz while in FIGURE 3-43 (b) this speed goes up to 78 Hz. The contrast drops in higher speed because the sampling time (therefore photon counting

statistics) for each pixel is reduced .The stretch in dimension along the y axis (fast axis) comes from a dynamic amplitude decrease at the scan frequency. Compared with the result in FIGURE 3-42c), both show a same area of 5 μm x 5 μm on the grating, while FIGURE 3-43 (b) has much higher resolution and contrast of 25.6 pixels per micrometer at 1.6 second for a frame. With the fast fiber scanner and original scanner, a five times better pixel resolution than FIGURE 3-42 (a).

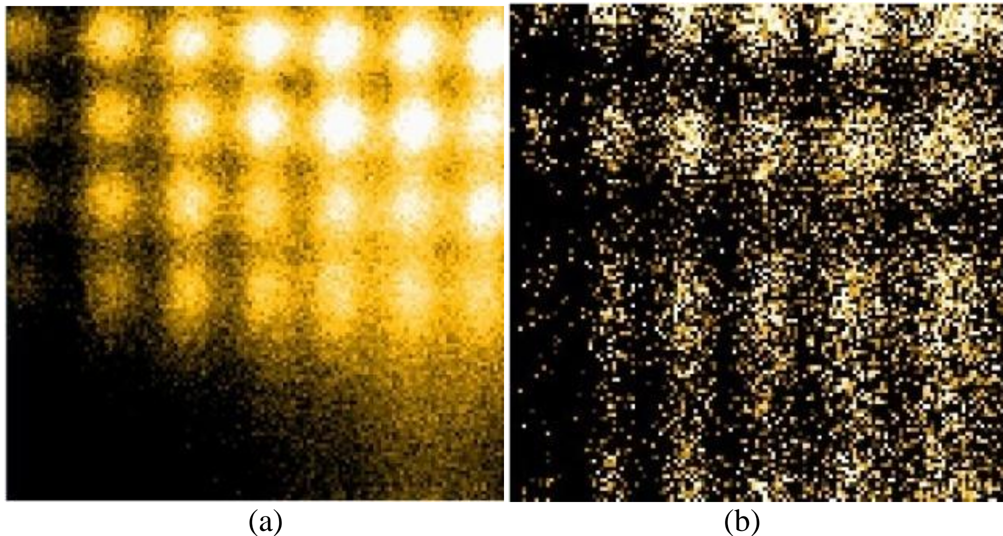

(a) (b)

FIGURE 3-43: Fast scanner open loop images, (a) Range: [10V*10V] 128*128 pixels at4 lines per second, (b) Range: [10V*10V] 128*128 pixels at 78 lines per second

3.7.2 Closed loop imaging

Since the Sylgard over damps the fast scanner dynamics, it was cleaned up and re-tested without any damping material applied (except the air). Meanwhile, the sensor was setup and calibrated and the closed loop images were obtained.

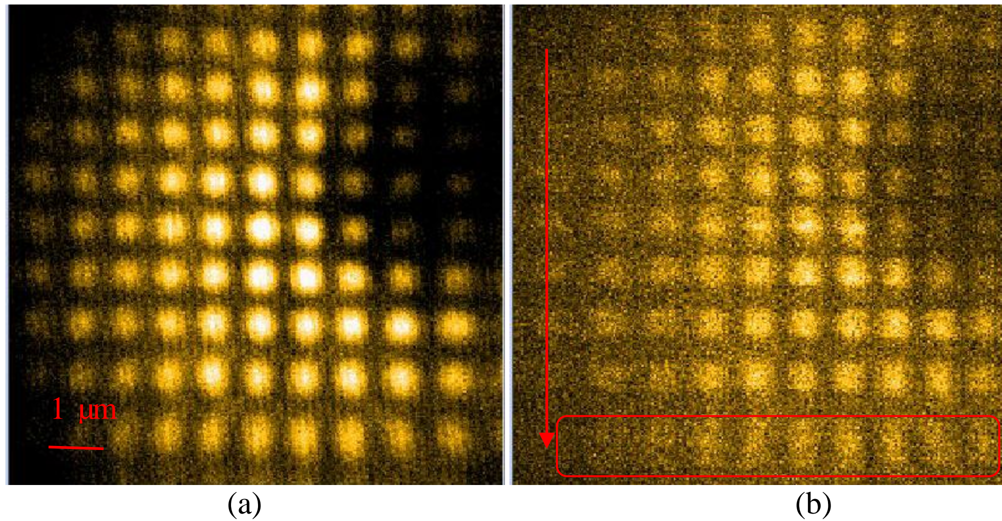

FIGURE 3-44: Fast scanner open loop images without damping materials, (a) 4 Hz, (b) 40 Hz.

FIGURE 3-44 shows two images obtained using fast scanner in open loop. Since the setup of the fiber location changes the distance of the fiber from the collimator which impacts the optical magnification, the scan range change from around 5 μm to about 8 μm. The grating imaged was the same one with 800 nm pitch. FIGURE 3-44 (a) image was obtained at speed of 4 Hz where the (b) image was obtained at speed of 40 Hz. The red line indicates the fast scan axis. The red rectangle area shows some image distortion due to the position phase shift error.

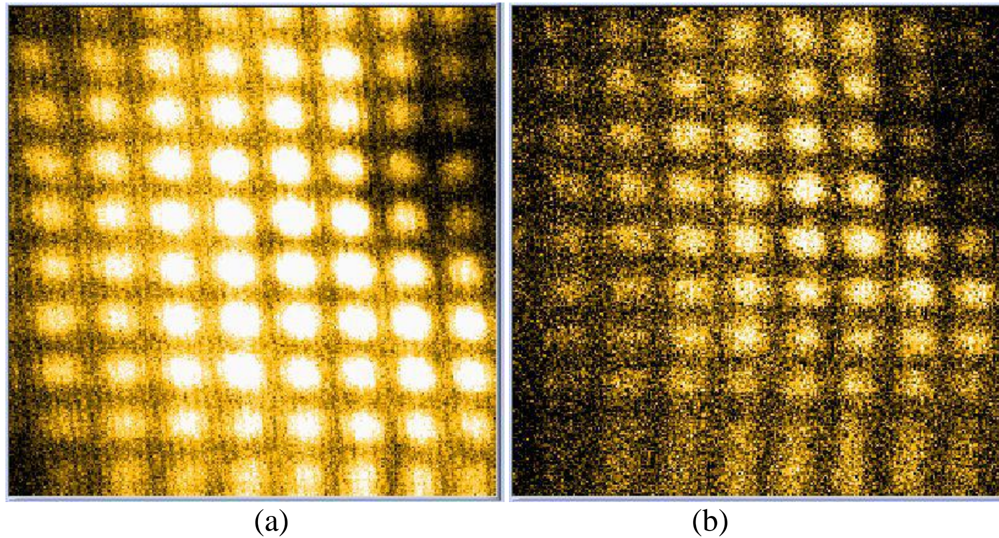

(a) (b)

FIGURE 3-45: Fast scanner closed loop images without damping materials, (a) 4 Hz, (b) 40 Hz.

FIGURE 3-45 shows two images obtained using fast scanner in closed loop. The distortions in the images mainly come from the sensors coupling problem in the sensor setup where the current control has not been compensated using equation (3.11).

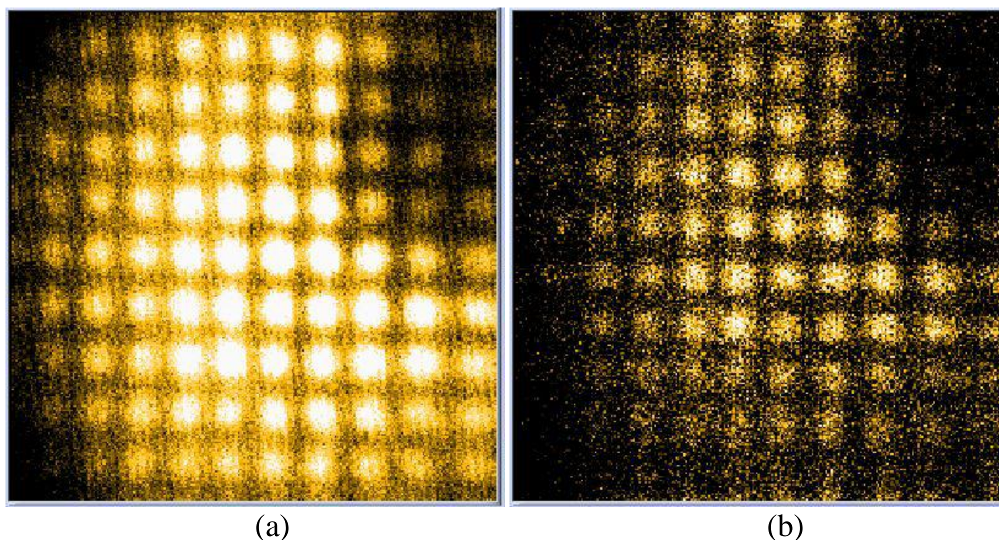

(a) (b)

FIGURE 3-46: Fast scanner images (x axis closed loop, y open loop) without damping materials, (a) 4 Hz, (b) 40 Hz.

FIGURE 3-46 images were obtained whole the slow axis (y) was in open loop, and the fasts axis (x) was in closed loop. The images are better than the previous set because

only the fast axis was mapped with the x sensor. The coupling angle between the sensors did not exist.

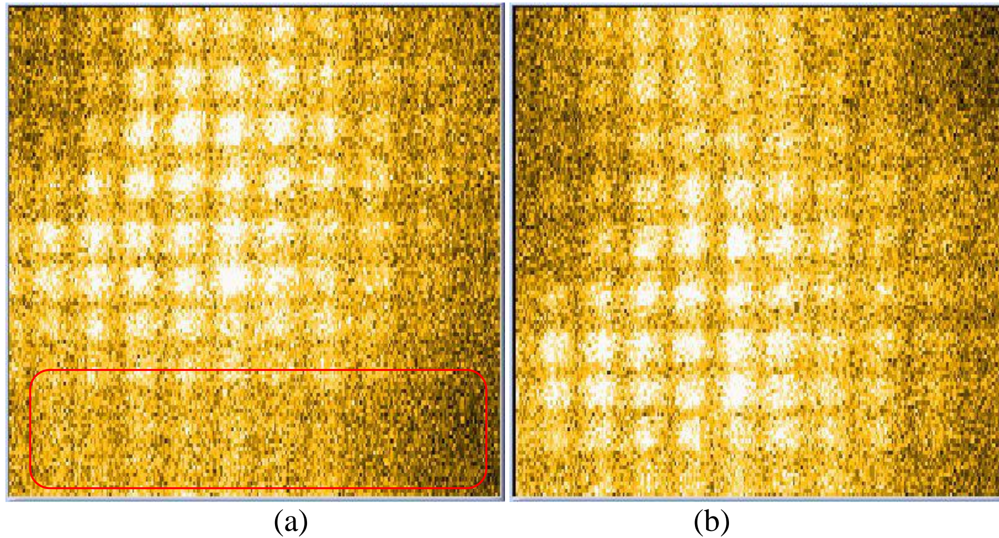

FIGURE 3-47: Feed forward control test with scanner running at 60 Hz (x closed loop, y open loop), (a) without feed forward, (b) with feed forward.

FIGURE 3-47 shows how the feed forward control algorithm improves the image quality. The left image was obtained without feed forward, and a large portion of the image (bottom part) is distorted because of the phase shift in high speed positioning. By applying feed forward control, the right image shows a complete scan image without losing information and accuracy. By tuning the feed forward parameters, zero phase shift can be achieved.

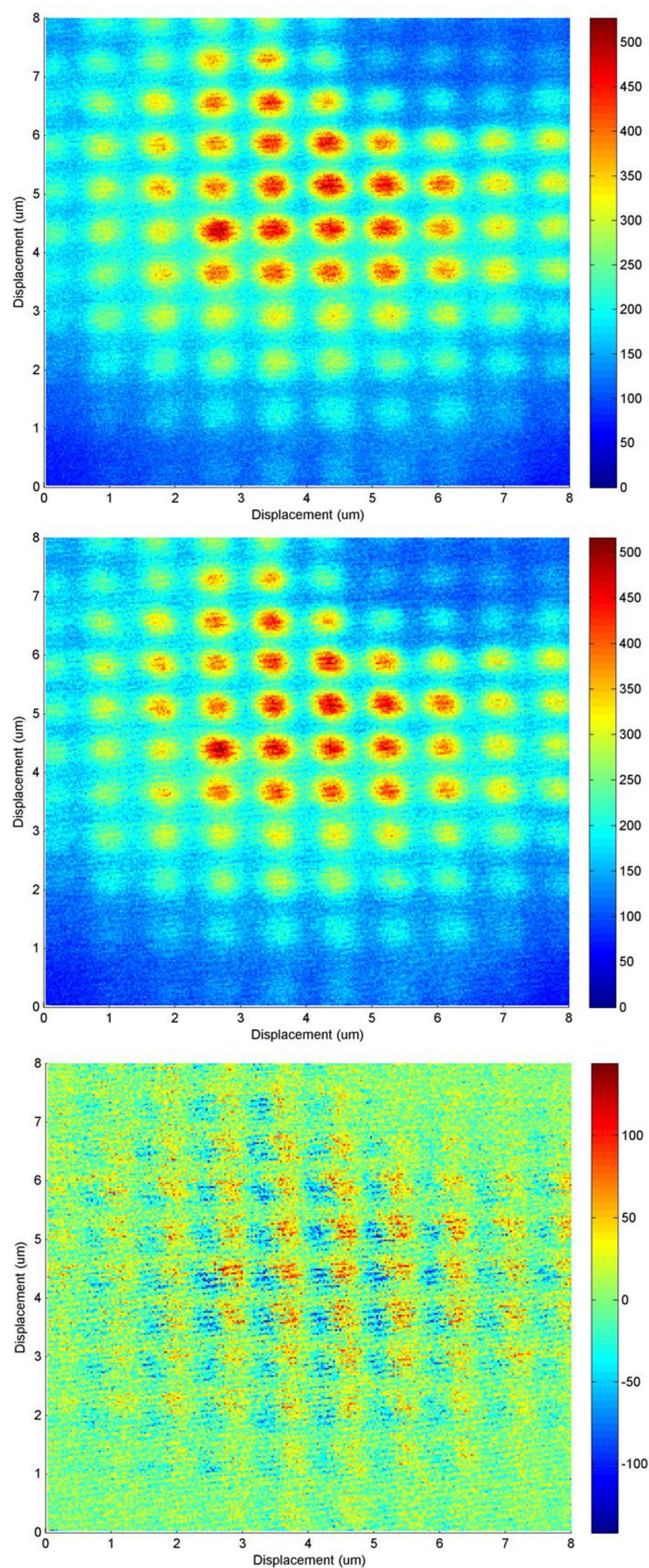

FIGURE 3-48: Repeatability test, top: image at location A at t_0, middle: image at location A at t_1, bottom: different counts at the corresponded pixel in two images.

The controller and software were set up to integrate the fast scanner with the *xyz* scanner to realize a dual scan algorithm. With such algorithm, a relative rough large slow scan is done by the *xyz* scanner, while the fast scanner is able to focus on the location of interest for rapid scanning afterwards. FIGURE 3-48 shows the repeatability of the process. In the test, first the *xyz* scanner was closed loop at (30 μm, 20 μm, z_1), *z* axis is set at z_1 with open loop to focus the image, the top image in FIGURE 3-48 was then obtained using the fast scanner at 2 Hz. After that, *xyz* scanner was commanded to go to (35 μm, 25 μm, z_1), and the fast scanner was run to get another image (out of focus). Then *xyz* went back to (30 μm, 20 μm, z_1), use the fast scanner to get the middle image in FIGURE 3-48, finally *xyz* went to (35 μm, 25 μm, z1) to get final one image (out of focus). The bottom figure shows the count deviation of each pixel between the top and middle images. The deviation was suspect coming from the drift in *z* axis since it was open loop control during the test.

3.8 Conclusion

This chapter demonstrated a new way of implementing confocal laser scanning microscopy by scanning the laser beam from the emit location. A fasts *xy* scanner was designed to scan the fiber at the speed of 100 Hz. The mechanical, sensor, and controller of the fast scanner were designed and demonstrated. The reasons limiting the bandwidth were analyzed. Another issue, ringing in the high speed scanning, was studied while an impulse shaping method was introduced to attenuate the ringing vibration. The energy theory applied as a new theoretical approach for the impulse shaping was initially studied and tested. Finally experiments were running to image an artifact grating to show the performance of the new system.

CHAPTER 4: CONTROLLER AND USER INTERFACE

The Nanoscope™ IIIa hardware and software was employed for open loop control, data acquisition, imaging, and as a graphic user interface (GUI) in the original generation of this microscope. It was not able to address the precision problem that exists in open loop systems. An analog PID circuit with Real-Time target computer was later employed for analog closed loop control and compensation of capacitance gage non-linearities. However, it added redundant components to the whole system, i.e. ADC/DAC, computers, which increased noise level of the positioning system, and reduced the resolution. Therefore further investigates of the controller hardware and software were required to enhance the performance.

4.1 Controller hardware types and Pros-Cons

Since the price of digital computers has dropped considerably and computing power is increasing, the design goal for the controller is bringing in a digital controller with LabVIEW™ supported hardware and software. The digital controller uses computers to act as system controllers. Satisfying the throughput requirements for data acquisition and processing, a standard dual core desktop computer was employed to achieve a real time control with reliable performance and deterministic timing.

The digital controller offers several advantages over the traditional analog controller. It is much easier to tune and adjust the control parameters and algorithms (i.e. adaptive control) in a digital controller than the analog controller since the process is running in

digital computer where the analog controller requires circuits with various components. Also, it can be integrated seamlessly into the scanning system, user interface and post process system, while an analog controller still needs a digital computer (i.e. Nanoscope™) for such tasks above, or even another computer for sensor calibration or other user-required functionality support. Thirdly, while there is some degradation over time the digital controller is more stable when exposure to environment disturbance while the analog components, i.e. resister, capacitor, potentiometer, connectors and wires will drift or degrade over time. The disadvantage of digital control is ADC/DAC bandwidth and quantization error. When the sampling bandwidth is tens of times faster than the designed system bandwidth, the dynamic response of the discrete digital system can achieve similar performance as an analog controller.

	Open Loop ; Fast Not accurate		Closed loop Accurate, more function support for imaging			
			Analog Fast		Digital Easy tune	
Controller	Nano scope™	Pure LabVIEW™	Nano scope with LabVIEW RT	Pure LabVIEW	Nano scope with LabVIEW RT	Pure LabVIEW
Pro	Good GUI and built in image processing	Easily switch to closed loop; Customized GUI and functions	Good GUI and built in image processing	Easily switch to open loop; Customized GUI and functions;	Good GUI and built in image processing to	Easily switch to open loop; Customized GUI and functions
Con	No multi-channels; Switch to closed loop takes time	Customized GUI takes time	No multi-channels; complicated	Customized GUI takes time	No multi-channels; complicated	Customized GUI takes time
DAQ occupied (for XY scan motion)	2 DAC	2 DAC	4 DAC 2 ADC	4 DAC 2 ADC	4 DAC 4 ADC	2 DAC 2 ADC

FIGURE 4-1: Controller hardware comparison.

FIGURE 4-1 shows a comparison among several different controllers. The digital controller using LabVIEW was chosen as it only requires two DAC/ADCs for closed

loop for *xy* scanner which is beneficial in noise control. In addition, LabVIEW is a convenient development platform for hardware interfacing and dynamic control. Therefore, it is straight forward to realize customized control algorithms and other functionalities, i.e. capacitance digital demodulation, digital filter, image processing. The software and controller is capable of realizing the basic functions of a typical commercial scanning and imaging controlled unit, e.g. scanning controls, contact mode AFM control, PID tuning, probe sensitivity test, force curve, multi channel imaging, etc... More functions can be integrated in future, like mechanical spectroscopy, image processing technology: fluorescence analysis for resonance energy transfer, single molecule analysis and fluorescence anisotropy. The addition of these novel imaging capabilities will make the system unique and readily extended to novel mechanical and optical probe technologies as they develop. This ability to incorporate technologies as they emerge enables a versatility that cannot be obtained with commercial products. The open source hardware, software and architecture of the system also make it a versatile instrument that is able to cater to a wide variety of measurement modalities and incorporation of arbitrary algorithms for real-time diagnostics.

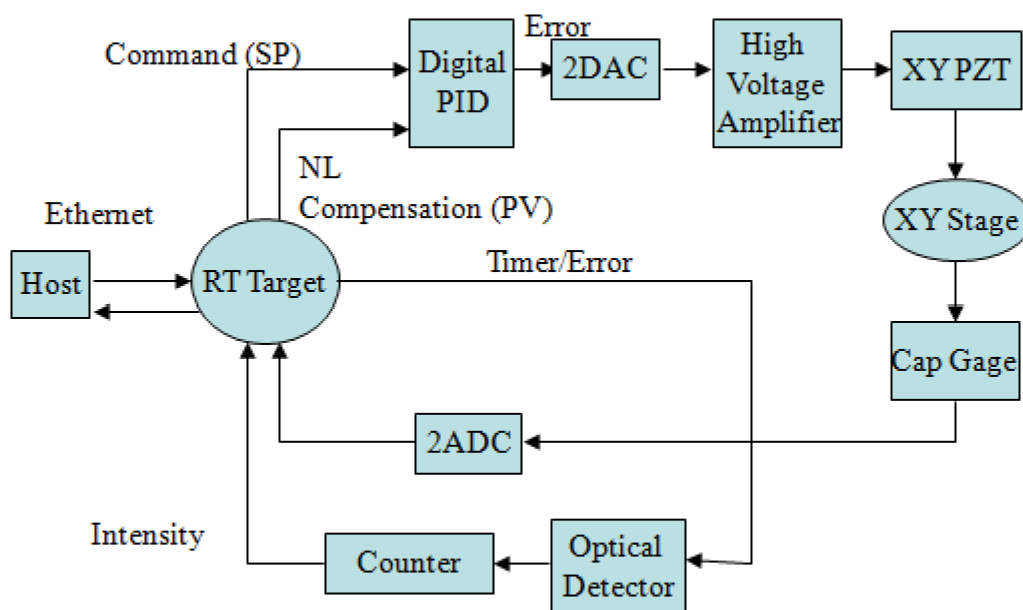

FIGURE 4-2: Block diagram indicating major components of the digital controller for two dimensional positions scanning.

FIGURE 4-2 shows a block diagram of the digital controller using LabVIEW Real-Time™. The controller used two computers to achieve real time control. One is the host computer running the user interface based on the LabVIEW development environment in Windows XP™. The other is the target computer running LabVIEW Real-Time™ operating system where all the deterministic codes for the program are executed. The communication is accomplished through a crossover Ethernet cable between the two computers. Scanning commands are input in the host computer and then sent to the target. The target performs the time sensitive code, i.e. set point generation, control, sensor data acquisition, and sending the data back to the host. The desired command and processing variable (non-linear compensation for displacement signal) go through the digital PID controller which generates the output voltage via DAC to the high voltage amplifier (HVA Gain = 15). The PZT actuator is powered by the voltage from the HVA to position the mechanical stages. The actual displacements of the stages are measured by the

capacitance sensors and converted into digital signals.

The digital controller is programmed and implemented either in software mode (Real-Time) or hardware mode (FPGA) or both.

4.1.1 Real-Time

The real time operating system is able to run applications with precise loop timing. This is important in measurement and scanning because every step during the process needs to be deterministic for positioning and imaging with relatively low uncertainties. For example, a time period for each loop can be guaranteed as low as one microsecond (MHz bandwidth) in a real-time operating system while a maximum about tens of milli-second timing (100 Hz bandwidth) resolution is possible in a Windows operating system.

Currently the NI LabVIEW Real-Time™ 8.6 is installed in a desktop personal computer with a 2.8 GHz dual core CPU as the target. It supports multi-core which enables the servo loop runs on a specific core to better allocate hardware resource to various tasks. An MXI cable connects the target with an MXI chassis through a PCI-E bus. A PXI-7852R smart DAQ card is installed in the chassis. It features a user-programmable FPGA chip for onboard processing and flexible I/O operation, and supports up to 750 kHz independent sampling rate for 8 analog inputs, 1 MHz independent sampling rate for 8 analog outputs with 16-bits resolution, and 96 digital lines at rates up to 40 MHz, see TABLE 4-1 for I/O usage with the current microscope system.

TABLE 4-1: I/O usage of the DAQ.

DAQ	occupation	
DAC	x, y, z actuators, carrier signal for sensor, fast scanner (4)	8
ADC	x, y, z sensors, fast scanner sensors (2)	5
DI/DO	2 channel counters (16), 1 digital line for TTL output	17

4.1.2 FPGA

A Field-programmable Gate Array (FPGA) is an integrated circuit designed to be hardware configured by the customer or designer after manufacturing—hence "field-programmable"[50]. It is programmable hardware which can be re-configurable to implement custom hardware functionality without building a real circuit. The FPGA has higher performance than the digital signal processors (i.e. Real-Time) for its hardware level parallelism. It simplifies the execution procedure through deterministic hardware dedicated to the task where the digital signal processor involves several resources operation in the system which may slow it down.

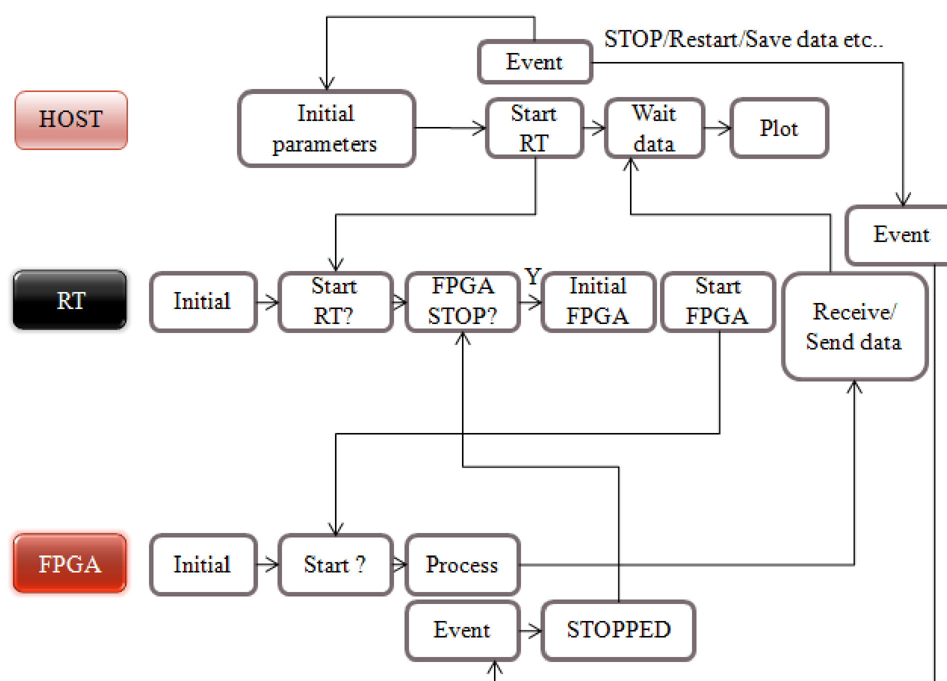

FIGURE 4-3: Communication layers of the interface hardware.

The PXI-7852R is equipped with a Virtex-5 LX50 FPGA. Most of the critical code is translated from real-time level to the FPGA level, i.e. I/O, PID controller, sensor demodulation to achieve high bandwidth signal processing on multiple channels of input

and output. FIGURE 4-3 shows the communication flow chart among the layers. The Real-Time level program handles non-critical tasks, i.e. steaming the data to host, responding to interrupter from host or FPGA. Though this configuration theoretically improves the speed and stability, it brings a lot issues when coding in FPGA, i.e. differences in data formats and debug procedures make it difficult to program.

4.2 Open loop and closed loop

TABLE 4-2: Positioning control methods comparison, higher score is better

XY scanner	resolution	Precision	Speed	Note
Open loop	2	1	3	Easy to realize
Open loop with calibrated commands	2	2	3	Need calibration before operation (Different scan parameters may have different calibration equation.)
Open loop with sensor	1 Using sensor to get the x y coordinates	3	1 Limit by sensor	Require signal post processing; Sensor bandwidth limit, sensor noise reduces resolution; real time image appeared the same in open loop
Closed loop	1	3	1 Limited by sensor, controller	Sensor and controller bandwidth limit, sensor noise and controller noise reduces resolution;

Positioning performance is important in the scanning probe microscope. The accuracy, resolution, bandwidth of the positioning determines the image resolution, and

speed. Depending on measurement requirements, different control algorithms are available. TABLE 4-2 outlines the differences among four positioning control algorithms. Open loop with calibrated command is popular in commercial products. It has high resolution (tens pm) and the accuracy is reasonable if calibrated. However the creep feature of the actuator causes drift leading to low repeatability in imaging over appreciable times (10’s to 100’s of seconds). Also, it is difficult to locate points of interest accurately in the imaged area since the position characteristic varies a due to hysteresis of actuator where the calibration equation does not work well. To address these issues, a closed loop control method is applied to the positioning system by introducing a sensor system to measure the displacement of the moving stage relative to the instrument frame. This method is also popular in the commercial scanner designs and is increasingly being applied to commercial scanning probe microscopes. It is able to achieve sub-nm resolution by using capacitance sensor or laser interferometer at several kilo Hertz bandwidth while the uncertainties over typical measurement time periods are within several tens of nanometers. This method increase the imaging repeatability and making it much easier for the user to navigate to interesting locations. Currently, the controller for the SMPM is capable of switching between open loop and closed loop operation by with controls on the GUI.

4.3 Scanning algorithm

To obtain images the scanning microscope sweeps the specimen point-by-point and line-by-line in a sequential manner. Two scanning trajectories are commonly applied to the scanner motion, image capture and reconstruction as shown in FIGURE 4-4. The left one is the raster scanning method commonly used in open loop control. The slow axis,

i.e. y , keeps moving during the fast axis scanning process. It adds a potential issue for closed loop control due to the xy actuator and sensor coupling problem. Therefore, the controller and mechanical part may not be fast enough to track the command. Also, the image is rotated a shallow angle requiring additional processing to restore the actual shape. The right one is the serpentine scanning method. The slow axis only steps when the fast axis changes the direction. Currently the raster scanning is employed as required by the user.

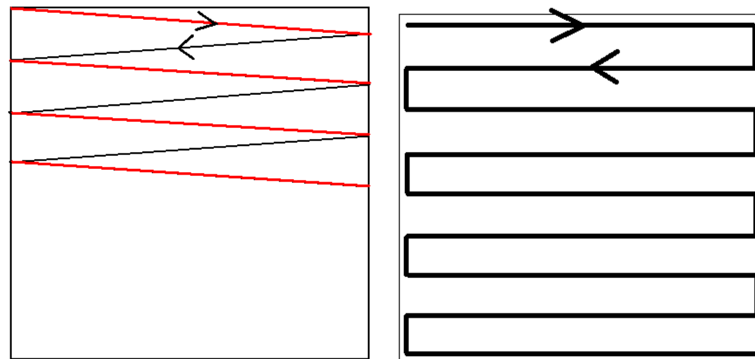

FIGURE 4-4: Scanning trajectories, Left: raster, Right: serpentine

Another issue related to positioning performance is the fast axis scanning signal. Triangular wave is the common command signal for the scanner. However, the high acceleration impulse at the reversal points causes vibration in the positioning stage resulting in image distortion at high scanning speeds. Advanced control algorithms such as impulse shaping, may alleviate this phenomenon by some extent, see Chapter 3. Another scanning pattern, a trapezoidal wave, is able to reduce the acceleration by increasing the dwelling time at the reverse point. However, this reduces the effective time for photon counting in confocal scanning microscope, therefore, a compromise needs to be made for optical probe between the SNR of the photon count and image distortion when applying this method. For AFM probes, this method requires the probe to have

higher bandwidth since, to reduce surface damage, the probe must navigate the surface in a shorter time.

The scanning speed can be increased by twice when the data is collected at both the forward and backward movement during the scanning process. Additional data processing in the software is easy to realize this functionality, however, this is rarely used in commercial products mainly because that, because of the phase shift between desired position and stage motion, every other line displaces with respect to the adjacent lines and this is not easily removed. This phase shift exists in both open loop and closed loop control. A sophisticated closed loop controller algorithm such as feed forward and measurement of the stage position may help to alleviate this, but it is still difficult to completely eliminate the phase shift for arbitrary scan ranges and speeds.

Also there exist a few details in the scanning procedure. Because of its discrete nature an analog low pass filter should be added after the DAC to smooth each step output. “Home” and “Initialize” of the high voltage amplifier are necessary to take the stage back to the home position to smoothly go to the start point during scan operation. Without these features, there is often a large, potentially damaging, step demand to the PZT actuator at the beginning or end of scanning.

4.4 Graphic user interface

The GUI is designed based on LabVIEW in the host computer and is shown in FIGURE 4-5. It is able to show the two channel images simultaneously. Each channel has a trace window and a real-time imaging window. The scan area can be entered by keyboard or mouse. The scanning speed, set point, and z height (for fine focusing in optical probe mode) can be adjusted in real-time. The data and images are saved in

background when required. Areas of interest can be selected using the mouse in the window located in the lower center and re-imaged on the imaging window.

FIGURE 4-5: GUI of the SMPM.

4.5 Conclusion

In this chapter, different controller hardware has been compared for various generations of the microscope development. Because of the powerful computing ability, a LabVIEW Real-Time™ application with FPGA module has been used as the system controller. The controller is designed to be switchable between open loop and closed loop operation for different applications, i.e. closed loop for low speed imaging and low uncertainties and open loop for higher speed. The scanning pattern is also discussed as well while the raster scanning method is adopted as requested by the user. Lastly, a GUI and basic functions are shown. It is noted that the open source nature of the controller enables future users to realize customized functions as requirements for the system change.

CHAPTER 5: INVERSTIAGTIONS OF OTHER HIGH BANDWIDTH DISPLACMENTS METHODS (KNIFE EDGE SENSOR AND FIBER INTERFEROMETRY)

Precision position sensing is a mature technology applied throughout precision machines and instrumentation. Today, the designer can select from a range of sensor methodologies that suits the particular application. For precision position measurement, the choice is typically between optical interferometry, optical lever, capacitance, inductance or transformer coupled methods and line scales based on optical, capacitive or inductive techniques. In this chapter, two high-resolution displacement measurement technologies based on optical light intensity are demonstrated.

5.1 Fiber interferometer

5.1.1 Introduction

The fiber optic interferometer is a high-precision measuring system and displacement sensor. This homodyne type interferometer is often used for short term displacement measurement, i.e. less than the fringe (half wavelength). Two basic setups are known : Mach-Zehnder [51] and Fabry-Perot interferometers[52-55]. FIGURE 5-1 shows a typical working principle of fiber FP interferometer. The interference results from the reflecting end surface of the fiber-air interface and an external reflecting target, i.e. mirror. The phase ϕ of the interference signal is calculated based on the wavelength (λ) of the light, the incidence angle of the light (θ), the thickness of the cavity (l) and the refractive index of the material between the reflecting surfaces (n), with n = 1.000

assuming the paths are in vacuum, shown in equation(5.1). Constructive interference occurs when the two reflected beams are in phase and the highest intensity or signal is obtained. In contrast, if the transmitted beams are out-of-phase, destructive interference occurs resulting in the lowest intensity at the detector.

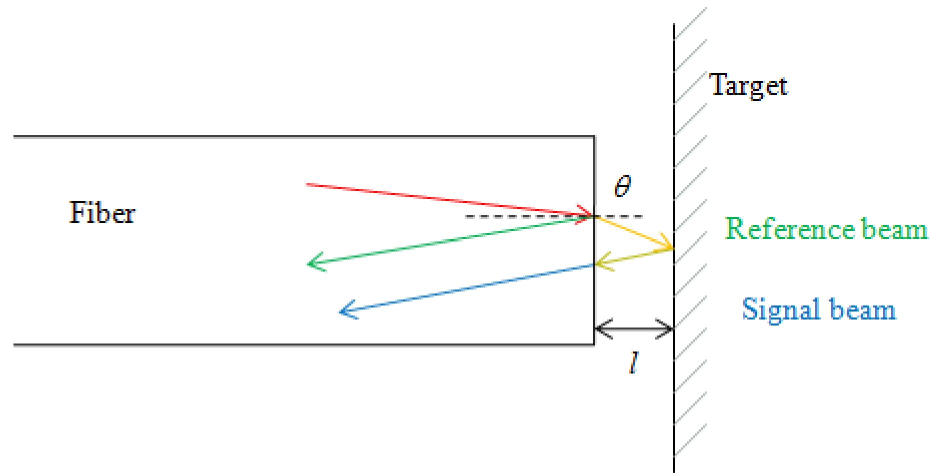

FIGURE 5-1: Interference illumination.

$$\phi = \frac{4\pi}{\lambda} nl \cos\theta \tag{5.1}$$

5.1.2 Experiment setup

FIGURE 5-2 and FIGURE 5-3 show the experimental setup in normal lab environment [56]. For the laser source, the Agilent 81600B-200 telecommunications IR test laser was adopted which has a line width of about 80 kHz , 1 pm wavelength stability over 24 h, and a wavelength tuning resolution of 0.1 pm over a range of 1440 to 1640 nm. The laser passes through a fused-tapered biconic isolator which stops the light travel from the opposite direction with an attenuation of -55 dB. In such way, the return reflection won't result a large parasitic fringe. The light keeps passing through an optically contacted evanescent wave coupler with a ratio of around 50:50 and a return loss of -70 dB. The fiber coupler is an optical fiber device spliced together to produce one or more

input fibers and one or several output fibers. Light from an input fiber can appear at one or more outputs, with the power distribution depending on the wavelength, polarization and splicing condition. One output of the coupler was fed into the interferometer cavity as the measurement head, the other channel was coupled with an angle polished connector (APC) which prevents unwanted reflections returning back into the fiber. The light emitted from the fiber at the measurement head was reflected and transmitted between the gold coating silicon and the cleaved end face of the fiber. The gold coating silica glass was attached to a PZT actuator which is capable of varying the cavity length over a few micrometers. The transmitted light comes back through the return APC and is received at an InGaAs photodiode.

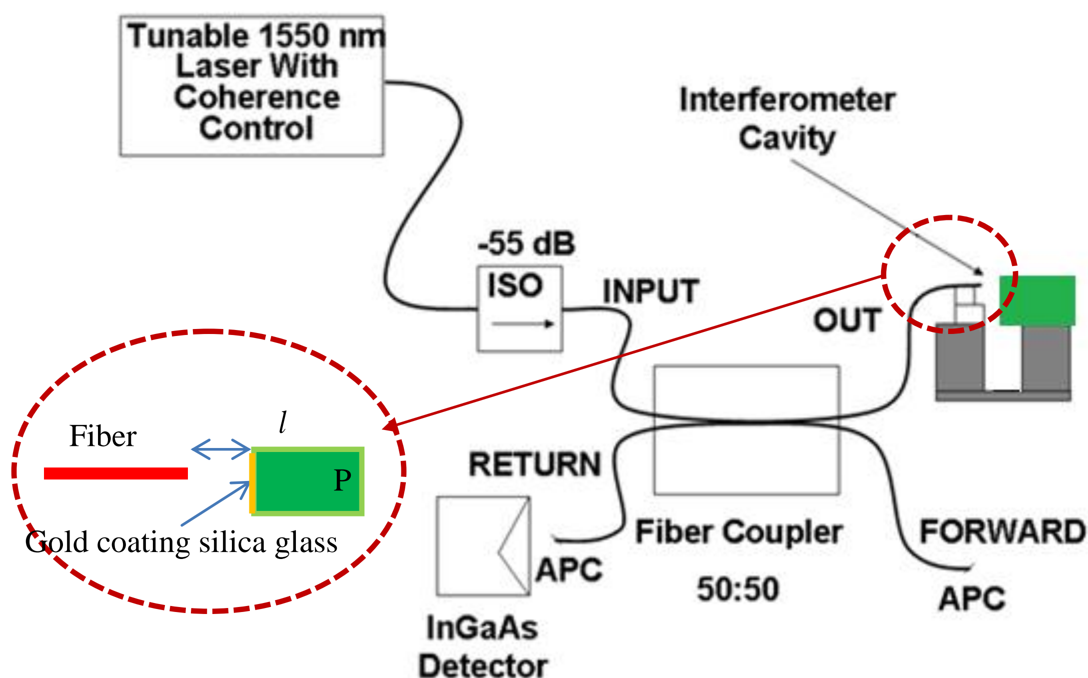

FIGURE 5-2: Experiment setup schematic shows the main components of the system. (Courtesy of Dr. Doug Smith, National Institute standard Technology, MD).

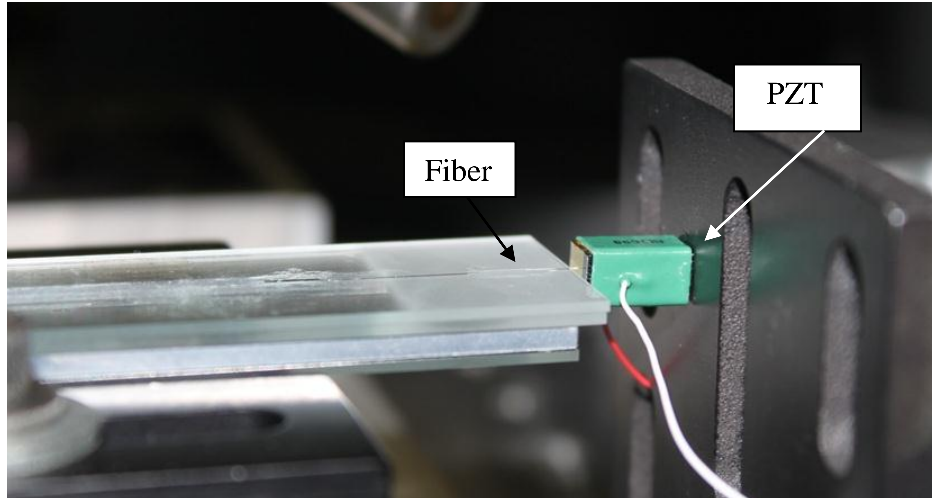

FIGURE 5-3: Photograph of the cavity setup in a normal lab environment.

There are two working principles of the fiber interferometer present during the process of measuring the distance between two reflecting surfaces, see sections 5.1.2 and 5.1.3.

5.1.3 Wavelength sweep mode

From equation(5.2), the maxima intensity occurs when $4l/\lambda = 2m+1$ (m = 0, 1, 2 …), and the minima occurs when $4l/\lambda = 2m$ assuming no phase shift caused by wavelength sweeping. When l is large enough, it is can be calculated from the following equation by sweeping the wavelength of the laser since the IR test laser is capable of being stably and accurately tuned over the working range with 0.1 pm resolution and ±4 pm uncertainty in stepped mode. We have

$$l = \frac{\lambda_m \lambda_{m+1}}{2\Delta\lambda} \qquad (5.2)$$

Where λ_m, λ_{m+1} are the wavelengths of two consecutive fringe maxima or minima. The minimum measureable l is limited by range of sweeping wavelength, which is around 6 μm based on equation (5.2) when $\Delta\lambda = 200$ nm (the maximum the laser source

can get). Theoretical uncertainty of l is calculated based on the combining uncertainty as the following equation, assuming λ_{m+1}, λ_m measurement are correlated. From equation (5.3), the uncertainty increases as l increases. Using the curve fitting method, the uncertainty of wavelength measurement can be as low as 0.1 nm, therefore the minimum uncertainty of l measurement is around 0.38 nm when $\Delta\lambda = 200$ nm.

$$\delta_l^2 = \frac{1}{4}\frac{\left(\lambda_m + \lambda_{m+1}\right)^2}{\left(\lambda_{m+1} - \lambda_m\right)^2}\delta_{\lambda_m}^2 \tag{5.3}$$

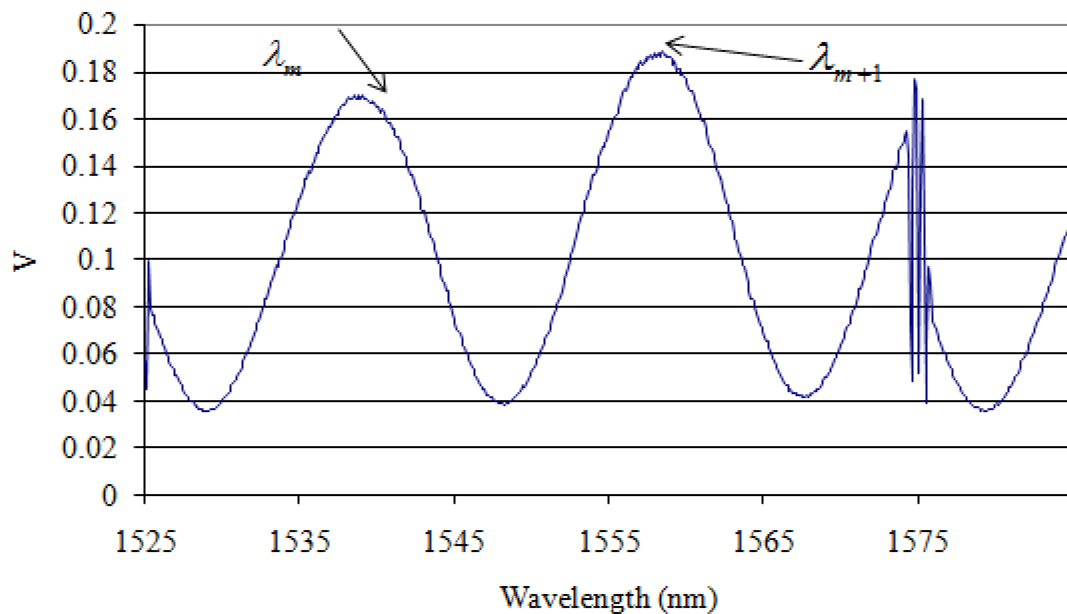

FIGURE 5-4: Voltage from photo detector as a function of wavelength with the cavity length set at around 0.5 diameter of the fiber (i.e. 125 μm).

An experiment was setup to verify the above equations. As FIGURE 5-4 shows, the cavity length (half of the separation between the two reflecting surfaces)was set as around 0.5 diameter of the fiber. Measurement of this separation was based on the fiber to surface separation observed in an optical microscope. . The wavelength was swept from 1525 nm to 1575 nm at a speed of 2 nm per second with an increment of 0.1 nm. The sample rate is 20 Hz which is relatively low due to the working mode of the laser system

and low speed data acquisition system. Choosing λ_m = 1538.4 nm, λ_{m+1} = 1558 nm at the two consecutive maximum measured intensities, the cavity length is calculated to be 61.4 μm which is close to 62.5 μm.

5.1.4 Cavity sweep mode

Another working mode for cavity length measurement is more straightforward and typically capable of higher bandwidth cavity length measurement. From equation(5.1), the cavity length variation will cause phase shift which is represented as light intensity or voltage change measured by the detector. Because of divergence of the light coming out of the fiber, the radiation light from the target mirror returning back into the fiber depends on the cavity length and reflectivity of the air-fiber, air-target (i.e. mirror) interface, therefore affect the detector output (the output is not uniformly periodic versus displacement), see more details at [57]. By calibration the voltage with proven displacement sensor, those effects can be removed.

Study was carried out to optimize parameters for highest resolution of displacement measurement. It is worth to point out that, sensitivity (Vnm^{-1} or nmV^{-1}) does not present the performance of the sensor system without defining the noise level and bandwidth. In principle, sensitivity can be very high when the gain is set high, however, the noise level also increase. Therefore, the SNR is a better measure to represent the performance. In theory, the SNR is depending mostly on the reflectivity (R) of the interface. See [57] for the mathematical development of R and intensity. The SNR increases dramatically when R approaching 1.0 (high-finesse cavity). In the current setup, the air-fiber interface had an R around 0.04 [56]. Under such conditions, the following procedure leads a way to obtain the highest sensitivity at quadrature where the detector output is Vq, then the small

change (less than half of wavelength) of l can be measured as $Vq + \Delta V$, which need to be calibrated to reduce the non-linearity of the sensor.

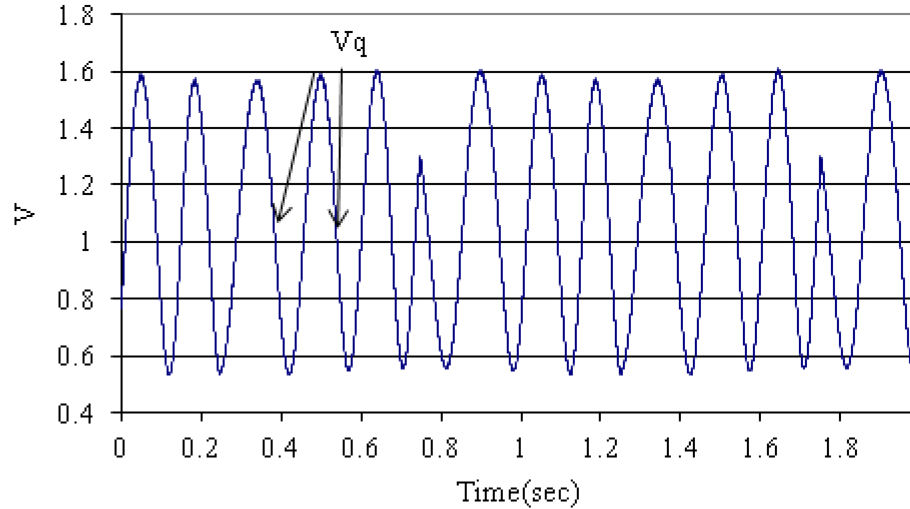

FIGURE 5-5: The detector outputs when the interferometer is working in cavity sweep mode.

Sensitivity experiment:

1. Set the FP cavity length l at about 0.25 D, and set $\lambda = 1500$ nm
2. Run PZT to sweep the cavity length by a few micrometers to get several fringes as shown in FIGURE 5-5.
3. Record the Vq, V_{IS} and find the maximum sensitivity from the fringes,

Where $Vq = \dfrac{V_{\max} + V_{\min}}{2}$, $Vis = \dfrac{V_{\max} - V_{\min}}{V_{\max}} \leq 1$

4. Increase wavelength by steps of 10 nm
5. Repeat step 2,3,4, until λ = 1640 nm
6. Calculate the sensitivity S based on equation (5.4) and the noise level

$$S = \frac{\lambda}{4\pi Vis Vq} \text{ (nm} \cdot \text{V}^{-1}\text{)} \tag{5.4}$$

Then increase l, repeat steps above.

Vq is the detector voltage at quadrature, V_{max} is the maximum detector voltage when sweeping the cavity, V_{min} is the minimum detector voltage.

5.1.4.1 l ~ 0.25D, Gain = 1, Power = 2 mW

In this setup, the cavity length was set about 0.25 diameter of the fiber, which was around 31 μm. The detector gain was set as one, and the laser power was 2 mW. The PZT was excited by 1 Hz, and 50 Vpp triangle sweep signal with a scan range around 4 ~ 5 μm (open loop). The laser coherence function is ON to decrease noise level at the DC-1 kHz range [56].

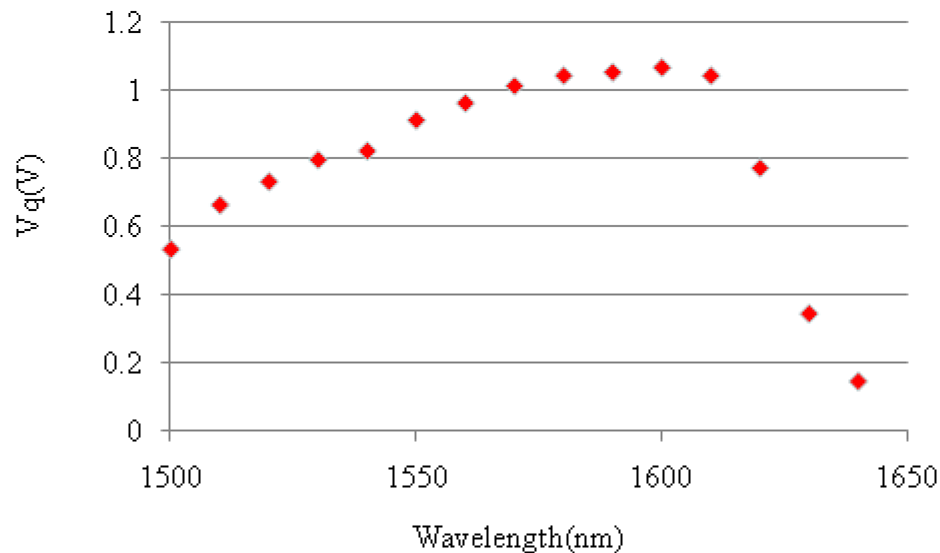

FIGURE 5-6: Vq versus wavelength change.

As shown in FIGURE 5-6, the Vq increased as the wavelength went up to around 1600 nm and then dropped. This is mainly because the response characteristic of the detector to different wavelength and the potential instability power output of the laser when it varies its wavelength.

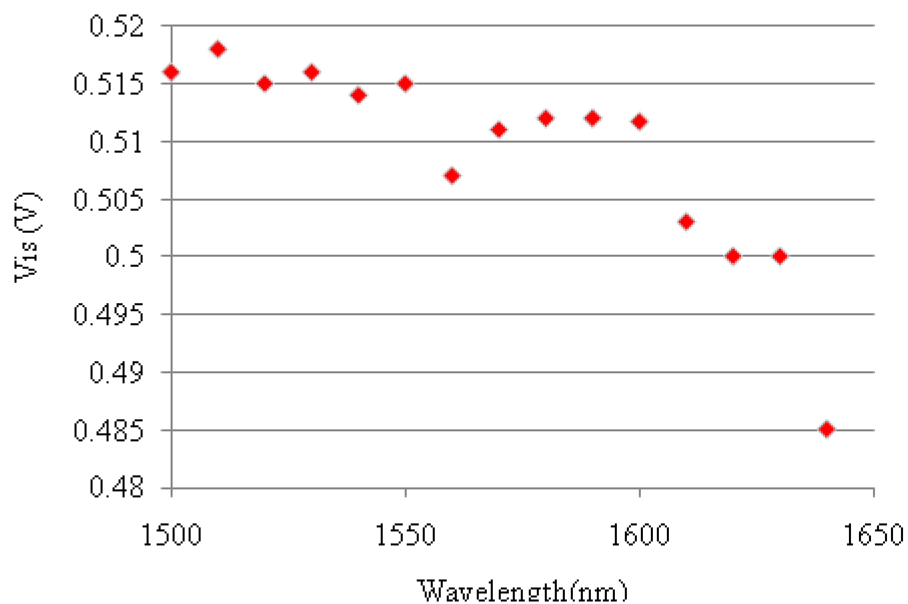

FIGURE 5-7: *Vis* versus wavelength change.

FIGURE 5-7 shows *Vis* of the wavelength. It was approximately around 0.5 though dropped by 5% as the wavelength increased.

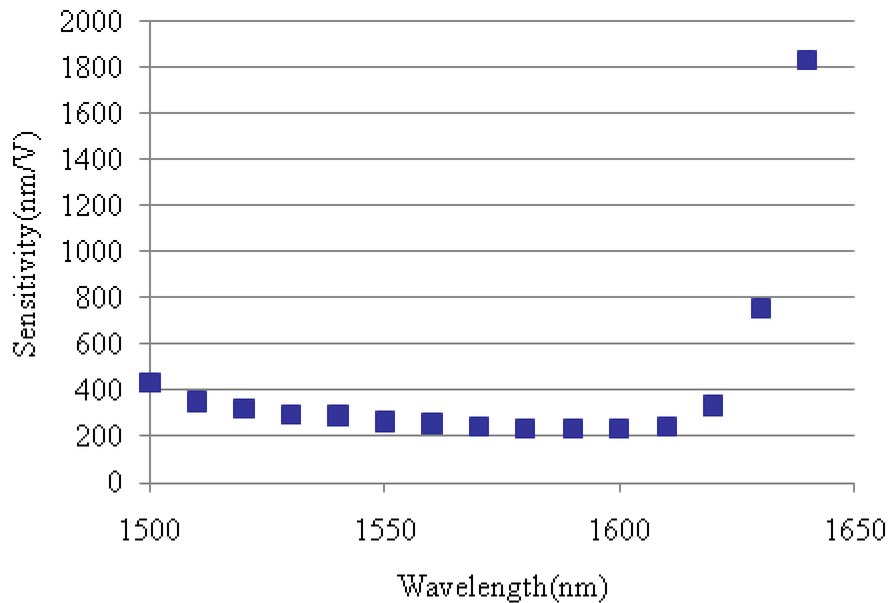

FIGURE 5-8: Sensitivity of laser at various wavelengths.

FIGURE 5-8 shows that the maximum sensitivity occurred near 1600 nm wavelength with a value of 233 nm $\cdot V^{-1}$. The *Vq* was dominated here in determining the sensitivity.

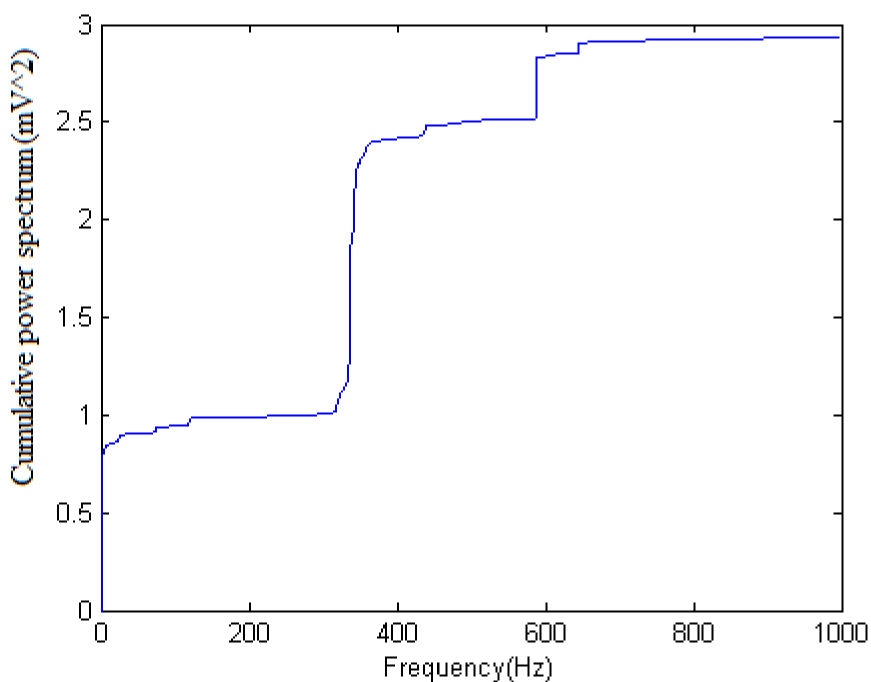

FIGURE 5-9: Cumulative power spectrum.

Assuming the noise performance of the detector keeps same as the wavelength varies, the wavelength with highest sensitivity, hereby is 1600 nm, gives best noise level. FIGURE 5-9 shows the cumulative power spectrum of two seconds noise data obtained at 1600 nm wavelength at the quadrature point. The short term standard deviation is 233 nm $\cdot V^{-1}$ sqrt(2.9) mV = 0.39 nm at 1 kHz bandwidth. It should be noted that the cavity length may change slowly during the test because of the creep feature of PZT actuator when it is in open loop control at the quadrature point.

5.1.4.2 l ~ 1D,Gain = 1, laser power = 2mW

After experiment at l ~ 0.25 D, the cavity length was increased to around one diameter of the fiber without changing other conditions, i.e. laser power and gain of the detector. FIGURE 5-10 and FIGURE 5-11 show the results. The visibility displays a sharp drop by 15% when wavelength was larger than 1600 nm which was only 5% in a shorter cavity length test. Though visibility increased at all wavelength as cavity

increased, it turned out that the sensitivity dropped to 400 nm $\cdot V^{-1}$ around 1570-1600 nm region because the intensity and *Vq* dropped when the cavity increased which reduced the amount of light traveling back to the detector. Assuming the detector noise level did not vary much by ignoring the optical path effect of longer spacing (cavity) of fiber-to-reflector, the displacement noise level will increase since the sensitivity drops.

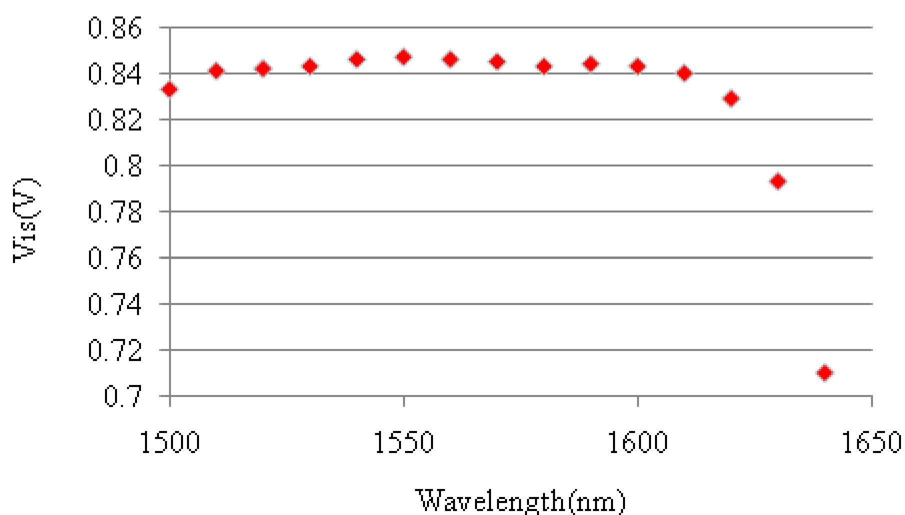

FIGURE 5-10: *Vis* versus wavelength change.

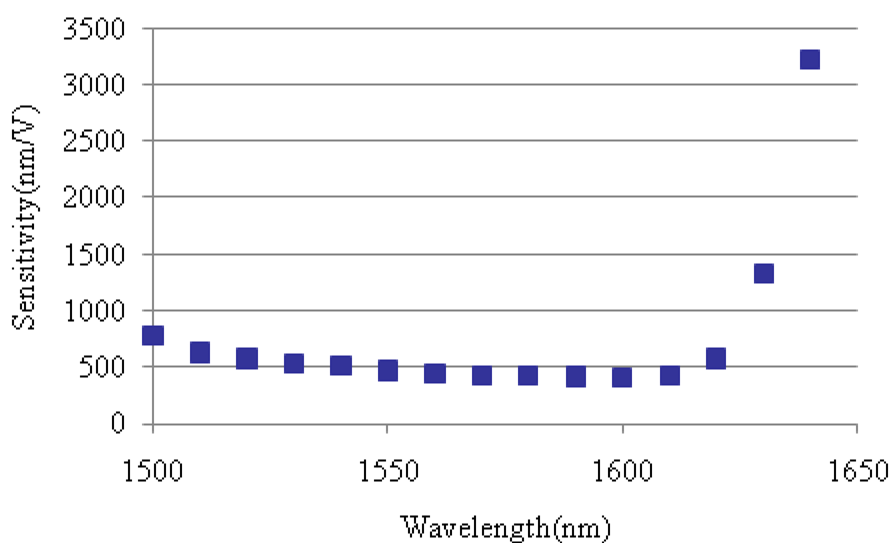

FIGURE 5-11: Sensitivity of laser at various wavelengths.

5.1.4.3 $l \sim$ 1D,Gain = 10, laser power = 0.6 mW,

The third try was to increase the detector gain to ten which raises the noise level on one hand, and enhanced the sensitivity on the other hand. The parameters were set as $l \sim$ 1D, Gain = 10, and laser power = 0.6 mW, the laser power was reduced to 0.6 mW to avoid the saturation of the detector (2 V).

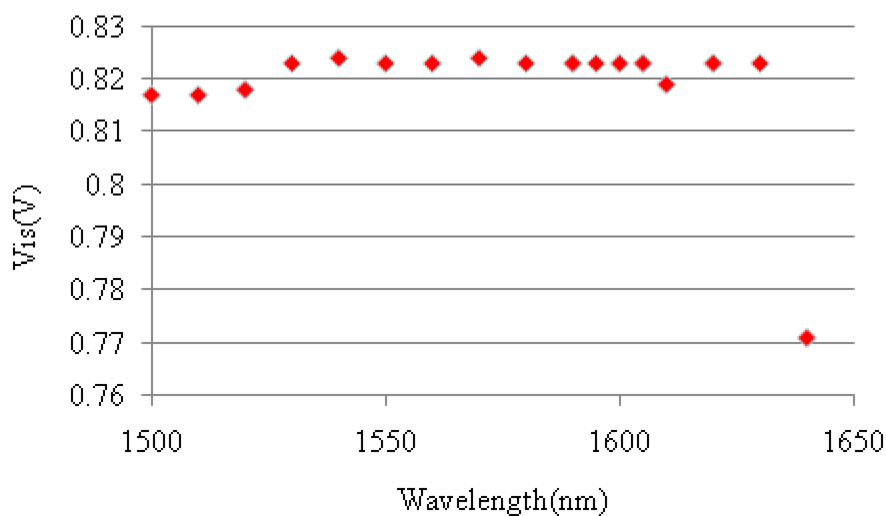

FIGURE 5-12: *Vis* versus wavelength change.

FIGURE 5-12 shows the *Vis* of various wavelengths. It was a lower than the low gain, high power and the same cavity length experiment in 5.1.4.2. That means that gain does not affect the visibility and the high power has minor effect on visibility as well.

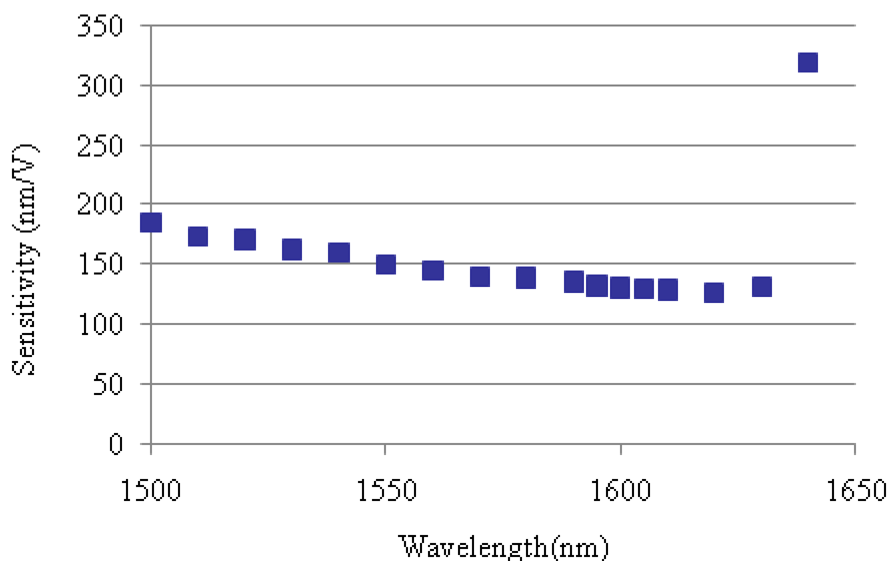

FIGURE 5-13: Sensitivity of laser at various wavelengths.

FIGURE 5-13 shows that the maximum sensitivity about 126 nm $\cdot V^{-1}$ occurring around 1620 nm wavelength at *l* ~ 1D. It was high because of the high gain setup for the detector.

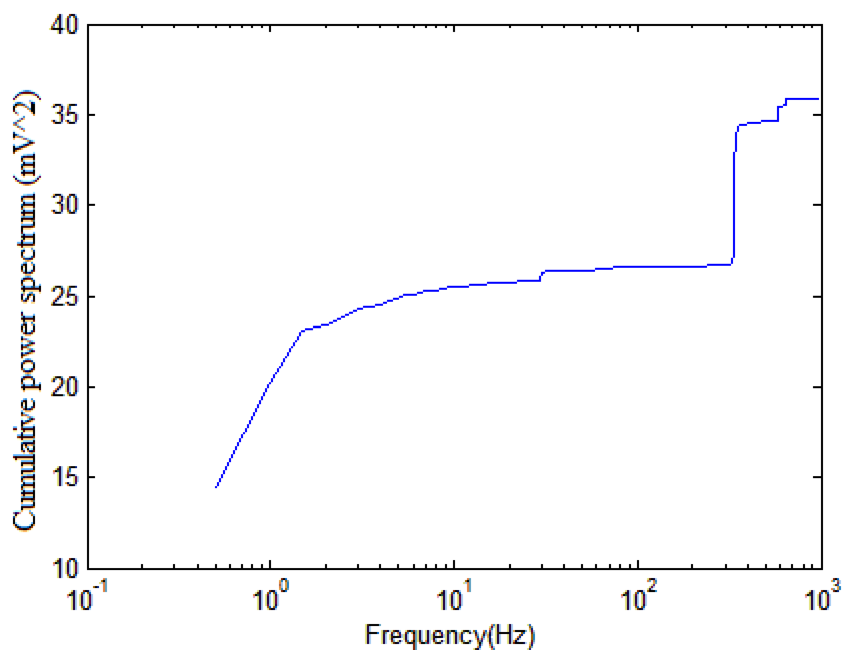

FIGURE 5-14: Cumulative power spectrum.

FIGURE 5-14 gives the short term standard deviation at around 126 nm $\cdot V^{-1}$ sqrt(36)

mV = 0.76 nm at 1 kHz bandwidth. The noise level goes up as compared with the situation that the cavity length is about 0.25D (σ = 0.39 nm).

5.1.4.4 l ~ 1.5 D, Gain = 10, laser power = 0.9 mW

Finally, we set the cavity length at around 1.5 diameter of the fiber, increased the laser power from 0.6 mW to 0.9 mW, and repeated the experiment.

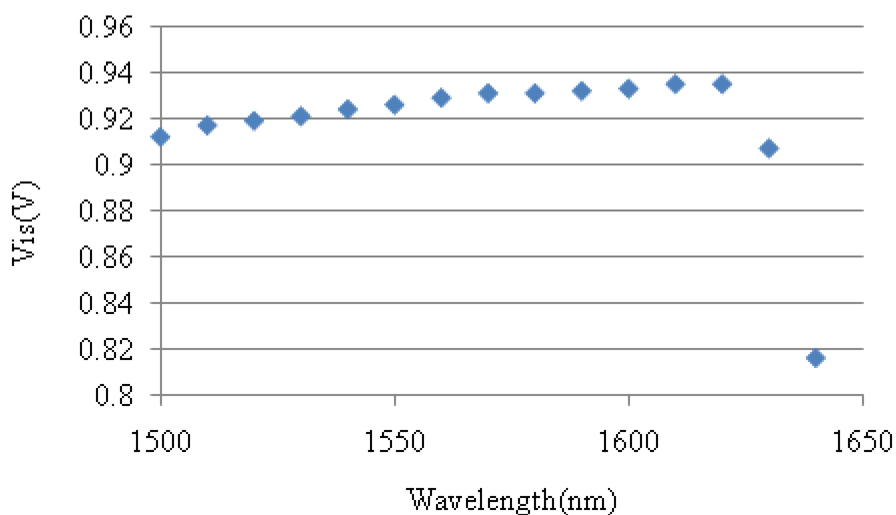

FIGURE 5-15: *Vis* versus wavelength change.

FIGURE 5-15 shows *Vis* of various wavelengths. It was very constant approximately at 0.92 which was the highest during these tests. Again, we can tell that the visibility increased when the cavity length enlarged.

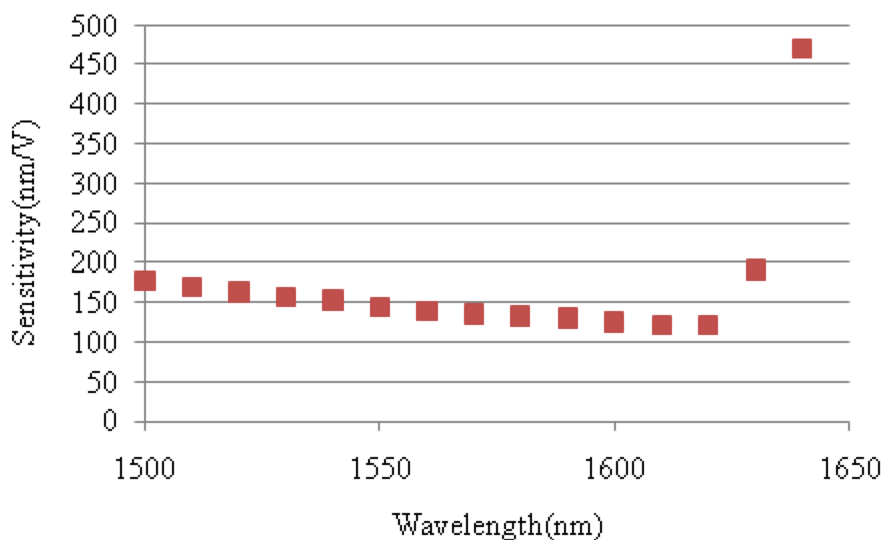

FIGURE 5-16: Sensitivity of laser at various wavelengths

FIGURE 5-16 shows that the maximum sensitivity about 120 nm $\cdot V^{-1}$ around 1620 nm wavelength.

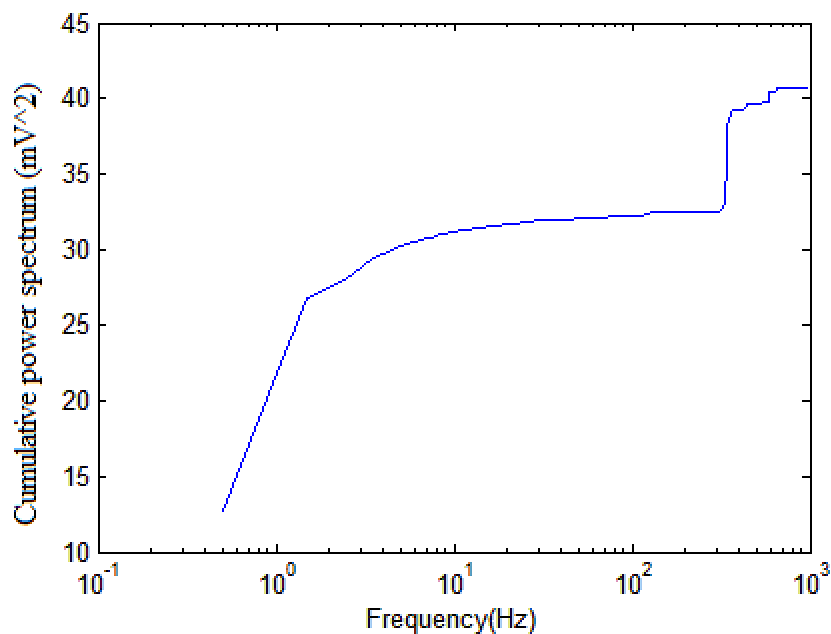

FIGURE 5-17: Cumulative power spectrum

The short term standard deviation is 120 nm $\cdot V^{-1}$ sqrt(41) mV = 0.76 nm at 1 kHz bandwidth. It was equal to the noise level of cavity length at 1D in 5.1.4.3. The laser power here was increased by 50% which increased the SNR, and this compensated the

SNR dropping caused by the increased cavity length.

5.1.4.5 Summary of results

We were able to draw several conclusions that, the visibility increases as the laser power or cavity length increases. In FIGURE 5-18, the sensitivity goes up when the cavity length reduces or the laser power or the gain increases. It is also depended on the characteristic of the photo detector's response to wavelength. Again, as noted in the first section, a very high sensitivity sensor might not work very well because of the high noise level which comes from the high gain. Therefore, it is good to put the noise level along with the sensitivity, or use SNR and range as the specifications. The noise level drops as the laser power increases and it should drop as well when the cavity length reduces because that the shorter optical path leads to lower disturbance from the environment.

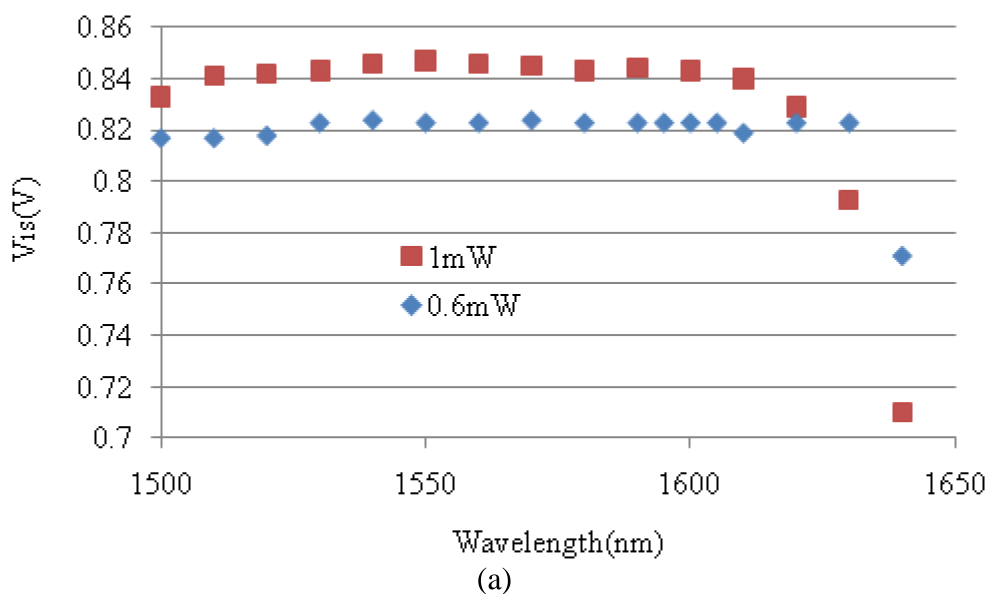

(a)

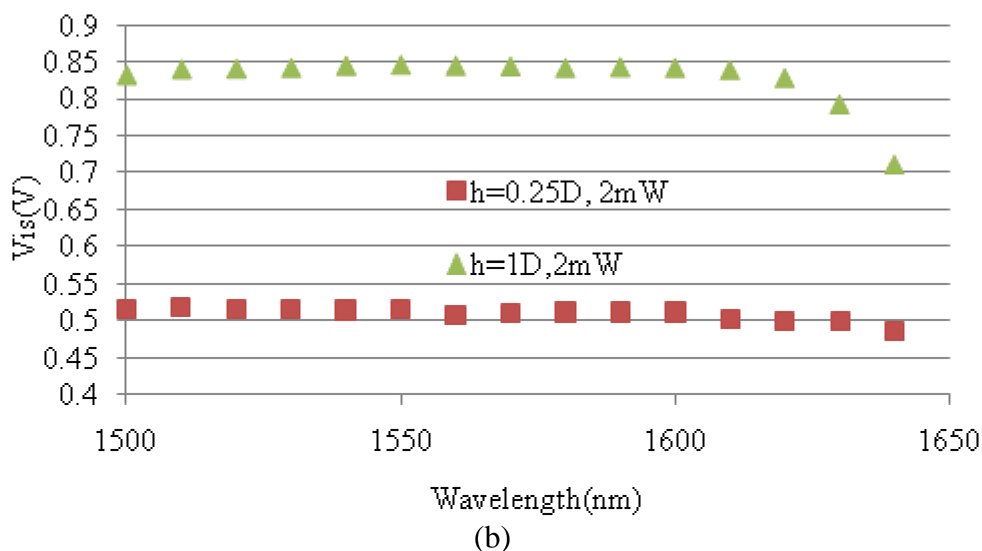

(b)

FIGURE 5-18: *Vis* comparisons. (a) Different power level, (b) different cavity length

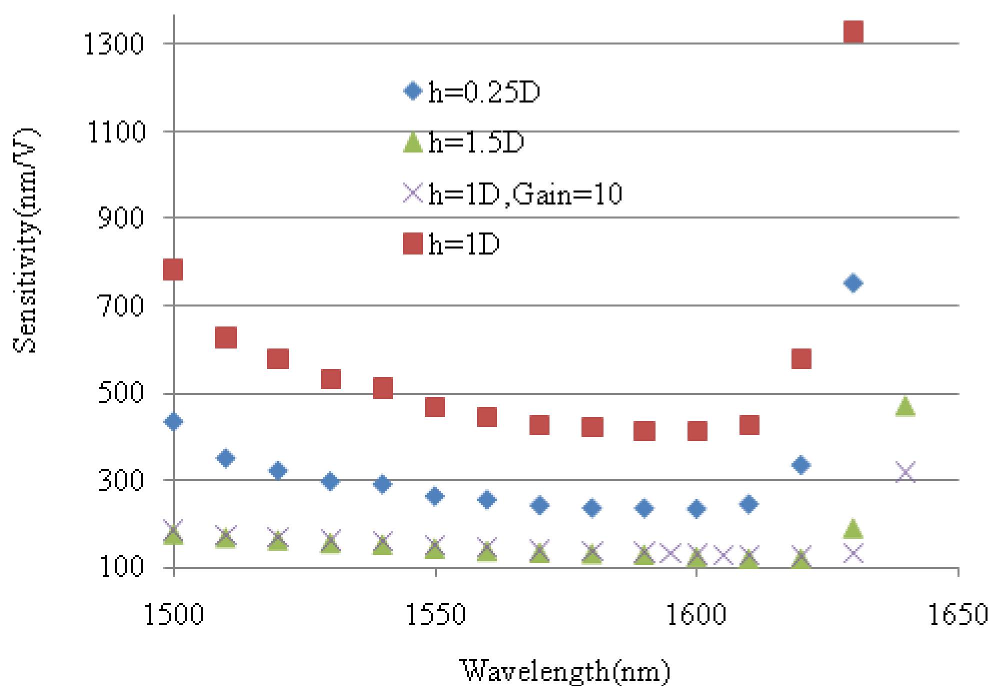

FIGURE 5-19: Sensitivity comparisons with different gain and cavity length

To get best SNR and high performance, the fiber interferometer need to be set up as high laser power, low cavity length to get high Vq, and low noise level. It should be

pointed out that low cavity length reduces the visibility, therefore a compromise need to make to choose a reasonable cavity length. When it reaches the point where the visibility starts to dominate over the noise level and Vq effects, the sensor performance will decrease. High laser power puts a demand on the equipment and usually it is difficult to maintain the stability of the power at high level. It is also apparent that there is a considerable noise contribution at 120 Hz. This commonly corresponds to mains interference from either electrical and/or optical interference. Filtering below 120 Hz will produce a gain of around 10 - 20% for most of the measurement configurations investigated in this study.

5.1.5 Two subsystems

It was desired to implement a multi-channel displacement measuring system from one laser source which is an expensive component in this system. For these to operate independently it is necessary to investigate if there is any crosstalk between the sub-systems. FIGURE 5-20 is a block diagram indicating the major components of a two FB setup. A fiber coupler is used to divide the laser into two equal beams to act as the light sources of the two sub-systems. FP1 is the previous system containing a PZT actuator for cavity sweeping, where the reflecting surface was glued on a stationary block in FP2. At first, we turned off the FP1's PZT, and obtained the power spectrum of FP2 shown in FIGURE 5-21. Then we turned on the FP1's PZT and did the cavity sweep, we measurement the power spectrum of FP2 again. FIGURE 5-22 shows that there were no significant changes appearing in the second power spectrum compared with the first one. Therefore, the two sub-systems were not coupled, and we can use one laser source as the sources for multi-channels system.

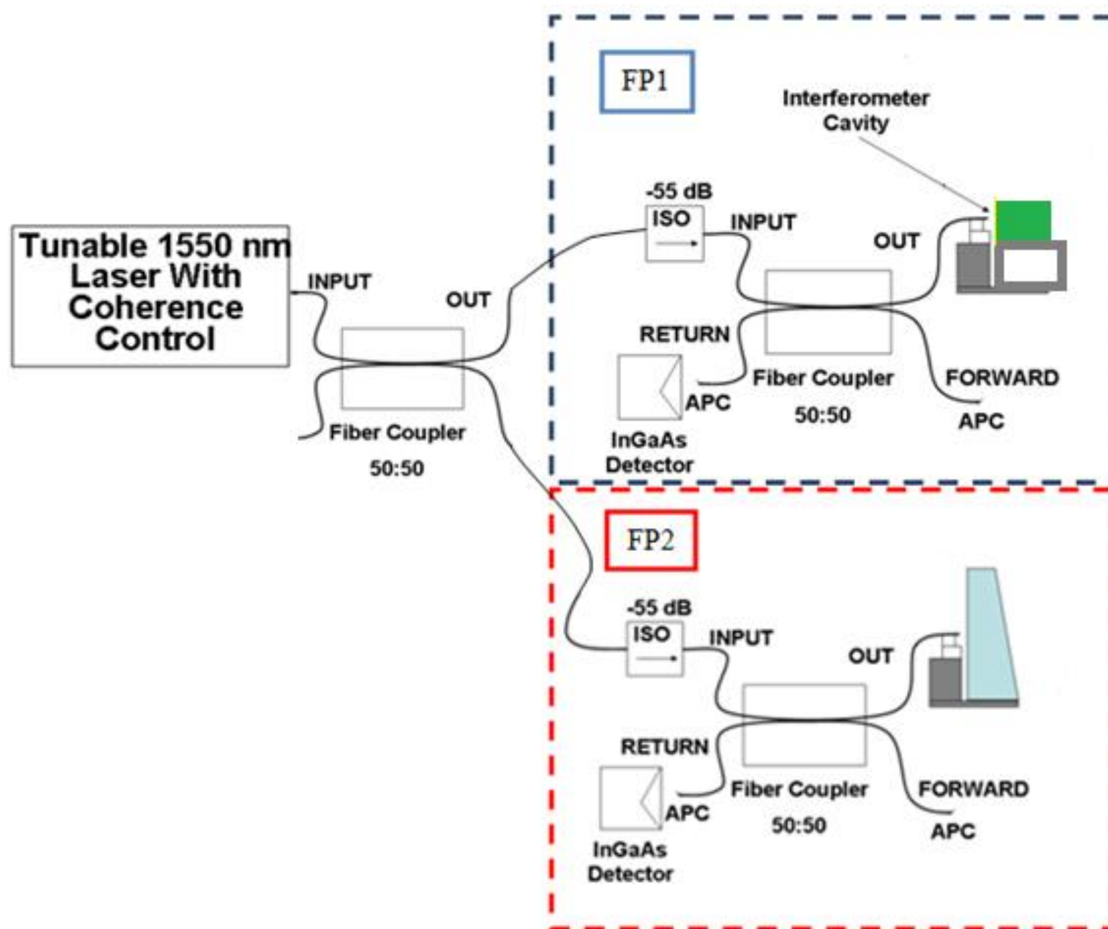

FIGURE 5-20: Schematic for two subsystem setup

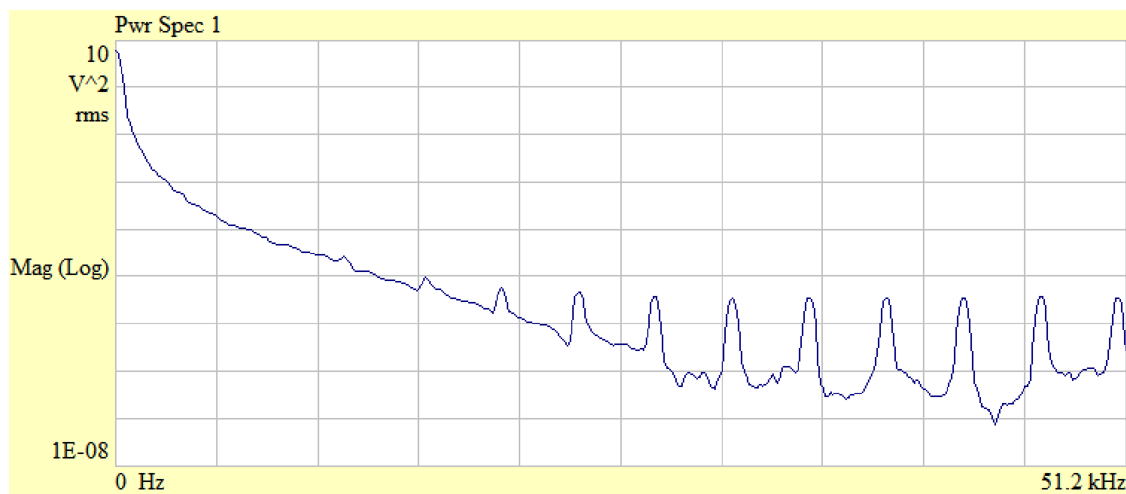

FIGURE 5-21: Power spectrum of FP2 when FP1's PZT is OFF

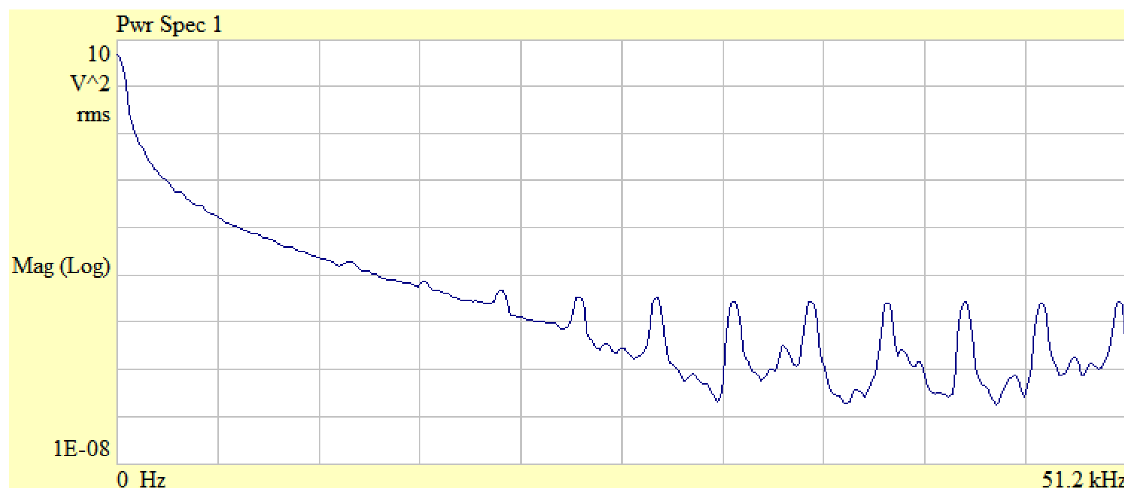

FIGURE 5-22: Power spectrum of FP2 when FP1's PZT is sweeping

5.1.6 Conclusion

In this section, a high resolution measuring system, fiber optic interferometer, was studied and tested in a normal lab environment. Two working modes of the interferometer were presented. The current setup is a low finesse of air-glass interface which gives sub-nanometer resolution at 1 kHz bandwidth with limited working range of a few micrometers. Various parameters were changes to find out the principle underneath determining the performance of the interferometer, i.e. power, cavity length, detector, wavelength. In addition, a two subsystem was developed and tested to verify the possibility of multi-channel measurements using a single laser source while reducing the system cost.

5.2 Optical fiber displacement sensor[45]

5.2.1 Introduction

Light emitting diode (LED) and laser diode (LD) illumination sources are now produced in large volumes oat economical prices. One configuration measures the intensity of the light as a direct function of the displacement of the knife edge across a

focal spot, hereafter referred to as a direct knife-edge method [58]. With this latter method and utilizing lock-in measurements of a modulated knife-edge, Puppin has reported 15 pm resolution over three micrometers with a relatively low bandwidth of less than 1 Hz.

Based on this idea, studies were carried out on two compact optical sensor setups. In one of the sensor implementations, a fiber is used as the micrometer sized illumination source. For comparison, the second implementation uses the collimated beam from a photo-interrupter and this has been assessed using the same experimental set up. A major benefit of the knife edge is its relatively low mass. For designs in which the edge can be obtained from the mechanism itself this will add no mass to the moving component of the mechanism. Additionally, precisely manufactured knife edges will be insensitive to motions collinear with the edge thereby enabling two (and three in some implementations) axis sensing. The sensors provide a working range of a few micrometers to millimeters with SNR greater than 10^4 at MHz bandwidth. This was demonstrated in a measurement of tuning fork oscillation. As such they are capable of providing nanometer resolution, high linearity and repeatability.

5.2.2 Principle of operation

Both optical displacement sensors in this study revolve around measurement of the intensity of a light beam as a function of position of an obstruction (knife edge) placed in the optical path. Theoretically, the noise limited resolution of the detector can be related directly to the displacement sensor sensitivity. Mathematically this can be expressed as

$$dx = G_{x/v}\sqrt{\frac{\int_{f_1}^{f_2} S(f)df}{P_s^2}} \qquad (5.5)$$

In equation (5.5), $S(f)$ [V^2 Hz^{-1}] is the power spectral density of the voltage signal from the sensor for zero optical power incident i.e. it is assumed that the dark current noise is dominant on the detector, P_s is the maximum optical power at the detector [W] and $G_{x/v}$ is the sensitivity of the sensor [m ·V^{-1}]. For a constant power spectral density S_o, equation (5.5) can be written as

$$dx = G_{x/v}\frac{\sqrt{S_o}}{P_s}\sqrt{BW} = G_{x/v}\frac{NEP}{P_s}\sqrt{BW} \qquad (5.6)$$

Where BW is the sensor bandwidth [Hz] and NEP is the rms voltage measured as an equivalent rms optical power incident on the detector [W]. In practice, NEP is depended on the photodiode noise which is the sum of thermal noise i_j of the shunt resistance and the shot noise i_d and i_{ph} resulting from the dark current and the photocurrent. The typical value of NEP for the photodiode we used is $1.5 \cdot 10^{-14}$ W·$Hz^{-1/2}$ at 20V bias (650nm). More noise analysis will be presented at section 5.2.4.

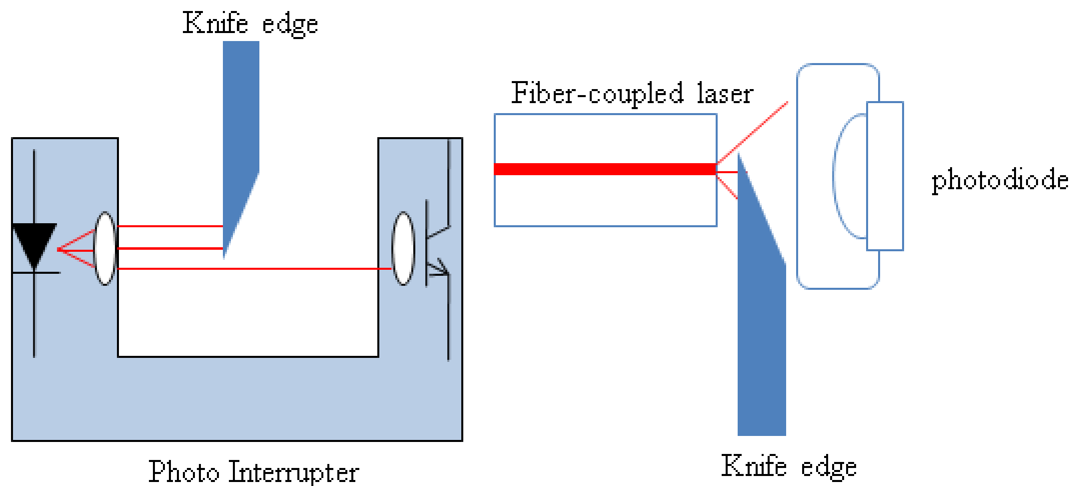

FIGURE 5-23: Schematic diagrams indicating measuring principle of the knife edge sensor. Left: Photo-interrupter source and detector, Right: Fiber based source and detector

FIGURE 5-23 left shows a configuration of a common photo interrupter. A photo interrupter is composed of an infrared emitter on one side and a shielded infrared detector on the other. Two small lenses are installed in front of them to collimate the beam from the source and collect the light at the detector. By emitting a beam of infrared light from one side to the other, the detector can generate a signal when an object passes through and blocks the beam. A normal knife edge is fixed in a moving object whose position is to be measured. When the edge moves up and down, it cuts through the beam and therefore, the detector produces a current that varies with the displacement of the motion of the knife edge. Since the beam is collimated, the location of the knife edge along the axis of the beam i.e. in the horizontal direction as drawn has little effect on the sensitivity. The sensing range is usually between 100 μm to 500 μm for commonly available commercial products.

Based on the photo interrupter, a more precise and flexible configuration was developed by using a laser coupled fiber as the emitter and a photodiode as the detector. In this configuration as shown in the right of FIGURE 5-23, the fiber becomes the illumination source and also conditions the beam from the laser or LD source. Laser diodes occupy volumes of only a fraction of a millimeter with the wire bonds being a substantial fraction of this volume. Additionally, given that fibers can be directly couple to the diode (known as butt coupling) it is feasible to produce the illumination source and detector in a compact assembly while a short full width at half maximum (FWHM) can be achieved from the fiber with a few micrometer diameter. There are a number of

attributes with this design, these being: i) the range of measurable displacement can be varied by changing the separation between the knife edge and the end of the fiber, ii) when the edge is close to the fiber and the diameter of the fiber is a few micrometers, resolution of nanometer with bandwidths of kilohertz are readily obtained, iii) The edge can be small, therefore it adds only a small mass to the object being measured, iv) no electrical connection are necessary for the moving component (knife edge) of this sensor, v) high bandwidth and fast response photodiodes are capable of hundreds of MHz bandwidth which is very useful for feedback control in high speed scanners, vi) the whole setup is compact and low cost.

This technique also has some drawbacks that are expressed as, i) the requirement for straightness of the knife edge to ensure independence from motion collinear to the edge, ii) the knife edge must remain at a fixed location along beam axis to maintain a constant sensitivity. This latter disadvantage might be overcome by collimating the laser at the expense of an additional lens.

5.2.3 Experimental measurement

Experiments were set up to test the performances of both sensor implementations. FIGURE 5-24 (a) shows a block of diagram indicating the components used in the laser-photodiode experiment and is referred as Type A configuration (denoted as Type A). A LD driver supplied by Thorlabs Inc. was employed to drive the LD which is, in turn, directly coupled with a fiber, a product of FiberMax (FMXL635-005-XXXB). For the facility of setup, the end of the fiber was fixed onto a *XY* scanner (InsituTec IT-XY-100) having a range of 100 μm in each axis. One end of a honed blade is glued on a manual micrometer stage to adjust the blade edge in x and y direction. A PIN photodiode

(FDS100 Thorlabs Inc.) operated in a biased mode (15 V) was used to measure the intensity of the laser via a basic circuit with an LF411N operational amplifier configured for transconductance with a selected feedback resistance value to provide a constant output voltage range corresponding the intensity of the LD i.e. inversely proportionate to LD power. Data acquisition system was built based on an NI LabVIEW Real-Time^{TM} system. Firstly turn on the laser, and tune the laser power to the required level. Adjust the feedback resistor in the circuit therefore the output of the amplifier will give an output close to 10V to saturate the analog to digital converter (ADC). Record that value as V_{full}, and then use a micrometer stage to let the knife edge approach the fiber in x direction until the output reaches half of V_{full}. After that, adjust the knife edge in y direction until it almost touch the fiber end, record the position as h. Finally position the XY scanner in x direction, record the position and the photodiode output and post-process the data. The h and power are varied afterwards and data are record respectively. FIGURE 5-24 (b) shows the similar setup for photo Interrupter experiment (denoted as Type B). The measurement circuit for the photo interrupter contains AMP02 operational amplifier works as a differential amplifier to offset the output from the detector. The gain is set to 51 to get a full +/- 10 V to saturate the ADC.

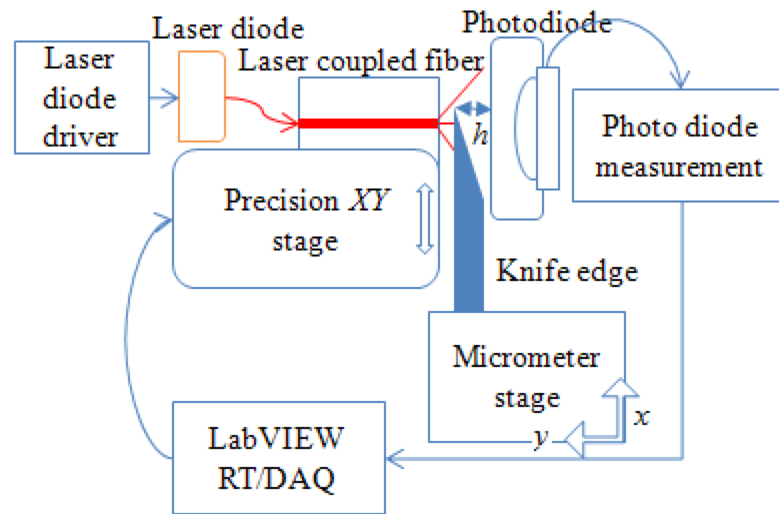

(a)

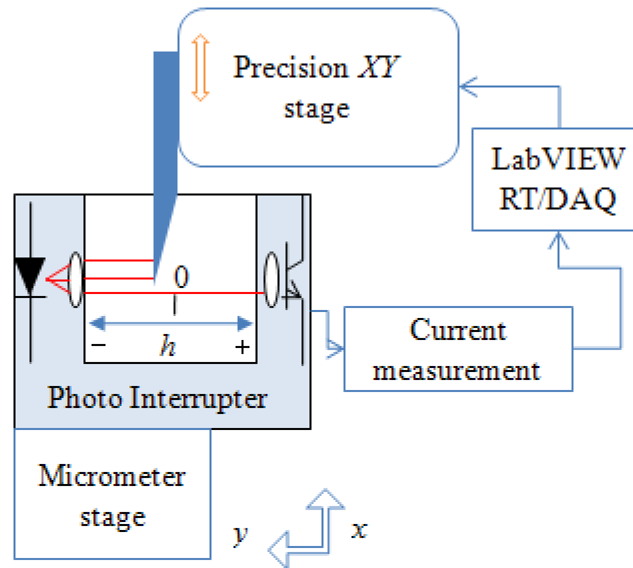

(b)

FIGURE 5-24: Block diagram of experimental configuration for the sensor tests. (a) Set up of LD and photodiode based knife edge sensor, (b) Set up of photo interrupter based knife edge sensor.

An experimental evaluation of the output characteristics of both types of sensor has been undertaken. For the Type A it is necessary to measure the sensor output at different spacing between blade edge and the fiber. To avoid problems with backlash of our knife edge positioning system, in these experiments it was necessary to measure the distance

from the detector, h varying from 0 mm to 3.1 mm, the latter value corresponding to the knife edge being as near to contact with the end of the fiber ferrule as was possible using the micrometer. Measurements of sensitivity and noise of this sensor were carried out at different settings of the laser power. Five levels of power at 1, 1.5, 2, 2.5 and 3mW were tested. Sampling of the sensor output voltage was obtained at a rate of 100,000 samples per second and 1,000 for measurements of noise and tracking of motion respectively. To measure the output from the sensors as a function of position of the knife edge relative to the sensor, a sinusoidal displacement x of 40 μm amplitudes were used at a frequency of 0.1 Hz (Type A) and 1 Hz (Type B). For the Type B sensor, although the beam is, in principle, collimated, data at three locations along the y axis were recorded where $h = 0$ mm corresponded to the knife edge being centrally located between source and detector along the y axis.

5.2.4 Results

5.2.4.1 Stability

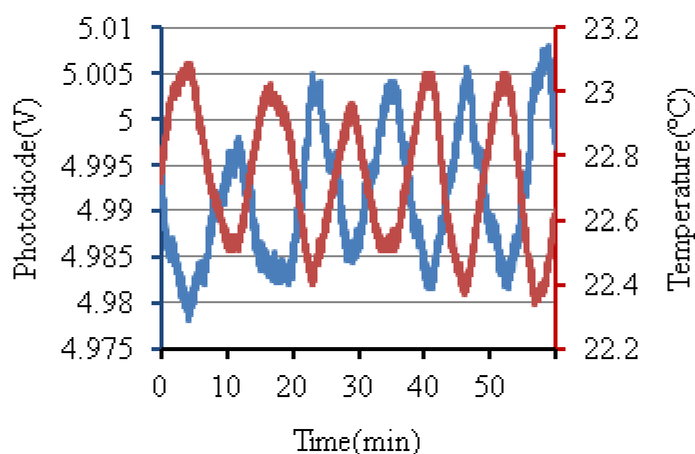

FIGURE 5-25: Stability tests of the measurement process for Type A sensor.

FIGURE 5-25 shows the output of Type A sensor data over a time period of one hour during a time when the room temperature control was cycling approximately ± 0.5 °C.

The experiment is set up as the knife edge sat approximately at the center of the fiber where it covered half the intensity (about 5 V at the output) corresponding to the photodiode reading half the maximum value. It contains a noise of about 10 mVpp value. The temperature of the lab recorded simultaneously shows a temperature drift which is a negatively correlated to the drift of the sensor within the experimental setup. The drift is likely comes from photometric system or the thermal expansion of the devices in the metrology loop, i.e. photodiode mount or knife mount. Since the stability significantly limits the performance of the long-term measurement in changing temperature environment, a more stable environmental temperature control and better detector and circuit design with less thermal drift is required.

5.2.4.2 Characteristic

FIGURE 5-26 show the output of the photodiode and sensitivity versus displacement of the knife edge in the x axis (see FIGURE 5-24 (a) corresponding to different fiber to knife edge separation h at a laser power of 3mW. From this figure the intensity looks Gaussian along x axis which is the scanning direction with the sensitivity increasing as the blade approaches the fiber. It reaches to a maximum of 0.66 $V \cdot \mu m^{-1}$ where the blade almost touches the fiber (at $h = 3.1$ mm) and 0.02 $V \cdot \mu m^{-1}$ (at $h = 0$ mm) where the blade is closest to the detector. The core diameter of the fiber is 3-4 μm and the jacket is 900 μm. The reason for this is the Gaussian profile of the beam. Closest to the detector the beam is expanded and the detector is detecting the expanded portion of the beam.

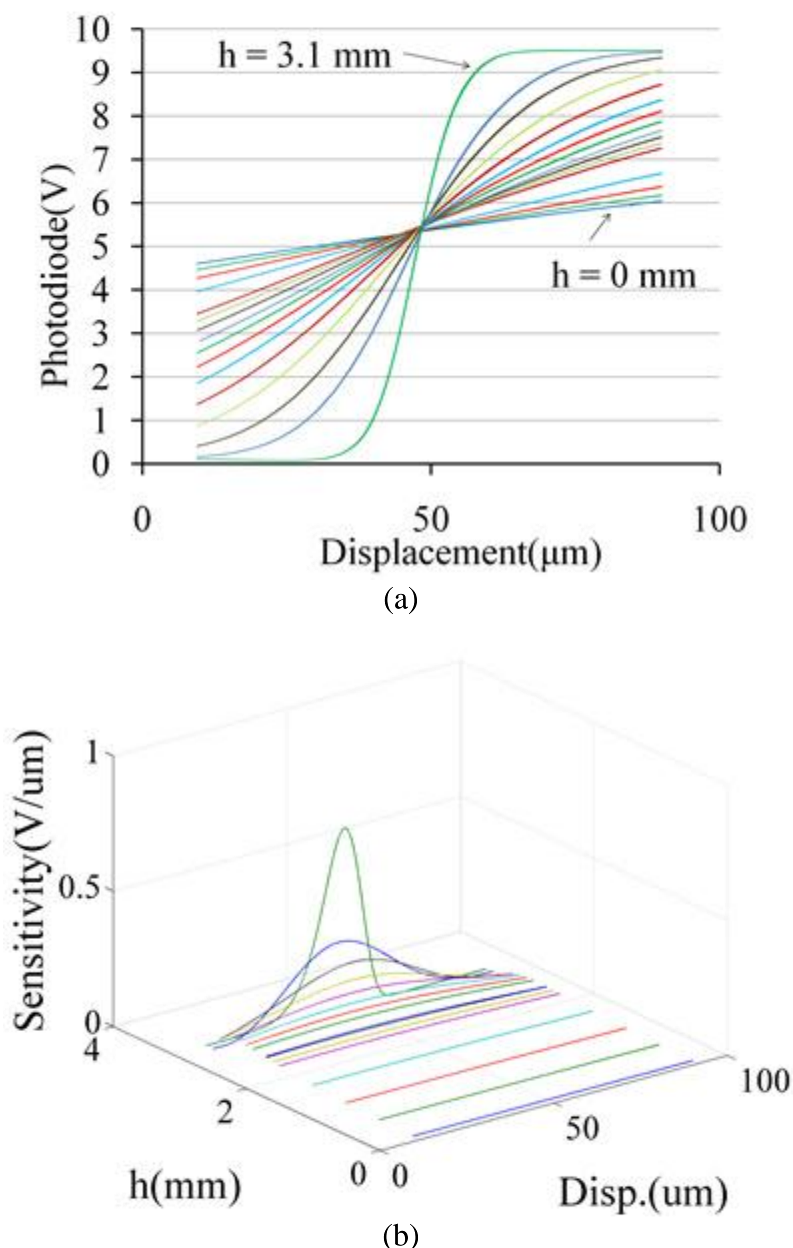

FIGURE 5-26: Performance of the Type A, laser diode based, displacement sensor. (a) The output of the photodiode versus displacement of the knife edge in the x axis corresponding to different fiber to knife edge separation h at a laser power of 3 mW, (b) the sensitivity of the photodiode versus displacement to different values of h at a laser power of 3 mW.

Results of other laser power levels from 1 mW to 2.5 mW show similar characteristics. FIGURE 5-26 (b) is a plot of sensitivity with x for different separations h between the knife edge and fiber. It is reasonable to define the working range of the

sensor at certain threshold values of sensitivity to provide an acceptable resolution. In this analysis, the range is defined by the translation in which the sensitivity remains within 10% of the peak value.

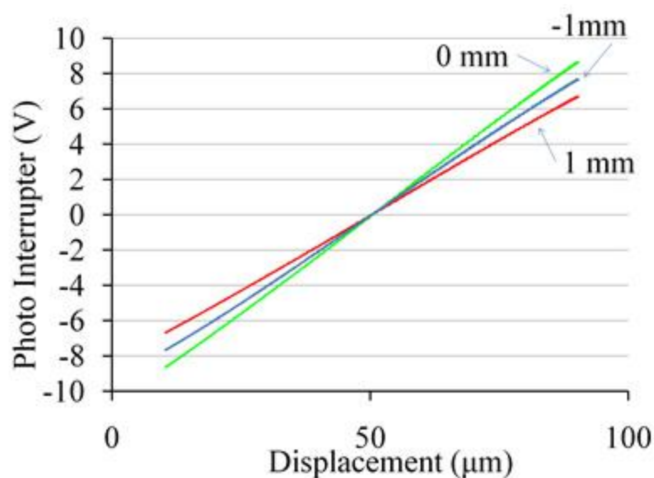

(a)

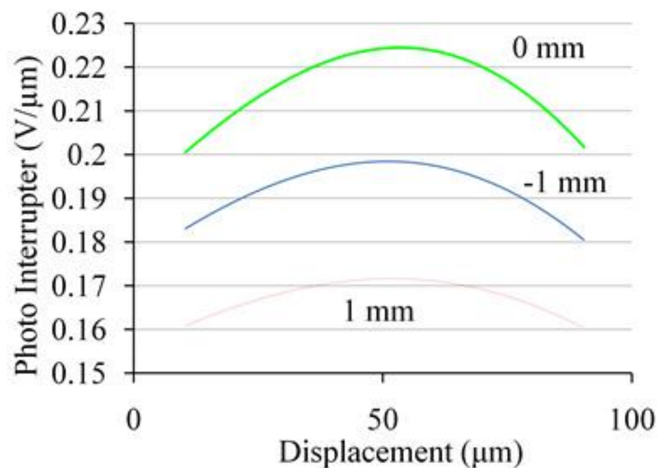

(b)

FIGURE 5-27: Performance of the Type B, photo interrupter based, displacement sensor. (a) The output of the photo interrupter versus displacement of the knife edge in the x axis corresponding to different fiber to knife edge separation h, (b) the sensitivity of the photo interrupter versus displacement to different values of h.

FIGURE 5-27 (a), (b) are respectively the output of the photo interrupter and its sensitivity versus displacement along x axis at different values of h (see FIGURE 5-24 (b). The emitter is collimated by a lens mounded into its mount. In principle, the

sensitivity to motion of the blade in direction x are supposed to be constant across the full 3.4 mm gap between emitter and detector of the interrupter (i.e. for different locations of h). However, this is not the situation due to the non-uniform intensity across the beam cross-section which gives corresponding different sensitivity. The sensitivity reaches its maximum value at the center between the emitter and detector, while it drops when the blade is located on either side of this position. Nevertheless, the sensitivity reaches a maximum of 0.2 $V \cdot \mu m^{-1}$ and much more linear than the behavior of Type A.

5.2.4.3 Error analysis

The noise sources come from the photodiode circuit, environmental temperature and vibration, stability of the laser, blade edge roughness, and reflection from the surface of the blade disturbing the stability of the laser.

Improper alignment of the fiber knife edge and detector will leads to coupling problems for multi-axis applications. It also reduces the intensity coming to the detector therefore causing a decrease of the SNR.

The ambient light adds a certain amount noise to the detector. This can be avoid by covering the whole set up with an opaque box or turning off the external light sources or using a band pass filter to filter out the light whose frequencies are not within the laser's. In our test, we adapted the first two methods to limit the effect of ambient light.

Temperature change will affect the knife edge's length which mimics the sensor output. The Thermal Expansion Coefficient of the steel (knife edge) is 11 x 10^{-6} C^{-1}, l = 0.005 m, with a temperature variations typically within 0.1 °C, the systematic thermal error is about 5 nm. We prepared another block target using a silica slice with a straight

line coated with aluminum. This will lower the thermal expansion to below 1 nm at the same conditions.

Laser stability is another concern here since the light reflect back from the razor surface back into the fiber and the optical destabilization feedback may disturb the laser generation mechanism although there is a feedback control for the diode current. By splitting a laser through an isolator and a fiber-coupler, and using one channel as a reference, the other as a measurement head, the isolator is able to attenuate the light coming back, and the instability of laser power can be solved by differential method.

Calibration error mainly comes from the calibration source. We used the XY positioner to calibrate the knife edge sensor. The linearity of the positioner is about 0.01% which corresponds to a 10 nm error at maximum position. Surface roughness of the edge will also cause deviations at the detector when the knife sensor is used in more than one axis.

The photometric system noise is one main error source limiting the resolution. It is studied in the following section.

The total noise current of the photometric system includes thermal noise i_j of the shunt resistance R_{sh}, the shot noise i_d and i_{ph} resulting from the dark current and the photocurrent, thermal noise current from the feedback resistor R_f, and amplifier noise current as expressed in equation (5.7) [59].

$$i_{n_total} = \sqrt{\frac{4kT}{R_{sh}} + 2q\left(I_D + I_{PH}\right) + \frac{4kT}{R_f} + i_{amp}^2 + \left(V_{amp} 2\pi C\right)^2 B} \qquad (5.7)$$

Where

B = Noise bandwidth

k = Boltzmann's constant, 1.38×10^{-23} (J K^{-1})

T = Temperature (K)

$q = 1.6\times10^{-19}$ (C)

I_D = Drak Current (A)

I_{PH} = Photocurrent (A)

i_{amp} = Amplifier input leakage current (A)

V_{amp} = Amplifier input noise voltage (V)

C = Amplifier input capacitance (F)

For the photodiode used in the circuit, the NEP @650 nm is $1.5\cdot10^{-14}$ W·Hz$^{-1/2}$ (35 MHz @20 V bias). The first two terms in equation (5.7) can be derived from NEP as $4.5\cdot10^{-29}$ A^2 Hz^{-1}. The feedback resistor R_f is several kilo Ohm giving a value of around 10^{-29} A^2 Hz^{-1} for the third term. The LF411N amplifier has 0.01 pA·Hz$^{-1/2}$ input noise current giving an estimated 10^{-28} A^2 Hz^{-1} for the fourth term. The total noise current is 0.0124 pA·Hz$^{-1/2}$ which corresponds to a noise level at an order of several μV·Hz$^{-1/2}$ given the input impedance is order of 10^8 Ohm.

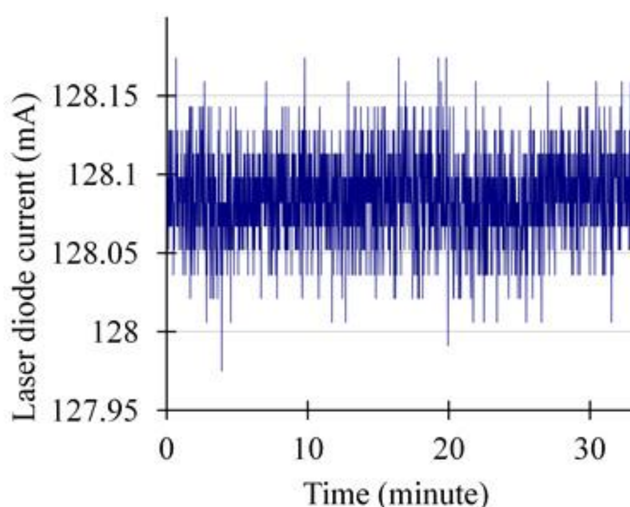

FIGURE 5-28: Laser diode driver supply current stability measurement.

The LD driver circuit has a stability of less than 0.01% and output level of 0.1 μA

rms where the output current is up to 250 mA. Current stability test with 3mW laser power in FIGURE 5-28 shows an rms noise of 28 μA which is at the limit of the measurement (9 μA quantization noise from the 16 bits ADC) and corresponds to a stability of better than 0.02% at a bandwidth of 100 kHz. To assess the displacement resolution of the sensor, the noise levels were measured with the XY scanner turned off and this measurement repeated with the XY scanner activate and maintained at a set point value $x = 50$ μm under closed loop control. This set point value corresponded to the knife edge being positioned at the maximum sensitivity location of the sensor. The noise level of former was consistently about 70% of the latter measurement independent of the LD power. The additional noise contribution is believed to come from the positioning controller error and therefore is mechanical.

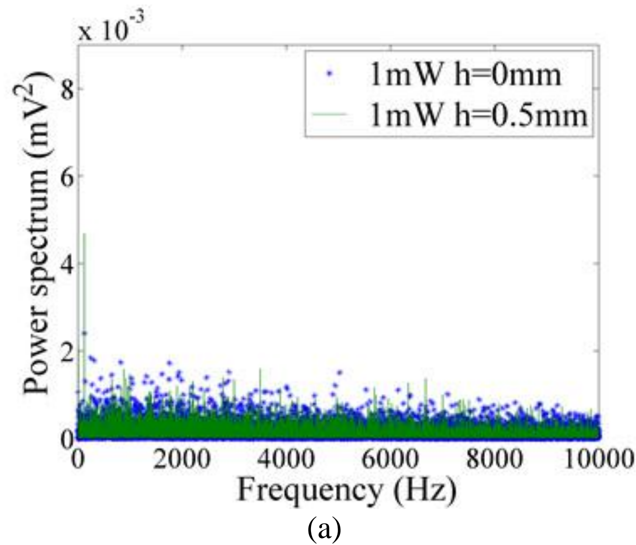

(a)

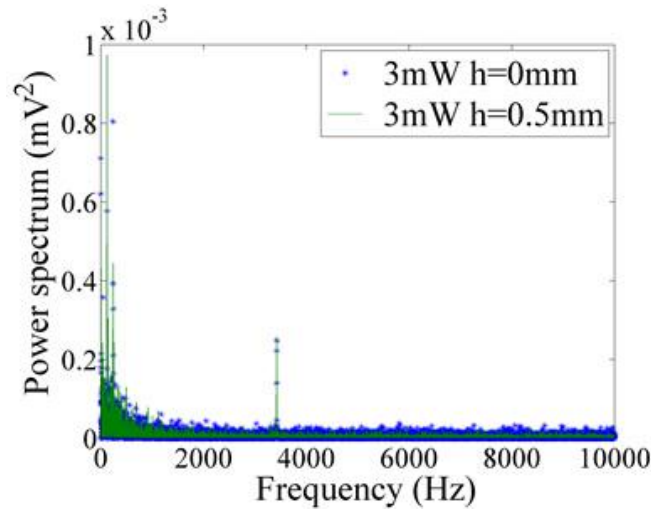

(b)

FIGURE 5-29: Noise level of the Type A sensor photodiode detector at different values of h. (a) Power spectrums of noise when the laser power is 1mW, (b) power spectrums of noise when the laser power is 3mW. Note that the range of the vertical scales (9 mV^2 at 1 mW and 1 mV^2 at 3 mW laser power) in proportion to the inverse square of the laser power.

Noise data was collected when the distance h between the blade and fiber varies while the power level is maintained at a constant value ranging from 1 mW to 3 mW. Power spectrum measurements in FIGURE 5-29 (a), (b) (note: the figures are plot linearly or logarithmically depending on which one is better presenting the information) show similar distribution and magnitude over a measured bandwidth of 10 kHz for different values of h. The results show that the noise level does not change significantly with h. However, the noise spectrum values for a 3 mW source are about 1/3 to that measured with a 1 mW source consistent with the detector noise model of equation (5.6). A 120 Hz and 240 Hz components were observed in the 3mW power spectrum which likely come from harmonic disturbance from the AC power lines (120 V at 60 Hz).

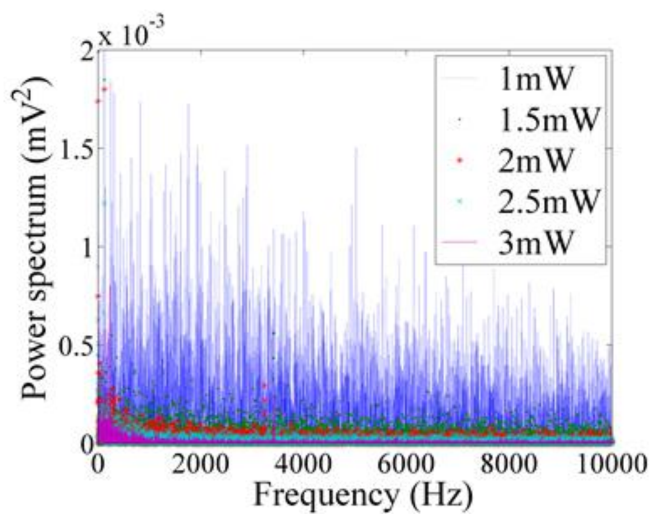

(a)

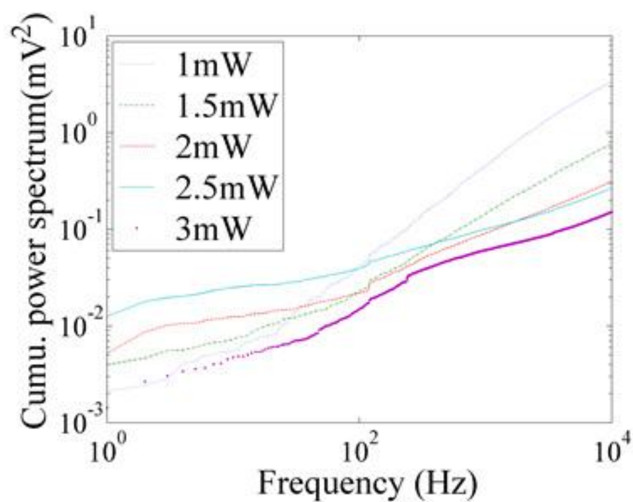

(b)

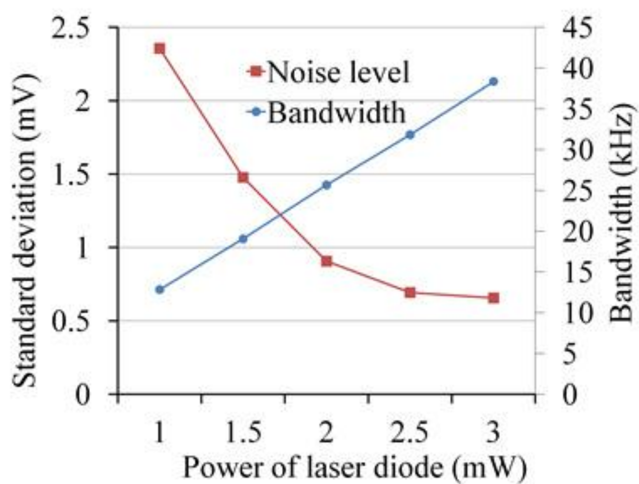

(c)

FIGURE 5-30: Noise level of the photodiode when the laser power varies. (a) Power spectrums of noise with different laser powers, (b) cumulative power spectrums of noise

with different laser powers, (c) standard deviations of the noise and preamplifier cut-off frequencies with laser power.

To determine noise of the measurement system, similar measurements have been obtained with the translational stage maintained under closed loop control at a constant value of $x = 50$ μm where the sensitivity of the sensor is at its peak. FIGURE 5-30 (a) is the power spectrum of noise when laser is controlled at different power levels. It shows that the lower the power level, the higher of the noise level, a result again correlating with the inverse relationship between amplifier gain and laser power. This is more remarkable at frequencies higher than 100 Hz. It can be observed that the noise distribution exhibits a 1/f characteristic below about 1 kHz. FIGURE 5-30 (b) shows the cumulative power spectrum of noise as the laser power varies. Noise density is about 7.45 $\mu V \cdot Hz^{-1/2}$ at 1mW laser power and 2.08 $\mu V \cdot Hz^{-1/2}$ at 3mW which would correspond respectively to an rms noise of around 0.668 mV and 0.245 mV at a bandwidth of 1 kHz. With the sensitivity (at maximum point or $x = 50$ μm) of $0.664 V \cdot \mu m^{-1}$ at 3mW power level and $h = 3.1$ mm, the displacement noise corresponds to around 0.37 nm, again at a bandwidth of 1 kHz. A higher illumination power level not only produces lower noise, but also enables a higher cut off frequency due to a lower gain in the photodiode circuit, see FIGURE 5-30 (c). The SNR is about 40,000 for 3mW and is 15,000 for 1mW at 1 kHz bandwidth. Ignoring the 1/f at lower frequencies, the SNR will be higher.

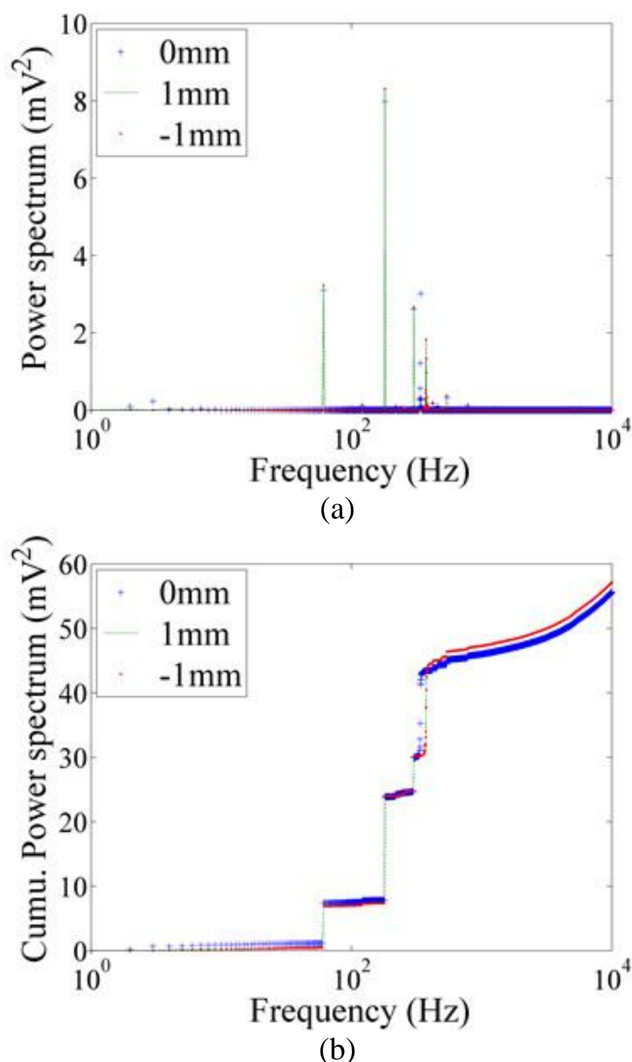

FIGURE 5-31: Noise level of the photo interrupter at different values of h. (a) Power spectrum of noise, (b) cumulative power spectrum of the noise.

Photo interrupter noise level data has been collected while the location of the blade along the optical axis (y axis) varies. As shown in FIGURE 5-31, the power spectrum with the knife edge at different locations is little changed. A considerably larger 60 Hz AC power frequency and its harmonics appear in the spectrum (60 Hz, 180 Hz, and 300 Hz). This corresponds to about 60-70% of the total noise power. The noise density is about 74.1 $\mu V \cdot Hz^{-1/2}$ which would give an rms noise of around 7.4 mV corresponding to 37 nm with a sensitivity of 0.2 $V \cdot \mu m^{-1}$ at a bandwidth of 10 kHz and SNR of around

2,700. In the absence of this 60 Hz spike, the cumulative power spectrum will drop down to around 9 mV^2 and the rms noise will be in the region of 3 mV corresponding to an rms displacement noise of 14 nm and a corresponding SNR of better than 8,000. The AC spike may come from unfiltered power used as a reference voltage and unshielded electrics.

5.2.5 Conclusion

This novel sensor based on the principle of photo interrupter and knife edge does not required complex signal conditioning circuit while maintaining a high SNR at reasonable bandwidth. The relatively small number of components and the fact that all can be made using microelectronic processing technology makes it possible to produce a measurement system having a small footprint. Its low cost, low mass and compact size features are desirable attributes for a non-intrusive, precision displacement sensor. Sensitivity goes up and the noise density remained relatively constant under the conditions of constant optical power level, reduced separation between the knife edge and source. In these measurements, it has been demonstrated that nanometer resolution in displacement measurement can be relatively easily obtained by placing knife edge close to the fiber having a core diameter of around 4 micrometers. Further study is necessary to investigate how the quality of blade edge influences the performance.

CHAPTER 6: PROBES

Two probes were employed in the SMPM using confocal scanning optical microscopy and a mechanical stylus. The confocal microscopy can dramatically improve the resolving power of the far-field optical microscopy which is limited by the fundamental physical diffraction limit. The typical spatial resolution is around tens t around a hundred nanometers, while the localized precision of the observed object can be down to a nanometer or less using various methods such as center-of-mass or de-convolution. Confocal methods still suffer from the diffraction limit representing a bottleneck to imaging nano-scale structures or objects. However, it provides a rapid, real-time, three dimensional localization of individual object at nanometer precision, i.e. single molecules, single fluorophores and quantum dots. For the mechanical stylus, two sensing methods, a tuning fork with an etched optical fiber glued on the end of one arm of the fork and a capacitance based probe were tested as an AFM like probe to measure the topography of the sample.

6.1 Optical probe

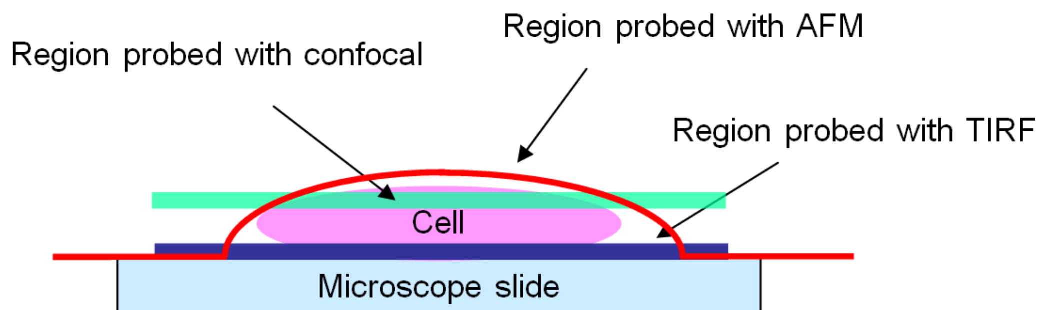

FIGURE 6-1: Schematic diagram indicating the regions probed by various optical techniques.

FIGURE 6-1 shows a schematic of a single live cell attached to a microscope cover slide. It also shows the regions probed by the three most common experimental imaging tools, namely, total internal reflection fluorescence microscopy (TIRF), atomic force microscopy, and confocal (fluorescence) microscopy. The SMPM design allows combination of mechanical and any of all three of these optical methods to be probed simultaneously, thus making it a unique design for biophysical investigations of cells, including the study of cells, cell membranes and the intracellular uptake of proteins and drug-containing nano particles. With this instrument it is possible to section at any given topographic depth below the top surface of the cell, and build a 3D map of the cell.

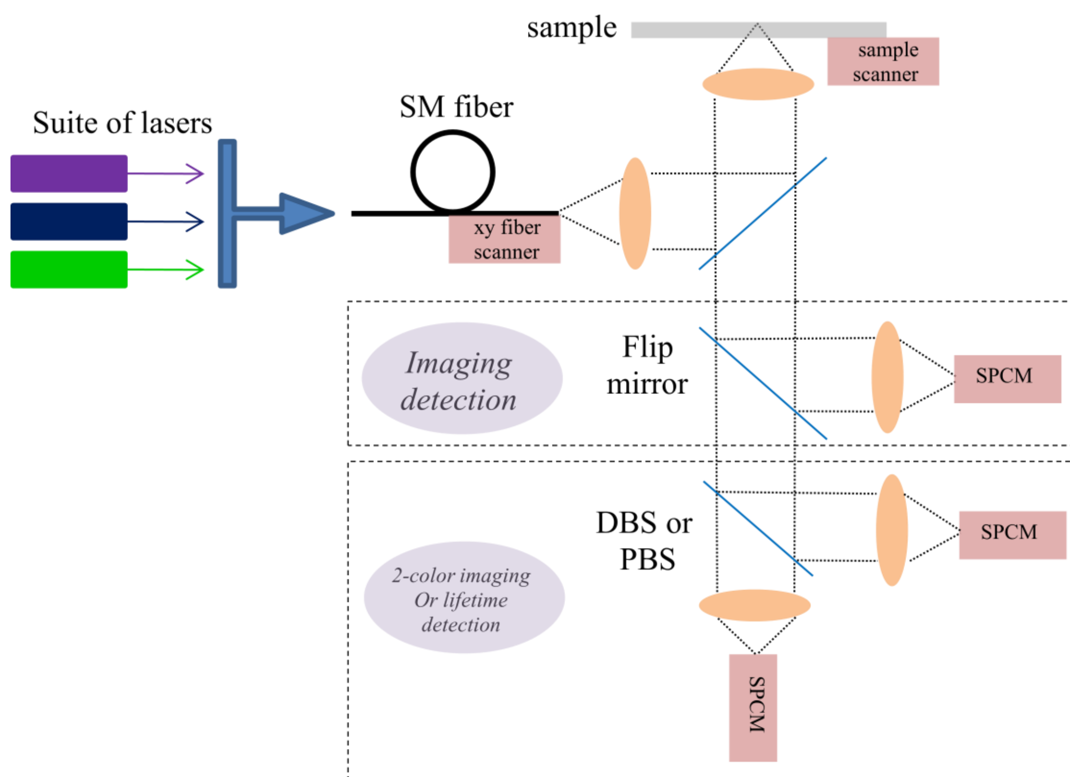

FIGURE 6-2: Schematic diagram of the confocal microscopy system [Courtesy of Dr. Patrick Moyer].

FIGURE 6-2 shows a schematic diagram of the confocal microscope system. The system is divided into four major modules: (1) the suite of excitation sources (air-cooled

argon ion laser, pulsed picosecond 470 nm laser or 532 nm neodymium-doped yttrium aluminum garnet laser), the single mode fiber spatial filter, and the fiber source scanner, (2) the sample holder and sample scanner, (3) the image detection system, Princeton Instruments spectroscopy CCD and (4) the two-color imaging and lifetime detection module. For more details about optical system and components, see [43]. FIGURE 6-3 is the photograph of the experimental setup with the optical components and the mechanical stage.

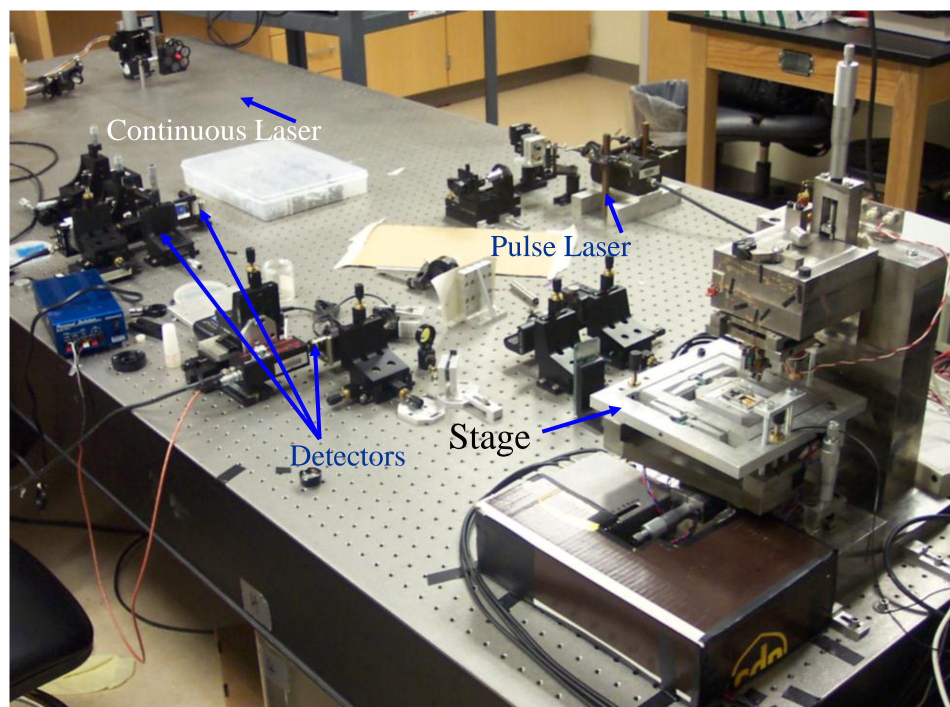

FIGURE 6-3: Experiment setup photograph (Courtesy of Dr. Kevin Elliott [22]).

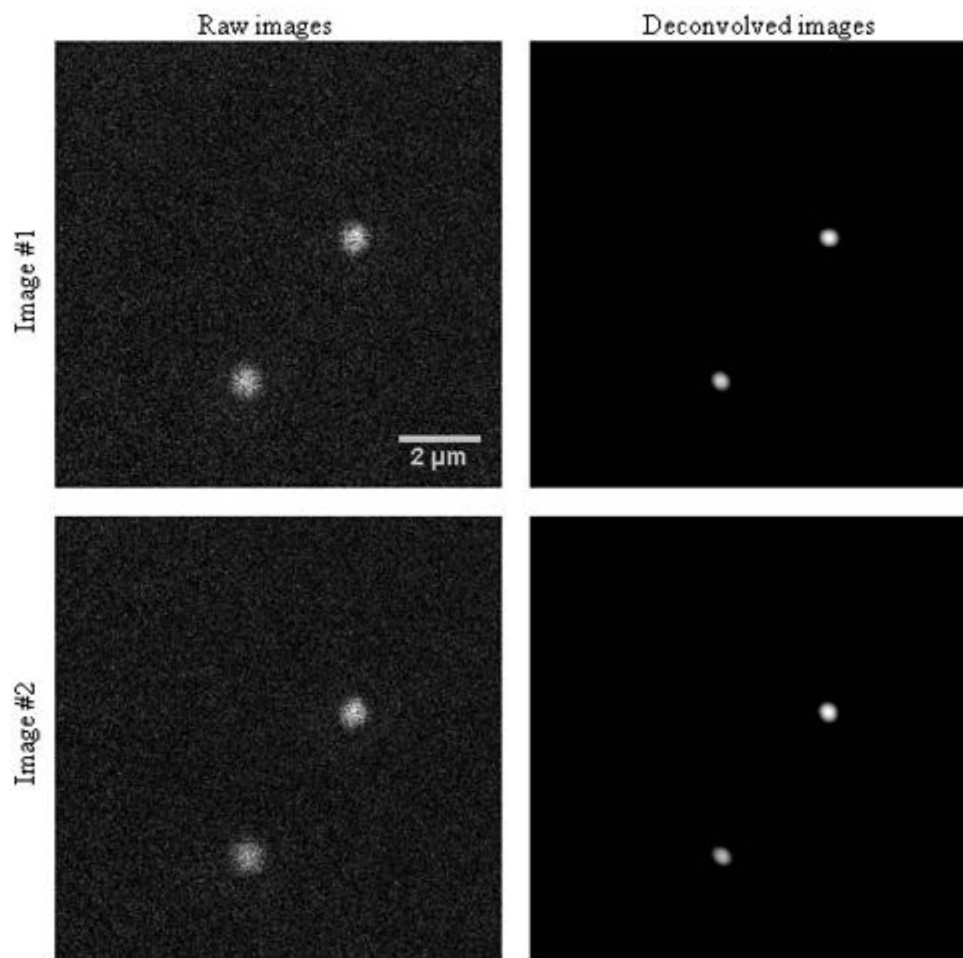

FIGURE 6-4: Sequential single quantum dot images (left panels) with corresponding de-convolved images (right panels). Localization of the two quantum dots is reproduced with 0.41 nm precision in the *x*-direction and 5.83 nm in the *y*-direction.

Single quantum dot localization measurements were performed to evaluate the precision of the mechanical positioning system and optical system. The sample was fabricated by spin coating single quantum dots onto a glass cover slip. The quantum dots used were CdSe/ZnS core-shell Evidots from Evident Technologies and they had an emission peak at 623 nm. FIGURE 6-4 shows two scans and the resultant de-convolutions of those two particular scans. We took five consecutive images and images 1 and 5 are shown. Using the de-convolved images, we located the position each of the quantum dots from the image. For the top right quantum dot, we averaged the positions

from the first two scans and compared them with the average positions of the last two scans. The resultant deviation in the x position is 0.41 nm and the deviation in the y direction is 5.83 nm. These numbers are typical for our measurements of many quantum dot pairs. There is a bit more error in the y direction, which results from the fact that we use a scanning system and that the quantum dots exhibit some blinking during imaging. This blinking can be observed in the raw images, particularly, the bottom quantum dot where the first few lines of the scan appear to indicate that the quantum dot is in a dark state. This result indicates an excellent localization capability for scanning confocal fluorescence imaging of single quantum dots or molecules using deconvolution technique. In the absence of the application of single molecule deconvolution and localization algorithms, our microscope is subject to the normal Rayleigh criteria ($r = 0.61*\lambda$ /N.A.) resolution of roughly 220 nm laterally and 450 nm axially [43].

6.2 Mechanical probes

6.2.1 Tuning fork

One feature of our scanning probe microscope is the integrated mechanical probe for surface topography of biological samples. We have implemented two mechanical probes for the initial study. One is a tuning fork crystal oscillator similar to the ones found in the electronics of a digital clock. These tuning forks have a resonant frequency of 32768 (2^{15}) Hz while in vacuum environment. An etched optical fiber was glued on the end of one arm of the fork as shown in FIGURE 6-5. The optical fiber is shaped through etching to get a sharp radius at the tip. An AC Wheatstone bridge circuit was applied with a lock-in amplifier (SR850, Stanford Research Systems) to measure the output of the tuning fork as a voltage. The RMS value of the output is about several millivolt when the time constant

was set to 1 ms. FIGURE 6-6 shows the tuning fork sensitivity when it touched the surface of an artifact ((VLSI Standards Inc. Model STS3-1800P) at about 45 degree angle. It has high Q and was more sensitivity than the capacitance probe. However, the contact interaction is more complex and less stable than the capactiance probe. The probe shows a hysteresis characteric and the red zoom indicates that, when the probe retracts back, the fiber bends downward as surface attraction (meniscus force) holds on to the tip. Hysteresis observed in these plots is due to the difference between contact and pull-off forces and the relatively large distance reflects the use of low compliance cantilevers. The hysteresis limits the ability for the probe to track the surface height. Because the tracking becomes un-stability when the tracking direction changes it was not possible to obtain repeatable images. More work is neede to address the numerous issues that will affect the ability to use the extreme sensitivity of the probe, i.e. length of the fiber, carrier signal, set point, fiber angle, fiber type, surface preparation, envrionmental condtion, etc…[60, 61] .

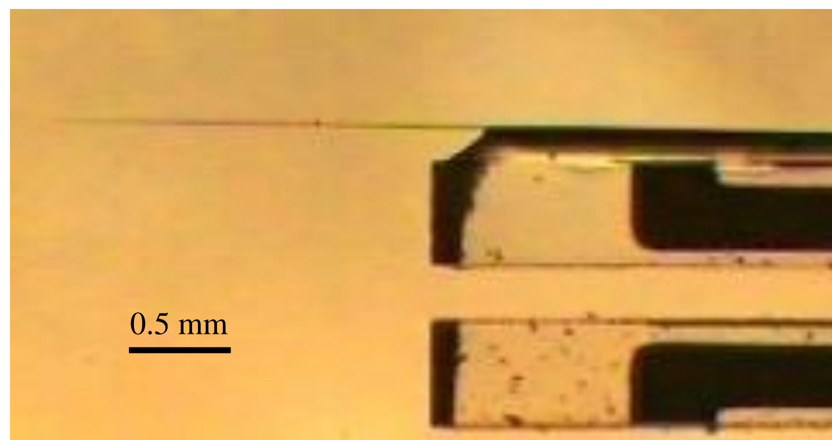

FIGURE 6-5: Photograph of the tuning fork with a fiber attached.

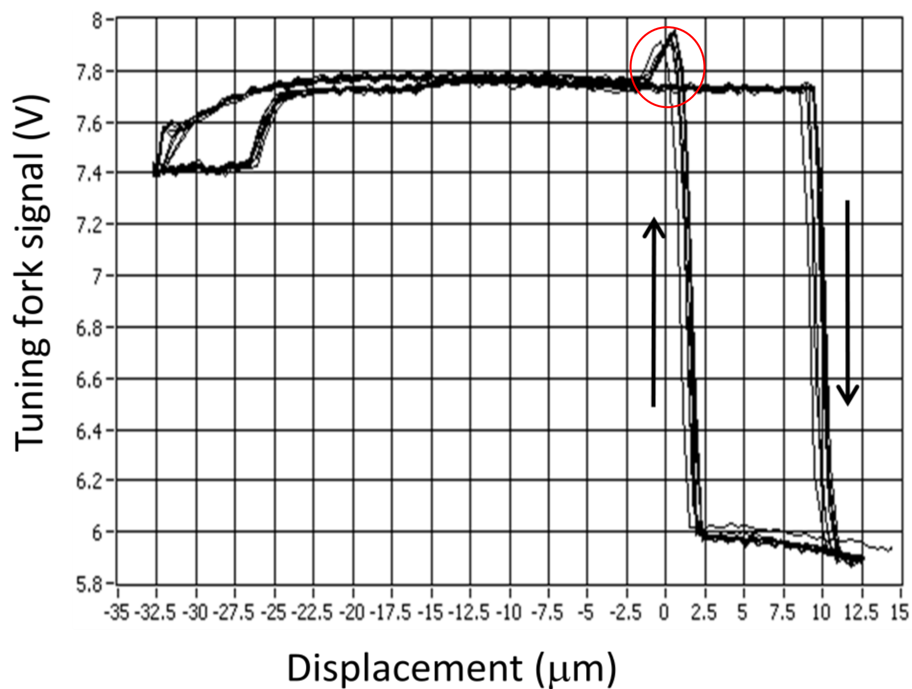

FIGURE 6-6: Characteristic of the tuning fork sensitivity (about 5.0 mV nm^{-1}, the diaplacement at x axis was not calibrated in the figure).

6.2.2 Capacitance probe

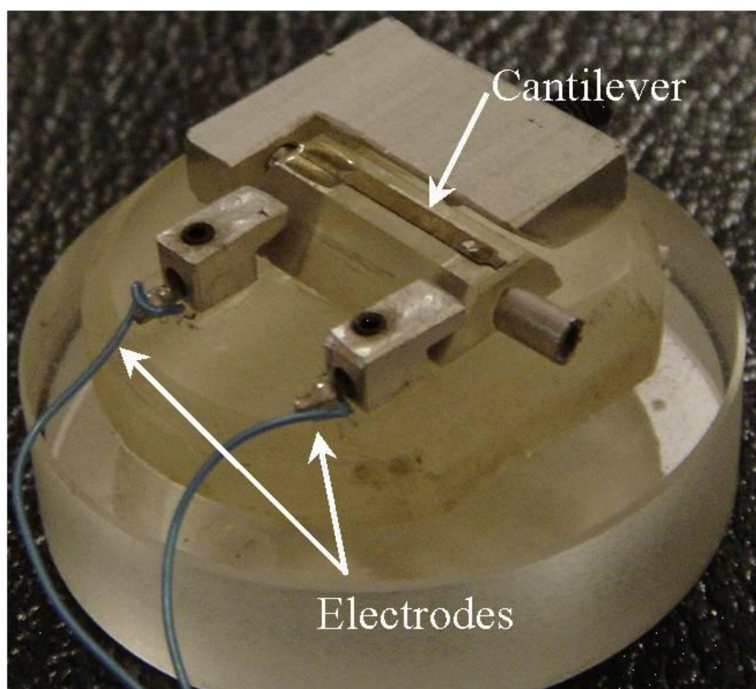

FIGURE 6-7: Photograph of a capacitance probe.

A capacitance base sensor comprising a silica cantilever beam of stiffness 35 N m^{-1} [62] is used as the probe in testing. FIGURE 6-7 shows its structure. A diamond stylus (not shown in the figure) with a radius of 5 μm was fixed on the beam/cantilever using epoxy. It was intended that this probe will be used to measure the bulk stiffness of cells. Its tip size was chosen to be a compromise between a flat punch and a profiling probe capable of imaging cells sufficient to position the tip centrally above a cell. The robustness and stability of this sensor make it ideal for long-term metrological testing. To determine deflection of the cantilever a lock-in amplifier Ref frequency was set as 40 kHz and the output source was 1 Vrms and the filter was set with 1 ms time constant (second order). An AC Wheatstone bridge circuit for converting the capacitance response to an ac voltage was the same one as the tuning fork.

A 10 μm square grating (VLSI Standards Inc. Model STS3-1800P) of 180 nm step height was measured using the capacitance probe. A sensitivity test was run first to get a set-point for PID control.

FIGURE 6-8 shows typical sensor signal voltages as a function of displacement while the specimen is cyclically displaced toward and away from the probe. Each scanning cycle contains 200 points. Increased displacement represents the specimen surface moving towards the probe tip. FIGURE 6-8 (a) shows the approach characteristics (10 cycles) for the probe. The sensitivity is about 0.63 mV nm^{-1} and it became 0.77 mV nm^{-1} as shown in FIGURE 6-8 (b) after 16 hours continuing scanning.

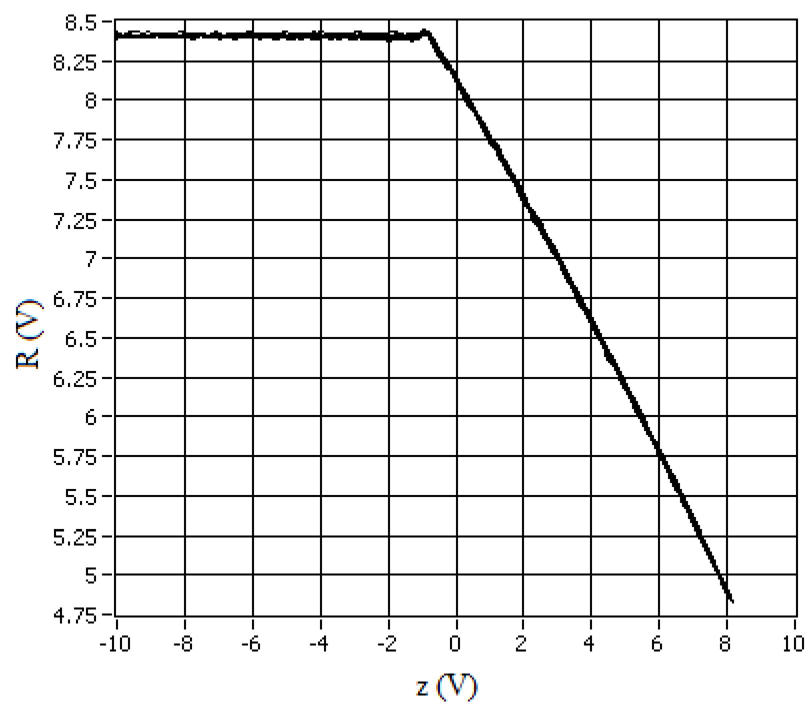

(a)

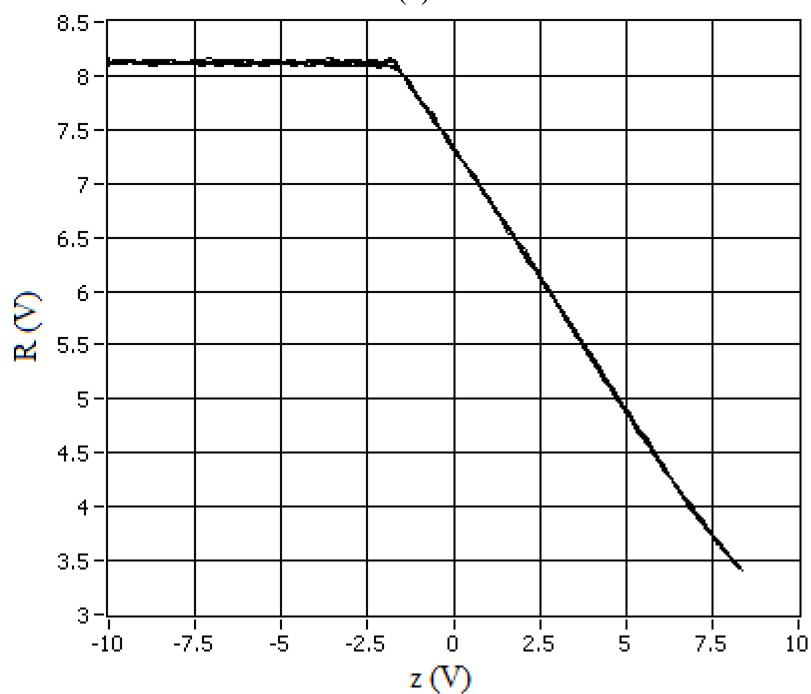

(b)

FIGURE 6-8: Characteristics of the capacitance probe sensitivity. (a) Before one night test, (b) after one night running.

A constant force on the probe tip is maintained by feedback from measurement of the capacitance of the probe which can be expressed as voltage R from the Lock-in amplifier.

The feedback control is achieved by using PID controller in LabVIEW RealTime™ target which keeps the R value at set point by generating the output value to the z PZT, thus z axis moves the stage up and down to reduce the steady-state error, and keep the cantilever deflection to be constant. By modulating the R value with a sine wave as the set point, the P and I can be gradually adjusted [39] from the host computer until the response curve does not osculate and follow the set point . TABLE 6-1 shows the scanning parameters.

TABLE 6-1: Scanning parameters

Parameter (unit)		Note
Scan range (V)	15*7	Capacitance sensor signal
Pixel	512*256	
PID dt (ms)	1	
Set point (V)	7.5	Lock in amplifier
Time constant (ms)	1	Lock in amplifier
Scanning rate	100 Hz	
x axis	$P = 0.0303$, $I = 6.68\text{E-}6$	
y axis	$P = -0.1531$, $I = 9.3\text{E-}5$	
z axis	$P = 0.05$, $I = -7\text{E-}6$	

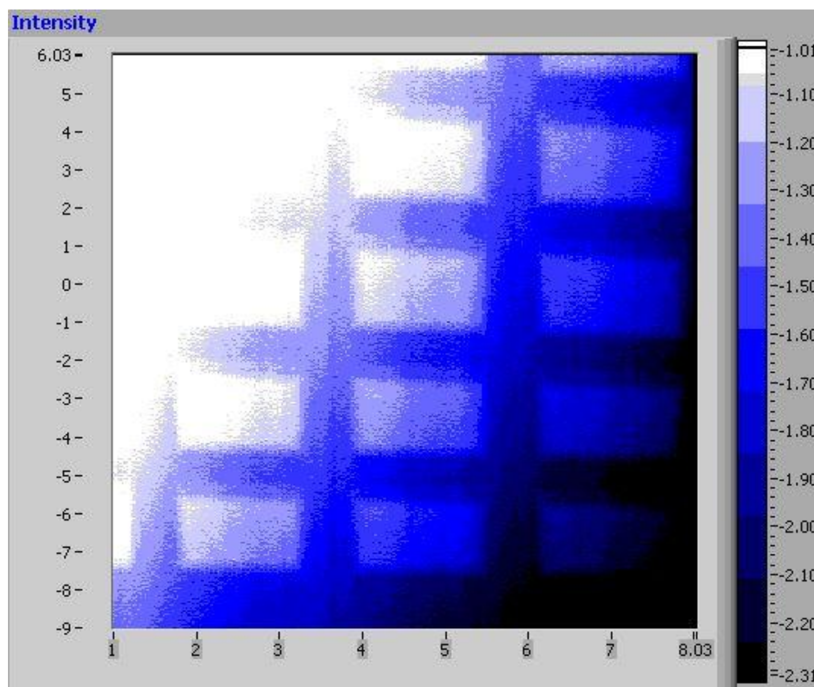

FIGURE 6-9: Screenshot of scanning grating image (values on two axis are not calibrated, unit: V).

FIGURE 6-9 is the real-time image shown in the user interface. The tilted image may be caused by the inclined sample holder. After the de-trend process in Matlab, the image is obtained shown in FIGURE 6-10. FIGURE 6-11 is one trace of the grating image. The PV noise is less than 50 nm which mainly arises from the noise of the z capacitance sensor (using analog demodulation board).

The deflection of the cantilever was detected using capacitance between the reverse face of the beam and the base support yielding a sensitivity of around 320 mV $\cdot\mu m^{-1}$. During imaging, the probe was controlled to a constant offset voltage of 0.75 V corresponding to an applied force of around 100 μN. While this is considered relatively high for imaging with a sharp probe, this is of the order of the meniscus forces for the large radius probe used in this study.

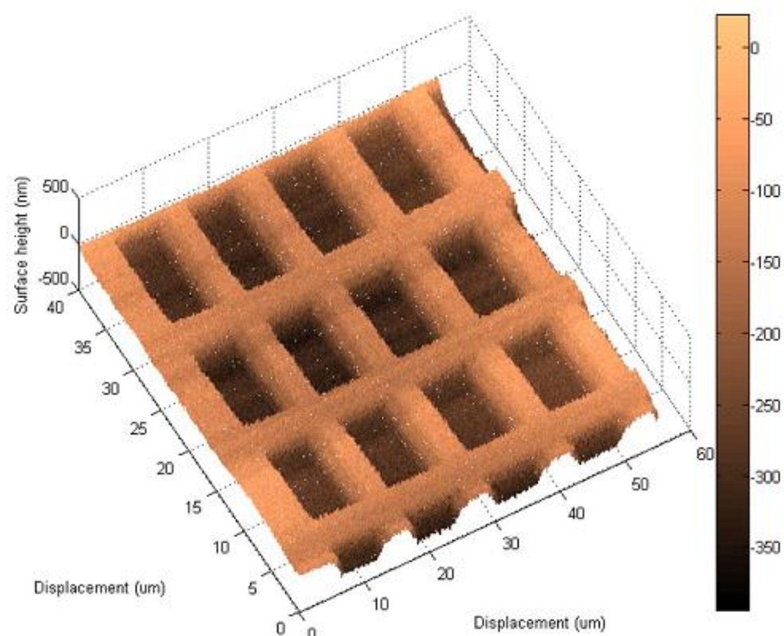

FIGURE 6-10: Grating image using Matlab reconstruction. The image is upside down since the platform moves up with positive applied voltage. Therefore, the grating actually has periods of bulges not holes.

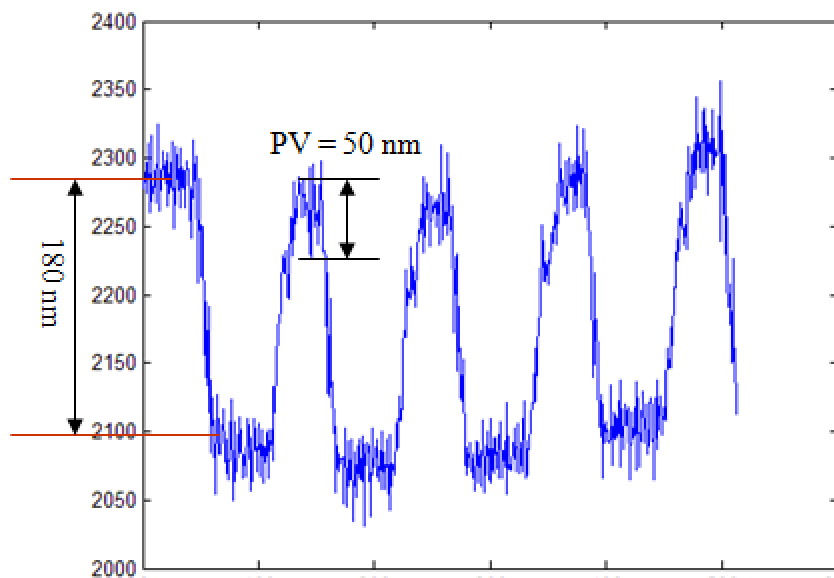

FIGURE 6-11: Trace of the grating image

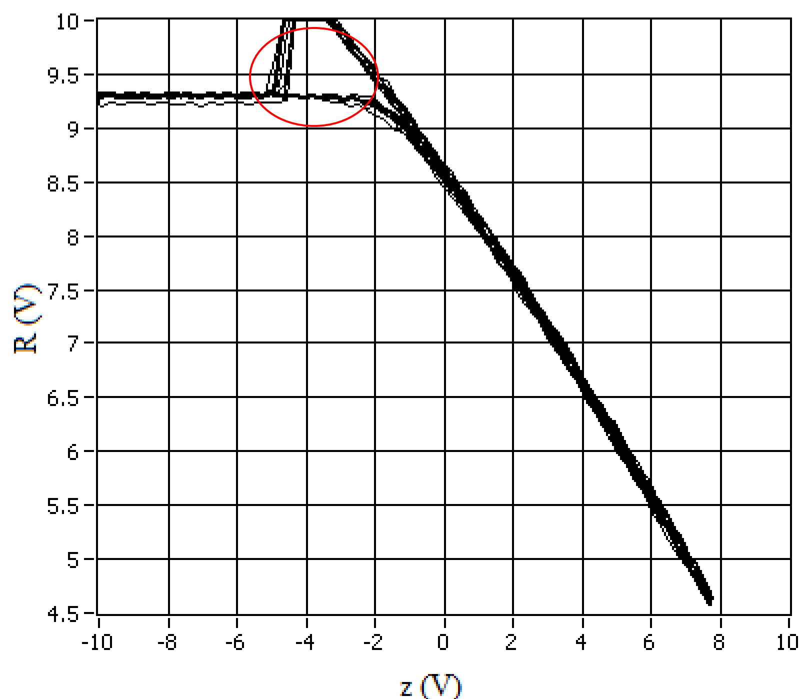

FIGURE 6-12: Probe sensitivity when the bio-specimen without solution

FIGURE 6-12 shows the sensitivity of the probe when scanning a bio-specimen in which the nutrient fluids had been removed.. The red circle indicates that when the probe retracts away from the cell, the cantilever bends downward as surface attraction (meniscus force) holds onto the tip. As PZT actuator continues retracting, the tip finally breaks free of surface attraction. From the sensitivity, an *R* value (about 8 V) was chosen as the set point, a cell sample was images over the full range of the stage (see [43] for more details), see FIGURE 6-13. In this figure, a number of J774 mouse macrophage cells can be seen clumped together on the relatively flat substrate.

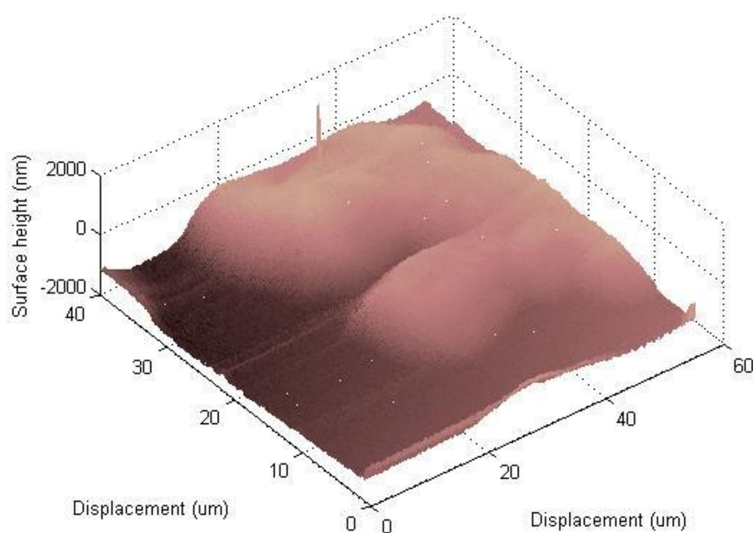

FIGURE 6-13: Scanned probe image of J774 mouse macrophage cells

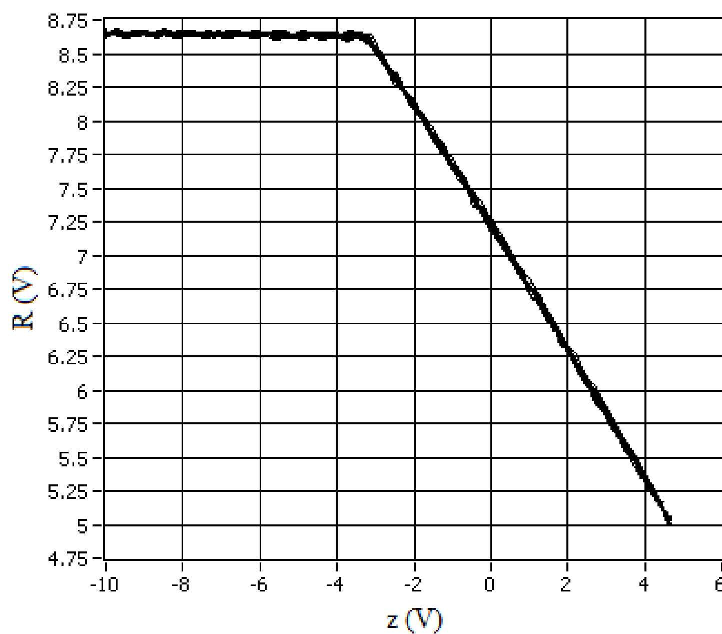

FIGURE 6-14: Probe sensitivity when the bio-specimen is with solution

We also did another test on the sample with the solution, see FIGURE 6-14 for its sensitivity curve versus displacement. It does not show an adhesion feature when the tip leaves away from the surface because there is no change in meniscus force when the tip and sample are in the solution. The *R* rose when the tip just touches the solution which

was not indicated in the curve. However, for unknown reason, we did not successfully obtain the image.

6.3 Conclusion

In this chapter, optical probe system and two mechanical probes are employed to obtain the traditional confocal imaging as well as 3D image topographies. The design and performance of the optical system is introduced and sub-nanometer localization in the x direction is demonstrated through single quantum dot imaging. The sensitivity and stability of the tuning fork probe and capacitance based probe are investigated. A grating and a cell sample measurements are demonstrated. The initial result shows a robust measurement at 1 Hz maximum speed was achieved. The noise level of the sample surface profile measurement is about 50 nm PV which mainly comes from the sensor circuit in the first generation stage development.

This instrument has been used by other researchers for a variety of physical studies. Reference to this work include [23-26]

CHAPTER 7: CONCLUSIONS AND FUTURE WORK

7.1 Conclusions

An in-house built, 3-D positioning and imaging stage (SMPM) is developed and used for biological study. The SMPM utilizes the mechanical force and optical probes which are stationary relative to the instrument frame while the specimen can be navigated in a three-dimensional space in the probing field, translating over a range of 45 μm by 45 μm by 10 μm in the x, y and z axes, respectively, at closed loop speeds of greater than 10 line scans a second with feedback sensing demonstrating nanometer resolution. Using this system, measurements of several artifact gratings using optical and force probes have been achieved. These artifacts include a fluorescent coating on a thin gold film having two dimensional periodicity of 800 nm, and a 10 μm square grating (VLSI Standards Inc. Model STS3-1800P) of 180 nm step height. Many researchers are now using this system for fluorescent imaging of biological and optical structures as well as three dimensional mapping of quantum dots in thin films and surface layers [23-26].

The SMPM implements piezoelectric (PZT) actuated flexure design with capacitance displacement sensor feedback control to obtain the desired positioning resolution. The sources impacting the positioning accuracy of the SMPM are studied, i.e. the sensor error, quantization noise, thermal drift, ground borne vibration, acoustic noise, drift and hysteresis of the actuator, straightness and rotation error from parasitic motions, Abbe

and cosine error. The resolution and bandwidth of the capacitance sensor for position measurement have been improved by implementing a field programmable gate array (FPGA) based digital synchronous demodulation technology as well as the custom designed, surface mount pre-amplifier. System positional dynamics are modeled and these models used to develop controllers and implement compensation to maximize measurement precision for a variety of dynamic scanning algorithms.

The SMPM is digitally controlled using LabVIEW Real-Time™ measurement system. Using this development environment, a graphical user interface for instrument control enables the measurement and positioning of specimen scanning and displays surface imaging results in real time. The software and controller is capable to realize the basic functions of a typical commercial scanning and imaging controlled unit, e.g. scanning controls, contact mode & tapping mode, PID tuning, probe sensitivity test, probe to specimen force curve characterization and multi channels imaging.

A novel dual scanning method for the fluorescence probes microscopy is developed with the SMPM where the fiber source for optical illumination is mounted to a flexure-based piezoelectric *xy* positioner (fast scanner). By scanning the fiber in the *xy* plane, the focused beam scans the sample in the object plane. Initial experimental results show that the scan range of the positioner was 60 μm in each axis at the fiber corresponding to a 5 x 5 μm scan of the spot in the object plane. Such attenuation may be of particular benefit for ultra-high resolution, metrological confocal microscopy. A dual scanning algorithm is implemented by integrating the fast scanner with the original *xyz* sample scanner.

Studies were carried out for a high resolution displacement sensor system. A pico-

meter level resolution fiber optic interferometer system was studied and tested. The current setup is a low finesse, air-glass interface which gives sub-nanometer resolution at 1 kHz bandwidth with limited working range, a few micrometers, at normal lab environment. Pico-meter level resolution from dc to kHz can be reached at vacuum environment over a more limited range.

Another novel sensor is based on the principle of photo interrupter and knife edge using laser coupled optical fiber which provides a simple and stable light source while maintaining a high optical power density within a few micrometer range. Such setup is beneficial for high resolution and low range application. Its low-cost, low-mass and compact size are desirable attributes for a non-intrusive, precision displacement sensor. In these measurements, it has been demonstrated that sub-nanometer resolution in displacement measurement at 1 kHz can be relatively easily obtained by placing knife edge close to a fiber having a core diameter of around 4 micrometers.

7.2 Future work

With the development of second generation design, a lot of problems were addressed and the system performance was improved. The following section provides some future work including individual redesign components.

The current fast scanner working in open loop operation has been validated as a method for confocal imaging. While the fast dynamic response and high resolution has potential to significantly increase productivity as a biological research tool there remain many challenges. These include; validation of this methodology for metrological measurement, optimizing damping, filtering for smoothing digitized drive signals, working in resonant mode, a high stiffness mount for the fast scanner, and developing

scan algorithms capable of recording and storing large data files. The integrated sensor in the fast scanner with tens nanometer resolution at several kilohertz limits the positioning performance. A linear version of stage with capacitance built in design will provide nanometer resolution. The speed can be increased by fixing the fiber directly onto the PZT actuator where the load can be greatly reduced. A more sophisticated control algorithm is required to reduce the ringing vibrations at high accelerations.

More functions can be integrated in future, like mechanical spectroscopy, image processing technology: fluorescence analysis for resonance energy transfer, single molecule analysis and fluorescence anisotropy. The addition of these novel imaging capabilities will makes the system unique and readily extended to novel mechanical and optical probe technologies as they develop. This ability to incorporate technologies as they emerge enables a versatility that cannot be obtained with commercial products.

The laser coupled optical fiber displacement sensor has many unique attributes as mentioned in Chapter 5. Further study is necessary to investigate how the quality of blade edge influences the performance. A smaller fiber, a more stable and high power laser diode source with current control, a smaller active area photodiode with dedicated electronics can be beneficial to the sensor performance. A compact design of such system is beneficial for the fast scanner sensor system.

Force probes including the tuning fork and capacitance based stylus need to be studied and investigated further for specimen imaging. Commercial AFM probes could also be integrated to benefit from a continuous supply and technical support for future users of this system.

REFERENCES

1. Tersoff, J. and D.R. Hamann, *Theory of the scanning tunneling microscope.* Physical Review B, 1985. **31**(2): p. 805.

2. Binnig, G., C.F. Quate, and C. Gerber, *Atomic Force Microscope.* Physical Review Letters, 1986. **56**(9): p. 930.

3. Meyer, et al., *Simultaneous measurement of lateral and normal forces with an optical-beam-deflection atomic force microscope*. Vol. 57. 1990, Melville, NY, ETATS-UNIS: American Institute of Physics.

4. Martin, et al., *Magnetic imaging by force microscopy with 1000 Å resolution*. Vol. 50. 1987, Melville, NY, ETATS-UNIS: American Institute of Physics.

5. Toledo, C., et al., *Near-field differential scanning optical microscope with atomic force regulation*. Vol. 60. 1992, Melville, NY, ETATS-UNIS: American Institute of Physics.

6. Butt and J. H, *Measuring electrostatic, van der Waals, and hydration forces in electrolyte solutions with an atomic force microscope*. Vol. 60. 1991, Cambridge, MA, ETATS-UNIS: Cell Press.

7. Hansma, H.G. and J.H. Hoh, *Biomolecular Imaging with the Atomic Force Microscope.* Annual Review of Biophysics and Biomolecular Structure, 1994. **23**(1): p. 115-140.

8. Butt, H.-J., B. Cappella, and M. Kappl, *Force measurements with the atomic force microscope: Technique, interpretation and applications.* Surface Science Reports, 2005. **59**(1-6): p. 1-152.

9. Rotsch, C., et al., *AFM IMAGING AND ELASTICITY MEASUREMENTS ON LIVING RAT LIVER MACROPHAGES.* Cell Biology International, 1997. **21**(11): p. 685-696.

10. Ohnesorge, F.M., et al., *AFM review study on pox viruses and living cells.* Biophysical Journal, 1997. **73**(4): p. 2183-2194.

11. Zlatanova, J., S.M. Lindsay, and S.H. Leuba, *Single molecule force spectroscopy in biology using the atomic force microscope.* Progress in Biophysics and Molecular Biology, 2000. **74**(1-2): p. 37-61.

12. Cattien, V.N. and et al., *Carbon nanotube tip probes: stability and lateral resolution in scanning probe microscopy and application to surface science in semiconductors.* Nanotechnology, 2001. **12**(3): p. 363.

13. Seiji, A., et al., *Nanotweezers consisting of carbon nanotubes operating in an atomic force microscope*. Vol. 79. 2001: AIP. 1691-1693.

14. Drake, B., et al., *Imaging crystals, polymers, and processes in water with the atomic force microscope.* Science, 1989. **243**(4898): p. 1586-1589.

15. Holmes, M., R. Hocken, and D. Trumper, *The long-range scanning stage: a novel platform for scanned-probe microscopy.* Precision Engineering, 2000. **24**(3): p. 191-209.

16. Axelrod, D., T.P. Burghardt, and N.L. Thompson, *Total Internal Reflection Fluorescence.* Annual Review of Biophysics and Bioengineering, 1984. **13**(1): p. 247-268.

17. Radmacher, M., K. Eberle, and H.E. Gaub, *An AFM with integrated micro-fluorescence optics: design and performance.* Ultramicroscopy, 1992. **42-44, Part 2**(0): p. 968-972.

18. Kassies, R., et al., *Combined AFM and confocal fluorescence microscope for applications in bio-nanotechnology.* Journal of Microscopy, 2005. **217**(1): p. 109-116.

19. Mathur, A.B., G.A. Truskey, and W. Monty Reichert, *Atomic Force and Total Internal Reflection Fluorescence Microscopy for the Study of Force Transmission in Endothelial Cells.* Biophysical Journal, 2000. **78**(4): p. 1725-1735.

20. Chandran, R.S., S.E. John, and M. Amit, *High-throughput scanning confocal microscope for single molecule analysis*. Vol. 84. 2004: AIP. 1216-1218.

21. Xiao, Y., V. Buschmann, and K.D. Weston, *Scanning Fluorescence Correlation Spectroscopy: A Tool for Probing Microsecond Dynamics of Surface-Bound Fluorescent Species.* Analytical Chemistry, 2004. **77**(1): p. 36-46.

22. Elliott, K.E., *DEVELOPMENT OF A VERSATILE SCANNING SYSTEM FOR MULTI-PROBE BIOMEDICAL MEASUREMENTS*, in *MEES*. 2008, UNC Charlotte: Charlotte.

23. Wesley, W., et al. *Evaluating Subsurface Damage with Quantum Dots*. in *Optical Fabrication and Testing*. 2010: Optical Society of America.

24. Williams, W.B., et al., *Using quantum dots to tag subsurface damage in lapped and polished glass samples.* Appl. Opt., 2009. **48**(27): p. 5155-5163.

25. Williams, W., *A Novel Fluorescence Based Method of Assessing Subsurface Damage in Optical Materials*, in *MEES*. 2010, UNC Charlotte: Charlotte.

26. Parker, W.C., et al., *High-resolution intracellular viscosity measurement using time-dependent fluorescence anisotropy.* Opt. Express, 2010. **18**(16): p. 16607-16617.

27. Smith, S.T., *Flexures: elements of elastic mechanisms*. 2000: Gordon & Breach.

28. Smith, S.T. and D.G. Chetwynd, *Foundations of Ultra-Precision Mechanism Design*. 1994: Taylor and Francis.

29. ThorLabs. *Piezoelectric Actuators*. 2011 [cited; Available from: http://www.thorlabs.us/NewGroupPage9.cfm?ObjectGroup_Id=61&popupcart=yes.

30. Ge, P. and M. Jouaneh, *Generalized preisach model for hysteresis nonlinearity of piezoceramic actuators.* Precision Engineering, 1997. **20**(2): p. 99-111.

31. Smith, S.T. and R.M. Seugling, *Sensor and actuator considerations for precision, small machines.* Precision Engineering, 2006. **30**(3): p. 245-264.

32. Xu, Y. and S.T. Smith, *Determination of squeeze film damping in capacitance-based cantilever force probes.* Precision Engineering, 1995. **17**(2): p. 94-100.

33. Baxter, L.K., *Capacitive Sensors: Design and Applications*. 1996: IEEE Press.

34. Precision, L. *DMT 22 capacitance sensor*. 2011 [cited; Available from: http://www.lionprecision.com/.

35. Harb, S.M. and D.G. Chetwynd, *Tilt errors in parallel plate capacitance micrometry*, in *International Congress in Precision Engineering*. 1995.

36. Wulp, H.V.D. and H. Wulp, *Piezo-driven stages for nanopositioning with extreme stability: theoretical aspects and practical design considerations*. 1997: Delft University Press.

37. Woody, S., et al., *Single- and multi-sine DFT demodulation with an application to precision capacitive sensors.* Precision Engineering, 2008. **32**(2): p. 79-87.

38. Hicks, T.R., P.D. Atherton, and L. Queensgate Instruments, *The NanoPositioning book: moving and measuring to better than a Nonometre*. 1997: Queensgate Instruments.

39. Ziegler, J.G.a.N., N. B., *Optimum settings for automatic controllers.* Transactions of the ASME, 1942. **64**: p. 759-768.

40. Goldstein, S.R., et al., *A confocal video-rate laser-beam scanning reflected-light microscope with no moving parts.* Journal of Microscopy, 1990. **157**(1): p. 29-38.

41. Pawley, J.B., *Handbook of biological confocal microscopy*. 2006: Springer.

42. Callamaras, N. and I. Parker, *Construction of a confocal microscope for real-time x-y and x-z imaging.* Cell Calcium, 1999. **26**(6): p. 271-279.

43. Lin, F., et al., *Confocal and force probe imaging system for simultaneous three-dimensional optical and mechanical spectroscopic evaluation of biological samples.* Review of Scientific Instruments, 2009. **80**(5): p. 055110.

44. Bal-Tec. *Truncated ball*. 2011 [cited; Available from: http://www.precisionballs.com/.

45. Feilong Lin, S.T.S., Hussain Ghazanfar, *Optical fiber displacement sensor and its application to tuning fork response measurement.* Precision Engineering, 2011.

46. ThorLabs. *MDT693A - 3 Axis Open Loop Piezo Control* 2011 [cited; Available from: http://www.thorlabs.us/thorProduct.cfm?partNumber=MDT693A.

47. SINGER, et al., *Preshaping command inputs to reduce system vibration*. Vol. 112. 1990, New York, NY, ETATS-UNIS: American Society of Mechanical Engineers.

48. Rappole, B.W., N.C. Singer, and W.P. Seering. *Input Shaping With Negative Sequences for Reducing Vibrations in Flexible Structures*. in *American Control Conference, 1993*. 1993.

49. Mohamed, Z. and M.O. Tokhi, *Command shaping techniques for vibration control of a flexible robot manipulator.* Mechatronics, 2004. **14**(1): p. 69-90.

50. Sadrozinski, H.F.W. and J. Wu, *Applications of Field-Programmable Gate Arrays in Scientific Research*. 2010: TAYLOR & FRANCIS.

51. Jackson, D.A., A. Dandridge, and S.K. Sheem, *Measurement of small phase shifts using a single-mode optical-fiber interferometer.* Opt. Lett., 1980. **5**(4): p. 139-141.

52. Perot, A. and C. Fabry, *On the application of interference phenomena to the solution of various problems of spectroscopy and metrology.* Astropys, 1899. **9**(87).

53. Yoshino, T., et al., *Fiber-Optic Fabry-Perot Interferometer and its Sensor Applications* IEEE Microwave Theory and Techniques, 1982. **30**(10): p. 1612 - 1621.

54. Petuchowski, S., T. Giallorenzi, and S. Sheem, *A sensitive fiber-optic Fabry-Perot interferometer* IEEE Quantum Electronics, 1981. **17**(1): p. 2168-2170.

55. Rugar, D., H.J. Mamin, and P. Guethner, *Improved fiber-optic interferometer for atomic force microscopy.* Applied Physics Letters, 1989. **55**(25): p. 2588.

56. Smith, D.T., J.R. Pratt, and L.P. Howard, *A fiber-optic interferometer with subpicometer resolution for dc and low-frequency displacement measurement.* Review of Scientific Instruments, 2009. **80**(3): p. 035105-035113.

57. Hernandez, G., *Fabry-Perot Interferometers*. 1988: Cambridge University Press.

58. Puppin, E., *Displacement measurements with resolution in the 15 pm range.* Review of Scientific Instruments, 2005. **76**(10): p. 105107.

59. Bass, M., *Handbook of optics*. 1995: New York : McGraw-Hill, c1995. 2nd edition.

60. Shane, W., et al., *Standing wave probes for microassembly*. Vol. 79. 2008: AIP. 085107.

61. Marcin, B.B., et al., *Development of a virtual probe tip with an application to high aspect ratio microscale features*. Vol. 76. 2005: AIP. 095112.

62. Howard, L.P. and S.T. Smith, *A metrological constant force stylus profiler* Rev. Sci. Instrum, 1994. **65**(4): p. 892-902.

APPENDIX A: Spreadsheet for xy fast scanner flexure design

$$I = \frac{bt^3}{12}$$

$$K = \frac{Ebt^3}{L^3}$$

$$K = \frac{12EI}{L^3}$$

$$k = \frac{EA}{L}$$

	flexture(aluminu	PZT						
						motion loss		
E	6.90E+10	4.40E+10				Kf/(Kp+kf)	<0.1	
I	8.33333E-13					Kp>9Kf		
L	0.009	0.02				Kp/10		8.80E+05
A		0.000036						
b(width)	0.01 m					k is limited by this first		
t(thickness)	0.001 m							
δ(motion)	1.51852E-05 m			15.2		atually displacment		15.2 um
K-Linear stiffness	9.47E+05	7.92E+06	when used for cacluation,		<		8.80E+05	
K-Linear stiffness	0.95	7.92	N/um					
Force=K*δ	14.37286499 N		E/10 for pzt					

F preload	40 N		20% of max

$$M_1 = \frac{6EIy}{L^2}$$

$$M_all = (0.5 * F_{preload} + 0.5 * k * \delta_y) * L$$

M1=6EIδ/L/L	6.47E-02					
M2=0.5*Fpreload*L	1.80E-01					
M_all	2.45E-01					
σy=M_all*t/2/I	146.8067355	1.5103574		MPa	yield strength	
					Al 7170	
						400Mpa
					Al 6061	270 MPa

$$\sigma = \frac{Mt}{2I}$$

resonance	4*k	k	
m	0.0121 kg		
wn	17688.7886 rad		8844.394301
fwn	2816.686083 Hz		1407.629096